
Higher Harmonic Control Analysis for Vibration Reduction of Helicopter Rotor Systems

Khanh Q. Nguyen, Ames Research Center, Moffett Field, California

October 1994



National Aeronautics and
Space Administration

Ames Research Center

Moffett Field, California 94035-1000



CONTENTS

LIST OF TABLES	v
LIST OF FIGURES	vi
NOMENCLATURE	x
SUMMARY	1
1 INTRODUCTION	2
1.1 Helicopter Vibrations	2
1.2 Literature Survey on HHC	5
1.3 Current Investigation	17
2 FORMULATION	19
2.1 Coordinate Systems	19
2.2 Hamiltonian Formulation	20
2.3 Aerodynamic Loads	23
2.3.1 Derivation of Blade Velocity	23
2.3.2 Aerodynamic Modeling	26
2.4 Rotor Wake Modeling	37
2.5 Blade and Rotor Hub Loads	40
2.6 Coupled Trim Analysis	47
2.7 Finite Element Discretization in Space	49
2.8 Solution Procedure	51
2.8.1 Nondimensional Procedure	52
2.8.2 Normal Mode Equations	52
2.8.3 Finite Element Discretization in Time	53
2.9 Higher Harmonic Control Model	56
2.10 Higher Harmonic Control Algorithms	57
2.11 Actuator Power Required for HHC Systems	59
3 RESULTS AND DISCUSSION	61
3.1 Correlation Study and HHC Effectiveness	61
3.1.1 Correlation Study	61

3.1.2	Secondary Effects of HHC	65
3.1.3	HHC Induced Blade Stall and Controller Performance	66
3.2	Sensitivity Analysis	67
3.2.1	Hingeless Versus Articulated Rotors	67
3.2.2	Parametric Study—Four-Bladed Hingeless Rotor	68
3.2.3	Parametric Study—Three-Bladed Articulated Rotor	70
4	CONCLUSIONS	73
	REFERENCES	75

TABLES

3.1 Rotor and blade properties	82
3.2 Blade natural frequencies	82

FIGURES

2.1	Rotor coordinate system—hub-fixed frame.	83
2.2	Blade coordinate system and deformations.	83
2.3	Trim configuration for helicopter in forward flight.	84
2.4	Trailing edge separation point—Kirchhoff's flow model.	84
2.5	Blade section aerodynamic environment.	85
2.6	Vortex system from a rotor blade (adapted from ref. 90).	86
2.7	Rotor wake in forward flight (top, adapted from ref. 93) and vortex ring representation (bottom, adapted from ref. 90).	87
2.8	Finite element model of a rotor blade.	88
2.9	Temporal finite element discretization of the rotor revolution.	88
2.10	HHC actuator system on a three-bladed rotor system.	89
3.1	Correlation of $3P$ vertical hub shear—variation with forward speed ($C_T/\sigma = 0.08$).	89
3.2	Correlation of $2P$ rotating inplane hub shear—variation with forward speed ($C_T/\sigma = 0.08$).	90
3.3	Correlation of $4P$ rotating inplane hub shear—variation with forward speed ($C_T/\sigma = 0.08$).	90
3.4	HHC suppression of $3P$ vertical hub shear ($C_T/\sigma = 0.08$).	91
3.5	HHC suppression of $2P$ rotating inplane hub shear ($C_T/\sigma = 0.08$).	91
3.6	HHC suppression of $4P$ rotating inplane hub shear ($C_T/\sigma = 0.08$).	92
3.7	Variation of HHC swashplate amplitudes with forward speed ($C_T/\sigma = 0.08$).	92
3.8	Variation of actuator power index with forward speed ($C_T/\sigma = 0.08$).	93
3.9	Effects of closed-loop HHC controller on the suppression of individual vibratory hub shear components ($V = 135$ knots, $C_T/\sigma = 0.08$).	93
3.10	Actuator amplitudes and power required for the suppression of individual components of vibratory hub shear ($V = 135$ knots, $C_T/\sigma = 0.08$).	94
3.11	Correlation of $3P$ vertical hub shear with and without HHC effects—variation with rotor thrust ($V = 60$ knots).	94
3.12	Correlation of $2P$ rotating inplane hub shear with and without HHC effects—variation with rotor thrust ($V = 60$ knots).	95
3.13	Correlation of $4P$ rotating inplane hub shear with and without HHC effects—variation with rotor thrust ($V = 60$ knots).	95
3.14	Variation of actuator amplitudes with thrust level ($V = 60$ knots).	96

3.15	Variation of actuator phase angle with thrust level ($V = 60$ knots).	96
3.16	Variation of actuator power index with thrust level ($V = 60$ knots).	97
3.17	HHC effects on the alternating flap bending moment ($V = 60$ knots).	97
3.18	HHC effects on the alternating lag bending moment ($V = 60$ knots).	98
3.19	HHC effects on the alternating torsional moment ($V = 60$ knots).	98
3.20	HHC effects on the alternating pitch-link load ($V = 60$ knots).	99
3.21	HHC effects on the rotor shaft torque ($V = 60$ knots).	99
3.22	Vibratory hub shear responses with fixed-gain HHC controller, $r = 0.0$ ($V = 135$ knots, $C_T/\sigma = 0.09$).	100
3.23	Variation of normal force coefficient at 0.93 radius with HHC off ($V = 135$ knots, $C_T/\sigma = 0.09$).	100
3.24	Variation of normal force coefficient at 0.93 radius with HHC on, fixed-gain controller, $r = 0.0$ ($V = 135$ knots, $C_T/\sigma = 0.09$).	101
3.25	Vibratory hub shear responses with fixed-gain HHC controller, $r = 0.0$ ($V = 135$ knots, $C_T/\sigma = 0.135$).	101
3.26	Variation of normal force coefficient at 0.93 radius with HHC off ($V = 135$ knots, $C_T/\sigma = 0.135$).	102
3.27	Variation of normal force coefficient at 0.93 radius with HHC on, fixed-gain controller, $r = 0.0$ ($V = 135$ knots, $C_T/\sigma = 0.135$).	102
3.28	Vibratory hub shear responses with adaptive-gain HHC controller, $r = 0.3$ ($V = 135$ knots, $C_T/\sigma = 0.135$).	103
3.29	Variation of normal force coefficient at 0.93 radius with HHC on, adaptive-gain controller, $r = 0.3$ ($V = 135$ knots, $C_T/\sigma = 0.135$).	103
3.30	Stall area on rotor disk with HHC off ($V = 135$ knots, $C_T/\sigma = 0.12$).	104
3.31	Stall area on rotor disk with HHC on, adaptive-gain controller, $r = 0.3$ ($V = 135$ knots, $C_T/\sigma = 0.12$).	105
3.32	Variation of $3P$ vertical hub shear with forward speed for different rotor systems ($C_T/\sigma = 0.08$).	106
3.33	Variation of $2P$ rotating inplane hub shear with forward speed for different rotor systems ($C_T/\sigma = 0.08$).	106
3.34	Variation of $4P$ rotating inplane hub shear with forward speed for different rotor systems ($C_T/\sigma = 0.08$).	107
3.35	Variation of actuator power index with forward speed for different rotor systems ($C_T/\sigma = 0.08$).	107

3.36	Effects of blade torsion stiffness on the uncontrolled vibratory hub shears ($V = 40$ knots, $C_T/\sigma = 0.08$).	108
3.37	Effects of blade torsion stiffness on the uncontrolled vibratory hub moments ($V = 40$ knots, $C_T/\sigma = 0.08$).	108
3.38	Effects of blade torsion stiffness on the HHC actuator power ($V = 40$ knots, $C_T/\sigma = 0.08$).	109
3.39	Effects of blade flap stiffness on the uncontrolled vibratory hub shears ($V = 40$ knots, $C_T/\sigma = 0.08$).	109
3.40	Effects of blade flap stiffness on the uncontrolled vibratory hub moments ($V = 40$ knots, $C_T/\sigma = 0.08$).	110
3.41	Effects of blade flap stiffness on the HHC actuator power ($V = 40$ knots, $C_T/\sigma = 0.08$).	110
3.42	Effects of blade lag stiffness on the uncontrolled vibratory hub shears ($V = 40$ knots, $C_T/\sigma = 0.08$).	111
3.43	Effects of blade lag stiffness on the uncontrolled vibratory hub moments ($V = 40$ knots, $C_T/\sigma = 0.08$).	111
3.44	Effects of blade lag stiffness on the HHC actuator power ($V = 40$ knots, $C_T/\sigma = 0.08$).	112
3.45	Effects of blade linear pretwist on the uncontrolled vibratory hub shears ($V = 40$ knots, $C_T/\sigma = 0.08$).	112
3.46	Effects of blade linear pretwist on the uncontrolled vibratory hub moments ($V = 40$ knots, $C_T/\sigma = 0.08$).	113
3.47	Effects of blade linear pretwist on the HHC actuator power ($V = 40$ knots, $C_T/\sigma = 0.08$).	113
3.48	Effects of blade center-of-mass offset from elastic axis on the uncontrolled vibratory hub shears ($V = 40$ knots, $C_T/\sigma = 0.08$).	114
3.49	Effects of blade center-of-mass offset from elastic axis on the uncontrolled vibratory hub moments ($V = 40$ knots, $C_T/\sigma = 0.08$).	114
3.50	Effects of blade center-of-mass offset from elastic axis on the HHC actuator power ($V = 40$ knots, $C_T/\sigma = 0.08$).	115
3.51	Effects of blade elastic axis offset from quarter chord on the uncontrolled vibratory hub shears ($V = 40$ knots, $C_T/\sigma = 0.08$).	115
3.52	Effects of blade elastic axis offset from quarter chord on the uncontrolled vibratory hub moments ($V = 40$ knots, $C_T/\sigma = 0.08$).	116
3.53	Effects of blade elastic axis offset from quarter chord on the HHC actuator power ($V = 40$ knots, $C_T/\sigma = 0.08$).	116
3.54	Effects of rotor thrust on the uncontrolled vibratory hub shears ($V = 40$ knots, $C_T/\sigma = 0.08$).	117

3.55	Effects of rotor thrust on the uncontrolled vibratory hub moments ($V = 40$ knots, $C_T/\sigma = 0.08$).	117
3.56	Effects of rotor thrust on the HHC actuator power ($V = 40$ knots, $C_T/\sigma = 0.08$).	118
3.57	Effects of blade torsion stiffness on the uncontrolled vibratory hub shears ($V = 135$ knots, $C_T/\sigma = 0.12$).	118
3.58	Effects of blade torsion stiffness on the HHC actuator power ($V = 135$ knots, $C_T/\sigma = 0.12$).	119
3.59	Effects of blade flap stiffness on the uncontrolled vibratory hub shears ($V = 135$ knots, $C_T/\sigma = 0.12$).	119
3.60	Effects of blade flap stiffness on the HHC actuator power ($V = 135$ knots, $C_T/\sigma = 0.12$).	120
3.61	Effects of blade lag stiffness on the uncontrolled vibratory hub shears ($V = 135$ knots, $C_T/\sigma = 0.12$).	120
3.62	Effects of blade lag stiffness on the HHC actuator power ($V = 135$ knots, $C_T/\sigma = 0.12$).	121
3.63	Effects of blade center-of-mass offset from elastic axis on the uncontrolled vibratory hub shears ($V = 135$ knots, $C_T/\sigma = 0.12$).	121
3.64	Effects of blade center-of-mass offset from elastic axis on the HHC actuator power ($V = 135$ knots, $C_T/\sigma = 0.12$).	122
3.65	Effects of blade elastic axis offset from quarter chord on the uncontrolled vibratory hub shears ($V = 135$ knots, $C_T/\sigma = 0.12$).	122
3.66	Effects of blade elastic axis offset from quarter chord on the HHC actuator power ($V = 135$ knots, $C_T/\sigma = 0.12$).	123

NOMENCLATURE

a	blade acceleration vector relative to an inertial frame
A	blade cross-sectional area
A_e	effective piston area of hydraulic actuator
A_n	coefficients of indicial functions
b_n	poles of unsteady aerodynamic model
c	blade chord
C	blade section chord force, $C = \bar{L}_v$
C	modal damping matrix
C_0	lift coefficient at zero angle of attack
C_1	compressible lift curve slope, $C_1 = C_{L_\alpha}/\beta$
C_c	chord force coefficient
$C_{col}, C_{long}, C_{lat}$	N_b per rev swashplate motions in the collective, longitudinal and lateral modes, respectively
C_d	blade section drag coefficient
CG	global damping matrix
C_L	blade section lift coefficient
C_{L_α}	lift curve slope at reference Mach number
C_{MV}	leading edge vortex induced pitching moment coefficient
C_N	normal force coefficient
C'_N	substitute normal force coefficient
C_{N_1}	critical normal force coefficient
C_{N_L}	linear part of normal force coefficient
C_{NV}	leading edge vortex induced normal force coefficient
C_T	rotor thrust coefficient
C_V	incremental lift coefficient, equation 2.70
CP_V	airfoil center of pressure due to vortex dynamics
d_0	viscous drag coefficient
d_1, d_2	pressure drag coefficients
D_F	fuselage drag
D_R	blade section drag component, $D_R = \bar{L}_u$
E	Young's modulus
e_a	chordwise offset of tensile axis ahead of elastic axis
e_d	chordwise offset of aerodynamic center behind elastic axis
e_g	chordwise offset of blade center-of-mass ahead of elastic axis
e_ξ, e_η, e_ζ	basis vector for the (ξ, η, ζ) coordinate system
f	trailing edge separation point, relative to leading edge
F	blade axial force
F	modal load vector
f'	quasi-steady trailing edge separation point
f''	effective trailing edge separation point
f_0	aerodynamic pitching moment coefficient at zero angle of attack
F^I	distributed inertial force vector

FG	global load vector
F_x, F_y, F_z	resultant blade section shears in x, y, z directions, respectively
F_x^H, F_y^H, F_z^H	rotor hub shears in fixed frame in X, Y, Z directions, respectively
F_x^R, F_y^R, F_z^R	rotor hub shears in the rotating frame, in x, y, z directions, respectively
G	shear modulus
GJ	effective sectional torsional stiffness
H	shape function matrix
\dot{h}	blade plunging velocity
\bar{h}	vertical distance from helicopter center of gravity to hub center, along Z axis
$\hat{i}, \hat{j}, \hat{k}$	basis vector for the (x, y, z) coordinate system
$\hat{I}, \hat{J}, \hat{K}$	basis vector for the (X, Y, Z) coordinate system
I_y, I_z	blade cross-sectional moment of inertia about y and z axis, respectively
J	quadratic performance index
K	modal stiffness matrix
k_0	chordwise offset of aerodynamic center from quarter chord
k_1, k_2	coefficients for nonlinear aerodynamic pitching moment
k_A	blade cross-sectional area radius of gyration
k_m	blade cross-sectional mass radius of gyration
k_{m_1}, k_{m_2}	blade cross-sectional mass radius of gyrations in the y and z directions, respectively
K_f	exponential constant for gross separation chord force
KG	global stiffness matrix
K_{M_h}	time constant for impulsive pitching moment due to blade plunging velocity
K_{M_α}	time constant for impulsive pitching moment due to pitch rate
K_t^G	Jacobian for the generalized load vector Q^G
K_α	time constant for impulsive lift component
L	blade section lift
l_i	length of the i th beam element
L_u, L_v, L_w	distributed blade airloads in the x, y, z directions, respectively
$\bar{L}_u, \bar{L}_v, \bar{L}_w$	distributed blade airloads in the ξ, η, ζ directions, respectively
m	blade section mass
M	Mach number
M	modal mass matrix
m_o	reference blade section mass
M_g	global mass matrix
M_x, M_y, M_z	resultant blade bending moments in the x, y, z directions, respectively
M_X^H, M_Y^H, M_Z^H	rotor hub moment components in the X, Y, Z directions in the hub fixed frame, respectively
M_x^R, M_y^R, M_z^R	rotor hub moment components in the x, y, z directions in the hub rotating frame, respectively
M_ϕ	blade sectional pitching moment about deformed elastic axis
n	number of beam elements for the blade modeling
N	blade section normal force

N_b	blade number
N_e	number of time elements for one rotor revolution
N_G	number of degrees of freedom for beam model
\mathbf{p}	modal displacement vector
p_e	effective pump pressure for hydraulic actuator
P_I	actuator power index
P_r	actuator power requirement
q	nondimensional airfoil pitch rate, $q = \frac{\dot{\alpha}c}{2V}$
\mathbf{q}	global displacement vector.
Q	fluid volume flow rate for hydraulic actuator
\mathbf{Q}	generalized load vector
r	control rate limiting factor or radial blade station
\mathbf{r}	blade displacement vector in the rotating blade frame
R	blade radius
s	temporal coordinate of time element or distance traveled by airfoil in semi-chord, $s = \frac{2}{c} \int V(t) dt$
S_n	accumulative index for higher harmonic swashplate amplitudes
t	time
T	rotor thrust or transfer matrix for HHC model
\mathbf{T}^1	coordinate transformation from hub fixed to rotating blade frame
\mathbf{T}^2	coordinate transformation from rotating frame with no precone to that with precone
\mathbf{T}^3	coordinate transformation from undeformed blade frame to deformed blade frame
T_f	time constant for boundary layer response
T_p	time constant for leading edge pressure response
T_v	time constant for leading edge vortex dynamics
T_{VL}	leading edge vortex convection rate
u	blade displacement in the x direction
v	blade displacement in the y direction
V	helicopter forward speed
\mathbf{V}	resultant blade velocity vector
\mathbf{V}_b	blade velocity vector
\mathbf{V}_w	air velocity vector
w	blade displacement in the z direction
W_z, W_θ	weighting matrices for z and θ , respectively
x, y, z	undeformed blade coordinate system
X, Y, Z	fuselage coordinate system
x_{CG}, y_{CG}	hub center position relative to helicopter center of gravity in the X and Y directions, respectively
\mathbf{y}_G	modal state vector
Y_F	fuselage side force
z, z_o	vectors of cosine and sine harmonics of controlled and uncontrolled vibratory hub loads, respectively

\mathcal{G}, \mathcal{K}	nonlinear aerodynamic factors
α	blade section angle of attack
α_f	effective angle of attack, used in the calculation of f
α_s	longitudinal shaft tilt relative to wind axis
β	compressibility factor, $\beta = \sqrt{1 - M^2}$
β_p	blade precone
Γ_0	vortex ring strength
$\delta T, \delta U, \delta W$	variations in blade kinetic and strain energies, and virtual work done by nonconservative forces
$\delta(\cdot)$	virtual variation
$\Delta(\cdot)$	$(\cdot)_n - (\cdot)_{n-1}$
ϵ	parameter having the order of w/R or v/R
η_a	leading edge suction recovery factor
η_r	referenced location on deformed elastic axis
θ	vector of cosine and sine harmonics of HHC inputs or control pitch angle
θ_1	blade pitch angle resulting from control pitch and geometric twist
θ_{1c}, θ_{1s}	lateral and longitudinal cyclic trim inputs, respectively
$\theta_{.75}$	collective blade pitch at 0.75 percent radius
θ_{tw}	blade linear pretwist
κ_x, κ_y	longitudinal and lateral tilts of linear inflow model
λ	rotor total inflow
Λ	blade yaw angle
λ_i	rotor induced inflow
μ	rotor advance ratio
ξ, η, ζ	rotating deformed blade coordinate system
ξ	temporal modal displacement vector for time element
ρ	air density or radial distance from core center and core radius
ρ_s	blade structural density
σ	rotor solidity ratio
τ_v	leading edge vortex time
ϕ	elastic blade twist about deformed elastic axis
Φ	gross separation correction factor for chord force
Φ	normal mode transformation matrix
$\phi(s)$	aerodynamic indicial response function
$\hat{\phi}$	geometric blade twist
ϕ_s	lateral shaft tilt
Ψ	rotor azimuth angle
ω	blade natural frequency
Ω	rotor rotational speed
$(\cdot)'$	$\partial(\cdot)/\partial x$
$(\cdot)''$	$\partial(\cdot)/\partial x^2$
(\cdot)	$\partial(\cdot)/\partial t$
$(\cdot)^*$	$\partial(\cdot)/\partial \Psi$

Subscripts and Superscripts

$(\cdot)_{av}$	average of (\cdot)
$(\cdot)_c, (\cdot)^c$	circulatory origin
$(\cdot)_i, (\cdot)^i$	impulsive or noncirculatory origin
$(\cdot)_{nc}, (\cdot)_{ns}$	n th harmonics of cosine and sine components of (\cdot) , respectively
$(\cdot)^A$	aerodynamic quantity
$(\cdot)^I$	inertial quantity
$(\cdot)^S$	structural quantity

HIGHER HARMONIC CONTROL ANALYSIS FOR VIBRATION REDUCTION OF HELICOPTER ROTOR SYSTEMS

Khanh Q. Nguyen

Ames Research Center

SUMMARY

An advanced higher harmonic control (HHC) analysis has been developed and applied to investigate its effect on vibration reduction levels, blade and control system fatigue loads, rotor performance, and power requirements of servo-actuators. The analysis is based on a finite element method in space and time. A nonlinear time domain unsteady aerodynamic model, based on the indicial response formulation, is used to calculate the airloads. The rotor induced inflow is computed using a free wake model. The vehicle trim controls and blade steady responses are solved as one coupled solution using a modified Newton method. A linear frequency-domain quasi-steady transfer matrix is used to relate the harmonics of the vibratory hub loads to the harmonics of the HHC inputs. Optimal HHC is calculated from the minimization of the vibratory hub loads expressed in term of a quadratic performance index. Predicted vibratory hub shears are correlated with wind tunnel data. The fixed-gain HHC controller suppresses completely the vibratory hub shears for most of steady or quasi-steady flight conditions. HHC actuator amplitudes and power increase significantly at high forward speeds (above 100 knots). Due to the applied HHC, the blade torsional stresses and control loads are increased substantially. For flight conditions where the blades are stalled considerably, the HHC input-output model is quite nonlinear. For such cases, the adaptive-gain controller is effective in suppressing vibratory hub loads, even though HHC may actually increase stall areas on the rotor disk. The fixed-gain controller performs poorly for such flight conditions. Comparison study of different rotor systems indicates that a soft-inplane hingeless rotor requires less actuator power at high speeds (above 130 knots) than an articulated rotor, and a stiff-inplane hingeless rotor generally requires more actuator power than an articulated or a soft-inplane hingeless rotor. Parametric studies for a hingeless rotor operating in a transition flight regime and for an articulated rotor operating at the level-flight boundary (high speed and high thrust conditions) indicate that blade parameters including flap, lag, torsion stiffness distributions, linear pretwist, chordwise offset of center-of-mass from elastic axis and chordwise offset of elastic axis from aerodynamic center can be selected to minimize the actuator power requirements for HHC.

1 INTRODUCTION

Inherent in the aircraft's design, vibration has remained one of the major problems facing helicopter development for years. With current passive vibration alleviation methodologies, vibration in helicopters has been reduced to an acceptable level over most of the flight envelope at the price of a substantial weight penalty. Currently, the maximum speed and maneuvering capabilities for most of the modern helicopters are limited by excessive vibration. With growing demands to expand the helicopter flight envelope and stringent requirements for lower vibration levels, effective and efficient vibration control systems are required. In this regard, the higher harmonic control systems have the potential for giving the helicopter a "jet-smooth" flight.

1.1 Helicopter Vibrations

Unlike fixed-wing aircraft, where vibrations primarily originate from the engines or are caused by atmospheric turbulence, the major source of vibration in a helicopter is the rotor. In fact, helicopter vibration is an aeroelastic problem which involves the complex interactions between the aerodynamic, inertial, and structural loads. The helicopter rotor, designed primarily to hover, is also required to have a forward flight capability and so must be able to move edgewise through the air. The primary source of helicopter vibration is the aerodynamic environment on the rotor disk. In this environment, a rotor blade section encounters a periodic variation in the free-stream velocity. At high forward speeds, the blades experience substantial transonic effects at the advancing tips, dynamic stall and reverse flow on the retreating side, and swept flow in the fore and aft regions of the rotor disk. Due to the aerodynamic environment and the inherent blade flexibilities, the rotor blades undergo large periodic motions which, in turn, are fed back as a source of input driving the aerodynamic loads. Therefore, rotor analysis must be considered as an aeroelastic problem since the blade motions are coupled with the aerodynamic loads.

In addition, the temporal and spanwise variations in the blade airload forms in a system of shed and trailed vorticities behind the rotor disk. This vortex system induces an unsteady rotor nonuniform inflow which directly affects the blade angle of attack and, in turn, influences the blade airloads. For certain flight conditions, close blade-vortex interaction is also a significant source of helicopter vibration. As in the case of the blade motion-airload interaction, the induced inflow-airload interaction forms a second closed-loop in the rotor aeroelastic problem.

The periodic variations in blade free-stream velocity and blade angle of attack produce blade airloads at many harmonics of the rotor rotational speed. Combined with the higher harmonic inertial loads, these result in multiharmonic blade loads transmitted through the rotor hub to the airframe and hence as a source of helicopter vibration.

In general, not all harmonics of the blade loads are transmitted to the fuselage. This is certainly true for a properly tracked rotor with equally spaced blades. For a tracked rotor, all blades have identical aeroelastic behavior except for an equal phase difference around the rotor azimuth. The blade loads consist of many harmonics of the rotor rotational speed which tend to lower magnitudes at the higher frequencies. For the vertical hub force and the rotor torque, only the blade loads harmonics at pN_b per rev (where N_b is the blade number, p is a nonnegative integer) are summed to yield the hub loads at

pN_b per rev. For the inplane hub shears and moments, only the blade load harmonics at $pN_b - 1$ and $pN_b + 1$ per rev contribute to the fuselage vibration at pN_b per rev. The sum of all other harmonics cancels out at the hub.

Regardless of which harmonics of the blade loads are transmitted through the hub, the resultant hub loads in the nonrotating frame—or fixed frame—occur only at pN_b per rev. For the case when p is zero, the steady components of the hub loads act as a source of steady forces and moments on the fuselage, while the hub loads harmonics at N_b per rev generally contribute to airframe vibration. The higher harmonics of hub load at $2N_b, 3N_b, \dots$ per rev are typically much smaller than the N_b per rev components and thus can be neglected. Although these vibratory hub loads dominate the vibration problem, they are not the only source of helicopter vibration. The vibration contributions from the engine, wake induced loads acting on the fuselage and control surfaces, the tail rotor, and small differences between blades are typically small.

Vibration has remained one of the major problem for helicopters. It affects the helicopter handling qualities, contributes to the fatigue of structural components, reduces the reliability of on-board electronic equipment, and influences weapon aiming precision in military aircraft. Vibration affects ride comfort, adds to the fatigue of pilots, crew, and passengers and also increases maintenance time and cost. The high vibration levels experienced by a helicopter could in many cases pose a limitation to the vehicle forward speed and maneuvering capabilities.

Currently, there are several approaches to reduce helicopter vibration (refs. 1–3). A natural approach, usually performed at the vehicle design phase, involves the placements of blade and fuselage natural vibration frequencies away from the rotor harmonic frequencies. These tuning effects help avoid blade and fuselage resonances with the rotor harmonics. This method, however, requires extensive modeling and testing of the blade and fuselage structural characteristics throughout the aircraft development phase. Recently, structural optimization techniques are under consideration to design the rotor and the fuselage in order to reduce the transmitted vibratory hub loads and the fuselage vibration.

In spite of careful rotor design, significant vibrations exist in flight, and this necessitates the addition of further vibration control devices. The passive vibration control devices currently used in helicopters can be classified according to whether the vibrations are reduced at the rotor, at the fuselage, or by isolating the rotor from the fuselage. Dynamic absorbers are the vibration control devices mounted on blades or rotor hub. These devices can be considered essentially as spring-mass systems and are tuned to vibrate in such a way that the oscillatory blade loads are canceled before being transmitted to the rotor hub. The problem of pendulum absorbers is that each mode of vibration requires a separate absorber, and this makes the complete absorber system rather complicated. Also, due to the inability of current rotor analysis to accurately predict the vibratory loads, pendulum absorbers can only be tuned through repetitive flight tests.

Rotor isolation is another popular vibration reduction technique and has been applied in several variations. Flexible mounting of the rotor structures to the fuselage can be designed in such a way as to minimize the transmission of the vibratory hub loads. In another variation, the rotor and the engine gearbox are mounted on a nodal-beam structure. The beam structure is configured such that the vehicle airframe is connected to the beam nodal points; hence, under excitation, only small oscillatory forces are transmitted to the fuselage. Another isolation device, typically known as the dynamic antiresonant

vibration isolator (DAVI), combines some of the best features of isolation and dynamic absorbers. Basically, this device consists of spring elements to which pendulums are attached. With proper tuning, the work done by the vibratory hub loads will be absorbed by the spring mechanism strain energy or consumed by the pendulum kinetic energy. In general, DAVI offers much better performance than simple isolation or absorber devices.

The vibration reduction methods in the fuselage use either vibration absorbers which are tuned to the troublesome frequencies and placed at selected locations in the fuselage or vibration isolators in the form of soft mounting of the cabin floor to the airframe structures. With proper airframe design, the critical locations can be placed close to the nodes of the fuselage excited modes. In general, the methods of reducing vibration in the fuselage can only achieve local effects.

Together, these four techniques represent the vibration control technology currently used on production helicopters. With proper design, tuning, and selection, they can provide a relatively comfortable ride over a large part of the helicopter flight envelope. However, these devices contribute to a significant weight penalty for the aircraft. Furthermore, their performance is quite restrictive and can deteriorate at high speeds and during maneuvers. Also, they are typically tuned only to selected locations in the airframe and work effectively for a certain range of the aircraft gross weight, payload distribution, and fuel loading.

Up to now, the specifications for the desired vibration levels have generally been lower than the levels that could be attained with production helicopters. In the past, such specifications had to be modified considerably to a level realizable with current technology. In 1976, the NASA Research and Technology Advisory Council Subpanel on Helicopter Technology recommended a cabin vibration level of 0.02 g. This level could be achieved only if there were a major technological breakthrough in vibration control methods.

Recently, a major advance in vibration control technology appears possible with the development of higher harmonic control (HHC), also known as multicyclic control. In contrast to passive vibration control systems which suppress the vibratory loads after they have been generated, an HHC system suppresses the vibrations at the source—the higher harmonic blade airloads. Higher harmonic control is an active vibration control system wherein the vibratory airloads are controlled at the higher harmonics of rotor rotational speed. Operated through an arrangement of sensors and microprocessors, higher harmonic inputs are applied to the blade generating new unsteady aerodynamic loads which, in combination with the resultant inertial loads, cancel the existing vibratory blade loads that cause the airframe vibration.

There are many ways to implement HHC on a rotor system. The most popular approach is blade root feathering using swashplate oscillations. Using servo-actuators, the swashplate is excited in the collective, longitudinal cyclic, and lateral cyclic modes at N_b per rev, resulting in blade pitch oscillations at three distinct frequencies of $N_b - 1$, N_b , and $N_b + 1$ per rev in the blade rotating frame. For other HHC systems, the higher harmonic inputs are applied using jet flaps (refs. 4–7), partial-span flaps (refs. 8–11), circulation control rotor (refs. 12 and 13), and individual blade control system (refs. 14 and 15).

1.2 Literature Survey on HHC

The concept of higher harmonic control was first proposed in the late forties, but it was not until 1961 when it was conceived as a potential vibration control method for helicopters. In 1948, Winson (ref. 16) suggested that the higher harmonic blade pitch could be applied to rotors tested on whirl towers to simulate the oscillatory blade stresses induced in forward flight. This idea was pursued by Jensen (ref. 17) in 1951, who applied second harmonic control to the S-52 metal main rotor blades operated on the Sikorsky rotor test stand.

In 1952, Stewart (ref. 18) suggested that the second harmonic control applied to rotors in forward flight could be used to delay the onset of retreating blade stall. Based on his analysis, Stewart discovered that the rotor disk loading could efficiently be redistributed using second harmonic control. For a particular flight condition, such loading redistribution could be adjusted to avoid retreating blade stall. The resulting effect would be to raise the speed limitation of helicopters. According to his analysis, helicopter speed limit could be increased by the order of 0.1 in terms of advance ratio. His analysis was, however, limited to a rigid flapping blade, and the airloads were calculated with quasi-steady aerodynamics and a uniform inflow distribution. Therefore, the severe aerodynamic effects associated with the transonic effects, separated flow conditions, and the participation of blade elastic modes in the rotor aeroelastic responses were all neglected.

In 1961, Arcidiacono (ref. 19) extended Stewart's analysis by considering both second and higher harmonic blade pitch control. In his report, Arcidiacono noted that a combination of second and third harmonic blade feathering could be used to delay the onset of retreating blade stall to an even higher advance ratio than that reported by Stewart. Like Stewart, Arcidiacono did not consider the effects of higher harmonic inputs on the rotor vibratory hub loads.

In 1961, for the first time, a flight test program was carried out to investigate the feasibility of using HHC for vibration reduction on an UH-1A two-bladed teetering rotor helicopter (ref. 20). Prompted by some earlier unpublished analyses and a design of the simple rotor head mechanism to generate second harmonic blade pitch, Bell Helicopter Company conducted a series of flight tests to determine the effects of HHC on rotor performance, blade airloads, blade and control loads, hub loads, and airframe vibration.

Investigating HHC effects on rotor performance, these investigators noted that no reduction in shaft torque was observed. Further investigation indicated that the drag reduction in the retreating side was accompanied by an increase in profile drag in the fore and aft portions of the rotor disk. These results confirmed Stewart's prediction that the second higher harmonic control could be used to alter the rotor disk loading, although no reduction in power was observed at 100 knots. The reduction in the stall-induced power was later found to be commensurate with an increase in the profile power due to changes in the blade section angle of attack.

On vibration, these authors stated that none of the combinations of second harmonic control amplitude and phase could completely suppress the vibration at any one of three fuselage stations being monitored. At best, the vibration measured at the station located right beneath the rotor hub was reduced by about 50 percent. These authors pointed out that the complex interactions between the various components of the vibratory hub loads were the cause of incomplete vibration reduction and concluded

that more comprehensive understanding of HHC effects was required before the system could become fully effective.

Since then, several investigators had conducted analytical simulation of HHC for vibration reduction. Daughaday (ref. 21) presented the analysis using a type of higher harmonic blade pitch control which required both temporal and spanwise variations. These higher harmonic blade pitches were necessary to reduce a set of even harmonic shaftwise hub forces for a two-bladed teetering rotor. In particular, this type of control schedule is quite impractical because it requires the adjustability of the blade pitch angle along the blade span. In this analysis, the rotor induced inflow is calculated using a vortex wake analysis, and the effects of shed vorticity were also included. In an analysis similar to that of Daughaday, Shaw (ref. 22) carried out an HHC investigation including the effects of third harmonic (rigid) blade root feathering on the vibratory hub forces for a three-bladed rotor.

Both of these results indicated that the higher harmonic shaftwise root forces could be eliminated using HHC and that the load suppressions were caused by the mutual cancellation of the higher harmonic aerodynamic and inertial components. Furthermore, interharmonic couplings—the interaction between the harmonics of inputs with another harmonics of outputs—were observed by both authors. Interharmonic couplings are expected to exist for all rotor systems. For example, even with the simplest mathematical model for a rigid flapping blade rotor in forward flight, the blade motion is described by a linear ordinary differential equation with periodically time-varying coefficients. For such an equation, it is well established that the input (or forcing) at one harmonic generates a multiharmonic output. Finally, Daughaday noted in his report that the HHC inputs required for vibratory hub load suppression changed significantly with forward speed.

Daughaday's analysis on the two-bladed teetering rotor was later extended by Balcerak and Erikson (ref. 23). The modifications included the torsional degree of freedom, which had been previously neglected by Daughaday, and the calculation of the blade inplane root shears. These authors calculated the higher harmonic blade pitch required to eliminate a set of even harmonics of shaftwise hub force together with a set of odd harmonics of inplane hub shear. Results from this study pointed out the importance of including the torsional degree of freedom, especially when the blade fundamental torsion frequency was close to the blade pitch harmonics. Also, the rotor aerodynamic performance was found to be relatively unaffected by the HHC inputs.

In 1972, the first wind tunnel investigation of HHC was reported by McCloud (refs. 4 and 5). The model rotor was a two-bladed teetering rotor with propulsive jet flaps. This rotor used a large jet flow expelled from the blade trailing edge to propel the rotor and applied the HHC through the angular deflection of the jet flow. In the model rotor, the jet flap was extended over the outer 30 percent of the blade radius. In the experiment, individual higher harmonic input components were applied to determine a set of influence coefficients relating the vibratory blade and hub load harmonics to the input harmonics. This set of influence coefficients formed a transfer matrix, which was then used to determine the higher harmonic input magnitudes and phases required to minimize the sum of the squares of the vibratory loads. These results showed that, in general, the vibratory hub load reduction was accompanied by an increase in the blade bending moments and vice versa. As noted by earlier investigators, the HHC inputs required for the suppression of vibratory hub loads were found to vary appreciably with the rotor forward speed. These experimental results were later supported by the analytical studies performed by Piziali and Trenka (ref. 6) and Trenka (ref. 7).

Sissingh and Donham also performed an HHC investigation in a wind tunnel using a four-bladed hingeless rotor (ref. 24). Due to the actuator hardware constraints, the rotor tip speed was significantly low compared to a full-scale helicopter. The resulting blade vibration frequencies were therefore very different from those of full-scale hingeless rotors. In the wind tunnel experiment, the higher harmonic blade root feathering was applied using swashplate excitations. The nonrotating swashplate was excited with servo-actuators oscillated at the fourth harmonic of the rotor rotational speed. This results in blade pitch harmonics at 3, 4, and 5 per rev which were superimposed on the basic collective and cyclic controls to suppress the third and fifth harmonics of the blade flap bending moments measured near the blade root. In effect, this suppression scheme tried to null out the fourth harmonics of the hub pitching and rolling moments in the fixed system. The vibratory hub loads, however, were not measured. The HHC model used for vibratory hub load suppression was similar to the one used by McCloud (ref. 5). With the applied HHC inputs, the results showed that these vibratory flap bending moments were drastically reduced and the HHC magnitudes generally increased with increasing advance ratios.

Starting in 1975, a series of wind tunnel investigations of HHC was conducted by McHugh and Shaw (refs. 25 and 26). The four-bladed soft-inplane hingeless rotor model being tested was fully instrumented so that secondary effects of HHC could be investigated. HHC inputs were applied by swashplate oscillations with servo-actuators. The vibratory hub loads were measured using a strain-gauge balance located beneath the actuators, in the fixed frame. Unlike Sissingh and Donham's experiment, the later experiments of McHugh and Shaw were conducted at close to the full-scale tip speed. Results from the experiment showed that the vibratory hub moments could be suppressed effectively with no significant increase in blade stresses. Also, all five components of the fourth harmonics hub loads—vertical, lateral, and longitudinal forces and pitching and rolling moments—could be reduced simultaneously with the three HHC inputs. However, the vibratory hub shears could not be completely suppressed for certain flight conditions, and this was attributed to the amplitude limitations of the servo-actuators. No significant penalties in rotor performance were observed in the HHC experiment. Noting that the HHC amplitudes and phases varied appreciably with forward speed, the authors suggested that an adaptive mechanism would be necessary to adjust the HHC inputs as required for varying flight conditions.

In 1975, McCloud presented an analytical investigation of HHC on a four-bladed articulated controllable-twist rotor (ref. 8). The analysis used an aeroelastic program developed for controllable-twist rotors by Kaman Aerospace. McCloud used the analysis to obtain the influence coefficients, relating the vibratory blade and hub load harmonics to the higher harmonic inputs, for the HHC model. In the study, McCloud confirmed the validity of the linear assumption made on the HHC input-output model. Using a weighting approach, he further showed that the suppression of the vibratory hub load could be accompanied by a 50 percent reduction in the blade bending stresses using the first four harmonics of the servo-flap inputs. Another analytical investigation of HHC on the controllable-twist rotor was presented by Lemnios and Dunn (ref. 9).

McCloud's HHC investigation on the four-bladed articulated controllable-twist rotor was carried out with a full-scale test in the Ames 40- by 80-Foot Wind Tunnel (ref. 10). In this experiment, the rotor blades were fully instrumented, and the rotor tip speed was about one-fourth that of production helicopters. The vibratory blade loads were obtained for different higher harmonic servo-flap deflections and at varying flight conditions, and the data were stored for a post-test analysis. In the data analysis, model reductions were performed using a regression analysis. The HHC model was then implemented

in a simulation program to compute the vibratory blade load reductions. The HHC mathematical model and controllers used in the simulation were identical to those of McCloud's analytical study presented in reference 8. Based on the simulated results, the authors reported that significant reductions occurred in both the blade flapwise bending moment and the control system loads using HHC. In addition, the data analysis also indicated that rotor performance could be improved using HHC.

In another HHC investigation of the same rotor, reported by McCloud and Brown in 1980 (ref. 11), the simulation included fuselage vibration measurements. In the earlier test, vibrations were measured using accelerators mounted on the rotor test apparatus (RTA). While varying the weighting options, they discovered that significant vibration reduction could be achieved with HHC at selected locations on the RTA. These authors also noted that components of the transfer matrix varied appreciably with forward speed and, like Shaw, suggested that a real-time parameter identification scheme would be required for practical HHC application.

In a paper reported by Hammond (ref. 27) and another one presented by Wood, Powers, and Hammond (ref. 28), results from the wind tunnel investigation of HHC on a four-bladed articulated model rotor were described. Like previous wind tunnel investigations, the HHC inputs were applied using swashplate oscillations. The vibratory hub loads were measured by a six-component balance mounted below the rotor hub. Using several trial inputs, these investigators were able to compute the fourth harmonic blade pitch required to suppress completely the 4 per rev vertical hub force. Then the authors outlined a general algorithm to acquire and control the multi-input multi-output HHC model and discussed the practical implementation of HHC in flight tests. In fact, the practical design issues concerned with the application of HHC to a production helicopter were later investigated by Powers (ref. 29).

The potential of HHC for future helicopter developments was reviewed by McCloud in 1980 (ref. 30). The potential benefits of HHC as an active control system for helicopter vibration suppression, blade stress reduction, and rotor performance improvement were outlined. Several types of rotors were reviewed as potential candidates for HHC applications including conventional, controllable-twist, propulsive and nonpropulsive jet flaps, circulation control, and advanced-controllable-twist rotors. Furthermore, practical implementations of HHC in flight test were also discussed.

In 1980, Shaw presented the results of a comprehensive analytical investigation of HHC comparing the potential benefits of servo-flap versus conventional blade root feathering, and studied the development of an automatic in-flight adaptive algorithm (ref. 31). The investigation was based on a coupled modal analysis and included a vortex wake induced inflow calculation. The shed wake effects were included using an approximation to the Theodorsen lift deficiency function. In the modal analysis, the inplane degree of freedom was uncoupled from the out-of-plane and the torsional degrees of freedom. The transfer matrix approach was adopted to relate the higher harmonic hub loads to the HHC inputs.

The analytical results indicated that nonlinearities in the HHC input-output model were small, on the order of 10 percent. Also, Shaw showed that significant reduction in vibration could be achieved with small to moderate increases in blade stresses. Investigating the distributions of the baseline and the incremental vibratory blade loads induced by HHC, Shaw pointed out that the vibration suppression was caused by the mutual cancellation between the aerodynamic and the inertial components of the transmitted vibratory loads at the blade roots. Cancellation of the blade root loads by using blade root

feathering generally caused an increase in both the aerodynamic and inertial loading distribution from the baseline values, thus resulting in an increase in blade stresses. Further investigation indicated that the increases in blade stress could be avoided if partial span flap, as opposed to blade root feathering, was used for vibration suppression.

Due to the HHC inputs, it was also found by Shaw that the control loads were increased by roughly 30 percent, and the change in rotor performance was negligible. For changing flight conditions, the closed-loop controllers with fixed gain performed satisfactorily over an advance ratio range as wide as 0.2. For the cases when this controller performed poorly, an adaptive gain controller was used. For the adaptive controller, the model parameters were estimated using the Kalman filter. Simulation results showed that the adaptive controller performed very well for varying flight conditions. Furthermore, the predicted actuator power requirement for HHC was less than 1 percent of the rotor induced power.

Starting in 1979, Shaw and Albion conducted wind tunnel investigation of HHC on a four-bladed hingeless rotor model in the Boeing V/STOL Wind Tunnel (refs. 32 and 33). The 10 foot diameter rotor was Mach scaled and operated at the full-scale tip speed. The HHC inputs were applied through the fixed-system swashplate excitation using four equally spaced hydraulic servo-actuators. The closed-loop controller suppressed simultaneously up to 90 percent the 4 per rev vertical hub shear, hub pitching, and rolling moments. The effectiveness of HHC was demonstrated for the advance ratios ranging from 0.1 to 0.3. The closed-loop system transient behaviors were investigated by applying a step disturbance through a swashplate command. Results indicated that the disturbance was suppressed within two rotor revolutions, or approximately 0.1 second. These results confirmed the quasi-static assumption made on the HHC model. Also, it was noted that the rotor trim states were not affected by the HHC inputs. However, the maximum penalty in rotor performance was large, on the order of 4 percent.

In 1980, Yen presented an analytical investigation of HHC on a two-bladed teetering and a four-bladed hingeless rotor (ref. 34). The analysis was based on C81, the Global Flight Simulation Program. For the two-bladed teetering rotor, trial amplitudes and phases of the second harmonic inputs were applied to suppress the second harmonics vertical hub shear. At the advance ratio of 0.3, the main rotor shaft torque was increased due to the applied HHC by 11 percent. The increase in shaft torque was attributed to blade stall which occurred in the fourth quadrant of the rotor disk.

For the four-bladed hingeless rotor, third, fourth, and fifth harmonics of blade pitch were simultaneously applied to suppress the vibratory hub loads. This resulted in reduction of more than 90 percent in the 4 per rev vertical hub shear, hub pitching, and hub rolling moments. For this hingeless rotor, the combined HHC inputs required were about 2.5 degrees, and the HHC penalty in rotor performance was found to be small. These results indicated that the second harmonic blade pitch, implemented on a two-bladed rotor, changed the rotor loading distribution and resulted in blade stall. Such effects had previously been suggested by Stewart (ref. 18). Furthermore, these results also implied that the blade pitch harmonics above the second, used for the vibratory hub load suppression, had a small or negligible effect on rotor performance.

In 1980, Hammond (ref. 35) reported a wind tunnel investigation of HHC on a dynamically Mach-scaled four-bladed articulated model rotor. The model rotor tip Mach number matched that of a full-scale value. As in Hammond's previous wind tunnel experiments, the HHC inputs were applied using swashplate oscillations. The transfer matrix approach was used for HHC modeling. Self-tuning regulators

were used for vibration suppression, and the model parameters were estimated using the Kalman filtering techniques. For a range of advance ratios between 0.2 to 0.4, the 4 per rev vertical hub shear and hub pitching moment were suppressed up to 70 percent from the baseline values. In general, the 4 per rev hub rolling moment could not be suppressed, however. Like other investigators, Hammond also reported a moderate increase in blade loads due to HHC.

Hammond and Hollenbaugh (ref. 36) investigated the application of different HHC control schemes to the vibration suppression problem. The HHC control schemes included the application of a single-input, multi-input, and multi-input with on-line adjustable blade twist. The last control scheme was quite similar to the one proposed by Daughaday (ref. 21) in which the added blade pitch required both spatial and temporal variations. The vibration suppression problem was solved using a nonlinear programming algorithm in which the quality criteria to be minimized included the sum of the peak-to-peak values of hub loads. The mathematical model used for the vibration problem was quite simple. It used either a rigid flapping or a coupled elastic flap-lag blade model, quasi-steady aerodynamics, and a linear inflow model. The results showed that for suppression of the oscillatory hub forces and moments on a four-bladed hingeless rotor, simultaneous application of the third, fourth, and fifth harmonics of the rigid blade pitch yielded good results. Better results were obtained with the addition of the variable time-dependent blade twist. However, a complete suppression of the oscillatory hub loads could not be achieved.

In 1981, Molusis, Hammond, and Cline (ref. 37) examined several HHC algorithms for vibration suppression. The performance of these algorithms was evaluated through wind tunnel testing. The model rotor and experimental setup were identical to that of Hammond's previous wind tunnel test (ref. 35). The HHC controllers were configured to suppress the fourth harmonic vertical, longitudinal, and lateral signals from a triaxial accelerator mounted beneath the rotor in the fixed frame. The rotor advance ratio was varied between 0.2 to 0.4, and the HHC system was modeled using the transfer matrix approach.

The HHC controllers tested could be separated into two types: the adaptive controllers and the gain schedule controllers. For the adaptive controllers, both the baseline vibration and the transfer matrix were estimated using Kalman filtering techniques. These adaptive controllers could be classified further depending on how the model parameters were updated. The adaptive controllers being evaluated were the deterministic and the cautious controllers. In particular, the deterministic (adaptive) controller used the estimated model parameters directly. For the cautious controller, the model parameters were also estimated using the Kalman filter. However, the cautious terms, which were calculated based on the covariances of the estimated parameters, were included in the control algorithm. If the parameter estimation was uncertain, then the controller decreased the gain in the control function. For the scheduled-gain controller, the transfer matrices were assumed to be known and were calculated off line. The two types of gain-scheduled controller being tested for different flight conditions in the wind tunnel included the perturbation and the proportional controllers. For the perturbation controller, the HHC model was linear about a nominal control value, whereas, for the proportional controller, the transfer matrix was fixed for the complete range of control values.

Wind tunnel results indicated that both gain-scheduled controllers performed poorly, and there was no definite reduction in the vibration level. It was suggested that a nonlinear behavior might be the cause for such poor performance. For the deterministic (adaptive) controller, the steady state vibration

level was reduced significantly. However, large response overshoots occurred before the vibration converged to the steady state value. The cautious controller offered the best performance among the four controllers. After initialization, the vibration converged smoothly to a minimum value. Over the range of forward speed tested, the cautious controller was able to suppress up to 90 percent of the fourth harmonic vertical and longitudinal accelerations. However, the 4 per rev lateral vibratory component could not be suppressed, in general.

In an analytical study, Molusis (refs. 38 and 39) investigated the inability of the HHC controllers to suppress the 4 per rev hub rolling moment as reported in reference 35 and the 4 per rev lateral acceleration as discussed in reference 37. Using the G400 simulation program for aeroelastic analysis (ref. 40), Molusis claimed that nonlinearity in the HHC modeling was a major factor for the incomplete vibration suppression. The nonlinearity was found to be more severe at the high forward speed. In fact, the incomplete vibration suppression was attributed to two factors: (1) the convergences of HHC algorithms to local minima, and (2) the constraints on the HHC amplitudes (the combined HHC amplitudes in Hammond's experiment were limited to 1.5 degrees). Furthermore, Molusis also noted that the parameter identification scheme using Kalman filtering technique could, in certain cases, lead to divergent HHC transient responses.

In 1982, Wood et al. (refs. 41-43) conducted an HHC flight test program on a modified OH-6A helicopter. The OH-6A is a light helicopter with a gross weight of about 3,000 lb. The flight test program was supported by the earlier wind tunnel results performed by Hammond. The HHC inputs were implemented by blade root feathering using swashplate oscillations, and a triaxial accelerometer was mounted beneath the pilot seat to sense and feed back the fourth harmonic vertical, longitudinal, and lateral vibrations to the controller. The flight speed was varied between zero to 100 knots, while HHC was applied using both open-loop (manual) and closed-loop controllers. For the closed-loop operation, the cautious controller presented in reference 37 was employed. Flight test results confirmed the effectiveness of HHC, as had been observed in wind tunnels. Up to a 90 percent reduction in vibration was obtained with combined HHC amplitudes less than 1 degree. The blade and control system fatigue loads were increased due to HHC; however, the load penalties were within the design limits. Shaft torque measurement showed no adverse effects of HHC on the aircraft performance.

Johnson (ref. 44) reviewed the class of HHC algorithms for vibration and blade load reduction proposed to date. As in previous investigations, a linear, quasi-static, frequency domain transfer matrix was adopted for the HHC modeling. Furthermore, the HHC models were classified into global (linear) and local (piecewise linear) models. Both open-loop and closed-loop controllers were considered. The criteria for vibration suppression or blade load reduction were expressed as a minimum variance or a quadratic performance index. The controllers were further classified according to the parameter identification scheme being used. As in previous reports, these included the deterministic, gain-updated, cautious, and dual controllers.

The performance of the controllers presented by Johnson was evaluated analytically by Chopra and McCloud (ref. 45). The performance evaluation was based on a numerical simulation which used the data obtained from McCloud's earlier wind tunnel results (ref. 11). They studied the effects of measurement noise, initial estimated error in the model parameters, control rate constraint, and variation in flight speed on the performance of four different controllers. In particular, these controllers were open loop and closed loop with off-line and on-line identification. The on-line identification scheme

was performed using the Kalman filter. Both global and local models were simulated. The closed-loop controller with a local model using on-line identification technique had the best performance. However, for the cases with large initial errors in the transfer matrix, large overshoots were found in the transient responses using this controller. For such cases, these authors proposed two different startup procedures to improve the transient responses: (1) trial HHC input sequences would be injected into the system to compute a better estimate of the transfer matrix using either the finite-difference or the least-square methods, and (2) the control rate constraint value would be made initially large to avoid the undesirable control excursion and eventually reduced for improved convergence characteristics.

In 1985, a successful wind tunnel demonstration of HHC was performed by Shaw et al. (ref. 46). The experimental investigation was conducted using a three-bladed dynamically scaled model rotor of the CH-47D helicopter tested in the Boeing Helicopters Wind Tunnel. The model rotor operated at full-scale tip speed, and the vibratory hub loads were measured using a strain-gauge balance mounted in the rotating frame. The higher harmonic blade feathering at the second, third, and fourth harmonics was applied to suppress the 3 per rev vertical hub force and the 2 and 4 per rev rotating inplane hub shears. Open-loop tests were conducted to obtain the transfer matrix values at several flight conditions. These transfer matrices were stored and later used with the fixed- or scheduled-gain controllers.

Wind tunnel results showed that HHC produced more than 90 percent reduction of all three vibratory hub shear components. Such reductions were obtained using the fixed-gain controller with a local model, in which the transfer matrices were calculated off line. Vibration reduction was shown for the complete range of flight conditions being tested, up to a forward speed of 188 knots. The suppression of the vibratory hub loads was accompanied by small to moderate changes in the blade and control system fatigue loads as well as a negligible change in rotor performance. However, the combined HHC amplitudes required for vibratory load reduction were relatively large—on the order of 2 and 3 degrees, respectively, at the forward speeds of 135 and 188 knots. These HHC amplitudes were significantly larger than those reported in reference 41. The reason, as suggested by Shaw, was due to the differences in blade dynamics between the two rotors.

Testing different HHC algorithms, these authors found that the scheduled-gain controller performed as well as the fixed-gain controller at varying flight conditions. It was interesting since the scheduled-gain controller selected the transfer matrices automatically from a data base, while the transfer matrices were selected manually for the fixed-gain controller. Also, both controllers used the local model. The adaptive controllers, similar to those reported in reference 37, were also tested; nevertheless, they generally exhibited poor performance. For certain fixed flight conditions, the adaptive controller was successful in suppressing the vibratory hub loads. For changing flight conditions, however, the transfer matrices identified by this controller diverged for certain values of the covariances of the measurement and process noises. Furthermore, some initial testing of the global adaptive controller indicated that it was either unstable or ineffective in suppressing the vibratory loads.

The HHC effectiveness shown in this wind tunnel experiment had other implications. First, it demonstrated that the vibratory hub loads could be suppressed with a relatively simple HHC controller—the fixed-gain controller. Second, the nonlinearities in the HHC model, if these existed, did not prevent the near complete suppression of the vibratory hub loads. In fact, open-loop results indicated that the vibratory responses were linear with HHC amplitudes, up to 3 degrees. These results were at variance

with those reported in references 37 and 38, and the differences may be attributed to the actual hardware implementation, the servo-actuator accuracy, and the data processing techniques.

In 1985, Lehmann reported an HHC investigation conducted in the the Deutsch-Niederlandischer Windkanal (DNW) (ref. 47). This wind tunnel investigation was supported by an earlier analytical study performed by Jacob and Lehmann (ref. 48). The higher harmonic blade pitch was applied to suppress the vibratory hub loads on a four-bladed hingeless model rotor of the BO-105 helicopter. The load balance was mounted in the fixed frame, beneath the rotor. The airspeed was varied between 10 and 50 meters per second which corresponded to advance ratios of 0.04 to 0.22. The HHC results indicated that all five vibratory hub load components—4 per rev vertical, longitudinal, and lateral hub forces and 4 per rev pitching and rolling moments—could be reduced simultaneously but could not be completely suppressed. Furthermore, Lehmann found that the rotor trim states were affected by the applied HHC inputs.

Analytical investigation of HHC for suppression of fuselage vibration was also carried out by Taylor, Farrar, and Miao (ref. 49). The HHC system being considered also employed swashplate oscillations. A four-bladed single rotor helicopter was simulated using the G400 rotor aeroelastic analysis. The controllers used were similar to those described in reference 35. Simulated results indicated that HHC produced up to 80 to 90 percent reduction in fuselage vibration. Secondary effects of HHC included a small reduction in rotor performance—on the order of 1 to 3 percent increase in rotor shaft torque—and small to moderate increase in blade stresses. The influences of measurement noise included in the simulation indicated that a 15 percent noise-to-signal ratio was acceptable for the HHC design. With the rotor system considered, the predicted HHC inputs required were on the order of 3 degrees.

Another comprehensive HHC simulation, also using the G400 program, was carried out by Davis (ref. 50). This study aimed at comparing the performance of three different controllers: deterministic, cautious, and dual. Both local and global models were used. For steady flight conditions, Davis noted that, with proper tuning, there was no distinguishable difference between the performance of these three controllers. The vibration reductions were 75 to 95 percent from the baseline values, and these were achieved with less than 1 degree of the combined HHC inputs. For transient maneuvers, it was found that the global controllers generally performed better than the controllers using the local model.

The effects of nonlinearity and interharmonic coupling of the HHC system were also investigated in reference 50. The major source of nonlinearity in the HHC model came from the blade bending mode responses, while the interharmonic coupling arose from both the blade responses and the higher harmonic airloads. Both of these effects might degrade the controllers' performance in terms of the HHC amplitude required and the vibration convergent rate. By selecting proper weighting factors on the HHC inputs at different flight conditions, the author noted that such degrading effects might be reduced.

The above simulation led to a study for implementing HHC on the Sikorsky S-76 helicopter (ref. 51). Analytical studies, design analysis, and risk reduction tests were all performed prior to the full-scale flight demonstration. The flight test program was designed to demonstrate HHC effectiveness on a modern medium-weight helicopter.

In 1986, flight demonstration of HHC on the S-76 helicopter was conducted and described in references 52 and 53. For flight tests, passive vibration control devices were either removed or switched off. Swashplate excitation was used to activate the higher harmonic blade pitch, and the cabin vibration level was monitored using accelerators mounted at several locations in the aircraft. Using open-loop testing, this was the first flight test to demonstrate the potential of HHC on a 10,000 lb helicopter for a range of forward speed up to 150 knots. With HHC, significant reductions in the fuselage vibration were attained. The effects on aircraft performance were found to be negligible, while the penalties in blade and control system fatigue loads were moderate and remained well within the design limits. Due to actuator power limitations, however, only a small percentage in cabin vibration reduction was achieved at forward speeds above 100 knots.

Also in 1986, Polychroniadis and Achache (refs. 54 and 55) presented an HHC flight test on an SA 349 Gazelle experimental research aircraft, a lightweight (4,500 lb) helicopter. The HHC inputs were implemented using swashplate excitation. Self-adaptive controllers used feedback signals from the vibration sensors placed at selected locations in the aircraft cabin. The controllers used in these flight tests were similar to the adaptive controllers presented in reference 37. For the flight tests, passive vibration control devices were removed from the aircraft. With HHC, a 70 to 90 percent reduction in vibration was achieved at forward speeds up to 250 km per hour (or 135 knots). These results indicated a superior performance in terms of vibration suppression using HHC over the previously used passive vibration control devices. The interactions between the vibratory hub loads and the airframe vibration were also investigated. These authors found that the vibration suppression using HHC was achieved by significant reductions in the second harmonic rotating inplane hub forces and moments. At the same time, the fourth harmonic components of the inplane hub loads were increased slightly.

In 1988, Jacklin (ref. 56) presented a numerical simulation evaluating the performance of five system identification techniques for HHC. These included the weighted least square method, the classical Kalman filter, a generalized Kalman filter, the classical least mean square filter, and the generalized least mean square filter. Both global and local models were considered. Results from both open-loop and closed-loop simulations were shown. The algorithms were evaluated in terms of accuracy, stability, convergence properties, computational speed, relative difficulties for practical implementation, and the level of vibration reduction. Noises and modeling errors were included in the simulation study. Based on the results, Jacklin concluded that the generalized least mean square method using the local model in the closed-loop operation was the most promising identification method for HHC.

In 1988, Sangha (ref. 57) presented an analytical investigation of HHC using the Rotor/Airframe Comprehensive Aeroelastic Program (RACAP). This study concentrated on the influences of the open-loop HHC on the fuselage vibration. Based on a correlation study, Sangha pointed out the importance of including hub motions for the prediction of fuselage vibration. In the design of an HHC system, he noted that it was the modal properties of the fuselage that were important, not those of the blade. However, such conclusion was made based only on the parametric study of the control system stiffness on the 4 per rev vibration at the pilot seat using the open-loop controller. However, other blade characteristics such as distributions of blade inertia and stiffness, which have strong influences on the HHC responses, were not addressed. Also, Sangha showed that the vibration reduction was caused primarily by the phase variations rather than the magnitude variations of the vibratory hub loads.

In 1989, Robinson and Friedmann (ref. 58) conducted an analytical investigation of HHC on a generic four-bladed hingeless rotor. The results were calculated using the coupled flap-lag-torsion aeroelastic analysis developed at the University of California, Los Angeles. Both quasi-steady and unsteady aerodynamic results were presented (ref. 59). The unsteady aerodynamic model employed was a finite-state time-domain version of the approximated Wagner or Theodorsen lift deficiency functions (refs. 60 and 61). These authors showed significant differences between the quasi-steady aerodynamic and the unsteady aerodynamic results for the computed 4 per rev vertical hub shear, and the differences were more pronounced at the high advance ratios. The results for the inplane hub shears were essentially identical between these two aerodynamic models.

Deterministic and cautious controllers were used to suppress the predicted vibratory hub loads using both the global and the local models. From the simulated results, no significant differences were found among the performance of the controllers being tested. The computed HHC inputs for vibration suppression were found to be noticeably different depending on which aerodynamic model was being used.

Also in 1989, Welsh and Blackwell presented an HHC study on the X-Wing (four-bladed) model rotor conducted in the Large Subsonic Wind Tunnel at the United Technology Research Center (ref. 12). For the X-Wing rotor, both trim controls and higher harmonic inputs were applied using the circulation control concept. In a circulation control airfoil, the combination of trailing edge blowing and Coanda effect can create more lift than conventional airfoils. In the model rotor, compressed air was supplied to a stationary annular plenum and passed through a series of stationary valves to receivers feeding the leading edge and trailing edge ducts mounted on the blade. The ducts in the blade carried the compressed air down the span and vented the air through slots to the Coanda surface of the airfoil. Unlike the standard swashplate excitation with mechanical linkages and actuators, the higher harmonic inputs could be applied without any moving part and at any harmonic of the rotor rotational speed. For this investigation, HHC was applied using trailing edge blowing at 2, 3, 4, and 5 per rev. The vibration was measured using a three-axis accelerometer mounted on the stand. Also, a balance was used to measure the vibratory hub loads, and the blade were fully instrumented with strain gauges so that the blade stress could be monitored. Reductions in both the vibration and the blade stresses were achieved using a fixed-gain controller in which the transfer matrix was calculated off line. The forward speed was varied between 60 to 175 knots, and the rotor operated at 50 and 100 percent full-scale tip speed.

With the HHC, the vibration was suppressed between 70 and 95 percent from the baseline level, and the blade loads were also reduced simultaneously. The blade load reduction was primarily caused by the second harmonic control, typically not realizable on a four-bladed rotor using conventional swashplate oscillation. Also, it was found that the coupling between the trim control and the HHC was so severe that such effects had to be included into the control algorithm to maintain the rotor in trim. Analytical investigation of HHC on the X-Wing circulation control rotor was also performed by Abramson (ref. 13).

Up to this point, all the active vibration control algorithms discussed are in the frequency domain. In 1981, Du Val, Gregory, and Gupta (ref. 62) advocated a time domain approach for the active control of helicopter vibration. In fact, this method was an extension of the linear quadratic Gaussian (LQG) regulator with a frequency shaped cost function. In essence, the proposed approach used a constant regulator with a filter in the feedback loop. The feedback variables, such as the fuselage accelerations, were passed through an undamped second-order oscillator, tuned to the frequency of N_b per rev. At

the filter resonant frequency, the regulator locked onto the phase and magnitude of the feedback signal without the need for harmonic analysis. The proposed technique also offered other advantages over the frequency domain approach. Since state feedback was used, on-line identification of the model parameters would not be necessary. Furthermore, linear system theory techniques could be employed for the design of a stable system.

Using a simple simulation program for the vibration control model, these investigators were able to show that this control scheme performed extremely well. With the feedback controllers generating the collective, longitudinal, and lateral cyclics and tail rotor controls, the reduction in vibration levels was more than 90 percent. However, the controller used for vibration suppression was initially designed for the hovering condition, and, as such, the effects of the periodic-time-varying coefficients in the plant model had been neglected. This control scheme was also used to suppress the vibration on an X-Wing model rotor (ref. 63).

In 1989, Wereley and Hall (ref. 64) presented an interesting and alternative view of the active vibration control algorithms currently being proposed. This study focused on evaluating the performance of these control algorithms within the context of classical control theory. These authors pointed out that all these active vibration algorithms, either in the time or the frequency domain, were in fact quite similar and could be considered, in the context of linear control theory, as the classical disturbance rejection problems. Furthermore, they claimed that the effectiveness of the HHC algorithms was rather limited by the quasi-static and the time-invariant assumptions imposed on the plant model. They also noted that all the HHC algorithms were fairly robust. And finally, they proposed two possible approaches for improving HHC performance. First, the periodic behavior of the rotor system should be included in the plant model. The second approach involved the development of a control algorithm for the particular periodic-time-varying plant model. However, these two approaches were still under investigation, and therefore no result was shown.

Besides the works discussed above, significant contributions to HHC had been performed by Kretz (refs. 65-67). Application of a nonlinear programming method to HHC algorithm was discussed by Perley et al. (ref. 68). A feasibility study for the application of HHC to the advanced blade concept rotor was reported in reference reference 69. Prediction of HHC responses with a coupled rotor-airframe vibration control model was presented in reference 70. And finally, general discussions about HHC also appeared in references 1, 2, and 71-74.

Besides the HHC using swashplate oscillation, several other vibration control methods using active control techniques were also investigated. These include individual blade control (IBC) (refs. 14 and 15) and active isolation (refs. 75 and 76) systems. In an IBC system, each individual blade is controlled by a separate servo-actuator, and, in fact, these servo-actuators are mounted on the rotating swashplate and thus rotate with the blades. The blade excitation can be achieved for any frequency. In reference 15, the IBC algorithms were formulated in the time domain using an extension of the standard linear quadratic regulator approach with the model-following systems. Without the restriction on the blade input frequency, the IBC system could be used to alleviate gust response and retreating blade stall, as well as to stabilize the rotor system.

Active isolation is another attractive concept for suppressing helicopter vibration. In this system, servo-actuators are mounted in the airframe structures and configured to oscillate in such a way as

to cancel out the vibration. Either time or frequency domain control algorithms can be used for this system. If the frequency domain technique is used, then the control algorithm for this system is similar to that of the HHC. However, determination of the optimal locations and the number of servo-actuators required for actual implementation of active isolation is a central issue with this technique. Preliminary investigation using an analytical method has indicated that this vibration control system can perform virtually as well as the HHC system (ref. 71).

1.3 Current Investigation

Based on the discussion presented above, HHC can be considered to be one of the most effective vibration control techniques currently available for helicopters. Virtually all the investigations carried out to date on a number of different rotor systems have shown that HHC produced substantial reduction in either the vibratory hub loads or the fuselage vibration. Even though some of the HHC algorithms have been shown to perform better than others, each appears feasible for practical implementation.

One problem which remains to be solved is the HHC amplitudes required for vibration suppression. While the results in reference 41 indicated that less than 1 degree in the combined HHC amplitudes was required, others—in particular, references 46 and 49—have shown that approximately 3 degrees was needed to control the vibration on their rotors. This difference might be attributed to the differences in blade dynamics of these rotors. This problem has a practical significance since the HHC amplitudes are directly related to the power requirement of hydraulic servo-actuators. Indeed, for certain rotor designs, the weight penalty imposed by the actuation system can prevent the practical implementation of HHC on such rotors. On the other hand, an HHC system with a low amplitude requirement needs actuators of smaller weight and thus has a low weight penalty. Also, the maintenance cost is low since a small oscillation amplitude translates to a longer actuator seal life. Furthermore, it is desirable to minimize the secondary effects of the HHC. A large higher harmonic blade pitch may alter the helicopter trim state and thus affects the aircraft performance and handling qualities. Also, for aircraft operating near the flight boundary, HHC inputs with sufficiently large magnitude may induce a premature onset of blade stall. Since a successful HHC system must operate efficiently in a severe aerodynamic environment, its performance should be investigated over the whole flight envelope.

The objectives of this study are to:

1. Develop a comprehensive aeroelastic analysis to calculate the rotor responses in forward flight including consistent and complete unsteady aerodynamic and wake effects.
2. Validate the rotor response calculation with measured data obtained from a model rotor tested in a wind tunnel.
3. Formulate the higher harmonic control analysis for open-loop and closed-loop controllers. Determine the power requirement for hydraulic servo-actuators.
4. Perform systematic parametric studies to investigate the effects of blade design parameters on the vibratory hub loads, HHC inputs, and power requirements. Results from these studies might be used to assess the role of blade dynamics on the efficiency of HHC systems and explain the differences in HHC amplitude requirement between different rotors. The design parameters include blade stiffness

distributions in the flap, lead-lag, and torsion directions, chordwise offset of the blade center of mass from the elastic axis, chordwise offset of the elastic axis from the blade quarter chord, and blade linear pretwist.

5. Examine application of HHC for articulated and hingeless rotors, in particular the HHC amplitude and actuator power requirements.

6. Investigate effects of HHC on blade bending stresses, control loads, and rotor performances under different flight conditions.

7. Investigate the application of HHC at severe flight conditions including high speeds and high thrust flight conditions, in particular the influence of higher harmonic blade pitches on blade stall.

The analytical study is conducted using a comprehensive coupled aeroelastic analysis developed at the Rotorcraft Center, University of Maryland (refs. 77–80). The formulation is based on the finite element method in both space and time. In this formulation, the rotor blade is modeled as an elastic beam undergoing flap bending, lead-lag bending, torsion, and axial deflections. The spatial finite element method based on the Hamilton principle is used to discretize the blade into a number of beam elements, each having 15 degrees of freedom.

Since accurate prediction of the blade airloads is crucial in the determination of the aeroelastic responses and the higher harmonic responses, a time domain nonlinear unsteady aerodynamic model developed by Leishman and Beddoes (refs. 81 and 82) has been used. This model consists of an attached compressible flow formulation (linear model) along with a representation of the nonlinear effects due to flow separation and dynamic stall. The impulsive—or noncirculatory—loads and reverse flow corrections are also included. Calculation of the rotor nonuniform induced inflow is performed using a free wake analysis adapted from a Comprehensive Analytical Model of Rotor Aerodynamics and Dynamics (CAMRAD) (ref. 83). The blade nonlinear periodic responses are solved from the normal mode equations using a temporal finite element technique. The vehicle trim controls and the blade responses are calculated iteratively as one coupled solution using a modified Newton method. Calculation of the HHC responses forms an integral part of the steady response solution in which the basic trim controls are superimposed with the higher harmonic components.

The HHC algorithms are formulated in the frequency domain. A linear quasi-static transfer matrix is adopted to relate the harmonics of HHC inputs to the harmonics of vibratory hub loads, and both local and global models are considered. The optimal HHCs are calculated based on the minimization of the vibratory hub loads expressed in term of a quadratic performance index. The transfer matrix is computed off line, and, for the local model, it is updated based on the secant method. Using the multiblade coordinate transformation, the HHC inputs in the rotating frame are transformed to the fixed frame, in terms of the swashplate higher harmonic motions. The higher harmonics swashplate motions are generated using a number of servo-actuators, and the hydraulic power required by these actuators is then calculated for a specified HHC input.

2 FORMULATION

This section is divided into two parts: the first part describes the baseline analysis with no HHC effects, and the second part describes the formulation of the HHC analysis.

In the first part, the coordinate systems and the Hamiltonian formulation of the blade governing equations are introduced. Then the blade aerodynamic and the rotor induced inflow models used in the analysis are described. The next section shows the calculations of the blade and rotor hub loads, and this is followed by the description of the coupled trim analysis. The subsequent section presents the spatial finite element method used in the formulation of the blade governing equations. Then, the solution technique for the blade responses as coupled with the vehicle trim analysis is shown.

The second part, starting with section 2.9, describes the higher harmonic control analysis. First, the HHC model and the control algorithms used to suppress the rotor vibratory hub loads are presented. These are followed by the formulation of the actuator power requirement for the HHC system. Then, the implementation of HHC into the overall analysis is discussed.

2.1 Coordinate Systems

The helicopter model consists of a rigid fuselage and a main rotor having N_b blades. The Cartesian coordinate system (X, Y, Z) is attached to the rotor hub which remains fixed to the fuselage, as shown in figure 2.1. This coordinate system, with the origin at the rotor hub center, represents the fixed or nonrotating frame. The Z axis is along the shaft axis, and the X and Y axes are in the hub plane, perpendicular to the shaft axis.

The rotor blade is modeled as an elastic beam rotating at a constant angular velocity Ω . Figure 2.2 shows the blade coordinate system. A Cartesian coordinate system (x, y, z) is attached to the undeformed rotating blade, which is at a precone angle β_p with respect to the hub plane. This coordinate system, with the origin coinciding with that for the fixed frame, represents the rotating frame. The x axis coincides with the blade elastic axis and points outboard; the y axis is in the plane of rotation and points toward the blade leading edge; the z axis is tilted at an angle β_p relative to the shaft axis.

For elastic deformation, a point P on the blade elastic axis undergoes displacements u, v, w in the x, y, z directions, respectively, and occupies a position P' on the deformed elastic axis. As shown in figure 2.2, the cross section containing P' undergoes a rotation θ_1 about the deformed elastic axis, where θ_1 can be expressed as (ref. 84)

$$\theta_1 = \theta + \hat{\phi} \quad (2.1)$$

and the twist $\hat{\phi}$ is given by

$$\hat{\phi} = \phi - \int_0^r w'v'' dx \quad (2.2)$$

where ϕ is the elastic twist of the blade cross section about the deformed elastic axis, $\hat{\phi}$ is the geometric twist, θ is the control pitch angle, $v' = dv/dx$ is the lag slope, and $w'' = d^2w/dx^2$ is the flap curvature.

An orthogonal coordinate system (ξ, η, ζ) is introduced at the deformed position P' such that the ξ axis is tangential to the deflected elastic axis. The η and ζ axes are the principal axes of the deformed cross section and remain normal to the deformed elastic axis. This deformed blade coordinate system is also shown in figure 2.2. The assumption, which is based on the fact that the blade cross section remains normal to the elastic axis after deformation, is in accordance with the Bernoulli-Euler beam theory. In general, the plane containing (η, ζ) and that containing (y, z) are not parallel.

2.2 Hamiltonian Formulation

The variational method of the Hamilton principle provides a way for finding the equations of motion of a dynamical system, and such approach has been adopted in the analysis. For a conservative system between prescribed initial and final conditions at time t_1 and t_2 , the Hamilton principle states that the actual motion of a dynamical system is that particular motion for which the time integral of the difference between the potential and kinetic energies is minimum (ref. 85). Since aeroelastic systems are nonconservative, the Hamilton principle is generalized to include forces which are not derivable from a potential function. The resulting generalized Hamilton principle, applicable to nonconservative systems, can be expressed in variational form as

$$\int_{t_1}^{t_2} (\delta\mathcal{U} - \delta\mathcal{T} - \delta\mathcal{W}) dt = 0 \quad (2.3)$$

where $\delta\mathcal{T}$ and $\delta\mathcal{U}$ are, respectively, the variations of kinetic and strain energies, and $\delta\mathcal{W}$ is the virtual work done by external forces.

From reference 84, the variation in strain energy for a Bernoulli-Euler beam undergoing moderate deflections in the axial, lead-lag, flap, and torsion directions is

$$\begin{aligned} \delta\mathcal{U} = & \int_0^R (F(\delta u' + v'\delta v' + w'\delta w') \\ & + (GJ\phi' + EAk_A^2(\theta + \phi)')(u' + \frac{1}{2}v'^2 + \frac{1}{2}w'^2) \\ & + EB_1\theta_1'^2\phi' - EB_2\theta_1'(v''\cos\theta_1 + w''\sin\theta_1))\delta\hat{\phi}' \\ & + (EC_1\phi'' + EC_2(w''\cos\theta_1 - v''\sin\theta_1))\delta\hat{\phi}'' \\ & + ((\bar{M}_z - EAe_a(u' + \frac{1}{2}v'^2 + \frac{1}{2}w'^2) - EB_2\theta_1'\phi')\cos\theta_1 \\ & + (\bar{M}_y - EC_1\phi'')\sin\theta_1)(\delta v'' + w''\delta\hat{\phi}) \\ & + ((\bar{M}_z - EAe_a(u' + \frac{1}{2}v'^2 + \frac{1}{2}w'^2) - EB_2\theta_1'\phi')\sin\theta_1 \\ & - (\bar{M}_y - EC_1\phi'')\cos\theta_1)(\delta w'' - v''\delta\hat{\phi}) dx \end{aligned} \quad (2.4)$$

where the axial force F is defined by

$$F = EA(u' + \frac{1}{2}v'^2 + \frac{1}{2}w'^2 + k_A^2\theta_1'\phi' - e_a(v''\cos\theta_1 + w''\sin\theta_1)) \quad (2.5)$$

and

$$\overline{M}_y = EI_y(v'' \sin \theta_1 - w'' \cos \theta_1) \quad (2.6)$$

$$\overline{M}_z = EI_z(v'' \cos \theta_1 + w'' \sin \theta_1) \quad (2.7)$$

and the sectional constants are

$$A = \iint_A d\eta d\zeta$$

$$Ae_a = \iint_A \eta d\eta d\zeta$$

$$I_y = \iint_A \zeta^2 d\eta d\zeta$$

$$I_z = \iint_A \eta^2 d\eta d\zeta$$

$$Ak_A^2 = \iint_A (\eta^2 + \zeta^2) d\eta d\zeta$$

$$J = \iint_A \left(\left(\eta - \frac{\partial \lambda}{\partial \zeta} \right)^2 + \left(\zeta + \frac{\partial \lambda}{\partial \eta} \right)^2 \right) d\eta d\zeta$$

$$B_1 = \iint_A (\eta^2 + \zeta^2)^2 d\eta d\zeta$$

$$B_2 = \iint_A \eta(\eta^2 + \zeta^2) d\eta d\zeta$$

$$C_1 = \iint_A \lambda^2 d\eta d\zeta$$

$$C_2 = \iint_A \zeta \lambda d\eta d\zeta$$

where A is the blade cross-sectional area effective in carrying tension; e_a is the offset of the tensile axis from the elastic axis, positive forward; I_y and I_z are the flapwise and chordwise area moments of inertia of the cross section; Ak_A^2 is the cross-sectional polar moment of inertia; J is the torsional constant including cross-sectional warping; λ is the warping function which is assumed to be antisymmetric about the chord line; C_1 is the warping rigidity; and B_1 , B_2 , and C_2 are other sectional constants. Furthermore, it is assumed in the analysis that the structural properties of the cross section are symmetric about the chord line.

The variation in kinetic energy for a rotating elastic beam is

$$\begin{aligned}
\delta T = & \int_0^R m((\Omega^2 x + 2\Omega\dot{v} - \ddot{u})\delta u \\
& + (\Omega^2(v + e_g \cos \theta_1) + 2\Omega(\beta_p \dot{w} - \dot{u}) \\
& + 2e_g \Omega(\dot{v}' \cos \theta_1 + \dot{w}' \sin \theta_1) - \ddot{v} + e_g \ddot{\phi} \sin \theta_1) \delta v \\
& - (\beta_p(\Omega^2 x + 2\Omega\dot{v}) + \ddot{w} + e_g \ddot{\phi} \cos \theta_1) \delta w \\
& - (k_m^2 \ddot{\phi} + \Omega^2(k_{m_2}^2 - k_{m_1}^2) \cos \theta_1 \sin \theta_1 \\
& + e_g \Omega^2 x(w' \cos \theta_1 - v' \sin \theta_1) + e_g \Omega^2 v \sin \theta_1 \\
& + e_g \Omega^2 \beta_p x \cos \theta_1 - e_g(\ddot{v} \sin \theta_1 - \ddot{w} \cos \theta_1)) \delta \hat{\phi} \\
& - e_g(\Omega^2 x \cos \theta_1 + 2\Omega\dot{v} \cos \theta_1) \delta v' \\
& - e_g(\Omega^2 x \sin \theta_1 + 2\Omega\dot{v} \sin \theta_1) \delta w' dx
\end{aligned} \tag{2.8}$$

where the sectional integrals are defined by

$$\begin{aligned}
m &= \iint_A \rho_s d\eta d\zeta \\
me_g &= \iint_A \rho_s \eta d\eta d\zeta \\
mk_{m_1}^2 &= \iint_A \rho_s \zeta^2 d\eta d\zeta \\
mk_{m_2}^2 &= \iint_A \rho_s \eta^2 d\eta d\zeta \\
k_m^2 &= k_{m_1}^2 + k_{m_2}^2
\end{aligned}$$

In the above expressions, m is the blade mass per unit length; ρ_s is the blade structural density; e_g is the center-of-mass offset from the elastic axis, positive forward; $mk_{m_1}^2$ and $mk_{m_2}^2$ are the flapwise and chordwise mass moments of inertia per unit length; and k_m is the cross-section radius of gyration per unit length.

An ordering scheme has been used in the derivation of the variations in potential and kinetic energies. Basically, the ordering scheme provides a set of guidelines to neglect the higher order terms which appear in the nonlinear equations. These guidelines are employed to simplify the equations of motion. By introducing ε , with $\varepsilon \ll 1$, a parameter of order v/R or w/R , the assumed orders of magnitude for the nondimensional quantities are

$$\begin{array}{ll}
EA/m_o \Omega^2 R^2 & \mathcal{O}(\varepsilon^{-2}) \\
x, m/m_o, \theta_{1c}, \theta_{1s} & \mathcal{O}(1) \\
EI_y/m_o \Omega^2 R^4, EI_z/m_o \Omega^2 R^4, GJ/m_o \Omega^2 R^4 & \mathcal{O}(1) \\
v/R, w/R, \hat{\phi}, \beta_p, k_A/R, k_{m_1}/R, k_{m_2}/R, EB_2/m_o \Omega^2 R^5 & \mathcal{O}(\varepsilon) \\
e_g/R, e_a/R, e_d/R & \mathcal{O}(\varepsilon^{3/2}) \\
u/R, EB_1/m_o \Omega^2 R^6 & \mathcal{O}(\varepsilon^2)
\end{array}$$

In general, terms with the highest order for a particular equation are considered first order terms. First order terms are retained in the u equation. For instance, if the highest order terms in the u equation have an order of ε^2 , then all terms with order ε^2 are retained, while higher order terms such as $\varepsilon^3, \varepsilon^4, \dots$ are neglected. Similarly, second order terms are retained in the v and the w equations, while some third order terms are retained in the $\hat{\phi}$ equation. Furthermore, these guidelines should be applied within the total energy expression, and the terms retained should constitute the self-adjoint characteristic of the structural matrices. That is, the resultant blade structural mass and stiffness matrices should be symmetric, while the antisymmetric structures of the damping matrix should reflect gyroscopic couplings.

The expression for $\delta\mathcal{W}$ is

$$\delta\mathcal{W} = \int_0^R (L_u^A \delta u + L_v^A \delta v + L_w^A \delta w + M_\phi^A \delta \phi) dx \quad (2.9)$$

where L_u^A, L_v^A , and L_w^A are the distributed airloads in the x, y, z directions, respectively, and M_ϕ^A is the sectional aerodynamic pitching moment about the deformed elastic axis. Based on the Hamilton formulation, a finite element analysis is formulated in section 2.7.

2.3 Aerodynamic Loads

This section describes the calculation of the blade section airloads. The external loads L_u^A, L_v^A, L_w^A and M_ϕ^A in equation 2.9 are the distributed airloads acting on a rotor blade. Calculation of the blade airloads requires information about the relative flow velocity and the Mach number as seen near a blade section. Therefore, the derivation of the relative flow velocity is presented first, and this is followed by the presentation of the aerodynamic model.

2.3.1 Derivation of Blade Velocity

In particular, the resultant velocity seen at a blade section consists of the incoming flow velocity, the instantaneous blade motions, and the induced inflow due to the trailed and shed vorticities. The general expression for the resultant blade velocity at a radial station x is given by

$$\mathbf{V} = -\mathbf{V}_w + \mathbf{V}_b \quad (2.10)$$

where \mathbf{V}_w is the wind velocity with contributions from the vehicle forward speed and the rotor inflow, and \mathbf{V}_b is the blade velocity relative to the hub fixed frame resulting from blade rotation and blade motions. The expression for the wind velocity is

$$\mathbf{V}_w = (\mu\Omega R)\hat{I} - (\lambda\Omega R)\hat{K} \quad (2.11)$$

where $\mu = V \cos \alpha_s / \Omega R$ is the rotor advance ratio; V is the vehicle forward speed; α_s is the rotor shaft tilt, positive forward; λ is the rotor nondimensional inflow; and ΩR is the rotor tip speed. The unit vectors $(\hat{I}, \hat{J}, \hat{K})$ are the basis vectors for the nonrotating coordinate system. The rotor inflow λ consists of two components and is expressed as

$$\lambda = \mu \tan \alpha_s + \lambda_i \quad (2.12)$$

where $\mu \tan \alpha_s$ (fig. 2.3) is the component of the forward flight velocity perpendicular to the hub plane, and λ_i is the nondimensional rotor induced inflow associated with the lift on the rotor. Calculation of the induced inflow λ_i involves extensive formulation, and the details are deferred to the next section. Since the velocity components in equation 2.11 are expressed in the nonrotating system, two transformations are required to change these to the rotating undeformed frame. The first transformation, which converts the coordinates in the hub fixed frame to the rotating frame with no precone, is given by

$$\mathbf{T}^1 = \begin{bmatrix} \cos \Psi & \sin \Psi & 0 \\ -\sin \Psi & \cos \Psi & 0 \\ 0 & 0 & 1 \end{bmatrix} \quad (2.13)$$

The second transformation relates the rotating coordinate system with no precone to that at a precone angle β_p and is expressed as

$$\mathbf{T}^2 = \begin{bmatrix} \cos \beta_p & 0 & \sin \beta_p \\ 0 & 1 & 0 \\ -\sin \beta_p & 0 & \cos \beta_p \end{bmatrix} \quad (2.14)$$

Therefore, subsequent substitution of \mathbf{T}^1 and \mathbf{T}^2 in equation 2.11 results in the wind velocity expression

$$\mathbf{V}_w = V_x \hat{i} + V_y \hat{j} + V_z \hat{k} \quad (2.15)$$

where V_x , V_y , and V_z are the components of the wind velocity, and

$$V_x = \mu \Omega R \cos \Psi \cos \beta_p - \lambda \Omega R \sin \beta_p \quad (2.16)$$

$$V_y = -\mu \Omega R \sin \Psi \quad (2.17)$$

$$V_z = -\mu \Omega R \cos \Psi - \lambda \Omega R \cos \beta_p \quad (2.18)$$

The general expression for the blade velocity is

$$\mathbf{V}_b = \dot{\mathbf{r}} + \boldsymbol{\Omega} \times \mathbf{r} \quad (2.19)$$

where $\mathbf{r} = (x_1, y_1, z_1)$, $\dot{\mathbf{r}} = (\dot{x}, \dot{y}, \dot{z})$, and $\boldsymbol{\Omega} = (\Omega \sin \beta_p, 0, \Omega \cos \beta_p)$. In particular, the expressions for \mathbf{r} and $\dot{\mathbf{r}}$ consist of the blade motion terms, and, being calculated at an arbitrary position (η, ζ) of the blade cross section, \mathbf{V}_b takes the form

$$\mathbf{V}_b = V_{b_x} \hat{i} + V_{b_y} \hat{j} + V_{b_z} \hat{k} \quad (2.20)$$

where V_{b_x} , V_{b_y} , and V_{b_z} are the components of the blade velocity, and

$$\begin{aligned} V_{b_x} = & \dot{u} - \lambda \dot{\phi}' - (\dot{v}' + w' \dot{\theta}_1)(\eta \cos \theta_1 - \zeta \sin \theta_1) \\ & - (\dot{w}' - v' \dot{\theta}_1)(\eta \sin \theta_1 + \zeta \cos \theta_1) - \Omega(v + \eta \cos \theta_1 - \zeta \sin \theta_1) \cos \beta_p \end{aligned} \quad (2.21)$$

$$\begin{aligned} V_{b_y} = & \dot{v} - \dot{\theta}_1(\eta \sin \theta_1 + \zeta \cos \theta_1) \\ & + \Omega((x + u - \lambda \hat{\phi}' - v'(\eta \cos \theta_1 - \zeta \sin \theta_1) \\ & - w'(\eta \sin \theta_1 + \zeta \cos \theta_1)) \cos \beta_p - (w + \eta \sin \theta_1 + \eta \cos \theta_1) \sin \beta_p \end{aligned} \quad (2.22)$$

$$V_{b_z} = \dot{w} + \dot{\theta}_1(\eta \cos \theta_1 - \zeta \sin \theta_1) + \Omega(v + \eta \cos \theta_1 - \zeta \sin \theta_1) \sin \beta_p \quad (2.23)$$

The resultant velocity at the blade cross section, expressed in the rotating undeformed coordinate system, is

$$\begin{aligned} \mathbf{V} &= U_x \hat{i} + U_y \hat{j} + U_z \hat{k} \\ &= (V_{b_x} - V_x) \hat{i} + (V_{b_y} - V_y) \hat{j} + (V_{b_z} - V_z) \hat{k} \end{aligned} \quad (2.24)$$

Since a strip analysis is used, airloads (the aerodynamic loads) are computed based on the angle of attack at the three-quarter chord location. With respect to the blade coordinate system, this requires the velocity components to be calculated at $(0, \eta_r)$. As such, the resultant velocity expressions simplify to

$$\begin{aligned} U_x &= \dot{u} - (v' + w' \dot{\theta}_1) \eta_r \cos \theta_1 - (\dot{w}' - v' \dot{\theta}_1) \eta_r \sin \theta_1 \\ &\quad - \Omega(v + \eta_r \cos \theta_1) - \mu \Omega R \cos \Psi + \lambda \Omega R \beta_p \end{aligned} \quad (2.25)$$

$$\begin{aligned} U_y &= \dot{v} - \dot{\theta}_1 \eta_r \sin \theta_1 + \mu \Omega R \sin \Psi \\ &\quad + \Omega(x + u - v' \eta_r \cos \theta_1 - w' \eta_r \sin \theta_1 - (w + \eta_r \sin \theta_1) \beta_p) \end{aligned} \quad (2.26)$$

$$U_z = \dot{w} + \dot{\theta}_1 \eta_r \cos \theta_1 + \Omega \beta_p (v + \eta_r \cos \theta_1) + \mu \Omega R \beta_p \cos \Psi + \lambda \Omega R \quad (2.27)$$

In deriving the above expressions, small angle assumptions were made on the precone angle β_p ; that is, $\sin \beta_p \approx \beta_p$, and $\cos \beta_p \approx 1$.

Finally, the blade velocity components are transformed into the blade deformed frame. Such information is required to calculate for the blade section airloads in the deformed frame. In particular, the transformation relating the coordinate system from the undeformed to the deformed frame is given by (ref. 84)

$$\mathbf{T}^3 = \begin{bmatrix} 1 - \frac{v'^2}{2} - \frac{w'^2}{2} & v' & w' \\ -(v' \cos \theta_1 + w' \sin \theta_1) & (1 - \frac{v'^2}{2}) \cos \theta_1 - v' w' \sin \theta_1 & \sin \theta_1 (1 - \frac{w'^2}{2}) \\ v' \sin \theta_1 - w' \cos \theta_1 & -(1 - \frac{v'^2}{2}) \sin \theta_1 - v' w' \cos \theta_1 & \cos \theta_1 (1 - \frac{w'^2}{2}) \end{bmatrix}$$

Thus, the resultant blade velocity expressed in the rotating deformed frame is

$$\mathbf{V} = U_R \hat{e}_\xi + U_T \hat{e}_\eta + U_P \hat{e}_\zeta \quad (2.28)$$

where

$$\begin{aligned} \frac{U_R}{\Omega R} = & \dot{u} - v + v'(x + \mu \sin \Psi) - \mu \cos \Psi(1 - \beta_p w') + \lambda(\beta_p + w') \\ & - \eta_r \cos \theta(1 + \dot{v}' - \dot{\theta} w') + \eta_r \sin \theta(\hat{\phi} - \dot{w}' - \dot{\theta} v') \\ & + v' \dot{v} + w' \dot{w} + \frac{1}{2} \mu \cos \Psi(v'^2 + w'^2) \end{aligned} \quad (2.29)$$

$$\begin{aligned} \frac{U_T}{\Omega R} = & \cos \theta((\dot{v} + u) - w \beta_p + \hat{\phi}(\lambda + \dot{w}) + v'(v - \dot{u})) \\ & + (x + \mu \sin \Psi)(1 - \frac{v'^2}{2}) + \mu \cos \Psi(v' + \hat{\phi}(\beta_p + w')) \\ & + \sin \theta((\dot{w} + \lambda) + v(\beta_p + w') - \hat{\phi}(\dot{v} + u) - \dot{u} w') \\ & - (x + \mu \sin \Psi)(v' w' + \hat{\phi} + \mu \cos \Psi(w' + \beta_p - \hat{\phi} v')) \end{aligned} \quad (2.30)$$

$$\begin{aligned} \frac{U_P}{\Omega R} = & \cos \theta((\dot{w} + \lambda) + \beta_p v + (v - \dot{u}) w' + \mu \cos \Psi(\beta_p + w' - \hat{\phi} v')) \\ & - (x + \mu \sin \Psi)(v' w' + \hat{\phi}) + \sin \theta(-(\dot{v} + u) + (\dot{u} - v) v' + w \beta_p \\ & - \hat{\phi}(\dot{w} + \lambda) - \mu \cos \Psi(v' + \hat{\phi}(\beta_p + w)) - (x + \mu \sin \Psi)(1 - \frac{v'^2}{2})) \\ & + \eta_r(\dot{\theta} + \dot{\hat{\phi}} + w' + \beta_p + \mu \cos \Psi \theta_{tw}) \end{aligned} \quad (2.31)$$

In the above expressions, only the second order terms are retained, while the higher order terms are neglected. This assumption is consistent with the fact that the blade deflections and velocities are small compared to other terms. Furthermore, small angle assumptions were made on $\hat{\phi}$ such that

$$\sin(\theta + \hat{\phi}) \approx \sin \theta + \hat{\phi} \cos \theta \quad (2.32)$$

$$\cos(\theta + \hat{\phi}) \approx \cos \theta - \hat{\phi} \sin \theta \quad (2.33)$$

2.3.2 Aerodynamic Modeling

Calculation of the blade section airloads is performed in the time domain using a nonlinear unsteady aerodynamic model developed by Leishman and Beddoes (refs. 81 and 82). Elements of the model and its application to the aeroelastic analysis are described in this section. Basically, this model consists of an attached flow formulation along with a representation of nonlinear effects due to flow separation and dynamic stall.

The basic approach adopted in formulating the unsteady aerodynamic model is to identify the physical phenomena associated with each process and to model the whole process by using a combination of linear dynamical systems. Basic elements of the model, representing each process, are described in terms of the indicial response functions. For a linear system, the indicial response is the system

response to a unit step input, with zero initial conditions. If the indicial response is known, then the system steady response can be computed using the Duhamel integral. In particular, if $\phi(s)$ is an indicial response function characterized in terms of the time variable s , then the system response $y(s)$ to an arbitrary forcing function $u(s)$ is

$$y(s) = \phi(s)u(0) + \int_0^s \phi(s - \sigma) \frac{du(\sigma)}{d\sigma} d\sigma \quad (2.34)$$

where σ is the dummy time variable of integration. Since the rotor aeroelastic analysis is primarily concerned with the periodic force response, the transient response associated with the initial condition is neglected.

Attached flow formulation— The attached flow formulation is applicable to flow regime where the airfoil lift and pitching moment vary linearly with the angle of attack. Even though nonlinear effects associated with the stall behavior have not yet been included, this formulation is a prerequisite to the complete model including flow separation and dynamic stall. The attached flow formulation has been generalized for the compressible flow, and, furthermore, it has been validated for airfoils that undergo arbitrary motions up to the transonic flow regime (ref. 86).

For the range of angle of attack typically encountered in rotor analysis, the following assumptions are made (fig. 2.4)

$$\bar{L}_w \approx L \quad (2.35)$$

with

$$C_L = C_0 + C_1\alpha \quad (2.36)$$

where C_1 is the compressible lift curve slope, with value taken from the static airfoil data at $M = 0.3$, and scaled by the Prandtl-Glauert correction factor giving

$$C_1 = \frac{(C_{L\alpha})_{M=0.3}}{\beta} \quad (2.37)$$

where $\beta = \sqrt{1 - M^2}$. Furthermore, since the angle of attack α is small

$$\begin{aligned} \alpha &= \tan^{-1} \left(\frac{-U_P}{U_T} \right) \\ &\approx \frac{-U_P}{U_T} \end{aligned} \quad (2.38)$$

where U_P is the downwash at the three-quarter chord location, and U_T is the incoming velocity component, parallel to the chord line.

With these assumptions, \bar{L}_w can be expressed as

$$\bar{L}_w(s) = \frac{1}{2} \rho c U_T^2 C_0 + L_w^c(s) + L_w^i(s) \quad (2.39)$$

where L_w^c is the circulatory lift, and L_w^i is the noncirculatory lift. In particular, \bar{L}_w is the component of the airloads acting perpendicular to the chord line and is usually referred to as the normal force,

also denoted by N . Using the indicial function formulation, the component of circulatory lift can be expressed as

$$L_w^c(s) = -\frac{1}{2}\rho c C_1 U_T \left[\phi_c(s) U_P(0) + \int_0^s \phi_c(s-\sigma) \frac{dU_P(\sigma)}{d\sigma} d\sigma \right]. \quad (2.40)$$

The circulatory indicial response $\phi_c(s)$ is given by (ref. 81)

$$\phi_c(s) = 1 - \left[A_1 \exp(-b_1 \beta^2 s) + A_2 \exp(-b_2 \beta^2 s) \right] \quad (2.41)$$

where the terms in bracket represent the lift deficiency due to vortices shed downstream into the airfoil wake. Without the Mach scaling parameter β^2 , this indicial function is similar to the classical Kussner function and differs only through the values of the coefficient. For this indicial function, $A_1 = 0.3$; $A_2 = 0.7$; $b_1 = 0.14$; $b_2 = 0.53$, while the coefficients for the Kussner function are (refs. 60 and 61): $A_1 = A_2 = 0.5$; $b_1 = 0.13$; $b_2 = 1.0$. The variable s represents the distance an airfoil travels in terms of semi-chord, and it can be expressed in terms of rotor coordinate as

$$s = \frac{2}{\Omega c} \int_0^\Psi U_T(\Psi) d\Psi \quad (2.42)$$

Similar to the circulatory lift, the impulsive lift component is given by

$$L_w^i(s) = -\frac{1}{2}\rho c U_T \left[\phi_i(s) U_P(0) + \int_0^s \phi_i(s-\sigma) \frac{dU_P(\sigma)}{d\sigma} d\sigma \right] \quad (2.43)$$

where $\phi_i(s)$ is the impulsive indicial response function. This function is derived based on the dynamics of the noncirculatory loading due to pressure wave propagation, and the initial value is computed using piston theory (ref. 61); that is

$$\phi_i(s) = \frac{4}{M} \exp\left(\frac{-s}{2MK_\alpha}\right) \quad (2.44)$$

where K_α is a time constant dependent on the Mach number (ref. 82), and

$$K_\alpha = \frac{1.5}{2(1-M) + 2\pi\beta M^2(A_1 b_1 + A_2 b_2)} \quad (2.45)$$

This impulsive loading can be considered as the compressible analog of the apparent mass terms used in many incompressible analyses.

Following the formulation of reference (ref. 87), the chord force \bar{L}_v , also denoted by C , can be expressed as

$$\bar{L}_v = \eta_a L \sin \alpha - \frac{1}{2}\rho U_T^2 c d_0 \cos \alpha \quad (2.46)$$

where η_a is the leading suction recovery factor which accounts for the inability of the airfoil to realize 100 percent suction in a real flow, and d_0 is the viscous drag or skin friction drag component.

With regard to the more familiar drag coefficient expression, which is often presented in terms of a quadratic polynomial in α as

$$C_d = d_0 + d_1 \alpha + d_2 \alpha^2 \quad (2.47)$$

it is worth noting that the drag coefficient can also be expressed in terms of the lift and chord forces; that is

$$C_d = d_0 + C_L \sin \alpha - C_c \cos \alpha \quad (2.48)$$

with C_c being the chord force coefficient. It can be shown that these two descriptions are equivalent, with the latter being more suitable for unsteady calculations. Assuming that the α is small, then equation 2.48 can be approximated as

$$C_d \approx d_0 + (1 - \eta_a)C_L \alpha \quad (2.49)$$

where the second term in the above expression is actually the pressure drag component. Together with equations 2.36 and 2.47, it can be shown that

$$d_1 = (1 - \eta)C_0$$

$$d_2 = (1 - \eta)C_1$$

These results imply that the pressure drag can be expressed solely in terms of the normal force. As such, the unsteady pressure drag can be computed from the time-dependent lift and chord forces.

The radial drag \bar{L}_u is computed based on the fact that only the viscous drag is affected by the velocity component in the radial direction (ref. 88). Hence, the pressure drag does not contribute to the radial drag component. In the radial direction of the rotor blade

$$\bar{L}_u = D_R = \frac{1}{2} \rho (U_R^2 + U_T^2) c d_0 \sin \Lambda$$

where Λ is the blade yaw angle, and

$$\sin \Lambda = \frac{-U_R}{\sqrt{U_R^2 + U_T^2}}$$

With the above expression, \bar{L}_u simplifies to

$$\bar{L}_u = \frac{1}{2} \rho c d_0 \sqrt{U_R^2 + U_T^2} U_R \quad (2.50)$$

As in the case of lift, the unsteady aerodynamic pitching moment also consists of circulatory and impulsive components. However, the pitching moment is dependent on the modes of forcing, or the types of airfoil motion. These modes of forcing basically govern the types of pressure distribution on the airfoil, which, in turn, have a direct effect on the pitching moment. In the analysis, the airfoil angle of incidence is assumed to consist of two types of airfoil motions: a pure heaving or vertical motion along the ζ axis, denoted by \dot{h} , and a pure pitch rate or the airfoil pitching motion about the elastic axis, denoted by q . Together these modes of airfoil motion contribute to α as

$$\alpha \approx -\frac{\dot{h}}{U_T} + \frac{q}{2}$$

where

$$q = \frac{-2\eta_r \dot{\alpha}}{U_T}$$

and η_r is the offset of the airfoil pitch axis from the three-quarter chord location.

With these modes of forcing, the unsteady pitching moment about the airfoil elastic axis is given by

$$M_\phi = \frac{1}{2}\rho U_T^2 c^2 f_0 - e_d c L_w^c + M_h^i + M_q^c + M_q^i \quad (2.51)$$

where f_0 is the pitching moment coefficient at zero lift about the aerodynamic center, and e_d is the chordwise offset of the aerodynamic center behind the elastic axis, expressed in terms of chord. The second term in the above equation represents the component of the circulatory lift acting at the aerodynamic center. The third term represents the contribution of the airfoil heaving motion to the noncirculatory pitching moment and is expressed as

$$M_h^i = -\frac{1}{2}\rho c^2 U_T \left[\phi_{M_h}^i(s) \dot{h}(0) + \int_0^s \phi_{M_h}^i(s-\sigma) \frac{d\dot{h}(\sigma)}{d\sigma} d\sigma \right] \quad (2.52)$$

with the corresponding indicial response function given by

$$\phi_{M_h}^i(s) = A_3 \exp\left(\frac{-s}{2Mb_3K_{M_h}}\right) + A_4 \exp\left(\frac{-s}{2Mb_4K_{M_h}}\right) \quad (2.53)$$

where $A_3 = 1.5$, $A_4 = -0.5$, $b_1 = 0.25$, $b_2 = 0.1$, and

$$K_{M_h} = 0.8 \frac{A_3 b_4 + A_4 b_3}{b_3 b_4 (1-M)}$$

Physically, this indicial function represents the decay of the impulsive loading along with the forward movement of the center of pressure. Due to a unit step input in \dot{h} , the pressure loading is initially uniform across the chord length, and the center of pressure is at midchord. As the loading decays exponentially, the pressure distribution becomes asymmetric, and the center of pressure tends toward the airfoil quarter chord.

The fourth term in equation 2.51 is the circulatory pitching moment due to the airfoil pitch rate q about the elastic axis and is given as

$$M_q^c(s) = -\frac{\pi}{16\beta} \rho c^2 U_T \left[\phi_{M_q}^c(s) q(0) + \int_0^s \phi_{M_q}^c(s-\sigma) \frac{dq(\sigma)}{d\sigma} d\sigma \right] \quad (2.54)$$

This is usually referred to as the pitch rate induced camber term, and its quasi-steady value is taken from the classical thin airfoil results. The associated indicial response is

$$\phi_{M_q}^c(s) = 1 - \exp(-b_5 \beta^2 s) \quad (2.55)$$

where $b_5 = 0.5$.

The noncirculatory pitching moment, the last term in equation 2.51, has contribution from the airfoil pitch rate q and is expressed as

$$M_q^i(s) = -\frac{1}{2}\rho c^2 U_T \left[\phi_{M_q}^i(s) q(0) + \int_0^s \phi_{M_q}^i(s-\sigma) \frac{dq(\sigma)}{d\sigma} d\sigma \right] \quad (2.56)$$

The corresponding indicial response given by

$$\phi_{M_q}^i(s) = -\frac{7}{12M} \exp\left(\frac{-s}{2MK_{M_q}}\right) \quad (2.57)$$

where

$$K_{M_q} = \frac{5.6}{15(1-M) + 3\pi\beta M^2 b_5}$$

Separated flow formulation– Extension of the aerodynamic formulation to the nonlinear regime requires the modeling of two distinct phenomena associated with the airfoil stall behavior, namely trailing edge and leading edge separations. The phenomenon of progressive trailing edge flow separation is associated with most types of airfoil stall under both static and dynamic conditions. Trailing edge separation starts from the airfoil trailing edge, and with increasing angle of attack, the separation point progresses toward the leading edge region. Such effects contribute to the nonlinear behavior in lift, drag, and pitching moment due to the loss in circulation. If supercritical flow develops under dynamic conditions, then the stall process is initiated by the leading edge or shock-induced separation. This phenomenon is characterized by the shedding of a strong vortex from the leading edge region. The leading edge vortex induces a large pressure disturbance wave, moving aft on the airfoil upper surface; produces abrupt changes in the flow field; and contributes to the large transient lift, drag, and pitching moment. This is a catastrophic process known as dynamic stall.

To simulate the nonlinear effects associated with trailing edge separation, Kirchhoff's flow model is used (ref. 89). This model relates the airfoil static normal force (or lift) and chord force behavior to the trailing edge separation location, a location at which the flow starts to detach from the airfoil upper surface. In this model, the expressions for the normal and chord forces are

$$C_N = C_1 \left(\frac{1 + \sqrt{f}}{2}\right)^2 \alpha \quad (2.58)$$

$$C_C = \eta_a C_1 \sqrt{f} \alpha^2 \quad (2.59)$$

where f is defined as the chordwise distance between the flow separation point and the airfoil leading edge, expressed in terms of chord and shown in figure 2.4. In particular, the value of f varies between zero and one and dictates whether the flow is fully attached ($f = 1$) or completely separated ($f = 0$).

A general expression for the pitching moment was not provided by the Kirchhoff model, and, therefore, the following empirical relation is used (ref. 81)

$$C_M = f_0 + [k_0 + k_1(1-f) + k_2 \sin \pi f^2] C_N \quad (2.60)$$

where $k_0 = \frac{1}{4} - x_{ac}$ is the aerodynamic center offset from the airfoil quarter chord, and k_1 and k_2 are empirical constants obtained from a curve fit to the static pitching moment coefficient for a particular airfoil.

Implementation of the above relations (eqs. 2.58 and 2.59) requires the explicit representation of the airfoil separation point f in terms of the angle of attack. In particular, using equation 2.58, an effective separation point can be inferred from the static lift coefficient for a given airfoil at a given Mach number. Specifically, if the static lift coefficient is known, then

$$f = \left[2\sqrt{\frac{C_N}{C_1\alpha}} - 1 \right]^2 \quad (2.61)$$

where C_1 is the lift curve slope at zero lift value. Curve-fitting relations are then used to describe the variation of f with α , and as such

$$f = \begin{cases} 1 - 0.3 \exp\left(\frac{\alpha - \alpha_1}{S_1}\right) & \text{for } \alpha \leq \alpha_1 \\ 0.04 + 0.66 \exp\left(\frac{\alpha_1 - \alpha}{S_2}\right) & \text{for } \alpha > \alpha_1 \end{cases} \quad (2.62)$$

where α_1 is the angle of attack at which $f = 0.7$, a breakpoint dividing flow behavior into partially attached ($f \geq 0.7$) and fully separated ($f < 0.7$) conditions. For a pair (α, f) and α_1 , the empirical constants S_1 and S_2 can be calculated by inverting equation 2.62 as

$$\frac{1}{S_1} = \frac{1}{\alpha - \alpha_1} \ln\left(\frac{1-f}{0.3}\right) \quad (2.63)$$

$$\frac{1}{S_2} = \frac{1}{\alpha_1 - \alpha} \ln\left(\frac{f - 0.04}{0.66}\right) \quad (2.64)$$

For a given Mach number, the variation of f with α is characterized in terms of only three empirical parameters: α_1 , S_1 , and S_2 . Thus, this model provides a compact structure for the reconstruction of the airfoil static nonlinear behavior. If the effects of the airfoil unsteady pressure distribution and the onset of separation can be evaluated, then this model can also be extended to the dynamic regime.

To model the onset of separation, it has been established by Beddoes (ref. 81) that only the peak pressure at the leading edge or ahead of the shock wave is important. Therefore, generalization of the dynamic effects based on the critical aspect of pressure distribution provides a useful means of implementing the criteria for leading edge or shock-induced separation. This generalized criterion also provides a way for finding the unsteady trailing edge separation based on the assumption that the boundary layer and separation development are also dictated by the behavior of the leading edge pressure. Hence, implementation of the criterion would modify the trailing edge calculation and simultaneously initiate the leading edge vortex shedding.

Under unsteady conditions, position of the separation point is governed by the dynamics of both the airfoil pressure distribution and the boundary layer responses. First, it is required to relate the airfoil unsteady leading edge pressure response to the forcing. Based on unsteady airfoil data, the dynamics of the airfoil pressure distribution with respect to the lift forcing can be represented by a first order linear dynamical system with a time constant T_p . In particular, the system input is C_{N_L} , the airfoil attached flow normal force coefficient, and the system output is C'_N , the substitute normal force value.

The indicial response of C'_N is given by

$$\phi_p(s) = 1 - \exp\left(\frac{-s}{T_p}\right) \quad (2.65)$$

where

$$C_{NL} = \frac{\bar{L}_w}{\frac{1}{2}\rho U_T^2 c} \quad (2.66)$$

and \bar{L}_w is given by equation 2.39. The time constant T_p depends on the Mach number and can be determined from unsteady airfoil data.

For the unsteady case, the response of the boundary layer is also subjected to dynamic behavior. Again, modeling of this process is accomplished by representing the boundary layer response by another first order linear dynamical system with a Mach dependent time constant T_f . In the model, the quasi-steady separation point, denoted by f' , is computed using the substitute normal value. This is accomplished through an effective angle of incidence α_f given by

$$\alpha_f = \frac{C'_N}{C_1}$$

The resulting value of f' is evaluated by substituting the value of α_f into equation 2.62. Then the indicial response of f'' , the effective trailing edge separation point, to changes in the airfoil pressure distribution takes the form

$$\phi_f(s) = 1 - \exp\left(\frac{-s}{T_f}\right) \quad (2.67)$$

In particular, f' represents the pressure distribution response, while f'' includes additional effects of the boundary layer response. Both values of C'_N and f'' can be computed using the superposition integral in the form of the Duhamel integral, and the effective separation point is then used to calculate the airfoil nonlinear lift, drag, and pitching moment. The value of the time constant T_f can be obtained from unsteady boundary layer calculations.

Physically, dynamic stall is characterized by the leading edge separation and the shedding of concentrated vorticity from the leading edge region. This vorticity is swept downstream over the chord and produces a significant increment in the airfoil lift, drag, and pitching moment. Since dynamic stall is a catastrophic process, the stall onset is modeled using a criterion such that the separation is initiated when the substitute normal force C'_N attains a critical value, C_{N_1} . Based on the calculation of C'_N proposed earlier, this criterion implies that, under dynamic condition, the critical lift condition may be reached at a higher angle of attack than the static condition. Typically known as dynamic stall delay, this effect contributes to the delay in the occurrence of stall under dynamic conditions. With regard to the angle of attack forcing, the dynamic stall delay is represented by the unsteady effects associated with the attached flow normal force and the time constant T_p . Also, it is worth pointing out that the value of T_p depends on the Mach number. The value of C_{N_1} corresponds to a critical leading edge pressure and is closely related to the airfoil maximum static lift coefficient. Furthermore, the value of C_{N_1} depends on both the airfoil geometry and Mach number.

Once leading edge separation has been initiated, the vortex lift C_{NV} , being the excess lift induced by the dynamic stall process, is governed by the incremental lift quantity C_V . The value of C_V is related to the difference in lift between the attached and the separated flow regimes. In particular, this process is governed by the rate of change of C_V . In the limit as the rate of change tends to zero, the value of C_{NV} decays exponentially to zero. Modeling of this process is realized by yet another linear dynamical system of the first order with a time constant T_V . Employing this model, the response of C_{NV} to the time rate of change of C_V can be expressed using the convolution integral as

$$C_{NV}(s) = \phi_v(s)C_V(0) + \int_0^s \phi_v(s - \sigma) \frac{dC_V(\sigma)}{d\sigma} d\sigma \quad (2.68)$$

where the indicial response function $\phi_v(s)$ has the form

$$\phi_v(s) = \exp\left(\frac{-s}{T_V}\right) \quad (2.69)$$

and

$$C_V = C_{NL} \left[1 - \left(\frac{1 + \sqrt{f''}}{2} \right)^2 \right] \quad (2.70)$$

As the leading edge vortex is swept downstream, the airfoil center of pressure varies significantly with the chordwise location of the vortex. The vortex convection rate is monitored using a nondimensional time based on the distance traveled by the airfoil in semi-chords. This rate has been determined from experimental data to be roughly less than half the free-stream velocity, while the actual rate is dependent on the Mach number. Based on physical considerations, a suitable representation of the airfoil center of pressure behavior takes the form

$$CP_V = \frac{1}{4} \left(1 - \cos\left(\frac{\pi\tau_v}{T_{VL}}\right) \right) \quad (2.71)$$

where τ_v is the vortex time, and T_{VL} represents the vortex convection rate. At the onset of separation, the vortex is at the leading edge, and τ_v is equal to zero. When the vortex reaches the airfoil trailing edge, τ_v is equal to T_{VL} . Therefore, by monitoring the excess lift and the center of pressure location, the vortex induced pitching moment can be calculated by

$$C_{MV} = -CP_V C_{NV} \quad (2.72)$$

The values of T_V and T_{VL} are determined from the airfoil unsteady data. After the vortex passes over the trailing edge, the effects of the vortex lift on the airfoil decay rapidly, and this phenomenon is accomplished by halving the time constant T_V for the period $T_{VL} < \tau_v \leq 2T_{VL}$.

Further modifications to the basic separated flow formulation have been made to better capture the interactions between the dynamic stall process, the trailing edge separation behaviors, and the airfoil kinematics. In most cases, these interactional effects are represented by modifying the appropriate time constants associated with each process. Specifically, increasing a time constant has the effect of slowing down the process, whereas reducing the time constant produces the opposite effect. Further details on these modifications can be found in reference 81.

A final modification made to the basic model concerns the remodeling of the Kirchhoff chord force expression (i.e., eq. 2.59). Such modification is necessary to model the drag divergence induced by the flow behavior after the onset of gross separation. For this, an additional parameter has been introduced to the chord force expression, which becomes

$$C_C = \eta_a C_1 \sqrt{f''} \alpha^2 \Phi \quad (2.73)$$

where

$$\Phi = (f'')^{0.5} K_f (C'_N - C_{N_1}) \quad (2.74)$$

for $C'_N \geq C_{N_1}$. The actual value of K_f can be determined from the airfoil static drag data.

In forward flight, the rotor is also subjected to a reverse flow region that increases with increasing forward speed. The reverse flow region is characterized by a complete reversal of the inplane velocity vector as shown in figure 2.5. This effect contributes to the reversal of the chord force and the pitching moment, and causes the shifting of the aerodynamic center from the region near quarter chord to approximately the three-quarter chord location. The lift and radial drag components are independent of the direction of the inplane velocity vector.

In the analysis, the computation of the blade airloads is performed using a finite-difference approximation to the Duhamel integrals. And with the inclusion of reverse flow correction, the unsteady aerodynamic loads, at the rotor time sample Ψ_n , are expressed in a discrete-time form as

$$\bar{L}_u(\Psi_n) = -\frac{\rho c}{2} \left[d_0 \sqrt{U_R^2 + U_T^2} U_R \right] \quad (2.75)$$

$$\bar{L}_v(\Psi_n) = -\frac{\rho c}{2} \text{sign}(U_T) \left[d_0 U_T^2 - \eta_a C_0 \sqrt{f''} \Phi |U_T| U_{P_e} + \eta_a C_1 \sqrt{f''} \Phi U_{P_e}^2 \right] \quad (2.76)$$

$$\begin{aligned} \bar{L}_w(\Psi_n) = \frac{\rho c}{2} \left[(C_0 + C_{NV}) U_T^2 - (C_1 \mathcal{K} + d_0) |U_T| U_{P_e} \right. \\ \left. + (\eta_a - 1) C_0 U_{P_e}^2 + 4c K_\alpha (\dot{U}_P - D_n) \right] \quad (2.77) \end{aligned}$$

$$\begin{aligned} M_\phi^A(\Psi_n) = \frac{\rho c^2}{2} \left[\text{sign}(U_T) \left((f_0 + \mathcal{G} C_0 + C_{MV}) U_T^2 - \mathcal{G} \mathcal{K} C_1 |U_T| U_{P_e} \right. \right. \\ \left. \left. - \frac{\pi}{8\beta} |U_T| (q_n - V_n) \right) - \frac{7}{12} c K_{qM} (\dot{q} - V_n) \right. \\ \left. - A_3 b_3 c K_{M_h} (\dot{U}_P - Z_{an}) - A_4 b_4 c K_{M_h} (\dot{U}_P - Z_{bn}) \right] \quad (2.78) \end{aligned}$$

where

$$U_{P_e} = U_{P_n} - X_n - Y_n \quad (2.79)$$

$$X_n = X_{n-1} e^{-0.14\beta^2 \Delta s} - 0.3 \Delta U_{P_n} e^{-0.07\beta^2 \Delta s} \quad (2.80)$$

$$Y_n = Y_{n-1} e^{-0.53\beta^2 \Delta s} - 0.7 \Delta U_{P_n} e^{-0.265\beta^2 \Delta s} \quad (2.81)$$

$$\Delta s = \frac{2R}{c} [\Delta\psi x - \mu (\cos \Psi_n - \cos \Psi_{n-1})] \quad (2.82)$$

$$\Delta\psi = \Psi_n - \Psi_{n-1} \quad (2.83)$$

$$\Delta U_{P_n} = U_{P_n} - U_{P_{n-1}} \quad (2.84)$$

$$U_P^* = \left(\frac{\partial U_P}{\partial \Psi} \right)_n \quad (2.85)$$

$$D_n = D_{n-1} e^{-\Delta\psi/cM_H K_\alpha} + \Delta U_{P_n}^* e^{-\Delta\psi/2cM_H K_\alpha} \quad (2.86)$$

$$\Delta U_{P_n}^* = U_{P_n}^* - U_{P_{n-1}}^* \quad (2.87)$$

$$V_n = V_{n-1} e^{-0.5\beta^2 \Delta s} + \Delta q_n e^{-0.25\beta^2 \Delta s} \quad (2.88)$$

$$\Delta q_n = q_n - q_{n-1} \quad (2.89)$$

$$q_n = 2\eta_r (\dot{\theta} + \dot{\phi} + w' + \beta_p + \mu \cos \Psi_n \theta_{tw}) \quad (2.90)$$

with

$$\eta_r = \begin{cases} -(e_d + c/2) & \text{if } U_T > 0 \\ -e_d & \text{otherwise} \end{cases} \quad (2.91)$$

$$V_{q_n} = V_{q_{n-1}} e^{-\Delta\psi/cM_H K_{qM}} + \Delta \dot{q}_n^* e^{-\Delta\psi/2cM_H K_{qM}} \quad (2.92)$$

$$\dot{q}^* = \left(\frac{\partial q}{\partial \Psi} \right)_n \quad (2.93)$$

$$\Delta \dot{q}_n^* = \dot{q}_n^* - \dot{q}_{n-1}^* \quad (2.94)$$

$$Z_{a_n} = Z_{a_{n-1}} e^{-\Delta\psi/cM_H K_{Mh b_3}} + \Delta U_{P_n}^* e^{-\Delta\psi/2cM_H K_{Mh b_3}} \quad (2.95)$$

$$Z_{b_n} = Z_{b_{n-1}} e^{\Delta\psi/cM_H K_{Mh b_4}} + \Delta U_{P_n}^* e^{-\Delta\psi/2cM_H K_{Mh b_4}} \quad (2.96)$$

$$\mathcal{K} = \left(\frac{1 + \sqrt{f_n''}}{2} \right)^2 \quad (2.97)$$

$$f_n'' = f_n' - D_{f_n} \quad (2.98)$$

$$D_{f_n} = D_{f_{n-1}} e^{-\Delta s/T_f} + (f_n' - f_{n-1}') e^{-\Delta s/2T_f} \quad (2.99)$$

$$\mathcal{G} = k_0 + k_1 (1 - f_n'') + \sin \pi f_n''^2 \quad (2.100)$$

$$C'_N = C_{N_{L_n}} - D_{P_n} \quad (2.101)$$

$$D_{P_n} = D_{P_{n-1}} e^{-\Delta s/T_p} + (C_{N_{L_n}} - C_{N_{L_{n-1}}}) e^{-\Delta s/2T_p} \quad (2.102)$$

$$\Phi = \begin{cases} (f_n'')^{0.5} K_f (C'_N - C_{N_1}) & \text{if } C'_N \geq C_{N_1} \\ 1 & \text{otherwise} \end{cases} \quad (2.103)$$

and for $C'_N > C_{N1}$

$$C_{NV_n} = C_{NV_{n-1}} e^{-\Delta s/T_v} + (C_{V_n} - C_{V_{n-1}}) e^{-\Delta s/2T_v} \quad (2.104)$$

$$C_{V_n} = C_{NL_n} \left[1 - \left(\frac{1 + \sqrt{f''_n}}{2} \right)^2 \right] \quad (2.105)$$

with C_{PV} and C_{MV} given by equations 2.71 and 2.72. The parameters \mathcal{K} , \mathcal{G} , and Φ dictate the nonlinear aerodynamic behavior, while the dynamic stall process is governed by C_{NV} . For quasi-steady aerodynamics, the recursive parameters $X_n, Y_n, U_P^* - D_n, V_n, V_{qn}, Z_{an}$, and Z_{bn} are set to zero.

Since the blade section airloads are calculated in the blade undeformed coordinate system, a transformation is required to convert these to the undeformed frame to be consistent with the virtual work expression, equation 2.9. For this, the aerodynamic forces in the undeformed frame are obtained from the coordinate transformation

$$\begin{Bmatrix} L_u^A \\ L_v^A \\ L_w^A \end{Bmatrix} = (\mathbf{T}^3)^T \begin{Bmatrix} \bar{L}_u \\ \bar{L}_v \\ \bar{L}_w \end{Bmatrix} \quad (2.106)$$

These force components, together with M_ϕ^A , are the motion-dependent airloads acting on a blade section and contribute to the virtual work expression in equation 2.9.

2.4 Rotor Wake Modeling

Calculation of the rotor nonuniform induced inflow is one of the most crucial steps in the prediction of blade aeroelastic response, blade loads, vibration, noise, and rotor performance. Currently, there are many inflow models available. These models try to capture, each with a different level of approximation, the complex structure of the vortex wake which is the most dominant feature of the inflow calculation. Complex models can yield accurate inflow prediction but require extensive computation. Simple models provide quick estimate, but somewhat less accurate results. In general, the balance between accuracy and computation efficiency dictates the selection of the wake model. This section describes the inflow models used in the present analysis.

As a consequence of the bound circulation variation associated with the lift on each blade, vortex elements leave the blade trailing edge and spiral downward below the rotor disk plane. This is in accordance with the law of conservation of vorticity, which requires the formation of vorticity associated with the spanwise as well as timewise variation in the bound circulation. The spanwise variation of circulation produces the trailed vorticity, and the timewise variation results in the shed vorticity oriented radially in the wake. Such effects have been depicted schematically, as shown in figure 2.6 (adapted from ref. 90). The effects of shed vorticity have already been included in the unsteady aerodynamic model (sec. 2.3), and, therefore, this section presents methods for computing the rotor induced inflow associated with the trailed vortex system.

In the analysis, different inflow models with varying levels of complexity were included. The simplest model assumes a uniform inflow distribution over the rotor disk and was first proposed by Glauert (ref. 91). This is an extension of the classical momentum theory to forward flight. In this model, the total rotor inflow is expressed in terms of the rotor thrust coefficient, advance ratio, and rotor shaft tilt as

$$\begin{aligned}\lambda &= \mu \tan \alpha_s + \lambda_i \\ &= \mu \tan \alpha_s + \frac{C_T/2}{\sqrt{\lambda^2 + \mu^2}}\end{aligned}\quad (2.107)$$

In another model, the rotor induced inflow is assumed to vary linearly across the rotor disk and is expressed as

$$\lambda_i = \frac{C_T/2}{\sqrt{\lambda^2 + \mu^2}} (1 + \kappa_x x \cos \Psi + \kappa_y x \sin \Psi) \quad (2.108)$$

where

$$\kappa_x = \frac{4}{3} \left[(1 - 1.8\mu^2) \sqrt{1 + \left(\frac{\lambda}{\mu}\right)^2} - \frac{\lambda}{\mu} \right] \quad (2.109)$$

$$\kappa_y = -2\mu \quad (2.110)$$

This is known as the Drees inflow model (ref. 91).

Since the induced inflow is, in fact, highly nonuniform across the rotor disk, the following model uses a vortex ring representation. In this model, the helical path of the concentrated tip vortex for one complete rotor revolution is idealized as a vortex ring. Since the velocity flow field induced by a vortex ring can be computed analytically (ref. 92), the rotor trailed wake structures can be represented by a system of vortex rings cascaded below the rotor disk, as shown in figure 2.7 (adapted from refs. 90 and 93). The resulting induced velocity at any point in the flow field is the net sum of the contribution from the individual vortex rings. The relative location between two rings can be determined by the advance ratio and the mean rotor inflow. While this model can be classified as a rigid wake model, the near singularities in inflow which are contributed by the tip vortices are well represented. The trailed vortex strength is assumed to be concentrated near the blade tip, and the strength of the vortex ring Γ_0 can be expressed in terms of the rotor thrust coefficient as

$$\Gamma_0 = 2\Omega R c \frac{C_T}{\sigma} \quad (2.111)$$

To cover the singularity condition at the vortex core, Γ_0 is further modified as (ref. 91)

$$\Gamma(\rho) = \Gamma_0 \left(\frac{\rho^2}{1 + \rho^2} \right) \quad (2.112)$$

where ρ is the ratio of the radial distance from the core center to the core radius. Typically, core radius of 5 to 7 percent of chord length is employed. This inflow model, however, fails to capture the nonsymmetric characteristic of the induced inflow across the rotor longitudinal axis.

To have a more realistic representation of the wake structures and to improve the accuracy of the inflow prediction, the wake analysis of CAMRAD has been incorporated into the aeroelastic analysis. These models capture, to various levels of approximation, the effects of the interlocking helical vortices of the wake and include prescribed or free wake models. The wake models consist of a set of discrete vortex elements representing the wake structure. The velocity induced by a vortex element is calculated by performing integrations over that element in the wake using the Biot-Savart law, and the resultant induced velocity is the sum of the contributions from all these vortex elements. The basic vortex elements employed by these models are the vortex line with constant or linear circulation distribution and the vortex sheet with uniform density or linear circulation variation. The strength of the vortex elements is determined by the radial and azimuthal variation of the bound circulation.

Basically, the wake geometry consists of discrete and skewed spiral wake, one behind each blade, and is determined by the locations of the wake element. These wake element locations are computed based on the blade motions, the free-stream convection velocity, and the convection and distortion due to the wake self-induced velocity. In essence, classification of the wake models depends largely on the method used in computing the wake distortion. For the rigid wake geometry, the wake elements are convected downward by the mean induced inflow, and the self-distorted wake geometry is neglected. To include the effects of wake distortion, the prescribed wake models include wake contraction using assumed model or empirical data. For the free wake models, the wake induced velocity is included in the computation of the wake self-distorted geometry.

Concentration of lift and circulation near the blade tip region results in the formation of the concentrated tip vortex which is the flow structure dominating the wake calculation. The concentrated tip vortex is trailed as a helix and forms behind each blade. In the wake analysis, this is modeled by a series of straight connecting finite-length vortices with a small core radius extended over the whole wake. There is also an inboard vortex sheet trailed from each blade which has a combined strength equal and opposite to that of the tip vortex. The inboard trailed vorticity is modeled by either a rectangular vortex sheet or a lattice of discrete straight-line vortex segments.

These wake models are composed of three parts: the near wake, the rolling-up wake, and the far wake. The near wake is part of the wake region just behind each reference blade where the induced velocity is calculated. Since both the radial and azimuthal variations of the wake vorticity are important in the calculation of the induced inflow, a full vortex panel representation is used for the near wake. In the near wake region, the tip vortex is partially rolled up, and hence a line vortex with strength equal to a fraction of the bound circulation near the blade tip is used. The wake region just downstream of the near wake is the rolling-up wake. The roll-up process may not be complete as the tip vortex encounters the following blade. Thus, modeling of the roll-up process is required to yield the proper magnitude of the induced velocity, due to such an interaction. For the rolling-up wake, two wake panels with linear circulation variation are used. In the far wake, the roll-up process is complete, and the tip vortex strength is assumed to be equal to the maximum bound circulation. This wake region extends from the roll-up wake boundary to the far wake. For the far wake, a single vortex sheet panel with linear circulation variation is employed. Typically, the near wake extends from 15 to 30 degrees azimuth

behind a reference blade, while the rolling-up wake extends to about 30 degrees azimuth behind the near wake boundary.

For a close blade vortex interaction, the induced velocity calculated using a lifting line model is not accurate since the induced loading would vary rapidly along the blade chord. Efficient modeling of this behavior is made using a correction factor based on the lifting surface solution in conjunction with the lifting line model. Furthermore, it has been established through experiments that the vortex core bursts and increases in size after such interaction. Even though the exact cause of such a phenomenon is still speculative, these wake models allow a vortex core to increase in size to roughly 10 percent of chord length after a blade-vortex interaction.

For the free wake model, the tip vortex is modeled using straight line segments, while rectangular sheets or line segments are used for the inboard wake. The rigid or prescribed wake geometry is used for the inboard vorticity, and only the distorted geometry of the tip vortex is computed. Basically, the distorted wake geometry is calculated by integrating the induced velocity at each wake element. For a given blade azimuth angle Ψ , the tip vortex geometry is given in terms of the displacement and the induced velocity of each wake element at the corresponding age. As the wake age is increased by $\Delta\Psi$, the wake distortion is updated based on the induced velocities calculated at these wake elements.

Coupling of the wake models obtained from CAMRAD and the rotor aeroelastic analysis is made by transferring the blade bound circulation, the blade motions, and the induced inflow between these two analyses. The process of finding consistent solutions for the blade unsteady airloads and the rotor induced inflow is solved iteratively. To start the iteration process, the blade airloads, bound circulation, and blade responses are computed using a uniform or linear inflow model. With the bound circulation and blade motions given, the wake vorticities and geometry are calculated. These are then used to recompute the nonuniform inflow, and the entire process is repeated until convergence is obtained.

2.5 Blade and Rotor Hub Loads

The resulting blade loads are computed using the force summation method. In addition to the distributed airloads, this method also requires information about the blade inertial loads, which can be determined from the blade motions. From Newton's Second Law, the sectional inertial forces acting at a blade section are

$$\mathbf{F}^I = \int \int \rho_s \mathbf{a} \, d\eta \, d\zeta \quad (2.113)$$

with $\mathbf{F}^I = [L_u^I, L_v^I, L_w^I]^T$; L_u^I , L_v^I , and L_w^I are, respectively, the distributed inertial forces acting in the x , y , and z directions in the blade undeformed frame; ρ_s is the blade structural density; \mathbf{a} is the blade acceleration relative to an inertial frame. In the blade undeformed frame, the blade acceleration has the form

$$\begin{aligned} \mathbf{a} &= a_x \hat{i} + a_y \hat{j} + a_z \hat{k} \\ &= \ddot{\mathbf{r}} + \Omega \times (\Omega \times \mathbf{r}) + 2(\Omega \times \dot{\mathbf{r}}) \end{aligned} \quad (2.114)$$

where $\ddot{\mathbf{r}}$, $\dot{\mathbf{r}}$, and \mathbf{r} are, respectively, the blade acceleration, velocity, and displacement vectors in the rotating blade frame, and Ω is the rotor rotational speed.

The inertial component for the blade pitching moment about the deformed elastic axis is

$$M_{\phi}^I = \int \int \rho [a_y (z_1 - w) - a_z (y_1 - v)] d\eta d\zeta \quad (2.115)$$

Using the sectional constants defined in section 2.2, the inertial load components can be expressed as (ref. 94)

$$L_u^I = -m [\ddot{u} - x - u - 2\dot{v} + \beta_p w + e_g \cos \theta_1 (v' - \ddot{v}') + e_g \sin \theta_1 (w' + \beta_p - \ddot{w}' + 2\dot{\theta}_1)] \quad (2.116)$$

$$L_v^I = -m [\ddot{v} - v + 2\dot{u} - 2\beta_p \dot{w} - e_g \cos \theta_1 (1 + 2v') - e_g \sin \theta_1 (\ddot{\theta}_1 + 2\dot{w}')] \quad (2.117)$$

$$L_w^I = -m [\ddot{w} + \beta_p (x + u) + 2\beta_p \dot{v} e_g \cos \theta_1 (\ddot{\theta}_1 - \beta_p v') - e_g \sin \theta_1 \beta_p (w' + 2\dot{\theta}_1)] \quad (2.118)$$

$$M_{\phi}^I = -m [k_m^2 \ddot{\theta}_1 - e_g \sin \theta_1 (\ddot{v} - v) + e_g \cos \theta_1 (\ddot{w} + x\beta_p) + (k_{m_1}^2 - k_{m_2}^2) \cos \theta_1 \sin \theta_1 (1 + 2v') + (k_{m_1}^2 \sin^2 \theta_1 + k_{m_2}^2 \cos^2 \theta_1) 2w'] \quad (2.120)$$

The resultant distributed loads consists of the aerodynamic and inertial components; that is

$$L_u = L_u^A + L_u^I$$

$$L_v = L_v^A + L_v^I$$

$$L_w = L_w^A + L_w^I$$

$$M_{\phi} = M_{\phi}^A + M_{\phi}^I$$

The resultant blade shears computed at a radial station r_o are

$$\begin{Bmatrix} F_x \\ F_y \\ F_z \end{Bmatrix} = \int_{r_o}^R \begin{Bmatrix} L_u \\ L_v \\ L_w \end{Bmatrix} dr \quad (2.121)$$

and the resultant blade bending moments are

$$\begin{Bmatrix} M_x \\ M_y \\ M_z \end{Bmatrix} = \int_{r_o}^R \begin{Bmatrix} -L_v(w - w_o) + L_w(v - v_o) + \Delta t_{11} M_{\phi} \\ L_u(w - w_o) - L_w(r - r_o + u - u_o) + \Delta v' M_{\phi} \\ -L_u(v - v_o) + L_v(r - r_o + u - u_o) + \Delta w' M_{\phi} \end{Bmatrix} dr \quad (2.122)$$

where u_o, v_o, w_o are, respectively, the blade axial, lead-lag, and flap displacements at the radial station r_o , and

$$\Delta t_{11} = 1 - \frac{\Delta v'^2 + \Delta w'^2}{2}$$

with

$$\begin{aligned}\Delta v'^2 &= v'^2 - v_o'^2 \\ \Delta w'^2 &= w'^2 - w_o'^2 \\ \Delta v' &= v' - v_o' \\ \Delta w' &= w' - w_o'\end{aligned}$$

Similarly, v_o' and w_o' are, respectively, the blade slopes in the lead-lag and flap directions computed at the radial station r_o .

At the blade root, r_o is zero, and so are the blade displacements. Therefore, the expressions for the blade bending moment simplify to

$$\begin{Bmatrix} M_x \\ M_y \\ M_z \end{Bmatrix} = \int_0^R \begin{Bmatrix} -L_v w + L_w v + \left(1 - \frac{v'^2 + w'^2}{2}\right) M_\phi \\ L_u w - L_w (r + u) + v' M_\phi \\ -L_u v + L_v (r + u) + w' M_\phi \end{Bmatrix} dr \quad (2.123)$$

Furthermore, these blade loads can be expanded using the Fourier series. For instance, the radial shear expression for the m th blade can be expressed as

$$F_x^m(\Psi) = F_{x_o}^m + \sum_{n=1}^{\infty} \left(F_{x_{nc}}^m \cos \Delta \Psi_m + F_{x_{ns}}^m \sin \Delta \Psi_m \right) \quad (2.124)$$

The Fourier series expansion of the other blade load components have a similar form.

The rotor hub loads are obtained by summing contributions from the individual blades. In the rotating frame, the hub loads are expressed as

$$F_x^R(\Psi) = \sum_{m=1}^{N_b} \left(F_x^m \cos \Delta \Psi_m - F_y^m \sin \Delta \Psi_m \right) \quad (2.125)$$

$$F_y^R(\Psi) = \sum_{m=1}^{N_b} \left(F_x^m \sin \Delta \Psi_m + F_y^m \cos \Delta \Psi_m \right) \quad (2.126)$$

$$F_z^R(\Psi) = \sum_{m=1}^{N_b} \left(F_z^m \right) \quad (2.127)$$

$$M_x^R(\Psi) = \sum_{m=1}^{N_b} \left(M_x^m \cos \Delta \Psi_m - M_y^m \sin \Delta \Psi_m \right) \quad (2.128)$$

$$M_y^R(\Psi) = \sum_{m=1}^{N_b} (M_x^m \sin \Delta\Psi_m + M_y^m \cos \Delta\Psi_m) \quad (2.129)$$

$$M_z^R(\Psi) = \sum_{m=1}^{N_b} (M_z^m) \quad (2.130)$$

where the azimuth for blade m is

$$\Psi_m = \Psi + \Delta\Psi_m \quad (2.131)$$

with

$$\Delta\Psi_m = m \frac{2\pi}{N_b} \quad (2.132)$$

Substituting the Fourier series expansions of the individual blade loads into the hub load expressions and using the properties of the sum of harmonics (ref. 91) yield

$$\begin{aligned} F_x^R(\Psi) = & \frac{N_b}{2} \sum_{p=1}^{\infty} \left\{ \cos(pN_b - 1)\Psi \left[F_{x_{(pN_b-1)c}} + F_{y_{(pN_b-1)s}} \right] \right. \\ & \left. + \sin(pN_b - 1)\Psi \left[F_{x_{(pN_b-1)s}} - F_{y_{(pN_b-1)c}} \right] \right\} \\ & + \frac{N_b}{2} \sum_{p=0}^{\infty} \left\{ \cos(pN_b + 1)\Psi \left[F_{x_{(pN_b+1)c}} - F_{y_{(pN_b+1)s}} \right] \right. \\ & \left. + \sin(pN_b + 1)\Psi \left[F_{x_{(pN_b+1)s}} + F_{y_{(pN_b+1)c}} \right] \right\} \end{aligned} \quad (2.133)$$

$$\begin{aligned} F_y^R(\Psi) = & \frac{N_b}{2} \sum_{p=1}^{\infty} \left\{ \cos(pN_b - 1)\Psi \left[-F_{x_{(pN_b-1)s}} + F_{y_{(pN_b-1)c}} \right] \right. \\ & \left. + \sin(pN_b - 1)\Psi \left[F_{x_{(pN_b-1)c}} - F_{y_{(pN_b-1)s}} \right] \right\} \\ & + \frac{N_b}{2} \sum_{p=0}^{\infty} \left\{ \cos(pN_b + 1)\Psi \left[F_{x_{(pN_b+1)s}} + F_{y_{(pN_b+1)c}} \right] \right. \\ & \left. + \sin(pN_b + 1)\Psi \left[-F_{x_{(pN_b+1)c}} + F_{y_{(pN_b+1)s}} \right] \right\} \end{aligned} \quad (2.134)$$

$$F_z^R(\Psi) = N_b \sum_{p=0}^{\infty} \left\{ F_{z_{(pN_b)c}} \cos(pN_b)\Psi + F_{z_{(pN_b)s}} \sin(pN_b)\Psi \right\} \quad (2.135)$$

$$\begin{aligned}
M_x^R(\Psi) = & \frac{N_b}{2} \sum_{p=1}^{\infty} \left\{ \cos(pN_b - 1)\Psi \left[M_{x(pN_b-1)c} + M_{y(pN_b-1)s} \right] \right. \\
& + \left. \sin(pN_b - 1)\Psi \left[M_{x(pN_b-1)s} - M_{y(pN_b-1)c} \right] \right\} \\
& + \frac{N_b}{2} \sum_{p=0}^{\infty} \left\{ \cos(pN_b + 1)\Psi \left[M_{x(pN_b+1)c} - M_{y(pN_b+1)s} \right] \right. \\
& + \left. \sin(pN_b + 1)\Psi \left[M_{x(pN_b+1)s} + M_{y(pN_b+1)c} \right] \right\} \tag{2.136}
\end{aligned}$$

$$\begin{aligned}
M_y^R(\Psi) = & \frac{N_b}{2} \sum_{p=1}^{\infty} \left\{ \cos(pN_b - 1)\Psi \left[-M_{x(pN_b-1)s} + M_{y(pN_b-1)c} \right] \right. \\
& + \left. \sin(pN_b - 1)\Psi \left[M_{x(pN_b-1)c} - M_{y(pN_b-1)s} \right] \right\} \\
& + \frac{N_b}{2} \sum_{p=0}^{\infty} \left\{ \cos(pN_b + 1)\Psi \left[M_{x(pN_b+1)s} + M_{y(pN_b+1)c} \right] \right. \\
& + \left. \sin(pN_b + 1)\Psi \left[-M_{x(pN_b+1)c} + M_{y(pN_b+1)s} \right] \right\} \tag{2.137}
\end{aligned}$$

$$M_z^R(\Psi) = N_b \sum_{p=0}^{\infty} \left\{ M_{z(pN_b)c} \cos(pN_b)\Psi + M_{z(pN_b)s} \sin(pN_b)\Psi \right\} \tag{2.138}$$

For the rotating inplane hub shears, it is worth noting that

$$\begin{aligned}
F_{x(pN_b-1)c}^R &= F_{y(pN_b-1)s}^R \\
F_{x(pN_b-1)s}^R &= -F_{y(pN_b-1)c}^R
\end{aligned}$$

and

$$\begin{aligned}
F_{x(pN_b+1)c}^R &= -F_{y(pN_b+1)s}^R \\
F_{x(pN_b+1)s}^R &= F_{y(pN_b+1)c}^R
\end{aligned}$$

Therefore, the rotating inplane hub shears are uniquely determined by either F_x^R or F_y^R alone. Similar properties exist for the rotating inplane hub moments M_x^R and M_y^R . Also, the rotating hub loads occur only at certain frequencies. The frequency contents of the vertical hub shear F_z^R and those of the torque M_z^R are the harmonics at pN_b per rev, where p is an integer, and $p = 0, 1, 2, 3, \dots$, whereas the rotating inplane components occur at $(pN_b - 1)$ and $(pN_b + 1)$ per rev, where p is a strictly positive integer. Therefore, only certain harmonics of the blade loads are summed up while others cancel at the

rotor hub. The filtering of the blade load harmonics at the hub is caused by the equal phasing differences of $\Delta\Psi_m$ between individual rotor blades. Furthermore, it has been assumed that the rotor is tracked. For a tracked rotor, all the blades exhibit exactly similar behavior except for the phase differences of $\Delta\Psi_m$.

Similarly, the expressions for the rotor hub loads in the fixed frame are

$$F_X^H(\Psi) = \sum_{m=1}^{N_b} (F_x^m \cos \Psi_m - F_y^m \sin \Psi_m) \quad (2.139)$$

$$F_Y^H(\Psi) = \sum_{m=1}^{N_b} (F_x^m \sin \Psi_m + F_y^m \cos \Psi_m) \quad (2.140)$$

$$F_Z^H(\Psi) = \sum_{m=1}^{N_b} (F_z^m) \quad (2.141)$$

$$M_X^H(\Psi) = \sum_{m=1}^{N_b} (M_x^m \cos \Psi_m - M_y^m \sin \Psi_m) \quad (2.142)$$

$$M_Y^H(\Psi) = \sum_{m=1}^{N_b} (M_x^m \sin \Psi_m + M_y^m \cos \Psi_m) \quad (2.143)$$

$$M_Z^H(\Psi) = \sum_{m=1}^{N_b} (M_z^m) \quad (2.144)$$

For a tracked rotor, the Fourier series expansions for these hub loads can be expressed as

$$\begin{aligned} F_X^H(\Psi) = & \frac{N_b}{2} \sum_{p=1}^{\infty} \left\{ \cos pN_b\Psi \left[F_{x_{(pN_b-1)c}} + F_{y_{(pN_b-1)s}} \right] \right. \\ & \left. + \sin pN_b\Psi \left[F_{x_{(pN_b-1)s}} - F_{y_{(pN_b-1)c}} \right] \right\} \\ & + \frac{N_b}{2} \sum_{p=0}^{\infty} \left\{ \cos pN_b\Psi \left[F_{x_{(pN_b+1)c}} - F_{y_{(pN_b+1)s}} \right] \right. \\ & \left. + \sin pN_b\Psi \left[F_{x_{(pN_b+1)s}} + F_{y_{(pN_b+1)c}} \right] \right\} \end{aligned} \quad (2.145)$$

$$\begin{aligned}
F_Y^H(\Psi) = & \frac{N_b}{2} \sum_{p=1}^{\infty} \left\{ \cos pN_b\Psi \left[-F_{x(pN_b-1)s} + F_{y(pN_b-1)c} \right] \right. \\
& \left. + \sin pN_b\Psi \left[F_{x(pN_b-1)c} + F_{y(pN_b-1)s} \right] \right\} \\
& + \frac{N_b}{2} \sum_{p=0}^{\infty} \left\{ \cos pN_b\Psi \left[F_{x(pN_b+1)s} + F_{y(pN_b+1)c} \right] \right. \\
& \left. + \sin pN_b\Psi \left[-F_{x(pN_b+1)c} + F_{y(pN_b+1)s} \right] \right\}
\end{aligned} \tag{2.146}$$

$$\begin{aligned}
M_X^H(\Psi) = & \frac{N_b}{2} \sum_{p=1}^{\infty} \left\{ \cos pN_b\Psi \left[M_{x(pN_b-1)c} + M_{y(pN_b-1)s} \right] \right. \\
& \left. + \sin pN_b\Psi \left[M_{x(pN_b-1)s} - M_{y(pN_b-1)c} \right] \right\} \\
& + \frac{N_b}{2} \sum_{p=0}^{\infty} \left\{ \cos pN_b\Psi \left[M_{x(pN_b+1)c} - M_{y(pN_b+1)s} \right] \right. \\
& \left. + \sin pN_b\Psi \left[M_{x(pN_b+1)s} + M_{y(pN_b+1)c} \right] \right\}
\end{aligned} \tag{2.147}$$

$$\begin{aligned}
M_Y^H(\Psi) = & \frac{N_b}{2} \sum_{p=1}^{\infty} \left\{ \cos pN_b\Psi \left[-M_{x(pN_b-1)s} + M_{y(pN_b-1)c} \right] \right. \\
& \left. + \sin pN_b\Psi \left[M_{x(pN_b-1)c} + M_{y(pN_b-1)s} \right] \right\} \\
& + \frac{N_b}{2} \sum_{p=0}^{\infty} \left\{ \cos pN_b\Psi \left[M_{x(pN_b+1)s} + M_{y(pN_b+1)c} \right] \right. \\
& \left. + \sin pN_b\Psi \left[-M_{x(pN_b+1)c} + M_{y(pN_b+1)s} \right] \right\}
\end{aligned} \tag{2.148}$$

whereas the expressions for the vertical shear F_z^H and the rotor shaft torque M_z^H in the fixed frame are the same as those in the rotating frame.

As these hub loads are transmitted to the fuselage, the steady components are the rotor thrust, longitudinal and side forces, rolling and pitching moments, and the rotor shaft torque. The higher harmonics contribute to helicopter vibration. In particular, helicopter vibration occurs at pN_b per rev, where p is a positive integer. As in the case of the rotating hub loads, only certain harmonics of the blade loads are transmitted to the hub fixed frame. Again, this happens because of the equal phasing between individual rotor blades. Furthermore, since the load harmonics tend to lower magnitudes at higher frequencies, helicopter vibration occurs primarily at N_b per rev.

2.6 Coupled Trim Analysis

Typically, the vehicle trim controls and the rotor steady responses are solved independently. The solution method is usually performed in the following manner: (1) For a prescribed flight condition, the trim controls are computed based on a rigid flapping blade assumption. For this, the rotor induced velocity is calculated based on the momentum value, and the quasi-steady approximation is used to calculate for the blade loads. This would lead to a crude approximation to the actual trim solutions. (2) Based on these trim solutions, the blade steady responses are then calculated. For this step, the elastic blade model together with more refined wake and aerodynamic analyses are employed. Then the rotor hub loads and a new vehicle equilibrium condition are computed. The new equilibrium condition is usually quite different from the one prescribed initially.

For a given flight condition, the trim controls and the blade steady responses must satisfy both the blade and the vehicle equilibrium conditions. The method incorporating the process of simultaneously solving for the blade responses and the trim controls is referred to as the coupled trim analysis. In this analysis, the blade steady responses are solved iteratively. With each new blade response update, the vehicle would attain a new equilibrium condition. Therefore, the trim controls are also updated so that the overall solutions satisfy the prescribed vehicle equilibrium conditions.

In this analysis, an uncoupled trim solution based on the rigid flapping blade assumption (ref. 95) is used as an initial guess for the coupled trim analysis. With these trim controls, the blade steady responses are calculated. Using the blade responses, the rotor hub loads and a new vehicle equilibrium condition are computed. The trim controls are then updated based on the new vehicle equilibrium condition. The process is repeated until the overall solutions converge. For a given flight condition, the converged trim control and blade response solution satisfy simultaneously the overall vehicle steady force and moment equations.

In particular, the general expression for the vehicle equilibrium condition can be expressed as

$$\mathbf{F} = 0 \quad (2.149)$$

where the exact form of $\mathbf{F}^T = [F_1, \dots, F_n]$ depends on the types of trim conditions considered. In the analysis, two types of trim are considered: propulsive and wind tunnel. The propulsive trim simulates a helicopter in a steady-level flight condition as shown in figure 2.3, and the vehicle equilibrium conditions must satisfy the following force and moment equations

$$F_1 = F_{X_0}^H + D_F \cos \alpha_{HP} - T \sin \alpha_s \quad (2.150)$$

$$F_2 = F_{Y_0}^H + Y_F \cos \phi_s + T \sin \phi_s \quad (2.151)$$

$$F_3 = F_{Z_0}^H - T \cos \alpha_s \cos \phi_s - D_F \cos \phi_s \sin \alpha_{HP} + Y_F \sin \phi_s \quad (2.152)$$

$$F_4 = M_{X_0}^H + M_{x_F} + T (\bar{h} \cos \alpha_s \sin \phi_s - y_{CG} \cos \phi_s) \\ + Y_F (\bar{h} \cos \alpha_s \cos \phi_s + y_{CG} \sin \phi_s) \quad (2.153)$$

$$F_5 = M_{Y_0}^H + M_{y_F} + T (\bar{h} \sin \alpha_s - x_{CG} \cos \alpha_s) + D_F (-\bar{h} \cos \alpha_{HP} + x_{CG} \sin \alpha_{HP}) \quad (2.154)$$

where F_1 , F_2 , and F_3 are, respectively, the vehicle force equilibrium equations in the X , Y , and Z directions in the hub-fixed frame, and F_4 and F_5 are the vehicle rolling and pitching moment equilibrium equations, respectively. The yawing moment equilibrium equation is not considered since the tail rotor dynamics are neglected in this analysis. Also, D_F is the fuselage drag; Y_F is the fuselage side force; T is the rotor thrust; x_{CG} , y_{CG} , and \bar{h} are, respectively, the relative location of the rotor hub center with respect to the vehicle center of gravity in the X , Y , and Z directions; α_s and ϕ_s are the longitudinal and lateral shaft tilts, respectively. Furthermore

$$\alpha_s = \alpha_{HP} - \theta_{FP}$$

where α_{HP} is the hub plane tilt relative to the flight direction, and θ_{FP} is the flightpath angle relative to an axis perpendicular to the weight vector. For propulsive trim, the unknown quantities to be determined from the vehicle equilibrium equations are

$$\mathbf{u}^T = [\alpha_s, \phi_s, \theta_{.75}, \theta_{1c}, \theta_{1s}] \quad (2.155)$$

where the rotor trim parameters $\theta_{.75}$, θ_{1c} , and θ_{1s} govern the blade pitch schedule. With no higher harmonic control, the blade pitch schedule can be expressed as

$$\theta(x, \Psi) = \theta_{.75} + \theta_{tw}(x - 0.75) + \theta_{1c} \cos \Psi + \theta_{1s} \sin \Psi \quad (2.156)$$

where x is the nondimensional radial length; θ_{tw} is the blade linear pretwist; $\theta_{.75}$ is the collective pitch angle at 75 percent radius; θ_{1c} and θ_{1s} are, respectively, the lateral and longitudinal cyclic pitch angles.

Wind tunnel trim simulates the rotor testing conditions in a wind tunnel. For such conditions, the longitudinal and lateral shaft tilt angles are typically prescribed. Therefore, the longitudinal and lateral force equilibrium equations need not be satisfied. As such, the unknown vector to be determined from the remaining equations F_3 , F_4 , and F_5 is

$$\mathbf{u}^T = [\theta_{.75}, \theta_{1c}, \theta_{1s}]$$

For certain wind tunnel tests, the trim procedure sometimes requires the suppression of the cyclic flapping angles measured at a reference blade station. For such cases, the expressions for F_4 and F_5 become

$$F_4 = w_{1c}^R = \frac{1}{\pi} \int_0^{2\pi} w^R \cos \Psi \, d\Psi \quad (2.157)$$

$$F_5 = w_{1s}^R = \frac{1}{\pi} \int_0^{2\pi} w^R \sin \Psi \, d\Psi \quad (2.158)$$

Finally, the solution technique is based on a modified Newton method, and, as such, the trim controls are updated at the i th iteration as

$$\mathbf{u}_{i+1} = \mathbf{u}_i + \Delta \mathbf{u}_i \quad (2.159)$$

where

$$\Delta \mathbf{u}_i = - \left. \frac{\partial \mathbf{F}}{\partial \mathbf{u}} \right|_{\mathbf{u}=\mathbf{u}_0} \mathbf{F}(\mathbf{u}_i) \quad (2.160)$$

where \mathbf{u}_0 are the trim controls obtained initially using the rigid flapping blade solution, and the Jacobian $\partial \mathbf{F} / \partial \mathbf{u}$ is calculated using the finite-difference approach. Due to computational requirement, the Jacobian for trim is computed only once initially and is not updated for subsequent iterations.

To improve numerical convergence, a numerical damping factor R is introduced into equation 2.159 which can be expressed as

$$\mathbf{u}_{i+1} = \mathbf{u}_i + R \Delta \mathbf{u}_i \quad (2.161)$$

Currently, there are two forms for R . In the first form, R is given by

$$R = 1 - r$$

where $0 \leq r < 1$. Additionally, R can also take the form

$$R = 1 - \exp(-\zeta_r i)$$

Typical value of ζ_r is $1/\sqrt{2}$.

2.7 Finite Element Discretization in Space

This section describes the finite element method used in the derivation of the blade governing equations. In particular, the finite element analysis is used here to remove the spatial dependence from the blade governing equations. For this, the rotor blade is discretized into a number of beam elements, and shape functions are used to relate the elemental degrees of freedom.

From the Hamiltonian formulation, the integrand of equation 2.3 can be expressed as

$$\Delta = \delta \mathcal{U} - \delta \mathcal{T} - \delta \mathcal{W} \quad (2.162)$$

and in discretized form

$$\Delta = \sum_{i=1}^n \Delta_i \quad (2.163)$$

where

$$\Delta_i = \delta \mathcal{U}_i - \delta \mathcal{T}_i - \delta \mathcal{W}_i \quad (2.164)$$

and $\delta \mathcal{U}_i$, $\delta \mathcal{T}_i$, and $\delta \mathcal{W}_i$ are, respectively, the variations in strain and kinetic energies and virtual work contribution of the i th element, and n is the number of beam elements. As shown in figure 2.8, each beam element has 15 degrees of freedom and consists of two end nodes and three internal nodes. Each end node has 6 degrees of freedom which are: u, v, v', w, w' , and $\hat{\phi}$. There are two internal nodes for the u degree of freedom and one internal node for the $\hat{\phi}$ degree of freedom. There are two main reasons for choosing $\hat{\phi}$ over ϕ as the torsional degree of freedom: (1) the choice of $\hat{\phi}$ preserves the banded structure of the global finite element matrices since the integral term $\int_0^x v'' w' dx$ is implicitly included in the formulation, and (2) the aerodynamic loads depend explicitly on the geometric twist $\hat{\phi}$. At the

element boundary, there is a continuity of displacement for the axial, lag, flap deflections, and twist, and a continuity of slope for the flap and lag bending.

In the formulation, the deflections at any point within an element can be expressed in terms of the shape functions and the nodal degrees of freedom. For the i th element

$$\begin{Bmatrix} u(s) \\ v(s) \\ w(s) \\ \hat{\phi}(s) \end{Bmatrix} = \mathbf{H}(s) \mathbf{q}_e \quad (2.165)$$

where the nodal vector \mathbf{q}_e consists of the 15 degrees of freedom for the beam element, and

$$\mathbf{q}_e^T = [u_1, u_2, u_3, u_4, v_1, v'_1, v_2, v'_2, w_1, w'_1, w_2, w'_2, \hat{\phi}_1, \hat{\phi}_2, \hat{\phi}_3] \quad (2.166)$$

The shape function matrix \mathbf{H} consists of the shape functions for the beam element degrees of freedom and has the form

$$\mathbf{H} = \begin{bmatrix} H_u^T(s) & \mathbf{0} & \mathbf{0} & \mathbf{0} \\ \mathbf{0} & H_v^T(s) & \mathbf{0} & \mathbf{0} \\ \mathbf{0} & \mathbf{0} & H_w^T(s) & \mathbf{0} \\ \mathbf{0} & \mathbf{0} & \mathbf{0} & H_{\hat{\phi}}^T(s) \end{bmatrix} \quad (2.167)$$

where the shape function vectors are

$$H_u(s) = \begin{Bmatrix} -4.5s^3 + 9s^2 - 5.5s + 1 \\ 13.5s^3 - 22.5s^2 + 9s \\ -13.5s^3 + 18s^2 - 4.5s \\ 4.5s^3 - 4.5s^2 + s \end{Bmatrix} \quad (2.168)$$

$$H_v(s) = H_w(s) = \begin{Bmatrix} 2s^3 - 3s^2 + 1 \\ l_i(s^3 - 2s^2 + s) \\ -2s^3 + 3s^2 \\ l_i(s^3 - s^2) \end{Bmatrix} \quad (2.169)$$

$$H_{\hat{\phi}}(s) = \begin{Bmatrix} 2s^2 - 3s + 1 \\ -4s^2 + 4s \\ 2s^2 - s \end{Bmatrix} \quad (2.170)$$

The local spatial coordinate s of the i th element is given by

$$s = \frac{x_i}{l_i}$$

where l_i is the length of the i th beam element; x_i is the local coordinate of the beam element, and $0 \leq x_i \leq l_i$. The shape functions for the lag and the flap bending deflections are the Hermitian

polynomials which allow continuity of deflections and slopes across the beam element. For the axial deflections and elastic twist, Lagrangian polynomials are used as shape functions which allow continuity of displacements across the beam element.

Similarly, the virtual displacements $\delta u, \delta v, \delta w$, and $\delta \hat{\phi}$ over the i th element can be expressed in terms of the same set of shape functions as

$$\begin{Bmatrix} \delta u(s) \\ \delta v(s) \\ \delta w(s) \\ \delta \hat{\phi}(s) \end{Bmatrix} = \mathbf{H}(s) \delta \mathbf{q}_e \quad (2.171)$$

where the virtual nodal vector $\delta \mathbf{q}_e$ is the variation of \mathbf{q}_e . Substitution of equations 2.165 and 2.171 into equation 2.164 gives

$$\Delta_i = \Delta_i(\mathbf{q}_e, \dot{\mathbf{q}}_e, \ddot{\mathbf{q}}_e, \delta \mathbf{q}_e) \quad (2.172)$$

Following equation 2.163, the assembly of the beam elements yields a set of nonlinear ordinary differential equations in terms of the nodal displacements. Let \mathbf{q} denote the global displacements for the rotor blade and $\delta \mathbf{q}$ the associated global virtual displacement; the global equations can be expressed implicitly as

$$\Delta = \Delta(\mathbf{q}, \dot{\mathbf{q}}, \ddot{\mathbf{q}}, \delta \mathbf{q}) \quad (2.173)$$

Derivation of the blade governing equations is completed by applying the geometric boundary conditions to equation 2.173. The rotor configuration, such as hingeless or articulated, dictates the displacement boundary conditions near the blade root. In particular, u, v, v', w, w' , and $\hat{\phi}$ are zero at the blade root for a hingeless rotor. For an articulated rotor with the flap and lag hinges coincident, u, v, w , and $\hat{\phi}$ are zero at the hinge. In the analysis, further modifications have been made to include the pitch link stiffness, different offsets for the flap and lag hinges, and the pitch link location.

After applying the boundary conditions, equation 2.173 takes the form

$$\Delta = \delta \mathbf{q}^T (\mathbf{M}_G \ddot{\mathbf{q}} + \mathbf{C}_G \dot{\mathbf{q}} + \mathbf{K}_G \mathbf{q} - \mathbf{F}_G) \quad (2.174)$$

where $\mathbf{M}_G, \mathbf{C}_G, \mathbf{K}_G$ are the global mass, damping, and stiffness matrices, respectively, and \mathbf{F}_G is the global force vector. Substituting the above equation into equation 2.3 (note that the blade steady response is periodic for a rotor operating in steady-level flights), these give

$$\int_0^{2\pi} \delta \mathbf{q} (\mathbf{M}_G \ddot{\mathbf{q}} + \mathbf{C}_G \dot{\mathbf{q}} + \mathbf{K}_G \mathbf{q} - \mathbf{F}_G) d\Psi = 0 \quad (2.175)$$

Note that the above equation has been expressed in terms of the rotor temporal coordinate Ψ .

2.8 Solution Procedure

This section describes the solution methods for the blade response and the vehicle trim controls. In the analysis, the blade governing equation (eq. 2.164) is transformed to the normal mode space using a

few coupled natural vibration modes. This is performed to reduce the computational time. The resulting normal mode equations are then solved using a finite element in time method. With the temporal finite element method, the blade normal mode equations are transformed into a set of nonlinear algebraic equations which are solved using a Newton method.

Starting with the description of the nondimensional procedure, this section presents the normal mode transformation and the temporal finite element method used in the determination of the blade aeroelastic responses. Finally, implementation of the aerodynamic model into the aeroelastic analysis is also discussed.

2.8.1 Nondimensional Procedure

The parameters used in the analysis are normalized according to the following procedure

Quantities	Nondimensional parameters
Length	R
Time	$1/\Omega$
Mass/length	m_o
Velocity	ΩR
Acceleration	$\Omega^2 R$
Force	$m_o \Omega^2 R^2$
Moment	$m_o \Omega^2 R^3$
Energy or work	$m_o \Omega^2 R^4$

where m_o is a reference blade mass per unit length.

2.8.2 Normal Mode Equations

To reduce computational time, the blade finite element equations are transformed into the normal mode space using a few coupled natural vibration modes. The blade natural vibration modes are obtained by solving an algebraic eigenvalue problem. By neglecting the external loads and the damping matrix, the blade governing equation can be expressed as

$$\mathbf{M}_G^s \ddot{\mathbf{q}} + \mathbf{K}_G^s \mathbf{q} = \mathbf{0} \quad (2.176)$$

Let

$$\mathbf{q} = \bar{\mathbf{q}} e^{i\omega\Psi}$$

Then equation 2.176 can be arranged to yield the following algebraic eigenvalue problem

$$\omega^2 \bar{\mathbf{q}} = (\mathbf{M}_G^s)^{-1} \mathbf{K}_G^s \bar{\mathbf{q}} \quad (2.177)$$

where the superscript s denotes structural quantities. These matrices are the structural inertial and stiffness matrices for the rotor blade and are symmetric. This eigenvalue problem can be solved using

the Jacobi method. The resulting eigenvalues, being ω^2 , are real, and the associated eigenvectors are also real and orthogonal. Physically, the eigenvectors represent the blade natural modes, and the square root of the associated eigenvalues represents the blade natural frequencies.

To apply the normal mode transformation, the blade global displacement vector \mathbf{q} is related to the modal displacement vector \mathbf{p} by the normal mode transformation

$$\mathbf{q} = \Phi \mathbf{p} \quad (2.178)$$

where Φ is an $N_G \times m$ matrix formed with the m blade free vibration modes. Applying the normal mode transformation to equation 2.175 results in

$$\int_0^{2\pi} \delta \mathbf{p} (\mathbf{M}\ddot{\mathbf{p}} + \mathbf{C}\dot{\mathbf{p}} + \mathbf{K}\mathbf{p} - \mathbf{F}) d\Psi = 0 \quad (2.179)$$

where

$$\begin{aligned} \mathbf{M} &= \Phi^T \mathbf{M}_G \Phi \\ \mathbf{C} &= \Phi^T \mathbf{C}_G \Phi \\ \mathbf{K} &= \Phi^T \mathbf{K}_G \Phi \\ \mathbf{F} &= \Phi^T \mathbf{F}_G \end{aligned} \quad (2.180)$$

are, respectively, the modal mass, damping, stiffness matrices, and load vector. In general, \mathbf{M} , \mathbf{C} , and \mathbf{K} contain periodically time-varying coefficients; that is

$$\begin{aligned} \mathbf{M}(\Psi) &= \mathbf{M}(\Psi + 2\pi) \\ \mathbf{C}(\Psi) &= \mathbf{C}(\Psi + 2\pi) \\ \mathbf{K}(\Psi) &= \mathbf{K}(\Psi + 2\pi) \end{aligned}$$

and \mathbf{F} is nonlinear. For periodic solutions, \mathbf{F} should also be periodic.

2.8.3 Finite Element Discretization in Time

The blade modal equation (eq. 2.179) can be integrated by parts to yield

$$\int_0^{2\pi} \begin{Bmatrix} \delta \mathbf{p} \\ \delta \dot{\mathbf{p}} \end{Bmatrix}^T \begin{Bmatrix} \mathbf{F} - \mathbf{C}\dot{\mathbf{p}} - \mathbf{K}\mathbf{p} \\ \mathbf{M}\dot{\mathbf{p}} \end{Bmatrix} d\Psi = \begin{Bmatrix} \mathbf{M}\dot{\mathbf{p}} \\ 0 \end{Bmatrix} \Big|_0^{2\pi} \quad (2.181)$$

For a periodic solution, the right hand side of the above equation is zero, and the above equation can be expressed as

$$\int_0^{2\pi} \delta \mathbf{y}^T \mathbf{Q} d\Psi = 0 \quad (2.182)$$

where

$$\mathbf{y} = \begin{Bmatrix} \mathbf{p} \\ \dot{\mathbf{p}} \end{Bmatrix}$$

and

$$\mathbf{Q} = \begin{Bmatrix} \mathbf{F} - \mathbf{C}\dot{\mathbf{p}} - \mathbf{K}\mathbf{p} \\ \mathbf{M}\dot{\mathbf{p}} \end{Bmatrix}$$

Using the finite element method, the time interval for one rotor revolution of 2π is divided into a number of time elements in a manner similar to the spatial finite element method described in section 2.7. This is illustrated in figure 2.9. The blade governing equations can then be expressed as the sum of the elemental expressions for all the time elements. In particular, equation 2.182 takes the form

$$\sum_{i=1}^{N_e} \int_{\Psi_i}^{\Psi_{i+1}} \delta \mathbf{y}_i^T \mathbf{Q}_i d\Psi = 0 \quad (2.183)$$

where $\Psi_1 = 0$, $\Psi_{N_e+1} = 2\pi$, and N_e is the number of time elements being used. The first order Taylor series expansion of equation 2.183 about a steady state value of $\mathbf{y}_o = [\mathbf{p}_o^T \ \dot{\mathbf{p}}_o^T]^T$ is

$$\sum_{i=1}^{N_e} \int_{\Psi_i}^{\Psi_{i+1}} \delta \mathbf{y}_i^T \mathbf{Q}_i(\mathbf{y}_o + \Delta \mathbf{y}) d\Psi = \sum_{i=1}^{N_e} \int_{\Psi_i}^{\Psi_{i+1}} \delta \mathbf{y}_i^T [\mathbf{Q}_i(\mathbf{y}_o) + \mathbf{K}_{ti}(\mathbf{y}_o) \Delta \mathbf{y}] d\Psi = 0 \quad (2.184)$$

where

$$\mathbf{K}_{ti} = \begin{bmatrix} \frac{\partial \mathbf{F}}{\partial \mathbf{p}} - \mathbf{K} & \frac{\partial \mathbf{F}}{\partial \dot{\mathbf{p}}} - \mathbf{C} \\ \mathbf{0} & \mathbf{M} \end{bmatrix}_i \quad (2.185)$$

For the i th time element, the temporal variation of the modal displacement vector can be expressed in terms of the shape functions and the temporal nodal displacement vector $\boldsymbol{\xi}_i$ as

$$\mathbf{p}_i(\Psi) = \mathbf{H}(s) \boldsymbol{\xi}_i \quad (2.186)$$

where the local temporal coordinate s for the i th time element is

$$s = \frac{\Psi - \Psi_i}{\Psi_{i+1} - \Psi_i}$$

and $0 \leq s \leq 1$. Note that $\Psi_{i+1} - \Psi_i$ is the time span of the i th time element. In equation 2.186, $\mathbf{H}(s)$ is the temporal shape function matrix which has the form

$$\mathbf{H} = [H_1 \mathbf{I}_m, \dots, H_{n_t+1} \mathbf{I}_m]$$

where \mathbf{I}_m is the $m \times m$ identity matrix, and m is the dimension of the modal displacement vector. In the above expression, the subscript n_t refers to the order of the polynomial used in approximating the temporal variation of the modal displacement vector. In particular, if an n th order polynomial is used in the approximation, then $n + 1$ nodes per degree of freedom are required to completely describe the variation of $\mathbf{p}_i(\Psi)$ within the time element. Therefore, \mathbf{H} is an $m \times m(n_t + 1)$ matrix, and $\boldsymbol{\xi}_i$ is an $m(m + 1)$ vector.

In this analysis, fifth-order polynomials are used in the approximation, and this results in the requirement of six nodes per degree of freedom for each time element. Between elements there is continuity of displacements. With this type of approximation, the shape functions used are the Lagrangian polynomial and are expressed as

$$\begin{aligned} H_1(s) &= \left(-625s^5 + 1875s^4 - 2125s^3 + 1125s^2 - 274s + 24 \right) / 24 \\ H_2(s) &= \left(3125s^5 - 8750s^4 + 8875s^3 - 3850s^2 + 600s \right) / 24 \\ H_3(s) &= \left(-3125s^5 + 8125s^4 - 7375s^3 + 2675s^2 - 300s \right) / 12 \\ H_4(s) &= \left(3125s^5 - 7500s^4 + 6125s^3 - 1950s^2 + 200s \right) / 12 \\ H_5(s) &= \left(-3125s^5 + 6875s^4 - 5125s^3 + 1525s^2 - 150s \right) / 24 \\ H_6(s) &= \left(625s^5 - 1250s^4 + 875s^3 - 250s^2 + 24s \right) / 24 \end{aligned}$$

With this description, the modal velocity vector can be expressed as

$$\dot{\mathbf{p}}_i = \dot{\mathbf{H}}(\Psi) \boldsymbol{\xi}_i \quad (2.187)$$

In a similar fashion, the expressions for the virtual modal displacement and velocity vector are

$$\delta \mathbf{p}_i = \mathbf{H}(\Psi) \delta \boldsymbol{\xi}_i \quad (2.188)$$

$$\delta \dot{\mathbf{p}}_i = \dot{\mathbf{H}}(\Psi) \delta \boldsymbol{\xi}_i \quad (2.189)$$

Substituting equations 2.186–2.189 into equation 2.184 yields

$$\sum_{i=1}^{N_e} \int_{\Psi_i}^{\Psi_{i+1}} \delta \boldsymbol{\xi}_i^T \mathbf{N}^T [\mathbf{Q}_i + \mathbf{K}_{t_i} \mathbf{N}] \Delta \boldsymbol{\xi}_i d\Psi = 0 \quad (2.190)$$

where

$$\mathbf{N} = \left\{ \begin{array}{c} \mathbf{H}(\Psi) \\ \dot{\mathbf{H}}(\Psi) \end{array} \right\} \quad (2.191)$$

For periodic solution, the boundary condition for the temporal finite element equation is

$$\mathbf{p}(0) = \mathbf{p}(2\pi)$$

Finally, since the $\delta \boldsymbol{\xi}_i$ are arbitrary for $i = 1, \dots, N_e$, equation 2.190 takes the form

$$\mathbf{Q}^G + \mathbf{K}_t^G \boldsymbol{\xi}^G = \mathbf{0} \quad (2.192)$$

where

$$\mathbf{Q}^G = \sum_{i=1}^{N_e} \int_{\Psi_i}^{\Psi_{i+1}} \mathbf{N}^T \mathbf{Q}_i d\Psi$$

$$\mathbf{K}_t^G = \sum_{i=1}^{N_e} \int_{\Psi_i}^{\Psi_{i+1}} \mathbf{N}^T \mathbf{K}_{ti} \mathbf{N} d\Psi$$

and

$$\Delta \xi^G = \sum_{i=1}^{N_e} \Delta \xi_i$$

Equation 2.192 is a set of nonlinear algebraic equations and can be solved using Newton's method. In particular, $\Delta \xi^G$ are solved iteratively, and the overall responses are updated using

$$\xi^G_{i+1} = \xi^G_i + \Delta \xi^G_i$$

During the iteration process, the vehicle trim controls are also updated according the procedure outlined in section 2.6. The converged trim control and blade steady response solutions satisfy simultaneously the vehicle steady force and moment equations (i.e., eq. 2.6) and the blade equilibrium conditions given by equation 2.182.

Implementation of the unsteady aerodynamic model described in section 2.3 required calculation of the aerodynamic states. Since the constructions of \mathbf{Q}^G and \mathbf{K}_t^G of equation 2.192 are essentially a time-marching algorithm, the recursive formulas in the expressions for the unsteady airloads can be adapted to the current analysis. Also, the unsteady aerodynamic states such as X_n , Y_n , or D_n are functions of the downwash velocity U_P or the airfoil pitch rate q which, in turn, are dependent on the blade motions and the trim controls. Therefore, as the blade responses and trim controls are updated, these aerodynamic states are also updated. In the limit, as the solutions converge, these aerodynamic states also converge to their corresponding values.

2.9 Higher Harmonic Control Model

In the HHC analysis, a linear frequency-domain quasi-steady model in terms of a transfer matrix is adopted to relate harmonics of the HHC inputs to harmonics of the vibratory hub loads. The optimal HHC inputs are calculated by minimizing the harmonics of the vibratory hub loads expressed in terms of a quadratic performance index. Using the multiblade coordinate transformation, HHC inputs in the rotating frame are transformed to the fixed frame in terms of swashplate motions. The higher harmonic swashplate motions are generated using a number of auxiliary servo-actuators, as shown in figure 2.10. The hydraulic power for the actuators is then calculated for the specified HHC inputs.

The higher harmonic blade controls are implemented by exciting the blade pitch at higher harmonics of rotational speed. For vibration control, the blade pitch schedule, expressed in the rotating frame, is given by

$$\begin{aligned} \theta(x, \Psi) = & \theta_{.75} + \theta_{tw}(x - 0.75) + \theta_{1c} \cos \Psi + \theta_{1s} \sin \Psi \\ & + \sum_{n=N_b-1}^{N_b+1} (\theta_{nc} \cos n\Psi + \theta_{ns} \sin n\Psi) \end{aligned} \quad (2.193)$$

where θ_{nc} and θ_{ns} are, respectively, the cosine and sine components of the HHC inputs. Note that the summation of the higher harmonic control inputs covers three frequencies: $N_b - 1$, N_b , and $N_b + 1$ per rev.

For the HHC model, a transfer matrix T is used to relate the input pitch harmonics and the output hub load harmonics; that is

$$z = z_o + T \theta \quad (2.194)$$

where the response vector z has ten components and consists of sine and cosine components of the vibratory hub loads—the vertical, longitudinal, and lateral hub shears and the pitching and rolling moments, and z_o is the uncontrolled response vector. In particular, the components of z or z_o are the higher harmonic components of the hub loads, as presented in section 2.5. The HHC input vector θ has six components and consists of sine and cosine components of the higher harmonic blade pitch at the three distinct frequencies of $N_b - 1$, N_b , and $N_b + 1$ per rev. In this analysis, the transfer matrix is generated using a finite-difference approach.

Note that the HHC model as given by equation 2.194 is equivalent to the first order Taylor series expansion of a more general static nonlinear description which is given by

$$z = f(z_o, \theta) \quad (2.195)$$

From this, the transfer matrix T is simply the Jacobian of f , calculated about a referenced input $\bar{\theta}$

$$T = \left. \frac{\partial f}{\partial \theta} \right|_{\bar{\theta}} \quad (2.196)$$

2.10 Higher Harmonic Control Algorithms

For minimum vibration, the optimal control input θ^* is determined from the minimization problem of the quadratic performance index J

$$\min J = \min \left(\frac{1}{2} z^T W_z z + \frac{1}{2} \theta^T W_\theta \theta \right) \quad (2.197)$$

subject to equation 2.194.

In the above expression, W_z and W_θ are weighting matrices for z and θ , respectively. The optimal control θ^* depends on the type of controller used. Two types of controllers are used in this analysis: open-loop and closed-loop deterministic controllers.

For the open-loop controller, only the global model is applicable, and the optimal control θ^* depends only on the uncontrolled response; that is

$$\theta^* = C z_o \quad (2.198)$$

where

$$C = -(T^T W_z T + W_\theta)^{-1} T^T W_z \quad (2.199)$$

and the transfer matrix is calculated about the uncontrolled response value. If the HHC system is linear, then the optimal control θ^* would suppress completely the vibratory response in one cycle.

For the closed-loop controller, the general relation as given by equation 2.194 is valid for each HHC cycle and is expressed as

$$z_n = z_{n-1} + T_n(\theta_n - \theta_{n-1}) \quad (2.200)$$

In this formulation, the dynamics of the HHC system have been neglected. This is justified by assuming that the rotor system is stable and that the HHC inputs are updated only after all the transient responses have died out. Furthermore, this assumption is justified based on the wind tunnel results of reference 33 which showed that the time constant for the HHC system is rather small, being less than two rotor revolutions. With this scheme, the HHC inputs are computed based on the current response vector

$$\theta_n = \theta_{n-1} + (1 - r)C_n z_{n-1} \quad (2.201)$$

where

$$C_n = - \left(T_n^T W_z T_n^T + W_\theta \right)^{-1} T_n^T W_z \quad (2.202)$$

and r is the control rate limiting factor with values ranging from 0.0 to less than 1.0. The factor $(1 - r)$ constrains the HHC control rate and helps to reduce large control excursions. This is useful from the actuator hardware point of view, and a suitable value of r can be used to stabilize the feedback system.

Two types of models are used to implement the closed-loop HHC system: local and global. In the local model, the relation in equation 2.200 is applicable for a sufficiently small range of control values, $\theta_n - \theta_{n-1}$. For the global model, the HHC model is assumed to be linear for the complete range of control value, and thus the transfer matrix remains constant for all cycles. For both models, the transfer matrix is calculated initially using the finite-difference approach. For subsequent HHC cycles, the global model uses the same transfer matrix calculated initially, while the local model updates it using

$$T_{n+1} = T_n + \frac{(y_n - T_n s_n) s_n^T}{s_n^T s_n} \quad (2.203)$$

where

$$y_n = z_{n+1} - z_n \quad (2.204)$$

and

$$s_n = C_n z_n \quad (2.205)$$

This updating scheme, generally known as the secant method, was proposed by Broyden (ref. 96) as a solution technique for systems of nonlinear equations. Even though the transfer matrix is computed using the local control response, this updating method is quite different from the widely adopted Kalman filter used in many HHC applications.

2.11 Actuator Power Required for HHC Systems

To calculate the actuator power required for an HHC system, the optimal HHC inputs are transformed in terms of swashplate motions (ref. 97)

$$\begin{pmatrix} C_{long,c} \\ C_{long,s} \\ C_{col,c} \\ C_{col,s} \\ C_{lat,c} \\ C_{lat,s} \end{pmatrix} = \begin{bmatrix} 0 & 1 & 0 & 0 & -1 & 0 \\ -1 & 0 & 0 & 0 & 0 & 1 \\ 0 & 0 & 1 & 0 & 0 & 0 \\ 0 & 0 & 0 & 1 & 0 & 0 \\ 0 & 1 & 0 & 0 & 1 & 0 \\ 1 & 0 & 0 & 0 & 0 & 1 \end{bmatrix} \begin{pmatrix} \theta_{(N_b-1)c} \\ \theta_{(N_b-1)s} \\ \theta_{N_b c} \\ \theta_{N_b s} \\ \theta_{(N_b+1)c} \\ \theta_{(N_b+1)s} \end{pmatrix} \quad (2.206)$$

where C_{col} , C_{long} , and C_{lat} are the $N_b P$ swashplate angles in the collective, longitudinal, and lateral modes, respectively, and the subscript c refers to cosine component and s refers to the sine component.

The actuator power P_R generated by a hydraulic pump is the product of the pump pressure p_e and the average pump flow rate Q_{av} (ref. 98)

$$P_R = p_e Q_{av} \quad (2.207)$$

For HHC applications, the pump flow rate must be sufficient to excite the $N_b P$ swashplate motions given by the prescribed HHC inputs. For a particular actuator, the flow rate Q depends on the swashplate oscillatory frequency and the actuator displacement; that is

$$Q = N_b \Omega S_n A_e \quad (2.208)$$

where A_e is the effective piston area, and S_n is the actuator displacement. The average pump flow rate Q_{av} is calculated assuming that an accumulator is used to smooth out the flow; thus

$$Q_{av} = \frac{2}{\pi} N_b \Omega S_n A_e \quad (2.209)$$

Throughout the helicopter flight regime, the actuators must operate at a constant fluid pressure selected to accommodate the maximum possible pitch-link load. Such loads occur at severe flight conditions such as a high g maneuvers or a high speed condition where a major part of the rotor disc is exposed to dynamic stall. For this analysis, it is assumed that the fluid pump pressure is a known constant. Therefore, the actuator power required for an N_b -bladed rotor can be expressed as

$$P_R = \frac{2}{\pi} N_b^2 \Omega A_e p_e c_n S_n \quad (2.210)$$

where c_n is a constant dependent on the radial locations of the actuators and the pitch link, and S_n is the accumulation index for the swashplate higher harmonic motion amplitudes. If the swashplate is

oscillated using four equally spaced hydraulic actuators, then S_n can be expressed as

$$\begin{aligned}
 S_n = & \sqrt{(C_{col,c} + C_{lat,c})^2 + (C_{col,s} + C_{lat,s})^2} \\
 & + \sqrt{(C_{col,c} - C_{lat,c})^2 + (C_{col,s} - C_{lat,s})^2} \\
 & + \sqrt{(C_{col,c} + C_{long,c})^2 + (C_{col,s} + C_{long,s})^2} \\
 & + \sqrt{(C_{col,c} - C_{long,c})^2 + (C_{col,s} - C_{long,s})^2}
 \end{aligned} \tag{2.211}$$

The actuator power for an HHC system is therefore dependent on the number of blades, the rotor rotational speed, the hydraulic pump pressure and diameter, the locations of the pitch links and actuators, and the HHC inputs. Since most of these parameters are fixed for a given rotor design, the associated actuator power is conveniently represented in term of a power index defined as

$$P_I = \frac{P_R}{(2/\pi) N_b^2 \Omega A_e p_e c_n} \tag{2.212}$$

This gives

$$P_I = S_n \tag{2.213}$$

Thus, for a given actuator design and pitch-link configuration, the actuator power depends only on the swashplate motions which are related to the HHC inputs. Also, it should be noted that this assumption is valid only when the maximum pitch-link loads are not significantly affected by the HHC inputs.

3 RESULTS AND DISCUSSION

In section 3.1, the predicted vibratory hub loads are correlated with experimental data to validate the analysis and to set general guidelines for further refinements to the analytical model. HHC effectiveness in suppressing the vibratory hub loads are then evaluated. Secondary effects due to HHC are also investigated including HHC penalties on blade stresses, control loads, rotor performance, and influences of HHC on blade stall. For the cases where the simple fixed-gain controller is not effective in suppressing the vibratory hub loads, results using an adaptive-gain controller is presented.

In section 3.2, a parametric study is carried out to investigate the influence of blade and rotor characteristics on the vibratory hub loads and the HHC actuator power. Comparative study is made for three different three-bladed rotor systems including an articulated rotor, a soft-inplane hingeless rotor, and a stiff-inplane hingeless rotor. Then, detail parametric investigations are carried out for a generic four-bladed soft-inplane hingeless rotor operated in a transition flight regime and a three-bladed articulated rotor operated in a quasi-steady maneuvering flight condition. These studies are carried out by varying the blade design parameters such as the blade flap, lead-lag, and torsion stiffness distributions, the chordwise offset of the blade center of mass from the elastic axis, the chordwise offset of the elastic axis from the quarter chord, and the blade linear pretwist.

3.1 Correlation Study and HHC Effectiveness

3.1.1 Correlation Study

To validate the analysis, a correlation study of predicted vibratory hub loads with experimental data is carried out. The data were obtained from a one-sixth dynamically scaled three-bladed articulated rotor model of the CH-47D helicopter which was tested by Boeing Helicopter Company in their wind tunnel (ref. 46). In the experiment, the vibratory hub loads were measured in the rotating frame using a strain-gauge balance located under the rotor hub. For this rotor, the dominant vibratory hub loads causing airframe vibration are the $3P$ vertical and the $2P$ and $4P$ rotating inplane hub shears. The vibratory hub moment components for this rotor are small, and these are not considered in the correlation study.

In the validation study, six beam elements are used to model the blade, and the corresponding blade parameters are presented in table 3.1. The calculated rotating blade natural frequencies for the coupled modes used in the correlation study are presented in table 3.2. In order to apply the nonlinear unsteady aerodynamic model (refs. 81 and 82), static characteristics for the VR-12 airfoil are used, while the three time constants used to model the unsteady aerodynamic characteristics are taken from reference 81. The basic trim controls are calculated corresponding to the wind tunnel conditions with a specified advance ratio, rotor thrust, and shaft tilt angle. For wind tunnel trim calculations, the cyclic flapping angles measured at the flapping hinges are suppressed to zero.

Correlation results are presented in terms of the magnitudes of the vibratory hub loads at the specified harmonics. For instance, the magnitude of the $3P$ vertical hub shear is given by

$$F_{Z_3} = \sqrt{F_{Z_{3,c}}^2 + F_{Z_{3,s}}^2} \quad (3.1)$$

Figures 3.1–3.3 show the correlation of vibratory hub shears over the range of forward speeds from hover to 188 knots. The thrust coefficient-solidity ratio (C_T/σ) is held at 0.08. Calculated results are shown for three aerodynamic models: (1) quasi-steady aerodynamics and linear inflow model (Drees), (2) nonlinear unsteady aerodynamics (including dynamic stall) and Drees' inflow model, and (3) nonlinear unsteady aerodynamics and free wake model.

Figure 3.1 shows the correlation of the $3P$ vertical hub shear. Predicted results obtained using nonlinear aerodynamics and free wake modeling agree quite well with measured data at low speed as well as high speed flight regimes. At forward speeds above 160 knots, the sharp rise in the $3P$ vertical hub shear is attributed to dynamic stall, and this effect is reflected in the analytical results using nonlinear aerodynamics and Drees' inflow model. The sharp peak in the $3P$ vertical hub shear in the transition flight regime (around 40 knots) is satisfactorily predicted using the free wake analysis. It is interesting to note that the simple model with quasi-steady aerodynamics with Drees' inflow correlates quite well with experimental data at the forward speeds above 100 knots. However, the calculated results using nonlinear aerodynamic and free wake models yield the best overall correlation with experimental data.

Figure 3.2 shows the correlation of the $2P$ rotating inplane hub shear. For the range of forward speed below 100 knots, the calculated results using all three aerodynamic models are almost identical except for the small peak in the $2P$ inplane hub shear in the transition flight regime, captured only with the free wake analysis. At the forward speeds above 135 knots, the results using nonlinear aerodynamics with both inflow models correlate better with the experimental data than the results with quasi-steady aerodynamics and Drees' inflow.

Correlation of the $4P$ rotating inplane hub shear is shown in figure 3.3. This figure also shows that the results obtained using the three aerodynamic models are almost identical for the forward speeds below 100 knots. At the forward speeds above 160 knots, the results obtained using nonlinear aerodynamics and Drees' inflow overpredict the $2P$ rotating inplane hub shear, while the results with quasi-steady and Drees' inflow underpredict the experimental values. At the high forward speed range, the calculated results using nonlinear aerodynamics and the free wake analysis yield the best correlation of the $4P$ rotating inplane hub shear with the experimental data. Based on the results of the validation study, subsequent investigations were all carried out using nonlinear aerodynamics and the free wake model.

For the flight conditions considered above, optimal closed-loop HHC is introduced in the analysis to suppress the vibratory hub loads. The fixed-gain closed-loop controller is used with no control rate limiting factor set to zero. This controller suppresses completely and simultaneously all three vibratory hub shear components over the forward speed range from hover to 160 knots. These results are shown in figures 3.4–3.6 in which the predicted vibratory hub shears calculated using nonlinear aerodynamics and the free wake model are compared with the experimental values. Also, the results are presented for the cases with both HHC off and HHC on. In the experimental data, there are some residues in the levels of the vibratory hub load being suppressed. These residues may be attributed to the measurement

and process noise which are not included in the calculated results. In fact, if measurement noise is included in the simulation, then the HHC controller suppresses the vibratory hub loads to the noise level. For the case at 188 knots, the HHC amplitudes required to suppress completely the vibratory hub shears were very large (on the order of 5 degrees), and a converged numerical solution could not be achieved. It is suspected that such a large higher harmonic blade pitch might have induced a massive blade stall which caused the numerical solution to diverge. Such effects will be investigated in more detail in section 3.1.3.

The higher harmonic swashplate motions required to suppress the vibratory hub shears are shown next. The HHC inputs are transformed in terms of the harmonics of the swashplate motions in the collective, longitudinal cyclic, and lateral cyclic modes. The magnitudes of these swashplate motions are then calculated, the results being presented in figure 3.7. These results indicate that, except in the transition flight regime, the amplitudes required by both cyclic modes are generally higher than the collective amplitudes. Above 100 knots, it is worth noting that both of the cyclic swashplate amplitudes increase significantly with the forward speed, while the collective component remains essentially constant.

The actuator power required by the HHC system, expressed in terms of the actuator power index, is presented in figure 3.8. The actuator power index represents an accumulative index for the swashplate motions. Also, it represents approximately the combined HHC amplitudes required by all the blades of a rotor. The results show that the power index increases moderately from hover to a peak value in the transition flight regime (at 30 knots), then decreases slightly up to the forward speed of 60 knots, and increases again quite significantly for the high speed range (above 60 knots). The power index at 160 knots is about three and a half times that in the transition flight regime, at 30 knots.

Further investigations of HHC swashplate motions and actuator power required are performed for the cases when only individual components of the vibratory hub shears are suppressed. For this study, the fixed-gain controller is used to suppress the vibratory hub shears for the same three-bladed articulated rotor considered previously. The flight speed is held at 135 knots at a thrust coefficient-solidity ratio of 0.08. Figure 3.9 shows the comparison between the controlled vibratory hub shears, when each component is suppressed individually. For comparison purposes, the uncontrolled values are also presented. The comparisons of HHC swashplate amplitudes and actuator powers are shown in figure 3.10. The inputs required to suppress all three vibratory hub shear components are also shown. The suppression of the $3P$ vertical hub shear is achieved with only the collective input, corresponding to the third harmonics of the blade pitch schedule. When this vibratory hub shear component is completely suppressed, there are small increases in the $2P$ and the $4P$ rotating inplane hub shears from the uncontrolled values. Although the collective swashplate amplitudes required for this case are nearly equal to those required for the complete suppression of all three vibratory hub shears, the actuator power required is much smaller.

For the case when the $2P$ rotating inplane hub shear is suppressed, only the cyclic swashplate motion corresponding to the second harmonic blade pitch is employed. Figure 3.9 shows that there is a small increase in the $3P$ vertical hub shear and a small decrease in the $4P$ rotating inplane hub shear due to this HHC component. It is worth noting from figure 3.10 that suppression of the $2P$ rotating inplane hub shear requires approximately the same amount of cyclic actuator input, as well as the actuator power, as that required for the suppression of all three vibratory hub shear components.

Finally, suppression of the $4P$ rotating inplane hub shear using only the cyclic swashplate motion, corresponding to the fourth harmonics of blade pitch, is accompanied by about 30 percent reduction in the $3P$ vertical hub shear and a small decrease in the $2P$ rotating inplane component (fig. 3.9). The swashplate amplitudes and the actuator power required to suppress this vibratory hub shear component are slightly smaller than those required to suppress only the $3P$ vertical hub shear.

Even though the baseline value for the $3P$ vertical hub shear is much larger than the $2P$ rotating inplane component (fig. 3.9), the actuator power required to suppress the former component is about one-quarter of that required for the suppression of the latter component. This is understandable since HHC uses the higher harmonic blade pitch to generate new airloads to suppress the vibratory hub loads. Since a rotor blade generates more lift (in the vertical direction) than drag (in the inplane direction) for a given change in blade angle of attack, the vertical hub shear is more sensitive to the higher harmonic inputs than the inplane components. Therefore, larger HHC inputs are required to suppress the $2P$ rotating inplane hub shear.

The validation study for the three-bladed articulated model rotor of the CH-47D is also performed for cases when the rotor thrust is varied. For this, the forward speed is held fixed at 60 knots corresponding to an advance ratio of 0.138. The rotor thrust coefficient-solidity ratio (C_T/σ) is varied from 0.04 to 0.14. This flight condition generally represents the transition flight regime. Figure 3.11 shows the correlation of the $3P$ vertical hub shear with and without HHC effects. With no HHC and at a low thrust level ($C_T/\sigma = 0.04$), the analytical results agree quite well with experimental data. For values of C_T/σ greater than 0.08, the calculated value of the $3P$ vertical hub shear overpredicts the experimental data. This vibratory hub shear component increases with thrust level, and the trend is captured well in the analytical results. The discrepancies at high thrust may be attributed to the differences between the calculated trim controls and the experimental values. These differences are small for the collective controls, whereas the differences in cyclic controls are as large as 3 degrees.

Figure 3.12 shows the correlation of the $2P$ rotating inplane hub shear for the same flight conditions. For most of the range of thrust level shown, the analytical results underpredict the experimental data. However, the increasing trend of the vibratory hub shear component with increasing rotor thrust is well predicted with the analysis. Correlation of the $4P$ rotating inplane hub shear is shown in figure 3.13 and indicates that the calculations underpredict the experimental data for the complete range of thrust. The analytical results indicate that this vibratory hub shear component, being much smaller as compared to other components, increases slightly with thrust level. It was also found that perturbations in the cyclic trim values have a substantial influence on the predicted vibratory inplane hub shears. The discrepancies between the predicted and the measured $4P$ rotating inplane hub shears may be attributed to the rotor inflow behavior at this flight condition, especially for wind tunnel testing. For a rotor tested in a wind tunnel at the transition flight regime, a significant source of unsteady airloads originates from the rotor wake which remains close to the rotor disk. Furthermore, this problem is exacerbated because the rotor wake geometry is also influenced by the presence of the wind tunnel walls and floor, and such recirculation effects have not been considered in the simulation study. Another factor which might affect the results of the correlation is the effect of the hub motion which was not included in the analysis. Compared to the hub loads predicted by other authors, the present analytical results are in much better agreement with the experimental values.

For the same flight conditions, HHC was introduced into the analysis to suppress the predicted vibratory hub shears. The fixed-gain HHC controller with no control rate limiting factor ($r = 0$) was used. Again, both analytical and experimental results are presented in figures 3.11–3.13. These figures show that the fixed-gain controller suppresses almost completely all three vibratory hub shear components. This effectiveness is confirmed by both analytical and experimental results. Since measurement and process noise were not considered in the analysis, the predicted vibratory hub shears are suppressed to a lower level than those obtained experimentally.

The corresponding swashplate amplitude and phase variations with thrust level are shown in figures 3.14 and 3.15, respectively. These results indicate that all components of the HHC swashplate amplitudes increase with the thrust level. The variation is almost linear for the collective swashplate amplitude. It is interesting to note that the phases of both cyclic actuators vary by about 60 degrees as C_T/σ is varied from 0.04 to 0.14 while the collective actuator phase remains relatively constant. The actuator power required by the HHC system, expressed in terms of the actuator power index, is shown in figure 3.16. Within the range of rotor thrust shown, the actuator power increases quite significantly with the rotor thrust level. The actuator power required at the high thrust level ($C_T/\sigma = 0.14$) is about four times that for the low thrust level ($C_T/\sigma = 0.04$).

3.1.2 Secondary Effects of HHC

Next, the effects of HHC on the alternating blade bending stresses, control system loads, and the rotor shaft torque are examined (figs. 3.17–3.21). Alternating blade bending stresses are quite important since these affect the structural life of rotor blades. In figures 3.17–3.19, the alternating blade bending moments near the blade midspan for the flap, lag, and torsion modes are shown, respectively, with and without HHC effects. Due to the applied HHC, there are reductions in both the flap and the lag bending moments at 0.48 and 0.31 radius, respectively (figs. 3.17 and 3.18). Interestingly, the magnitudes decrease with thrust level and can be as much as 30 percent less than the baseline values.

In contrast, the alternating blade torsional moment at the blade midspan increases during HHC application over the range of thrust levels shown in figure 3.19. The increase in this blade stress component can be as much as 50 percent of the baseline values. Figure 3.20 shows the alternating pitch-link load as a function of thrust level. With HHC, it increases up to 48 percent from the uncontrolled values. An increase in the alternating blade torsional moment at midspan and the control loads were also observed in wind tunnel testing. These increases are expected since the HHC inputs are in fact implemented by exciting the blade torsional modes.

The effects of HHC on rotor performance, presented in terms of the rotor torque in figure 3.21, are negligible. Changes in the rotor shaft torque with HHC on range from a 0.35 percent increase at the low thrust level ($C_T/\sigma = 0.04$) to a 0.5 percent reduction at the high thrust level ($C_T/\sigma = 0.14$). Negligible changes in the rotor shaft torque with HHC were also noted in the wind tunnel investigation (ref. 46).

3.1.3 HHC Induced Blade Stall and Controller Performance

In order to investigate the influence of HHC on blade stall, a flight condition at 135 knots ($\mu = 0.3$) and $C_T/\sigma = 0.09$ is used. For this, the global (fixed-gain) controller ($r = 0$) is used to suppress the three vibratory hub shear components: $3P$ vertical and the $2P$ and the $4P$ rotating inplane hub shears. The vibratory responses presented in figure 3.22 show that all three components of the vibratory hub shear are completely suppressed within three HHC cycles. As an indicator of blade stall, the blade section normal force coefficients computed at 93 percent blade radius for the cases with HHC off and HHC on are shown in figure 3.23 and 3.24, respectively. In these figures, C'_N is the stall monitor value of the normal force coefficient, C_N is the total normal force coefficient (including dynamic stall effects), and the stall boundary is the critical normal force value, C_{N_1} . As discussed in the formulation, dynamic stall is initiated when the value of C'_N exceeds the critical normal force value, C_{N_1} . A stall margin is thus defined as the difference between the values of C'_N and C_{N_1} .

Figure 3.23 shows that, with no HHC, the stall margin value for this particular blade section near the blade tip is roughly 0.4 to 0.5 for the complete range of the rotor azimuth. However, figure 3.24 shows that, with HHC on, the stall margin for this particular blade section is reduced, especially in the retreating side of the disk in the fourth quadrant. This result, although limited to a particular blade section, indicates that the HHC inputs used to alleviate helicopter vibration might promote blade stall.

Further investigation of the HHC effects on blade stall is made by raising the C_T/σ to 0.135 for the same forward speed. This hypothetical flight condition exceeds the level-flight structural envelope and maneuver capability of the CH-47 helicopter (ref. 99). Again, the global controller ($r = 0$) is first used to suppress the vibration, and the resulting vibratory hub shear responses are shown in figure 3.25. Clearly, complete vibration suppression for this flight condition can not be achieved using the global controller. Over the range of HHC cycles, the vibratory hub shears have essentially the same magnitudes as the uncontrolled values.

In figures 3.26 and 3.27, the resulting section normal force coefficients near the blade tip (93 percent radius) for the case discussed above are shown without and with HHC over one rotor revolution. The results presented in figure 3.27 are obtained at the sixth HHC cycle. Without HHC, the blade section is already stalled in the fourth quadrant, whereas, with HHC on, there are two large lift overshoots that cross over the stall boundary in the retreating blade tip region (fig. 3.27). These results indicate that for a rotor operating with considerable stall on the rotor disk, the HHC inputs used to suppress the vibratory hub loads escalate the stall phenomena and thus deteriorate the HHC performance.

For the same flight condition, the local model with a control rate limiting factor, $r = 0.3$, is then used to suppress the vibration. Figure 3.28 shows the time history of the vibratory hub shear responses. This figure shows that the local controller, although having a sluggish transient behavior (within the first two cycles), is quite effective in suppressing all three vibratory hub shear components. At the eighth HHC cycle, there is a reduction of more than 95 percent for all three hub shear components. This controller effectiveness is attributed to two effects. First, the transfer matrix at this flight condition is nonlinear, and the local model is more suitable for such conditions. Second, the control rates are constrained to suppress large control excursions, and this is beneficial for avoiding excessive blade stall. The resulting blade section normal force coefficients at 93 percent blade radius for the eighth HHC

cycle are shown in figure 3.29. These results should be compared with those presented in figure 3.26. Even though this controller promotes some blade stall on the retreating side of the disk, the resulting lift variation appears much smoother than that obtained with the global controller.

For the same forward speed, the rotor thrust is now reduced to the $C_T/\sigma = 0.12$ level. This flight condition represents the level-flight boundary condition of the CH-47 aircraft (ref. 99). For this flight condition, the vibration is suppressed within four cycles using the local controller with a control rate limiting factor of 0.3. The effects of HHC in promoting blade stall, viewed from above the rotor disk, are shown in figures 3.30 and 3.31. In these figures, the stall area on the disk is hatched and corresponds to the locations where the value of C'_N is greater than the C_{N_1} value. Figure 3.30 shows that with no HHC the rotor is already stalled in the third and fourth quadrants of the disk, as might be expected. However, the retreating blade tip region is stall free. Figure 3.31 indicates that, with HHC on, the stall area spreads up to the blade tip region in the fourth quadrant of the disk. Again, this result confirms that HHC inputs used to suppress vibration can indeed promote blade stall.

As a final note in this investigation, the results presented are limited to the wind tunnel simulation of the three-bladed articulated rotor model of the CH-47D helicopter. For other rotors with different blade numbers or with a different hub design, such as hingeless or bearingless, the results may be entirely different. The HHC inputs used to suppress the rotor vibratory hub loads might not induce blade stall on the rotor disk. Furthermore, the trim conditions used in this study simulate the flight conditions of the CH-47D which is a tandem helicopter. For a single main rotor helicopter, the trim requirements are entirely different, and a different HHC-stall-induced behavior may be expected.

3.2 Sensitivity Analysis

3.2.1 Hingeless Versus Articulated Rotors

The above investigation was performed for a typical articulated rotor system. Next, the vibration suppression characteristics of two hingeless rotor configurations are analyzed and compared with results of the articulated rotor system. These three-bladed hingeless rotors represent, respectively, a soft-inplane (lag frequency = $0.71P$) and a stiff-inplane (lag frequency = $1.4P$) configuration. Both rotors have a fundamental flap frequency of $1.1P$. For these results, wind tunnel flight conditions are simulated with the forward speed ranging from zero to 188 knots and at a thrust coefficient-solidity ratio of 0.08.

Figure 3.32 shows the variation of the $3P$ vertical hub shear with forward speed for three rotor systems. Below 100 knots, the calculated $3P$ vertical hub shears for these rotors are quite comparable. At the higher forward speeds, the $3P$ vertical hub shear for the stiff-inplane rotor increases rapidly with speed, while this component remains the lowest for the articulated rotor system.

Variation of the $2P$ rotating inplane hub shear with forward speeds for these three rotors is shown in figure 3.33. For forward speeds below 135 knots, the $2P$ rotating inplane hub shears for the articulated and the soft-inplane hingeless rotors are quite similar, whereas at higher speeds, the vibratory hub shear component for the soft-inplane hingeless rotor is about 30 percent lower than that for the articulated rotor system. For the stiff-inplane rotor, the $2P$ vibratory hub shear increases considerably for forward

speeds above 100 knots. This is understandable since the blade fundamental lag mode frequency for the stiff-inplane rotor of $1.4P$ is closer to the resonant frequency of $2P$ than the other two rotor systems. Figure 3.34 shows the $4P$ rotating inplane hub shears. The magnitudes of this high frequency hub shear are much smaller than those of the low frequency $2P$ hub shear and are quite similar for all three rotor systems.

Next, HHC inputs are applied to suppress the vibratory hub shear components for these three rotor configurations. Because the HHC system is quite effective in suppressing completely the $3P$ vertical and the $2P$ and $4P$ rotating inplane hub shears, the controlled vibratory hub shears are not shown. Even though the vibratory hub moments for the hingeless rotor are not small, especially at the high forward speeds, these are not suppressed in this study, so subsequent HHC results can be compared directly with those obtained earlier for the articulated rotor.

Figure 3.35 shows the actuator power index required by the HHC system at different forward speeds. For the stiff-inplane hingeless rotor above 100 knots, the HHC inputs required to suppress the vibratory hub shears become very large, and the problem associated with the convergence of the numerical solution hinders any more results. For moderate to high forward speeds, the power index for the soft-inplane hingeless rotor is larger than that required for the articulated rotor. It is interesting to note that in the transition flight regime, the actuator power index is the largest for the soft-inplane rotor even though the vibratory hub loads are the largest for the stiff-inplane configuration. However, for forward speeds above 140 knots, the power index for the soft-inplane hingeless rotor becomes lower than that for the articulated rotor system. In fact, at 160 knots, the power index for the soft-inplane hingeless rotor is less than half that of the articulated rotor. For forward speeds above 50 knots, the actuator power index required by the stiff-inplane hingeless rotor is the largest among the three rotor systems considered.

3.2.2 Parametric Study—Four-Bladed Hingeless Rotor

Next, the sensitivity of the uncontrolled vibratory hub loads and the actuator power for a hingeless rotor with respect to various blade design parameters is examined. For this simulation, a four-bladed soft-inplane hingeless rotor is chosen as a baseline configuration. The structural characteristics of this rotor blade are similar to those of the three-bladed soft-inplane hingeless rotor considered earlier, i.e., the blade fundamental flap and lag mode frequencies are $1.1P$ and $0.7P$, respectively. Propulsive trim with steady level flight is simulated for forward speed of 40 knots corresponding to a rotor advance ratio of 0.09. This airspeed corresponds to the transition flight regime where the rotor would experience a high level of vibration. The rotor thrust coefficient-solidity ratio is held at 0.08. The fixed-gain HHC controller is now configured to suppress the $4P$ vertical, the $3P$ and $5P$ rotating inplane hub shears, and the $3P$ and $5P$ rotating hub moments.

Blade torsion stiffness— The blade torsion frequency is varied by adjusting the blade torsion stiffness of the inboard section. In this simulation, blade rotating fundamental torsion frequency is varied from $3P$ to $7P$, and the baseline value is $4.5P$. Figure 3.36 shows the uncontrolled vibratory hub shears with blade torsion frequency. For most of the range of frequencies shown, the rotor vibratory hub shear components are quite insensitive to the blade torsion stiffness. An exception is for frequencies close to $3P$ where there is a considerable reduction in the $4P$ vertical hub shear and a moderate increase

in the $3P$ inplane hub shear. This is attributed to the resonance of blade torsional response with the forcing at $3P$. The vibratory hub moments are presented in figure 3.37, which shows that the $3P$ hub moment increases moderately with blade torsion stiffness. The $5P$ hub moment is small compared to the $3P$ component and is quite insensitive to blade torsion stiffness. The variation of the actuator power index with blade torsion frequency is shown in figure 3.38. It is interesting to note that the power index is lowest at the blade torsion frequency of about $3.85P$, for which the actuator power index is less than half that at the torsion frequency of $7P$.

Blade bending stiffness— Blade bending stiffnesses in the flapwise and chordwise directions are varied to study their effects on the vibratory hub loads and the actuator power. Blade bending stiffness in the flapwise direction affects the blade elastic flap modes, and its variation is presented in terms of the blade second rotating flap mode frequency. Figure 3.39 shows the uncontrolled vibratory hub shear variation with blade flap mode frequency; the baseline value is $2.85P$. Variation of the flapwise stiffness affects all three vibratory hub shear components. The $4P$ vertical hub shear is a minimum when the blade frequency is about $3P$, while the $3P$ inplane hub shear is a minimum when the blade frequency is $2.65P$. The $5P$ inplane hub shear component is small compared to the other two components, and its magnitude decreases steadily with an increase in flap stiffness. Variations of the $3P$ and $5P$ hub moment with blade flap bending stiffness are shown in figure 3.40. Within the range of flap frequencies shown, it is interesting to note that the $5P$ hub moment increases sharply as the flap frequency is reduced below $2.6P$, while the $3P$ hub moment reaches a minimum at this frequency value. In figure 3.41, the actuator power remains constant for the range of flap frequencies above $2.9P$ and increases sharply for the range of flap frequencies below this value.

Variation of the blade chordwise stiffness is presented in terms of the blade second rotating lag mode frequency; the baseline value is $5.8P$. The uncontrolled vibratory hub shears are presented in figure 3.42. For this rotor configuration, the vibratory hub shears are quite sensitive to the placement of the blade second lag mode frequency. The magnitude amplification of hub shears is quite pronounced as the blade chordwise frequency is placed at the corresponding harmonic. It is interesting to note that the resonant conditions exist not only for the inplane shears but also for the vertical component. In fact, at resonance, the $4P$ vertical hub shear increases by four and a half times the baseline value. Magnitude amplification is also shown in figure 3.43 where the vibratory hub moments are presented. This figure shows that the $5P$ hub moment increases noticeably as the lag frequency approaches $4P$, while the effect of lag stiffness on the $3P$ hub moment is small. The actuator power index variation shown in figure 3.44 indicates that minimum power required is achieved by placing blade lag frequencies either at $3.6P$ or at $6.2P$ away from the resonant frequencies at the rotor harmonics.

Blade linear pretwist— Blade pretwist redistributes blade steady airloads in the spanwise direction and introduces elastic flap-lag coupling. In this study, blade linear pretwist is used with values ranging from zero to -16 degrees. The baseline blade configuration has a pretwist of -8 degrees. Figures 3.45 and 3.46 show, respectively, the vibratory hub shears and moments with blade pretwist. These figures show that the $4P$ vertical and the $3P$ inplane hub shears and the two hub moment components all decrease with increasing blade pretwist. The $5P$ inplane hub shear is small and increases slightly with increasing blade pretwist. The actuator power is shown in figure 3.47, where a reduction of 20 percent in the actuator power is achieved with a blade pretwist of -16 degrees as compared to an untwisted blade.

Blade chordwise center-of-gravity offset— Blade chordwise center-of-gravity (c.g.) offset from the elastic axis introduces inertial coupling between the flap and torsion modes. For this study, the elastic axis is assumed to be at the quarter chord, and a positive c.g. offset represents the blade center of mass placed ahead of the quarter chord, toward the blade leading edge. The baseline rotor configuration has no offset. Figures 3.48 and 3.49 show that the $4P$ vertical and the $3P$ inplane hub shears and the $3P$ hub moment are all reduced as the blade c.g. is shifted forward of the elastic axis. The $5P$ inplane hub shear and the $5P$ inplane hub moment are small compared to the other vibratory hub load components and increase slightly as the blade chordwise c.g. is moved ahead of the elastic axis. From figure 3.50, the actuator power increases sharply as the blade c.g. is placed more than 2 percent of chord ahead of the elastic axis and increases slightly as the blade c.g. is placed behind the elastic axis. In fact, the actuator power is lowest when the blade c.g. is placed at 2 percent of chord length, ahead of the elastic axis.

Offset of elastic axis from quarter-chord axis— The offset of blade elastic axis from the blade quarter chord introduces aerodynamic pitch-flap coupling, and its effects on the vibratory hub loads and HHC system were examined. The offset is positive when the blade elastic axis is placed ahead of the quarter chord, and, for the baseline rotor, the elastic axis is at quarter chord (zero offset). Figures 3.51 and 3.52 show the variations of the vibratory hub loads with the variation of this offset value. Variations of the vibratory hub loads are quite similar to those observed when the blade c.g. is varied with respect to the elastic axis location. Figure 3.53 shows the actuator power variation with location of elastic axis, and a similar behavior is observed to that shown in figure 3.50. Placing the elastic axis in front of the quarter chord helps reduce the major vibratory hub load components. A minimum in actuator power is achieved by placing the elastic axis 3 percent of chord length ahead of the quarter chord. At this minimum value, a 17 percent reduction in actuator power is achieved from the baseline value.

Blade thrust— Rotor thrust, expressed in terms of C_T/σ , is varied from 0.06 to 0.12, and the results are shown in figures 3.54–3.56. Figures 3.54 and 3.55 show that all the vibratory hub load components increase noticeably with an increase in rotor thrust. The actuator power variation is presented in figure 3.56, which shows that, at high thrust ($C_T/\sigma = 0.12$), the power required is twice that for the baseline case ($C_T/\sigma = 0.08$). Within the range of rotor thrusts shown, the actuator power varies almost linearly with the rotor thrust.

3.2.3 Parametric Study—Three-Bladed Articulated Rotor

Next, the sensitivity of the uncontrolled vibratory hub loads and the actuator power for the baseline three-bladed rotor with respect to various blade design parameters is examined. For this simulation, the level-flight boundary condition of the aircraft is used, i.e., $V = 135$ knots ($\mu = 0.3$), and $C_T/\sigma = 0.12$. The closed-loop HHC controller with control rate limiting factor is used to suppress the $3P$ vertical and the $2P$ and $4P$ rotating inplane hub shears. The blade and rotor properties considered previously in the correlation study (table 3.1) are used as a baseline rotor configuration.

Blade torsion stiffness— In this simulation, the blade fundamental torsion frequency is varied from $3.8P$ to $6.8P$; the baseline value is $4.86P$. The uncontrolled vibratory hub shear variation with blade torsion frequency is presented in figure 3.57. For most of the frequency range shown, the vibratory inplane hub shears are quite insensitive to the blade torsion frequency. For the torsion frequencies below

the baseline value, the $2P$ rotating inplane hub shear increases slightly, while the $4P$ inplane component decreases slightly from the baseline values. The $3P$ vertical hub shear increases moderately with blade torsion stiffness. In fact, there is a 35 percent reduction in the $3P$ vertical component as the blade torsion frequency is reduced from $6.8P$ to $3.8P$. The actuator power index variation with blade torsion frequency is shown in figure 3.58. From an actuator design point of view, it is interesting to note that a torsionally stiff blade requires less actuator power than a torsionally soft blade. A torsionally stiff blade with frequency greater than $4.5P$ consumes roughly 40 percent less actuator power than a blade with torsion frequency placed at $3.8P$. For torsion frequencies greater than $4.5P$, the actuator power index is insensitive to the blade torsion vibration characteristics.

Blade bending stiffnesses— Blade bending stiffnesses in the flapwise and chordwise directions are varied to study their effects on the vibratory hub loads and the actuator power. Figure 3.59 shows the uncontrolled vibratory hub shear variation with the blade flap mode frequency, where the baseline frequency value is $2.66P$. Variation of flapwise stiffness significantly affects the $3P$ vertical hub shear, while the inplane components are less sensitive to this parameter. The value of the $3P$ vertical hub shear is highest for low flap stiffness. As the flap frequency is increased, this vibratory hub shear component reaches a minimum at $2.78P$, increases to a local maximum at $3P$, and then decreases again for flap frequencies greater than $3P$. The peak value which occurs at $3P$ may be attributed to the resonant condition. The $2P$ rotating inplane hub shear increases slightly with increasing flap stiffness, while the $4P$ component remains relatively unchanged. The actuator power index variation with flap frequency is shown in figure 3.60. This figure indicates that minimum actuator power is achieved at the first flap bending frequency of $2.65P$. Reducing the flap stiffness from this optimum value does not significantly change the actuator power required, whereas increasing it would increase the actuator power by a small amount.

Variation of the blade chordwise stiffness is presented in terms of the blade first lag bending frequency; the baseline frequency is $6.4P$. The uncontrolled vibratory hub shears are presented in figure 3.61. The sharp increase in the $4P$ rotating inplane hub shear as the blade lag bending frequency approaches $4P$ is attributed to the resonant condition. At this frequency, the $4P$ inplane hub shear increases by five times the baseline value. For the range of frequencies greater than $4.5P$, this vibratory hub shear component is quite insensitive to the blade lag stiffness. Within the range of blade lag frequencies shown, the $2P$ rotating inplane hub shear is insensitive to blade lag stiffness, while the $3P$ vertical component varies significantly. At the lag frequency of $4P$, the $3P$ vertical hub shear is highest. As the lag stiffness is increased, the $3P$ vertical hub shear component reaches a local minimum at $4.6P$, increases to a local maximum at $5.7P$, decreases again to another local minimum at $6.4P$, and again increases at the higher frequency values. The actuator power index variation is shown in figure 3.62. The HHC power required to suppress vibration is quite insensitive to the blade lag stiffness, except when the lag frequency is placed at $4P$, at which point the actuator power is increased by 30 percent from the baseline value.

Blade chordwise c.g. offset— The baseline rotor configuration has a nonzero c.g. offset distribution as shown in table 3.1. Figure 3.63 shows the uncontrolled vibratory hub shear as a function of blade chordwise c.g. offset from the elastic axis, expressed in percentage of chord length. Except for the baseline configuration, the chordwise c.g. offset considered in this parametric investigation is made by a uniform variation across the blade span. Figure 3.64 shows that all three vibratory hub shear components are reduced as the blade c.g. is moved ahead of the elastic axis. The most significant reduction is the

$2P$ rotating inplane hub shear which is reduced by more than half as the blade c.g. is shifted uniformly by more than 6 percent of chord length ahead of the elastic axis. Figure 3.64 shows that the actuator power is reduced as the blade chordwise c.g. is placed ahead of the elastic axis. In fact, by moving the blade c.g. from the elastic axis toward the blade leading edge by 10 percent of chord length reduces the actuator power index by 40 percent.

Offset of elastic axis from quarter chord— Figure 3.65 shows the uncontrolled vibratory hub shear variation with the offset of elastic axis from quarter chord. The $3P$ vertical and the $4P$ inplane hub shears are quite insensitive to this parameter, while the $2P$ inplane hub shear varies significantly with the elastic axis location. As the elastic axis is shifted forward of the blade quarter chord, the $2P$ inplane component reduces to a minimum at 5 percent of chord length offset and increases at higher offset value. Figure 3.66 shows the actuator power index variation with the offset of the elastic axis from quarter chord. From this figure, the actuator power is lowest when the elastic axis is placed at 5 percent of chord length ahead of the quarter chord, at which point the actuator power is reduced by half from the baseline value.

4 CONCLUSIONS

An analytical formulation has been developed to calculate the vibratory hub loads for helicopter rotors in forward flight and the corresponding higher harmonic control inputs to suppress these loads. The analysis was based on a finite element method in both space and time domains. A nonlinear time domain unsteady aerodynamic model, based on the indicial response formulation, was used to calculate the blade airloads. The rotor induced inflow was calculated using a free wake analysis. The vehicle trim control settings and blade steady responses were solved as one coupled solution using a modified Newton method. The HHC responses form a part of the steady response calculations where the basic collective and cyclic trim inputs were superimposed with the higher harmonic components. A linear frequency-domain quasi-steady model, in terms of a transfer function, was used to relate the harmonics of the HHC inputs to the harmonics of the vibratory hub loads. Optimal HHC was calculated from the minimization of the vibratory hub loads, expressed in terms of a quadratic performance index.

The calculated vibratory hub loads, with and without HHC effects, have been correlated with wind tunnel data obtained from a three-bladed articulated scaled model rotor. The secondary effects of HHC were also investigated including the influences of HHC on blade stall. Systematic parametric studies have been performed on different rotor systems to investigate the effects of blade design variables on the vibratory hub loads, HHC inputs, and actuator power requirements. The following conclusions were drawn from this study:

1. Good correlation of predicted vibratory hub loads was obtained with experimental data at different flight conditions. A refined aerodynamic model including compressibility effects and dynamic stall helped improve the correlation at high forward speeds. The inclusion of the free wake analysis improved the correlation in the transition flight regime. For the three-blade model rotor operated at low speed, the correlation of the $3P$ vertical and the $2P$ rotating inplane hub shears was adequate, while the calculated $4P$ rotating inplane hub shear was significantly lower than the experimental values.

2. The fixed-gain HHC controller was quite effective in suppressing the rotor vibratory hub shears for most of the rotor operating conditions. The HHC actuator amplitudes and power requirements increased substantially at high forward speed range (above 100 knots, or $\mu = 0.2$) and increased moderately with the rotor thrust level. For complete vibratory hub shear suppression, a large percentage of the actuator power is required to suppress the $2P$ rotating inplane hub shear component on a three-bladed rotor. At high forward speeds, a soft-inplane hingeless rotor required less actuator power than an articulated rotor, whereas the actuator power requirement for a stiff-inplane hingeless rotor was generally higher than that for an articulated or a soft-inplane hingeless rotor.

3. For a rotor operating in the transition flight regime, HHC caused moderate reduction in the flap and lag bending stresses near the blade midspan, whereas it increased the control system fatigue loads and the blade torsional stresses significantly. HHC effects on overall rotor performance were found to be negligible at the low speed regime.

4. For a rotor operated at or outside the flight boundary, the adaptive-gain controller suppressed almost completely the rotor vibratory hub shears, even though HHC might actually increase the stalled flow region on the rotor disk. For such flight conditions, the fixed-gain controller was ineffective in suppressing the vibratory hub loads.

5. For a four-blade soft-inplane hingeless rotor operated in the transition flight regime ($\mu = 0.09$, $C_T/\sigma = 0.08$),
- The actuator power was quite sensitive to the blade torsion stiffness, while the baseline vibratory hub loads were less sensitive. Placing blade torsion frequency at $3.85P$ resulted in a minimum actuator power.
 - Placing blade second elastic flap frequency above $2.9P$ helped reduce the actuator power.
 - The uncontrolled vibratory hub loads were sensitive to the placement of the blade second elastic lag frequency. Placing blade second elastic lag frequency at $3.6P$ or at $6.2P$ helped reduce the actuator power.
 - An increase in blade linear pretwist reduced the actuator power.
 - Placing blade center of mass 2 percent of chord length ahead of the elastic axis and placing the elastic axis 3 percent of chord length forward of the quarter-chord axis helped reduce the actuator power.
 - The uncontrolled vibratory hub loads and the actuator power increased with rotor thrust.
6. From a sensitivity study of blade design parameters for a three-bladed articulated rotor operating at the level-flight boundary ($\mu = 0.3$, $C_T/\sigma = 0.12$),
- The $3P$ vertical hub shear was sensitive to the blade torsion stiffness, while the inplane components were less sensitive. The actuator power was quite insensitive to the blade torsion frequency, except near the resonant frequency of $3P$.
 - The $3P$ vertical hub shear was sensitive to the placement of the blade first flap bending frequency, while the inplane vibratory hub shear components and the actuator power were less sensitive. Both the $3P$ vertical and $4P$ rotating inplane hub shear were sensitive to the blade lag stiffness. Placing the blade first elastic lag frequency at $4P$ increased the $4P$ rotating inplane hub shear by five times and the actuator power by one-third from the baseline values.
 - Placing the blade center of mass ahead of the elastic axis helped reduce both the uncontrolled vibratory hub shears and the actuator power. Placing the elastic axis at 5 percent of chord length ahead of the quarter chord minimized the $2P$ rotating inplane hub shear as well as the actuator power.

Items (5) and (6) above indicate that blade parameters had moderate to strong influence on the amplitude and actuator power requirements for an HHC system. Therefore, the design of an optimum blade which is best suited for HHC application (i.e., with minimum actuator power requirement) is, in principle, feasible.

REFERENCES

1. Reichert, G.: Helicopter Vibration Control—A Survey. Proceeding of the Sixth European Rotorcraft and Powered-Lift Aircraft Forum, Sept. 1980.
2. Loewy, R. G.: Helicopter Vibrations: A Technological Perspective. J. American Helicopter Society, vol. 29, no. 4, Oct. 1984, pp. 4–30.
3. Balmford, D. E. H.: The Control of Vibration in Helicopters. Aeronautical J., Feb. 1977, pp. 63–67.
4. McCloud, J. L. III: Studies of a Large Scale Jet-Flap Rotor in the 40- by 80-Foot Wind Tunnel. Proceedings of the American Helicopter Society Mideast Regional Symposium on Status of Testing and Modeling of V/STOL Aircraft, Oct. 1972.
5. McCloud, J. L. III; and Kretz, M.: Multicyclic Jet-Flap Control for Alleviation of Helicopter Blade Stresses and Fuselage Vibration. Proceedings of the AHS/NASA Ames Specialists Meeting on Rotorcraft Dynamics, NASA SP-352, Feb. 1974, pp. 233–238.
6. Piziali, R. A.; and Trenka, A. R.: A Theoretical Study of the Application of Jet-Flap Circulation Control for Reduction of Rotor Vibratory Forces. NASA CR-137515, May 1974.
7. Trenka, A. R.: A Theoretical Study of the Application of Jet Flap Circulation Control For Reduction of Rotor Vibratory Forces—Addendum. NASA CR-137729, Oct. 1975.
8. McCloud, J. L. III: An Analytical Study of a Multicyclic Controllable Twist Rotor. Proceedings of the American Helicopter Society 31st Annual Forum, May 1975.
9. Lemnios, A. Z.; and Dunn, F. K.: Theoretical Study of Multicyclic Control of a Controllable-Twist Rotor. NASA CR-151959, Apr. 1976.
10. McCloud, J. L. III; and Weisbrich, A. L.: Wind Tunnel Test Results of a Full-Scale Multicyclic Controllable-Twist Rotor. Proceedings of the American Helicopter Society 34th Annual Forum, AHS Paper No. 78-60, May 1978.
11. Brown, T. J.; and McCloud, J. L. III: Multicyclic Control of a Helicopter Rotor Considering the Influence of Vibration, Loads, and Control Motion. Proceedings of the AIAA/ASME/ASCE/AHS 21st Structures, Structural Dynamics, and Material Conference, May 1980, pp. 82–100.
12. Blackwell, R. H., Jr.; and Welsh, W. A.: Higher Harmonic and Trim Control of the X-Wing Circulation Control Wind Tunnel Model Rotor. Proceedings of the American Helicopter Society 45th Annual Forum, May 1989, pp. 65–79.
13. Abramson, J.; and Rogers, E. O.: Optimal Theory Applied to Higher Harmonic Control of Circulation Control Rotors. Proceedings of the American Helicopter Society 37th Annual Forum, May 1981, pp. 26–36.
14. Ham, N. D.: A Simple System for Helicopter Individual-Blade-Control Using Modal Decomposition. Vertica, vol. 4, no. 1, 1980, pp. 23–28.

15. McKillip, R. M., Jr.: Periodic Control of the Individual-Blade-Control Helicopter Rotor. *Vertica*, vol. 9, no. 2, 1985, pp. 199-225.
16. Winson, J.: Testing of Rotors for Fatigue Life. *J. Aeronautical Science*, vol. 15, no. 7, July 1948, pp. 392-402.
17. Jensen, H. T.: Design and Operational Features of the Sikorsky Helicopter Rotor Stand. Institute of Aeronautical Sciences, Preprint No. 262, Feb. 1951.
18. Stewart, W.: Second Harmonic Control on the Helicopter Rotor. Aeronautical Research Council, Reports and Memoranda No. 2997, Aug. 1952.
19. Arcidiacono, P. J.: Theoretical Performance of Helicopters Having Second and Higher Harmonic Feathering Control. *J. American Helicopter Society*, vol. 6, no. 2, Apr. 1961, pp. 8-19.
20. Drees, J. M.; and Wernicke, R. K.: An Experimental Investigation of a Second Harmonic Feathering Device on the UH-1A Helicopter. U.S. Army Transportation Research Command, TR-62-109, Fort Eustis, Va., June 1963.
21. Daughaday, H.: Suppression of Transmitted Harmonic Rotor Hub Loads by Blade Pitch Control. U.S. Army Aviation Materiel Laboratories, TR-67-14, Fort Eustis, Va., Nov. 1967.
22. Shaw, J.: Higher Harmonic Blade Pitch Control for Helicopter Vibration Reduction: A Feasibility Study. Aeroelastic and Structures Research Laboratory Report ASRL TR1501, Massachusetts Institute of Technology, Dec. 1968.
23. Balcerak, J. C.; and Erickson, J. C.: Suppression of Transmitted Harmonic Vertical and Inplane Rotor Loads by Blade Pitch Control. U.S. Army Air Mobility and Development Laboratory, TR-69-39, Fort Eustis, Va., July 1969.
24. Sissingh, G. J.; and Donham, R. E.: Hingeless Rotor Theory and Experiment on Vibration Reduction by Periodic Variation of Conventional Controls. Proceedings of the AHS/NASA Ames Specialists Meeting on Rotorcraft Dynamics, NASA SP-352, Feb. 1974, pp. 261-277.
25. McHugh, F. J.; and Shaw, J.: Benefits of Higher Harmonic Blade Pitch: Vibration Reduction, Blade Load Reduction, and Performance Improvement. Proceedings of the American Helicopter Society Mideast Regional Symposium on Rotorcraft Technology, Aug. 1976.
26. McHugh, F. J.; and Shaw, J.: Helicopter Vibration Reduction with Higher Harmonic Blade Pitch. *J. American Helicopter Society*, vol. 23, no. 4, Oct. 1978, pp. 26-35.
27. Hammond, C. E.: Helicopter Vibration Reduction via Higher Harmonic Control. Proceedings of the Rotorcraft Vibration Workshop, NASA Ames Research Center, Feb. 1978.
28. Wood, E. R.; Powers, R. W.; and Hammond, C. E.: On Methods for Application of Higher Harmonic Control. Proceedings of the Fourth European Rotorcraft and Powered-Lift Aircraft Forum, Sept. 1978.
29. Powers, R. W.: Preliminary Design Study of a Higher Harmonic Blade Feathering Control System. NASA CR-159327, June 1980.

30. McCloud, J. L. III: The Promise of Multicyclic Control. *Vertica*, vol. 4, no. 1, 1980, pp. 29–42.
31. Shaw, J.: Higher Harmonic Blade Pitch Control: A System for Helicopter Vibration Reduction. Ph.D. Thesis, Massachusetts Institute of Technology, May 1980.
32. Shaw, J.; and Albion, N.: Active Control of Rotor Blade Pitch for Vibration Reduction: A Wind Tunnel Demonstration. *Vertica*, vol. 4, no. 1, 1980, pp. 3–11.
33. Shaw, J.; and Albion, N.: Active Control of the Helicopter Rotor for Vibration Reduction. *J. American Helicopter Society*, vol. 26, no. 3, July 1981, pp. 32–39.
34. Yen, J. G.: Vibration Reduction with Higher Harmonic Blade Feathering for Helicopters with Two-Bladed Teetering and Four-Bladed Hingeless Rotors. Proceedings of the American Helicopter Society 36th Annual Forum, AHS Paper No. 80–69, May 1980.
35. Hammond, C. E.: Wind Tunnel Results Showing Rotor Vibratory Loads Reduction Using Higher Harmonic Blade Pitch. *J. American Helicopter Society*, vol. 28, no. 1, Jan. 1983, pp. 10–15.
36. Hammond, C. E.; and Hollenbaugh, D. D.: Quantification of Helicopter Vibration Ride Qualities. Proceedings of the Seventh European Rotorcraft and Powered-Lift Aircraft Forum, Sept. 1981.
37. Molusis, J. A.; Hammond, C. E.; and Cline, J. H.: A Unified Approach to the Optimal Design of Adaptive and Gain Scheduled Controllers to Achieve Minimum Helicopter Rotor Vibration. Proceedings of the American Helicopter Society 37th Annual Forum, May 1981, pp. 188–203.
38. Molusis, J. A.: Investigation of Unexplained Behavior and Nonlinearity Observed in Wind Tunnel Tests of Higher Harmonic Control. U.S. Army Research and Technology Laboratories, TR-83-D8, Fort Eustis, Va., Aug. 1983.
39. Molusis, J. A.: The Importance of Nonlinearity on the Higher Harmonic Control of Helicopter Vibration. Proceedings of the American Helicopter Society 30th Annual Forum, May 1983, pp. 624–647.
40. Beliewa, R. L.: Aeroelastic Analysis for Helicopter Rotor Blades with Time-Variable, Nonlinear Structural Twist and Multiple Structural Redundancy—Mathematical Derivation and User's Manual. NASA CR-2638, 1976.
41. Wood, E. R.; Powers, R. W.; Cline, J. H.; and Hammond, C. E.: On Developing and Flight Testing a Higher Harmonic Control System. *J. American Helicopter Society*, vol. 30, no. 1, Jan. 1985, pp. 3–20.
42. Gupta, B. P.; Logan, A. H.; and Wood, E. R.: Higher Harmonic Control for Rotary Wing Aircraft. Proceedings of the AIAA/AHS/ASEE Aircraft Design Systems and Operations Meeting, Oct. 1984.
43. Straub, F. K.; and Byrns, E. V., Jr.: Application of Higher Harmonic Blade Feathering on the OH-6A Helicopter for Vibration Reduction. NASA CR-4031, Dec. 1986.
44. Johnson, W.: Self-Tuning Regulators for Multicyclic Control of Helicopter Vibrations. NASA Technical Paper 1996, Mar. 1982.

45. Chopra, I.; and McCloud, J. L. III: A Numerical Simulation Study of Open-Loop, Closed-Loop and Adaptive Multicyclic Control System. Proceedings of the American Helicopter Society Northeast Region National Specialists Meeting on Helicopter Vibration, Technology for the Jet Smooth Ride, Nov. 1981, pp. 63-77.
46. Shaw, J.; Albion, N.; Hanker, E. J.; and Teal, R. S.: Higher Harmonic Control: Wind Tunnel Demonstration of Fully Effective Vibratory Hub Force Suppression. J. American Helicopter Society, vol. 34, no. 1, Jan. 1989, pp.14-29.
47. Lehmann, G.: The Effects of Higher Harmonic Control on a Four-Bladed Hingeless Model Rotor. Vertica, vol. 9, no. 3, 1985, pp. 273-284.
48. Jacob, H. G.; and Lehmann, G.: Optimization of Blade Pitch Angle for Higher Harmonic Control. Vertica, vol. 7, no. 3, 1983, pp. 271-286.
49. Taylor, R. B.; Farrar, F. A.; and Miao, W.: An Active Control System for Helicopter Vibration Reduction by Higher Harmonic Blade Pitch. Proceedings of the American Helicopter Society 36th Annual Forum, AHS Paper No. 80-71, May 1980.
50. Davis, M.: Refinement and Formulation of Helicopter Real-Time Self-Adaptive Active Vibration Controller Algorithms. NASA CR-3821, 1983.
51. O'Leary, J. J.; Kottapalli, S. B. R.; and Davis, M.: Adaptation of a Modern Medium Helicopter (Sikorsky S-76) to Higher Harmonic Control. Proceedings of the AHS/NASA Ames Research Center Second Decennial Specialists Meeting on Rotorcraft Dynamics, Nov. 1984.
52. Miao, W.; Kottapalli, S. B. R.; and Frye, H. M.: Flight Demonstration of Higher Harmonic Control (HHC) on the S-76. Proceedings of the American Helicopter Society 42nd Annual Forum, June 1986, pp. 777-791.
53. Walsh, D.: Flight Test of an Open-Loop Higher Harmonic Control System on an S-76A Helicopter. Proceedings of the American Helicopter Society 42nd Annual Forum, June 1986, pp. 831-843.
54. Polychroniadis, M.; and Achache, M.: Higher Harmonic Control: Flight Test on an SA 349 Research Gazelle. Proceedings of the American Helicopter Society 42nd Annual Forum, June 1986, pp. 811-820.
55. Achache, M.; and Polychroniadis, M.: Development of an Experimental System for Active Control of Vibration on Helicopters—Development Methodology for an Airborne System. Vertica, vol. 11, nos. 1 and 2, 1987, pp. 123-138.
56. Jacklin, S. A.: Performance Comparison of Five Frequency Domain System Identification Techniques for Helicopter Higher Harmonic Control. Presented at the Second International Conference on Rotorcraft Basic Research, University of Maryland, College Park, Md., Feb. 1988.
57. Sangha, K. R.: Bearingless Rotors and Higher Harmonic Control Modeling Using RACAP. Proceedings of the American Helicopter Society 44th Annual Forum, June 1988, pp. 293-304.

58. Robinson, L. H.; and Friedmann, P. P.: Analytical Simulation of Higher Harmonic Control Using a New Aeroelastic Model. Proceedings of the AIAA/ASME/ASCE/AHS 30th Structures, Structural Dynamics and Material Conference, Paper No. 89-1321, Apr. 1989.
59. Dinyavari, M. A. H.: Application of the Finite-State Arbitrary Motion Aerodynamic to Rotor Blade Aeroelastic Response and Stability in Hover and Forward Flight. Proceedings of the AIAA/ASME/ASCE/AHS 26th Structures, Structural Dynamics and Material Conference, Paper No. 85-0763, Apr. 1985.
60. Fung, Y. C.: An Introduction to the Theory of Aeroelasticity. John Wiley and Sons, N.Y., 1955.
61. Blisplinghoff, R. L.; Ashley, H.; and Halfman, R. L.: Aeroelasticity. Addison-Wesley Publishing Company, Cambridge, Mass., 1955.
62. Du Val, R. W.; Gregory, C. Z.; and Gupta, N. K.: Design and Evaluation of a State-Feedback Vibration Controller. J. American Helicopter Society, vol. 29, no. 3, July 1984, pp. 30-37.
63. Du Val, R. W.; and Saberi, H.: Active Control of the RSRA/X-Wing Vehicle Using a Time-Domain Approach. Proceedings of the American Helicopter Society 44th Annual Forum, May 1988, pp. 221-230.
64. Wereley, N. M.; and Hall, S. R.: Linear Control Issues in the Higher Harmonic Control for Helicopter Vibrations. Proceedings of the American Helicopter Society 45th Annual Forum, May 1989, pp. 955-971.
65. Kretz, M.: Research in Multicyclic and Active Control of Rotary Wing. Proceedings of the First European Rotorcraft and Power-Lift Aircraft Forum, Sept. 1975.
66. Kretz, M.: Research on Multicyclic and Active Control of Rotor Wing. Vertica, vol. 1, 1976, pp. 95-105.
67. Kretz, M.; and Larché, M.: Future of Helicopter Rotor Control. Vertica, vol. 4, no. 1, 1980, pp. 13-22.
68. Weisbrich, A.L.; Perley, R.; and Howles, H.: Design Study of Feedback Control System for the Multicyclic Flap System Rotor. NASA CR-151960, Jan. 1977.
69. O'Leary, J.; and Miao, W.: Design of Higher Harmonic Control for the ABC. J. American Helicopter Society, vol. 27, no. 1, Jan. 1982, pp. 52-57.
70. Hanagud, S.; Meyyappa, S. S.; and Craig, J. I.: A Couple Rotor/Airframe Vibration Model with Higher Harmonic Control Effects. Proceedings of the American Helicopter Society 42nd Annual Forum, June 1986, pp. 821-829.
71. King, S. P.: The Minimisation of Helicopter Vibration through Blade Design and Active Control. Aeronautical J., Aug. 1988, pp. 247-263.
72. Johnson, W.: Recent Development in the Dynamics of Advanced Rotor Systems. NASA TM-86669, Mar. 1985.

73. Friedmann, P. P.: Recent Trends in Rotary-Wing Aeroelasticity. *Vertica*, vol. 11, nos. 1 and 2, 1987, pp. 139-170.
74. Langrebe, A. J.; and Davis, M.: Analysis of Potential Helicopter Vibration Reduction Concept. Proceedings of the AHS/NASA Ames Research Center Second Decennial Specialists Meeting on Rotorcraft Dynamics, Nov. 1984.
75. Strehlow, H.; Mehlhose, R.; and Obermayer, M.: Active Helicopter Rotor-Isolation with Application of Multi-Variable Feedback Control. Proceedings of the Third European Rotorcraft and Powered-Lift Aircraft Forum, 1977.
76. Kuezynski, W. A.; and Madden, J.: The RSRA Active Isolation/Rotor Balance System. *J. American Helicopter Society*, vol. 25, no. 2, Apr. 1980, pp. 17-25.
77. Nguyen, K. Q.; and Chopra, I.: Actuation Power Requirement for Higher Harmonic Control (HHC) Systems. Presented at the Second International Conference on Rotorcraft Basic Research, University of Maryland, College Park, Md., Feb. 1988.
78. Nguyen, K. Q.; and Chopra, I.: Application of Higher Harmonic Control (HHC) to Hingeless Rotor Systems. Proceedings of the AIAA/ASME/ASCE/AHS 30th Structures, Structural Dynamics and Material Conference, Paper No. 89-1215, Apr. 1989.
79. Nguyen, K.; and Chopra, I.: Application of Higher Harmonic Control (HHC) to Rotors Operating at High Speed and Maneuvering Flight. Proceedings of the American Helicopter Society 45th Annual Forum, May 1989, pp. 81-96.
80. Panda, B.; and Chopra, I.: Dynamics of Composites Rotor Blades in Forward Flight. *Vertica*, vol. 11, nos. 1 and 2, Jan. 1987, pp. 187-211.
81. Leishman, J. G.; and Beddoes, T. S.: A Generalized Model for Unsteady Aerodynamic Behavior and Dynamic Stall Using the Indicial Method. Proceedings of the American Helicopter Society 42nd Annual Forum, June 1986, pp. 243-265.
82. Leishman, J. G.: Validation of Approximate Indicial Aerodynamic Functions for Two-Dimensional Subsonic Flow. *J. Aircraft*, vol. 25, no. 19, Oct. 1988, pp. 914-922.
83. Johnson, W.: A Comprehensive Analytical Model of Rotor Aerodynamics and Dynamics, Part I: Analysis and Development. NASA TM-81182, June 1980.
84. Hodges, D. H.; and Dowell, E. H.: Nonlinear Equations of Motion for the Elastic Bending and Torsion of Twisted Nonuniform Rotor Blades. NASA TN D-7818, Dec. 1984.
85. Lanczos, C.: *The Variational Principles of Mechanics*. Dover Publications, Inc., N.Y., 1970.
86. Leishman, J. G.; and Crouse, G. L.: A State-Space Model of Unsteady Aerodynamics for Flutter Analysis in a Compressible Flow. Proceedings of the 27th Aerospace Sciences Meeting, Paper No. 89-0022, Jan. 1989.
87. Leishman, J. G.: An Analytical Model for Unsteady Drag. *AIAA J. Aircraft*, vol. 25, no. 7, July 1988, pp. 665-666.

88. Gormont, R.: A Mathematical Model of Unsteady Aerodynamics and Radial Flow for Application of Helicopter Rotors. U.S. Army Air Mobility Research and Development Laboratory, TR-72-67, May 1973.
89. Incompressible Aerodynamics. Thwaites, B., ed., Dover Publications, Inc., New York, 1987.
90. Bramwell, A. R. S.: Helicopter Dynamics. Edward Arnold Ltd., London, 1976.
91. Johnson, W.: Helicopter Theory. Princeton University Press, Princeton, N.J., 1980.
92. Castles, W.; and De Leeuw, J. H.: The Normal Component of the Induced Velocity in the Vicinity of a Lifting Rotor and Some Examples of Its Application. NACA Report 1184, 1954.
93. Egolf, T. A.; and Massar, J. L.: Helicopter Free Wake Implementation on Advanced Computer Architecture. presented at the Second International Conference on Rotorcraft Basic Research, University of Maryland, College Park, Md., Feb. 1987.
94. Bir, G. S.; and Chopra, I.: Gust Response of Hingeless Rotors. J. American Helicopter Society, vol. 31, no. 2, Apr. 1986, pp. 33-46.
95. Panda, B.; and Chopra, I.: Flap-Lag-Torsion Stability in Forward Flight. J. American Helicopter Society, vol. 30, no. 4, Oct. 1985, pp. 30-39.
96. Dennis, J. E.; and Schnabel, R. B.: Numerical Methods for Unconstrained Optimization and Non-linear Equations. Prentice Hall, Englewood Cliffs, N.J., 1983.
97. Biggers, J. C.; and McCloud, J. L. III: A Notes on Multicyclic Control by Swashplate Oscillation. NASA TM-78475, June 1980.
98. Warring, R. H.: Hydraulic Handbook. Gulf Publishing Company, Houston, Tex., 1983.
99. Stepniewski, W. Z.; and Keys, C. N.: Rotary-Wing Aerodynamics. Dover Publications Inc., N.Y., 1984.

Table 3.1. Rotor and blade properties

Element	$\frac{EI_y}{m_0\Omega^2 R^4}$	$\frac{EI_z}{m_0\Omega^2 R^4}$	$\frac{GJ}{m_0\Omega^2 R^4}$	$\frac{m}{m_0}$	$\frac{k_m^2 \cdot 10^3}{R^2}$	$\frac{x_I}{c}$	$\frac{l}{R}$
1	0.002596	0.07536	0.001331	1.0000	0.3312	0.03226	0.1500
2	0.003326	0.07782	0.002538	0.8199	0.2779	0.02268	0.1500
3	0.003744	0.08020	0.002546	0.8807	0.2728	0.03194	0.2000
4	0.003966	0.08020	0.002578	1.2065	0.2528	0.04616	0.2200
5	0.006306	0.05961	0.003470	0.9938	0.1269	0.01694	0.1352
6	0.016667	0.01785	0.014480	4.5808	0.2433	0.00385	0.1162

Blade number, N	3
Blade radius, R	5.23 ft
Rotor rotational speed, Ω	22.226 Hz
Reference blade mass per unit length, m_0	0.0322 lb/in.
Chord length/radius, c/R	0.07446
Solidity ratio, σ	0.0711
Pitch-link stiffness, $K_p/m_0\Omega^2 R^3$	0.015165
Flap hinge offset	0.0286 R
Lag hinge offset	0.1448 R
Root cut-out	0.21 R
Blade linear pretwist, θ_{tw}	-14 deg
Lock number, $\gamma = 3\rho c R c_{l_\alpha}/m_0$	6.8468
Lift curve slope, c_{l_α} at $M = 0.3$, per radian	6.1306
Viscous drag coefficient, c_{d_0}	0.0085
Leading edge suction recovery factor, η	0.97
Pitching moment coefficient at zero angle of attack, c_{m_0}	-0.005
Hover tip Mach number	0.6415

Table 3.2. Blade natural frequencies

Mode	Blade natural frequency, per rev
Rigid lag	0.504
Rigid flap	1.023
First elastic flap	2.660
Rigid torsion	4.865
Second elastic flap	5.210
First elastic lag	6.391
Third elastic flap	8.918
First elastic torsion	11.439

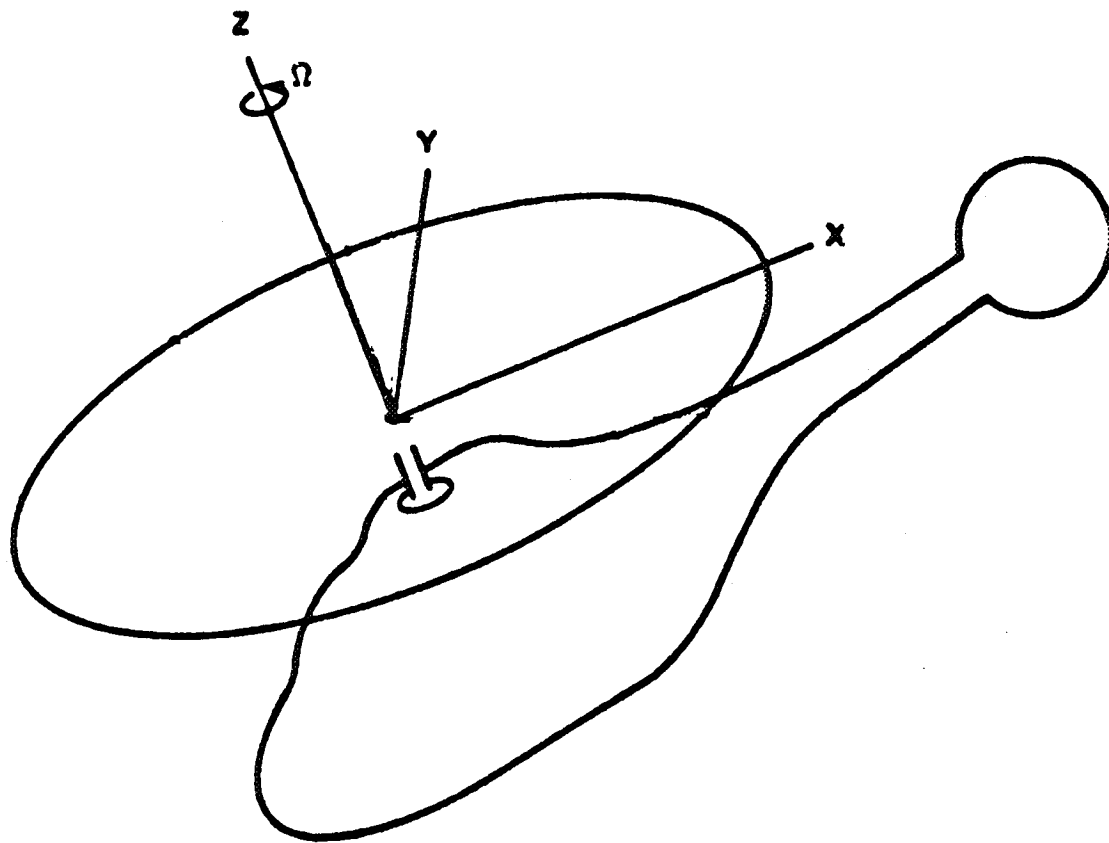


Figure 2.1. Rotor coordinate system—hub-fixed frame.

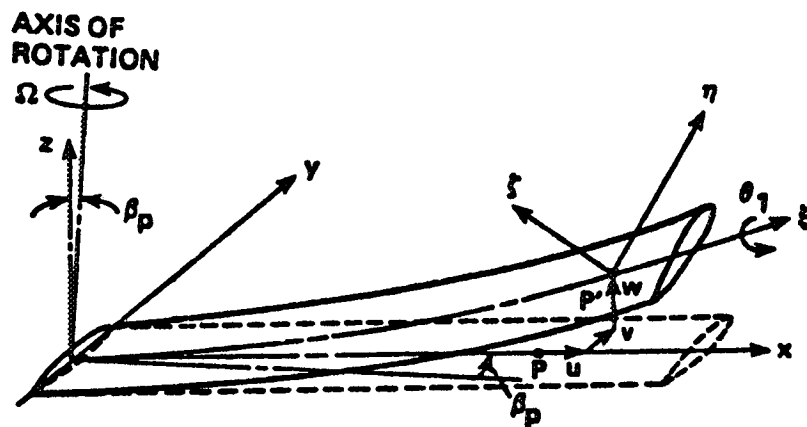


Figure 2.2. Blade coordinate system and deformations.

0-2.

Figure 2.4. Trailing edge separation point—Kirchhoff's flow model.

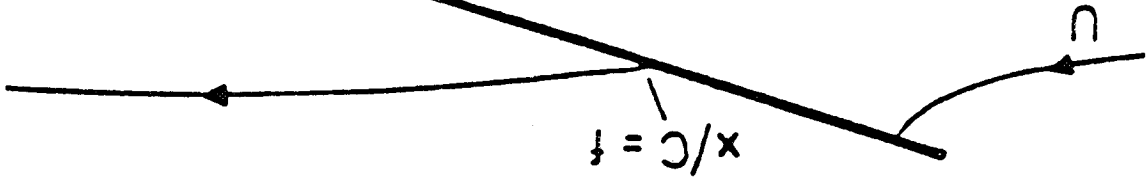
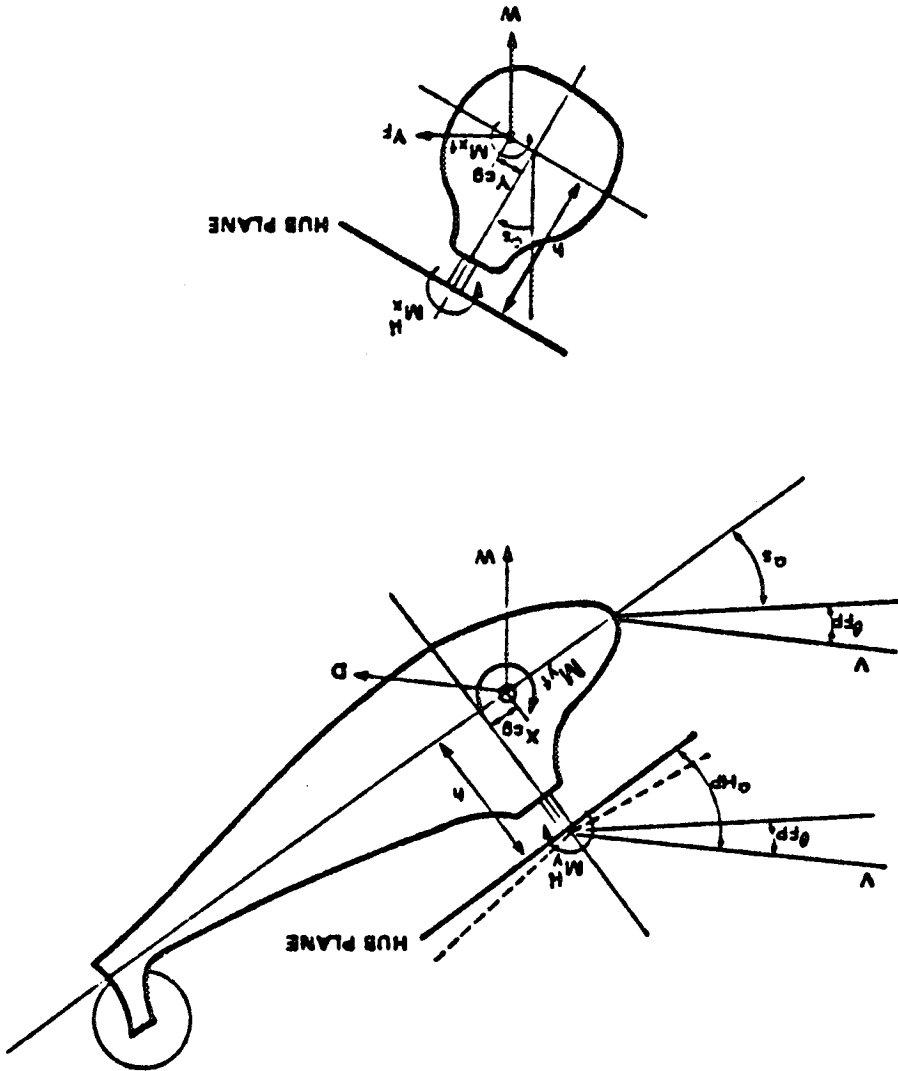


Figure 2.3. Trim configuration for helicopter in forward flight.



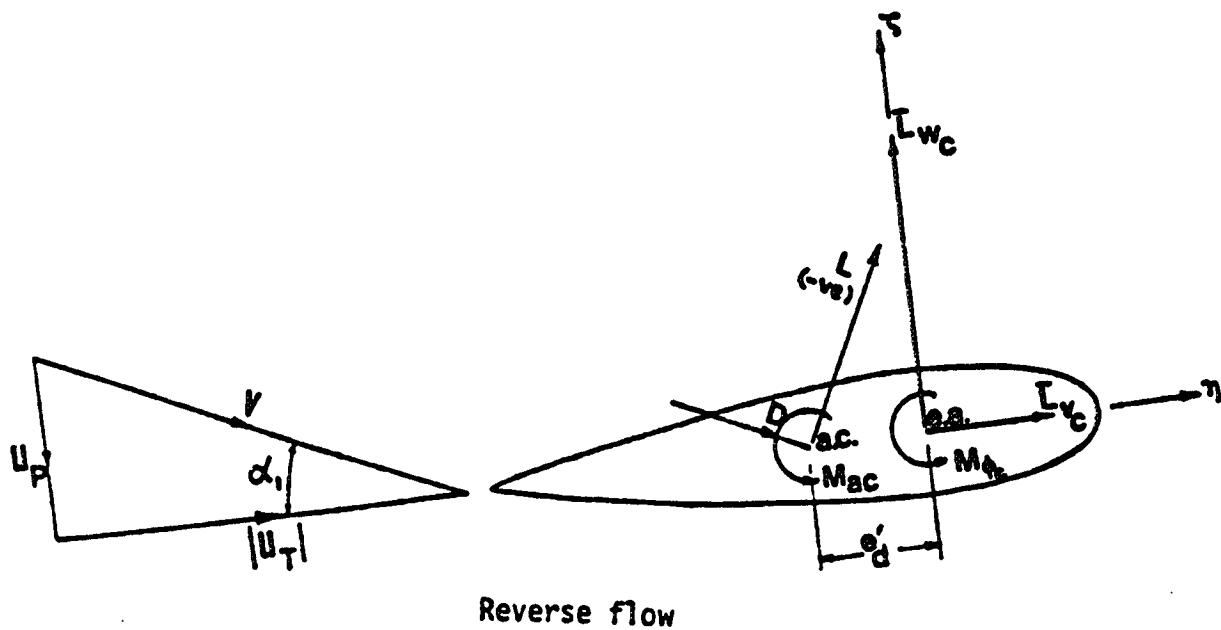
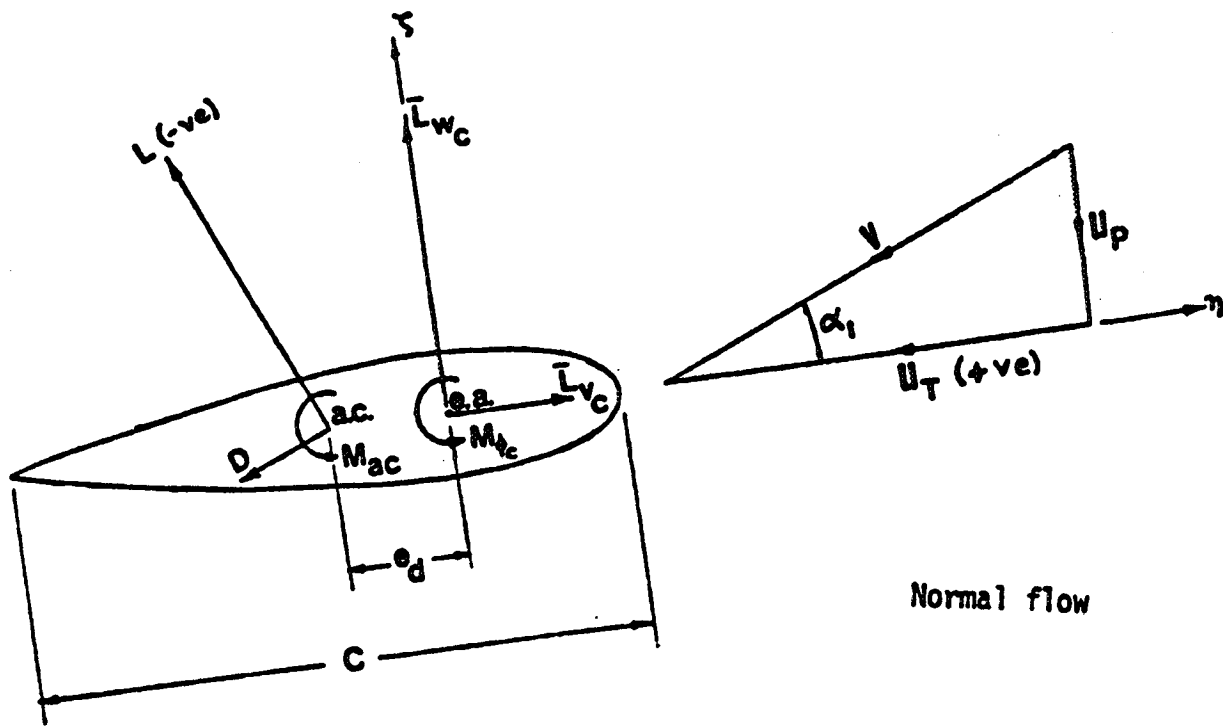


Figure 2.5. Blade section aerodynamic environment.

Blade spanwise lift distribution,
continuous and discrete

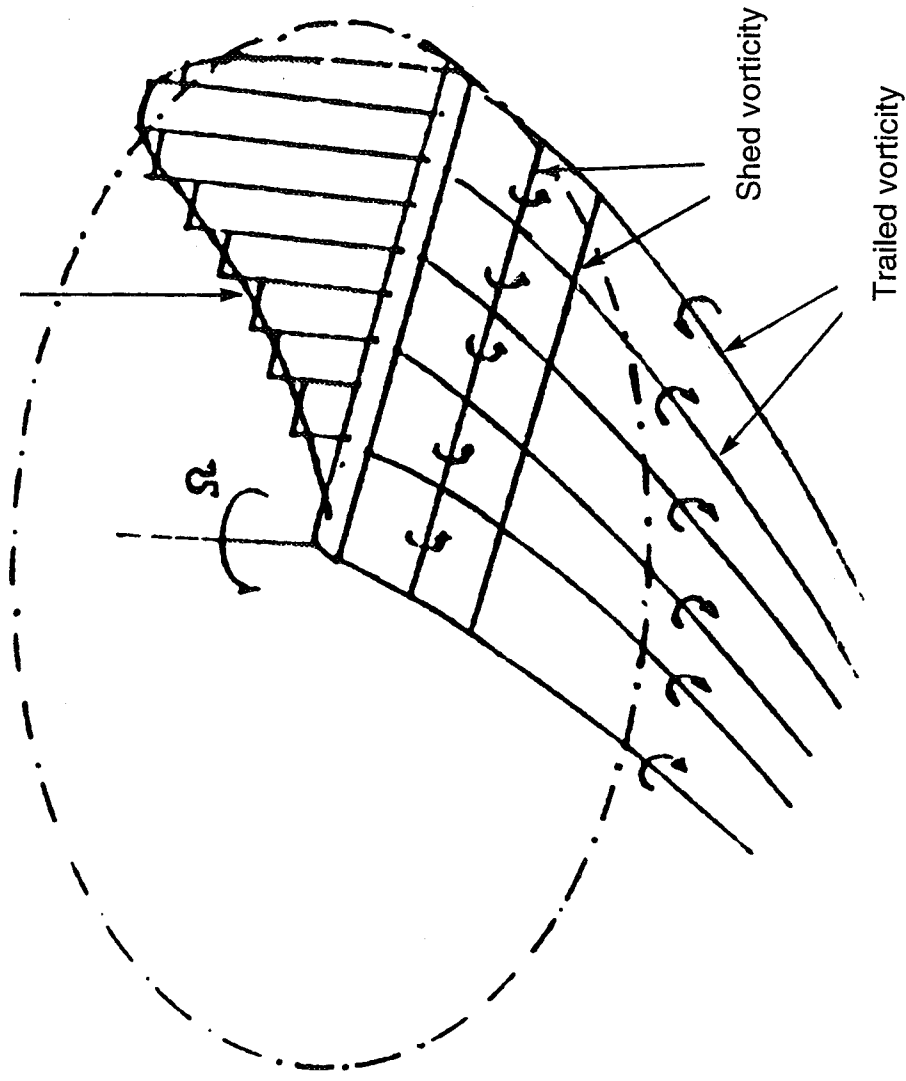


Figure 2.6. Vortex system from a rotor blade (adapted from ref. 90).

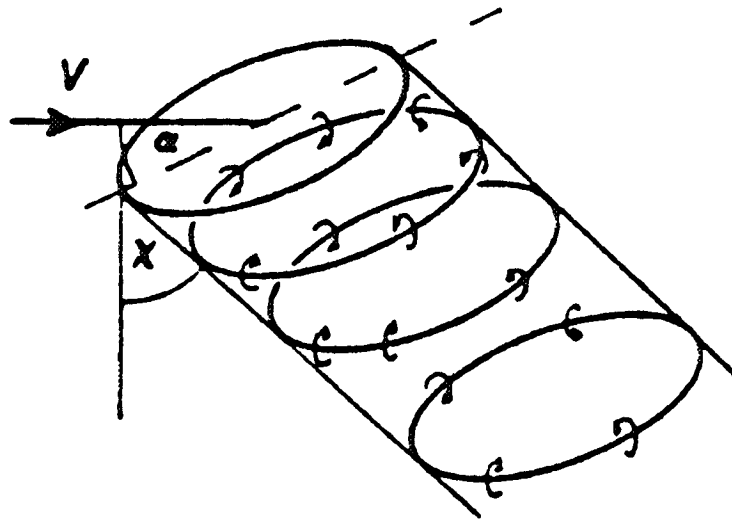
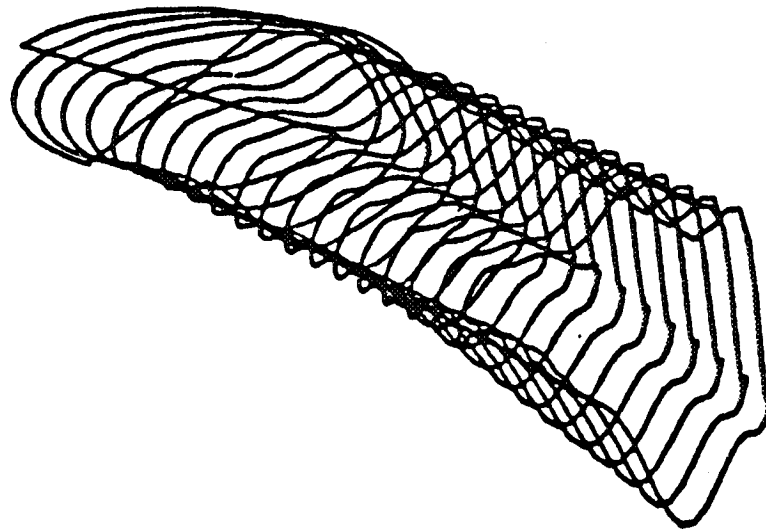


Figure 2.7. Rotor wake in forward flight (top, adapted from ref. 93) and vortex ring representation (bottom, adapted from ref. 90).

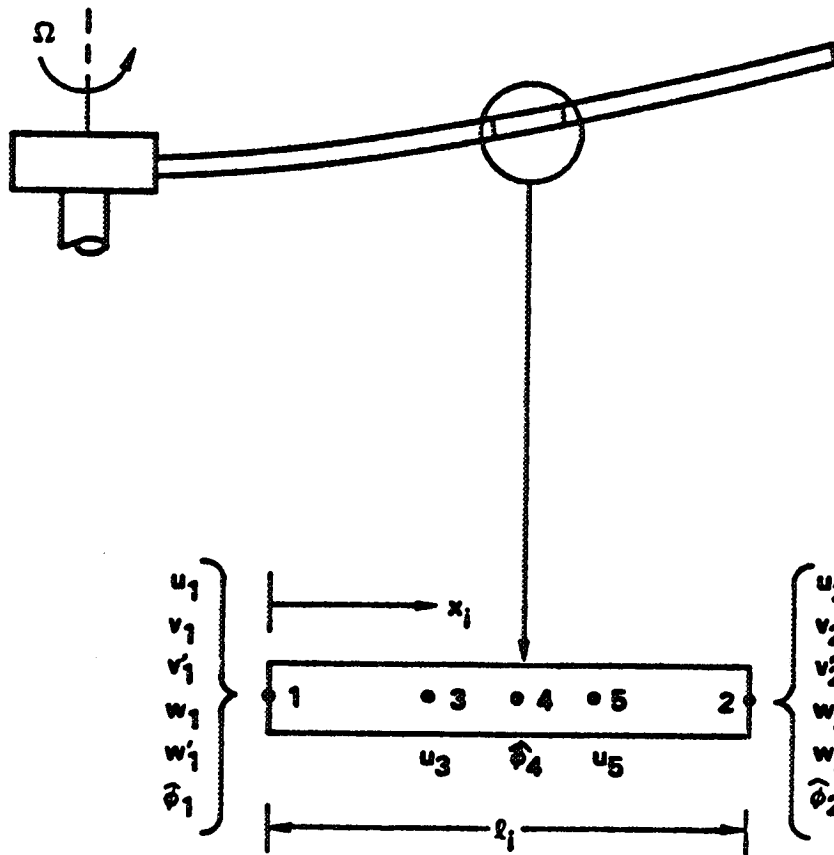


Figure 2.8. Finite element model of a rotor blade.

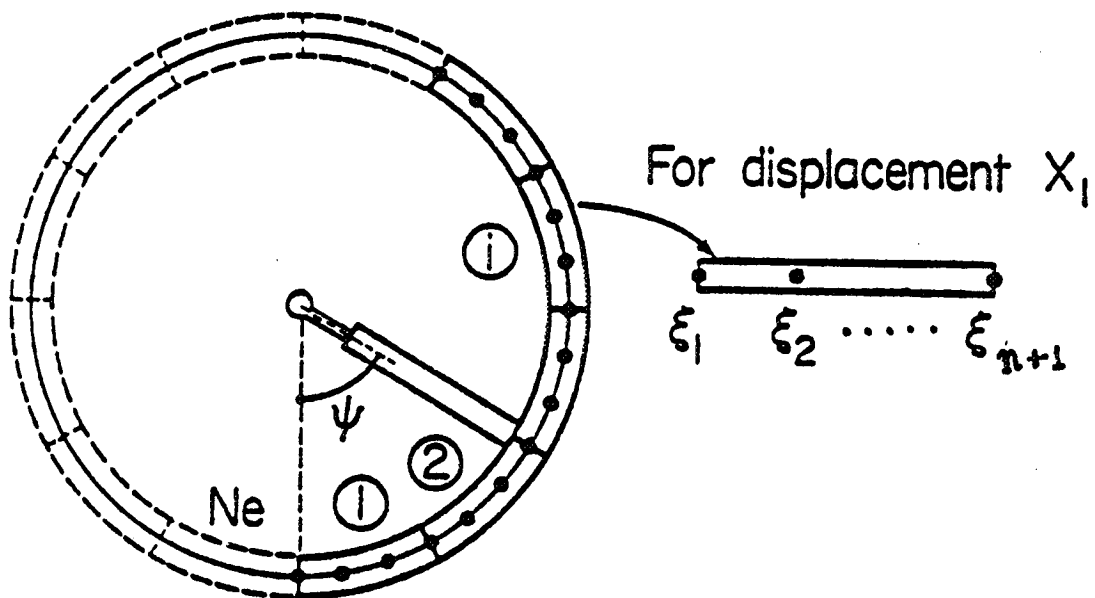


Figure 2.9. Temporal finite element discretization of the rotor revolution.

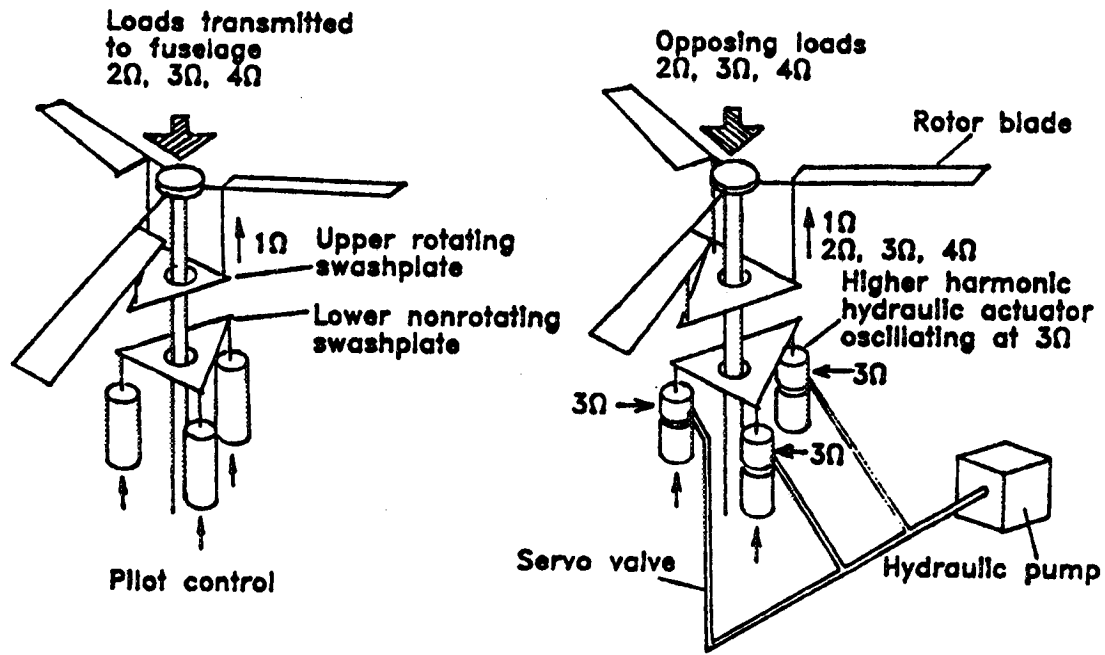


Figure 2.10. HHC actuator system on a three-bladed rotor system.

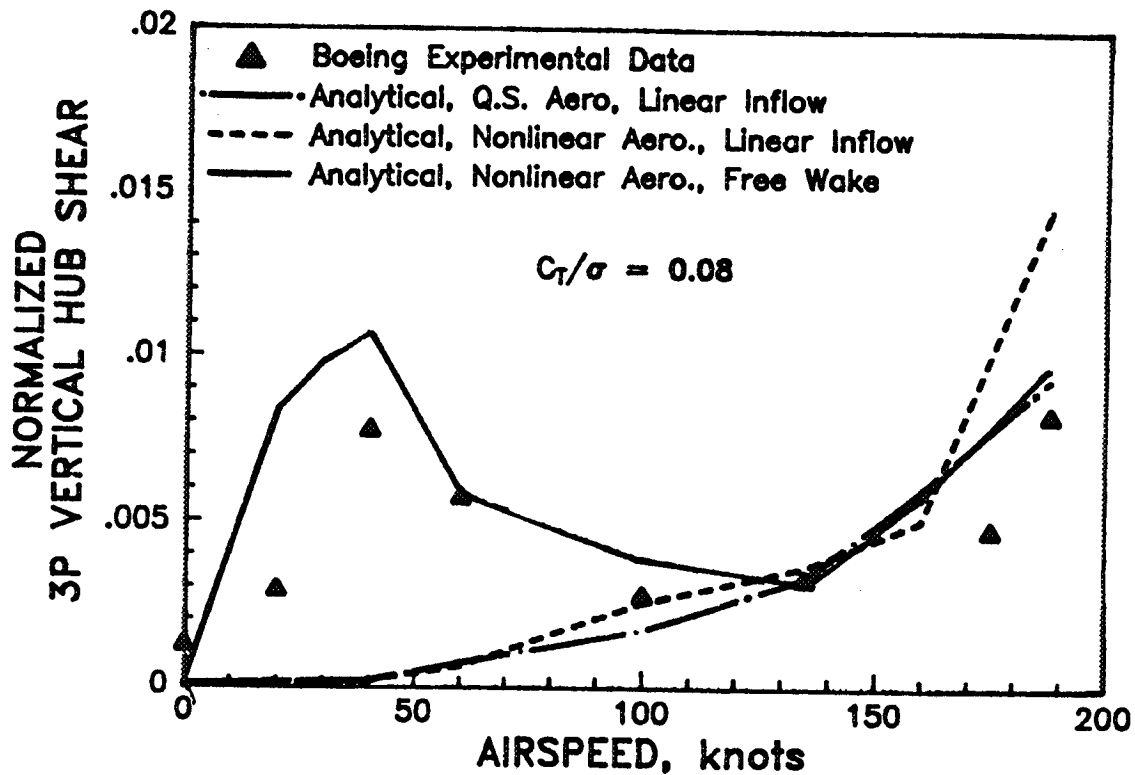


Figure 3.1. Correlation of 3P vertical hub shear—variation with forward speed ($C_T/\sigma = 0.08$).

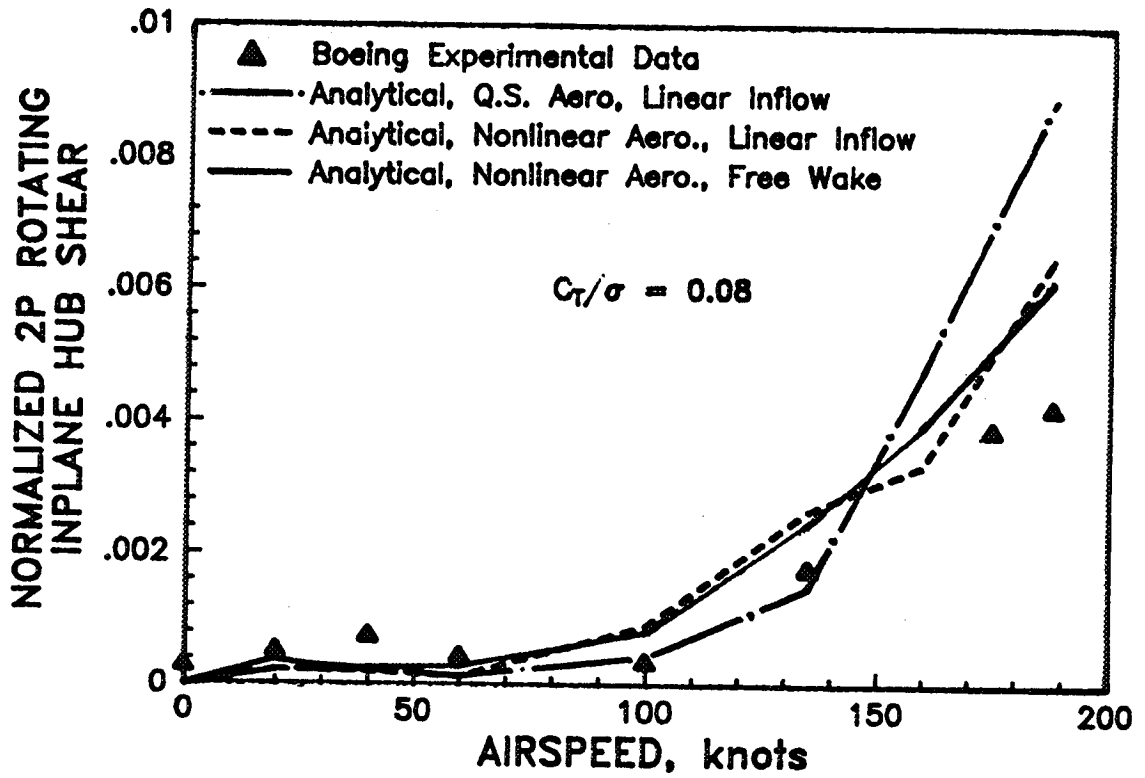


Figure 3.2. Correlation of 2P rotating inplane hub shear—variation with forward speed ($C_T/\sigma = 0.08$).

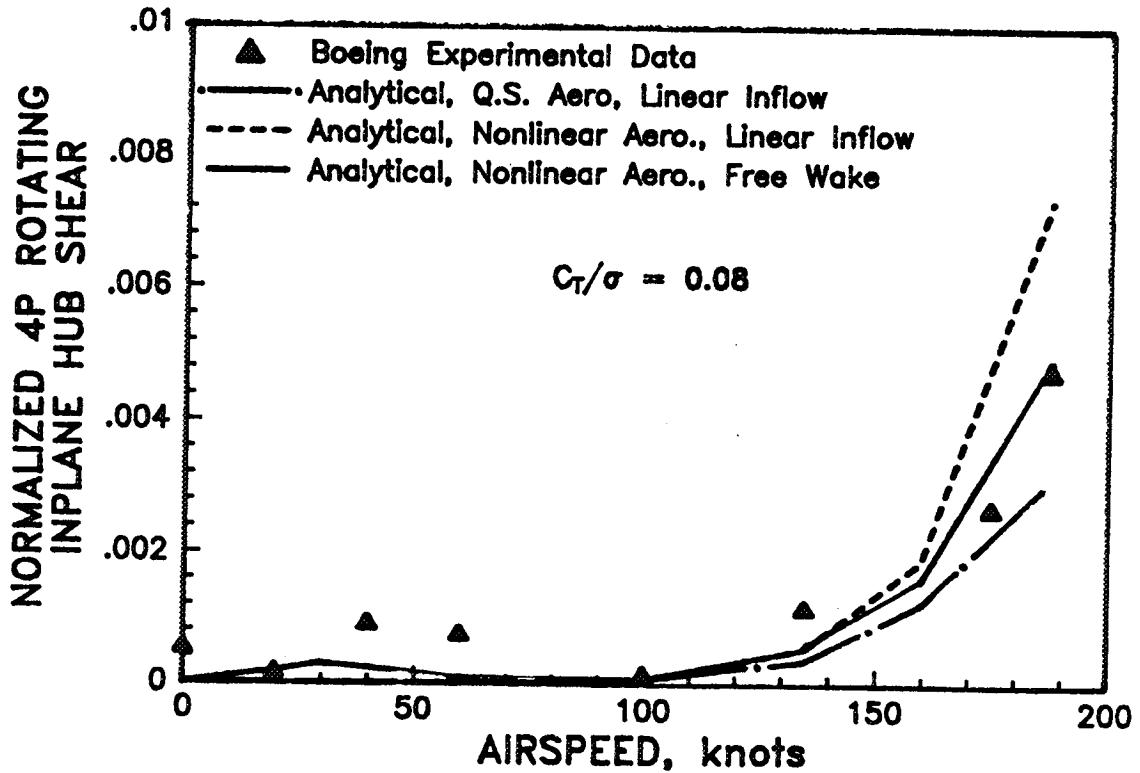


Figure 3.3. Correlation of 4P rotating inplane hub shear—variation with forward speed ($C_T/\sigma = 0.08$).

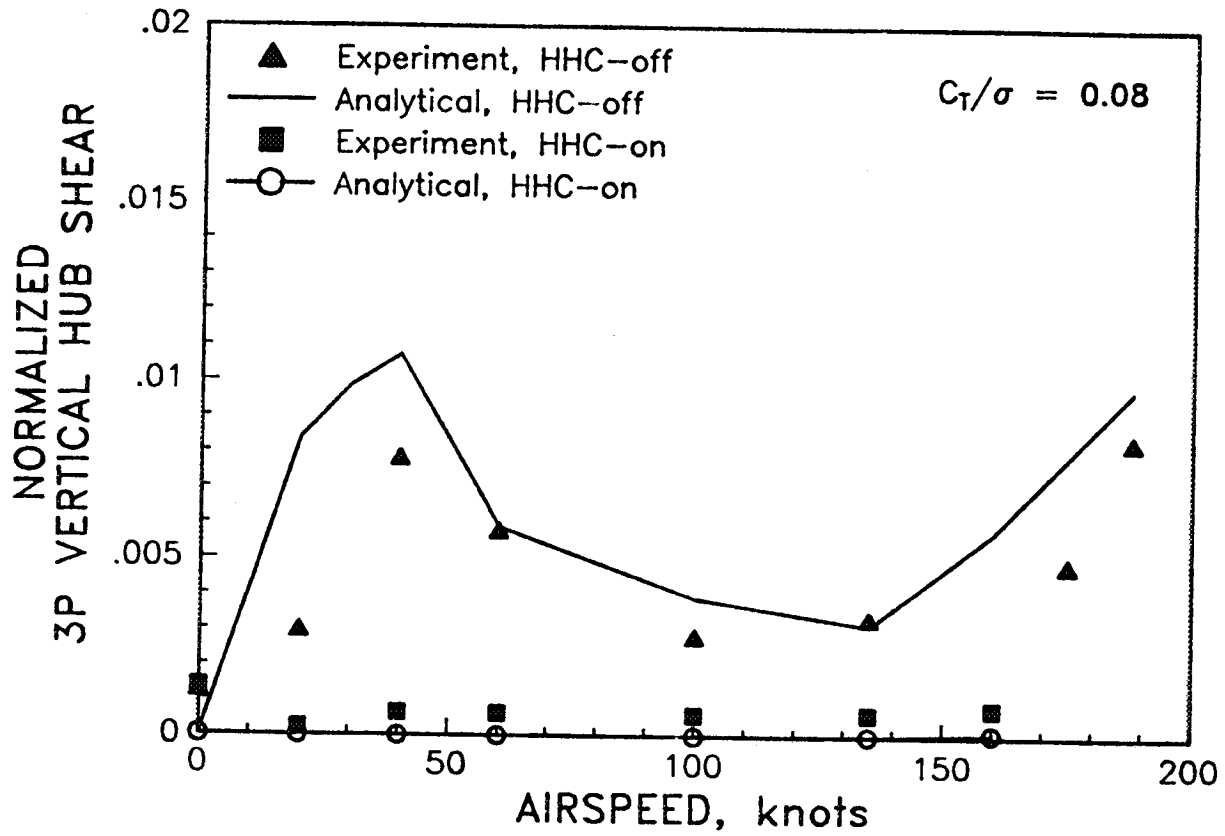


Figure 3.4. HHC suppression of 3P vertical hub shear ($C_T/\sigma = 0.08$).

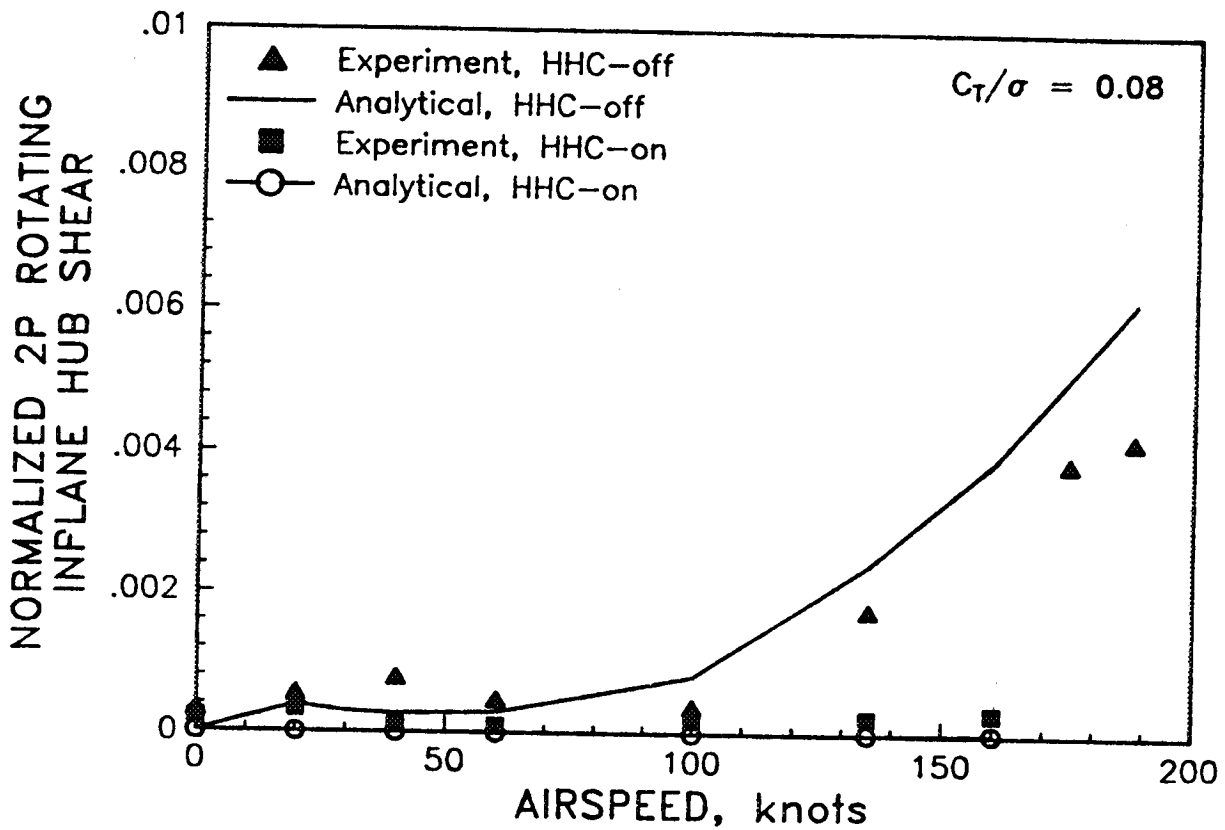


Figure 3.5. HHC suppression of 2P rotating inplane hub shear ($C_T/\sigma = 0.08$).

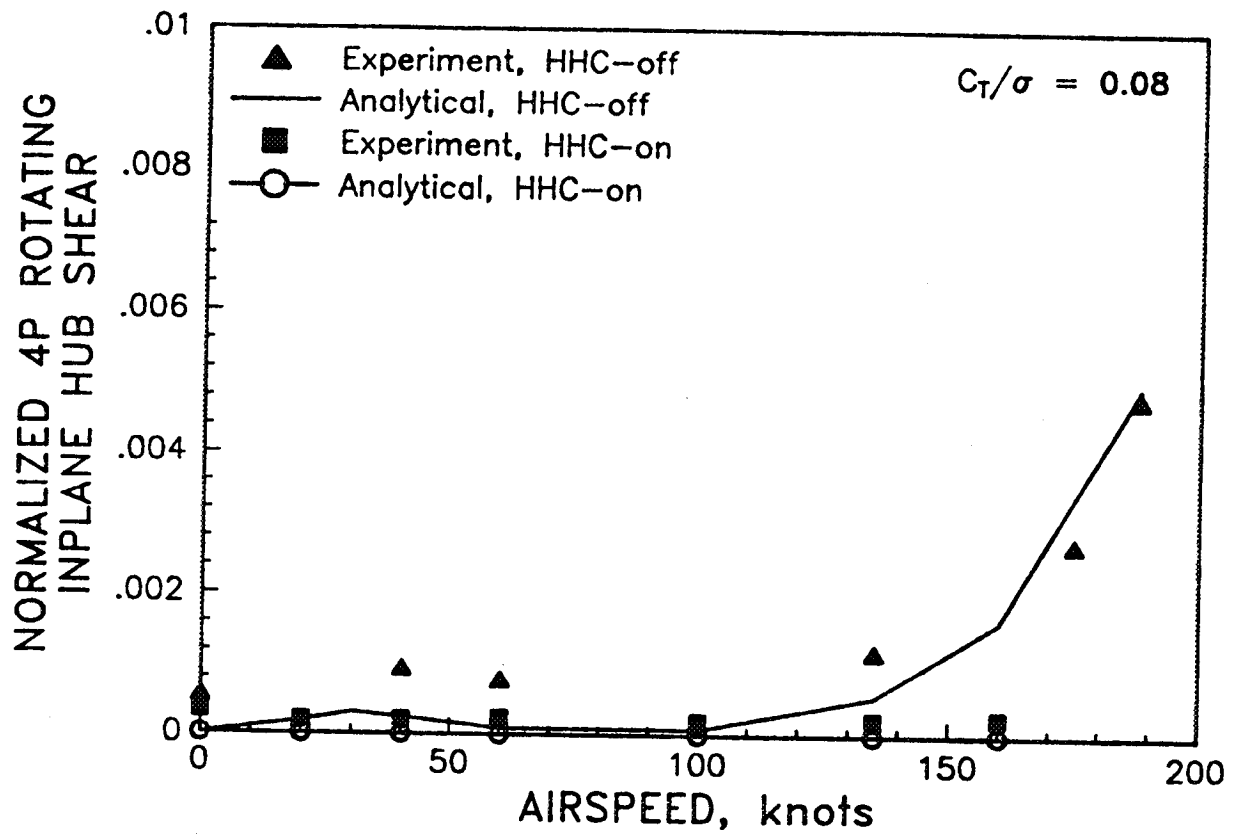


Figure 3.6. HHC suppression of 4P rotating inplane hub shear ($C_T/\sigma = 0.08$).

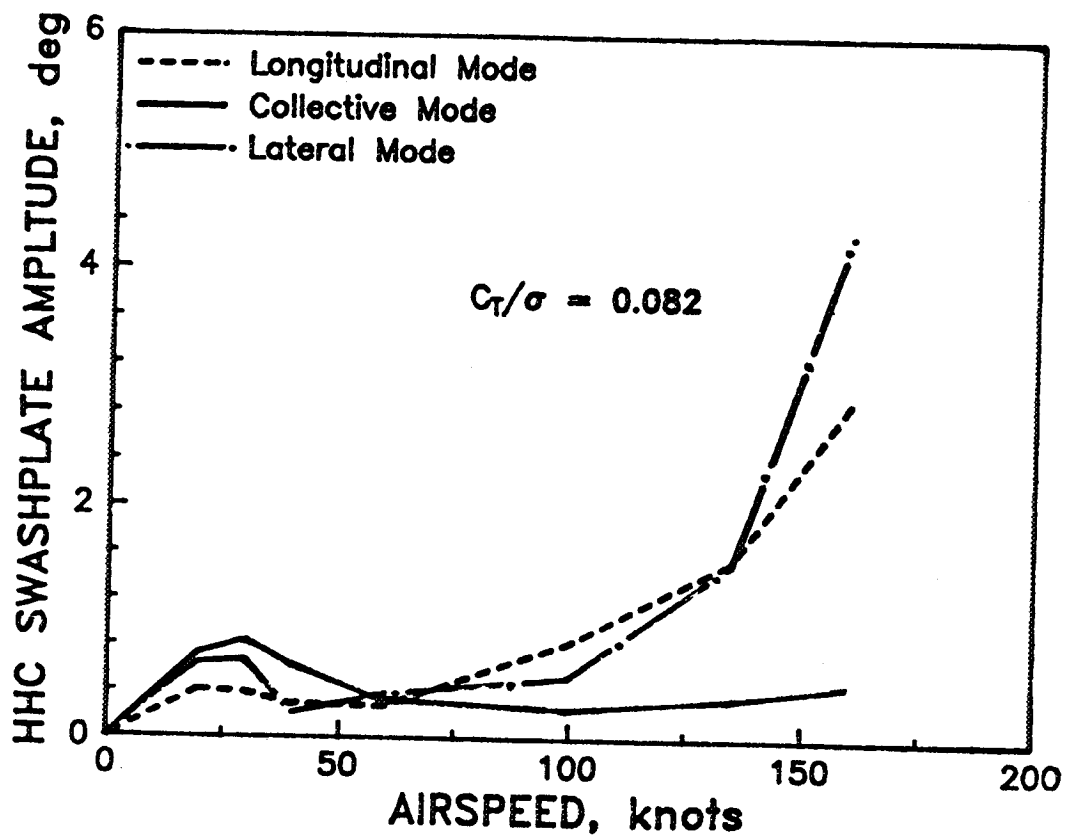


Figure 3.7. Variation of HHC swashplate amplitudes with forward speed ($C_T/\sigma = 0.08$).

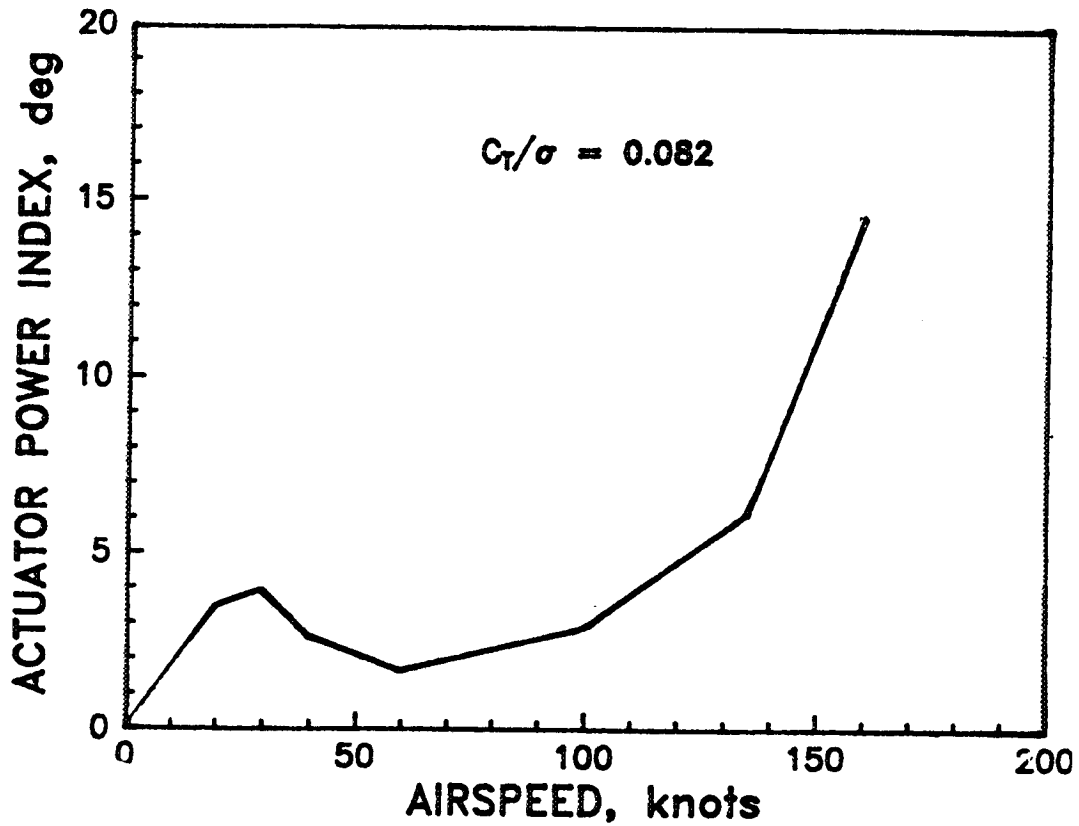


Figure 3.8. Variation of actuator power index with forward speed ($C_T/\sigma = 0.08$).

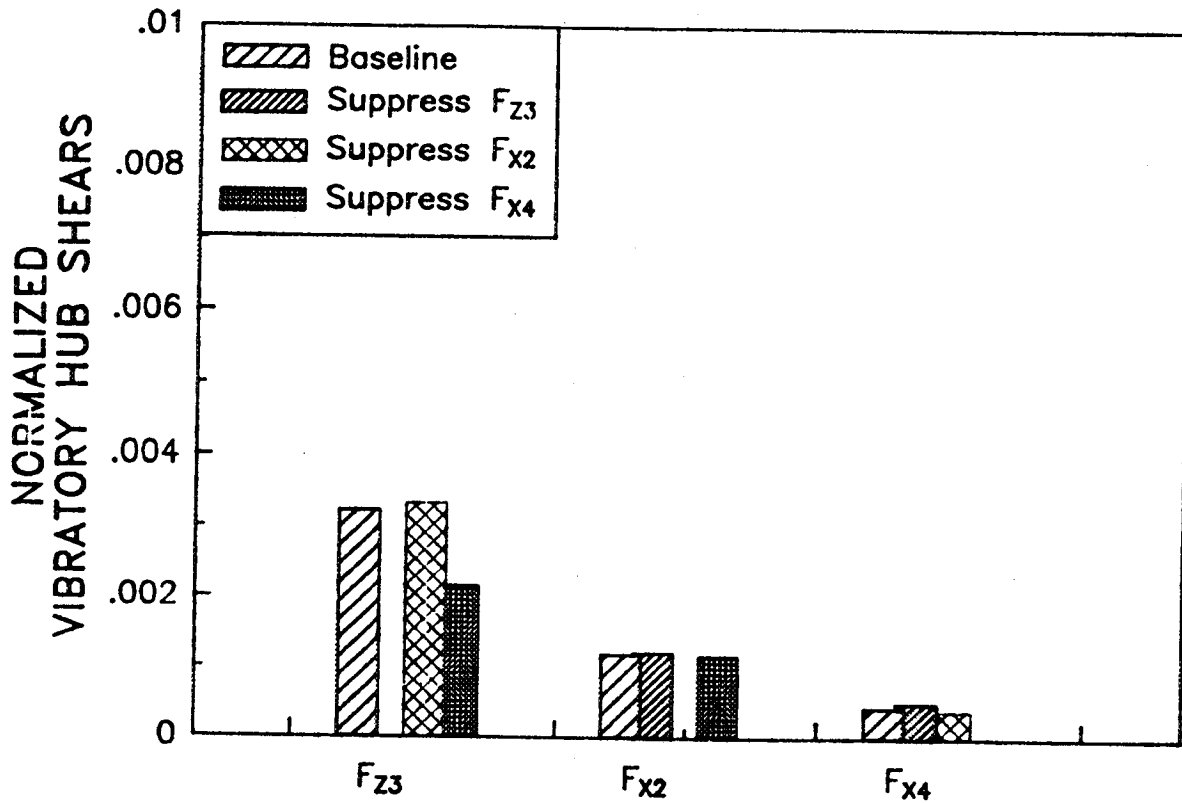


Figure 3.9. Effects of closed-loop HHC controller on the suppression of individual vibratory hub shear components ($V = 135$ knots, $C_T/\sigma = 0.08$).

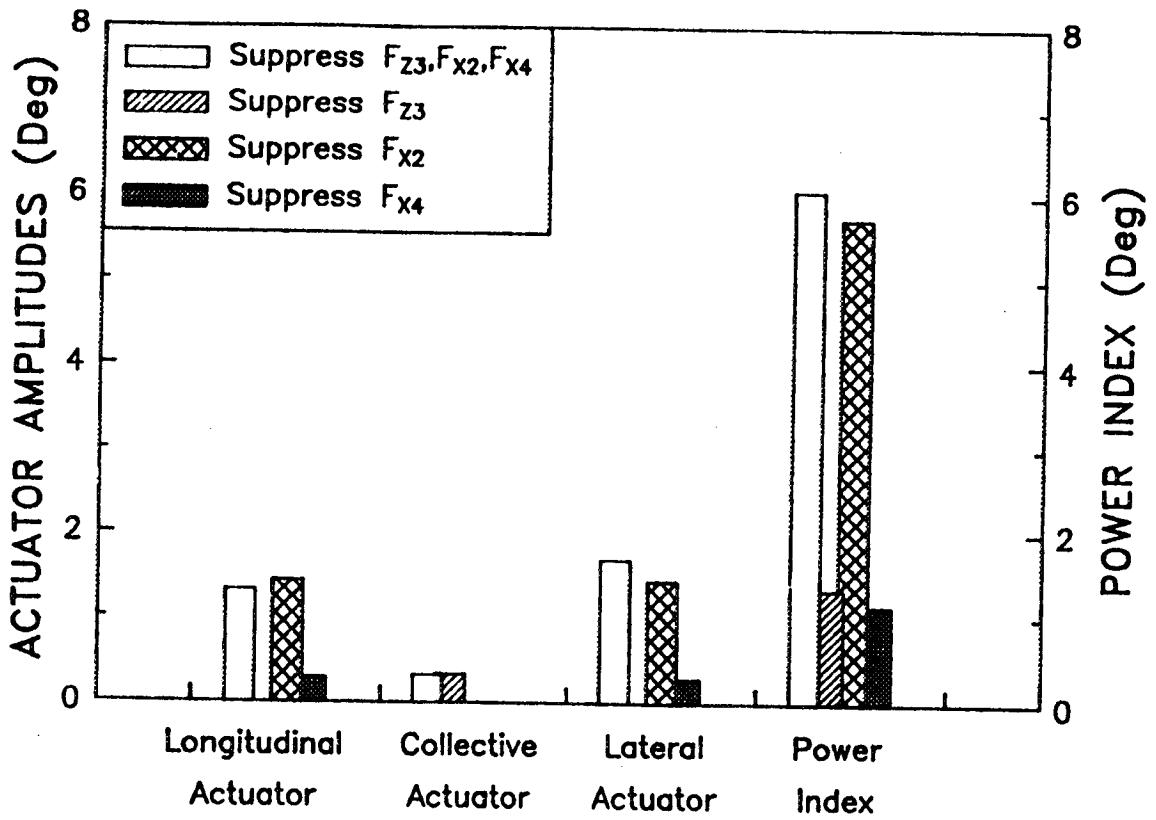


Figure 3.10. Actuator amplitudes and power required for the suppression of individual components of vibratory hub shear ($V = 135$ knots, $C_T/\sigma = 0.08$).

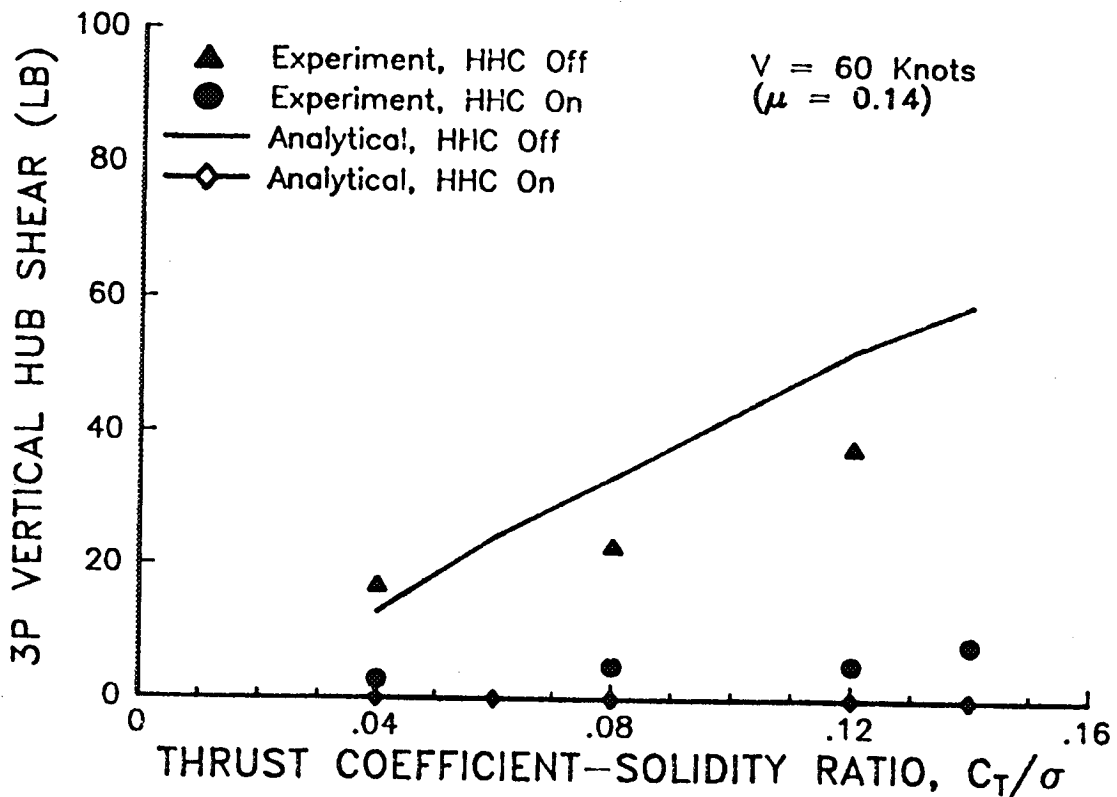


Figure 3.11. Correlation of 3P vertical hub shear with and without HHC effects—variation with rotor thrust ($V = 60$ knots).

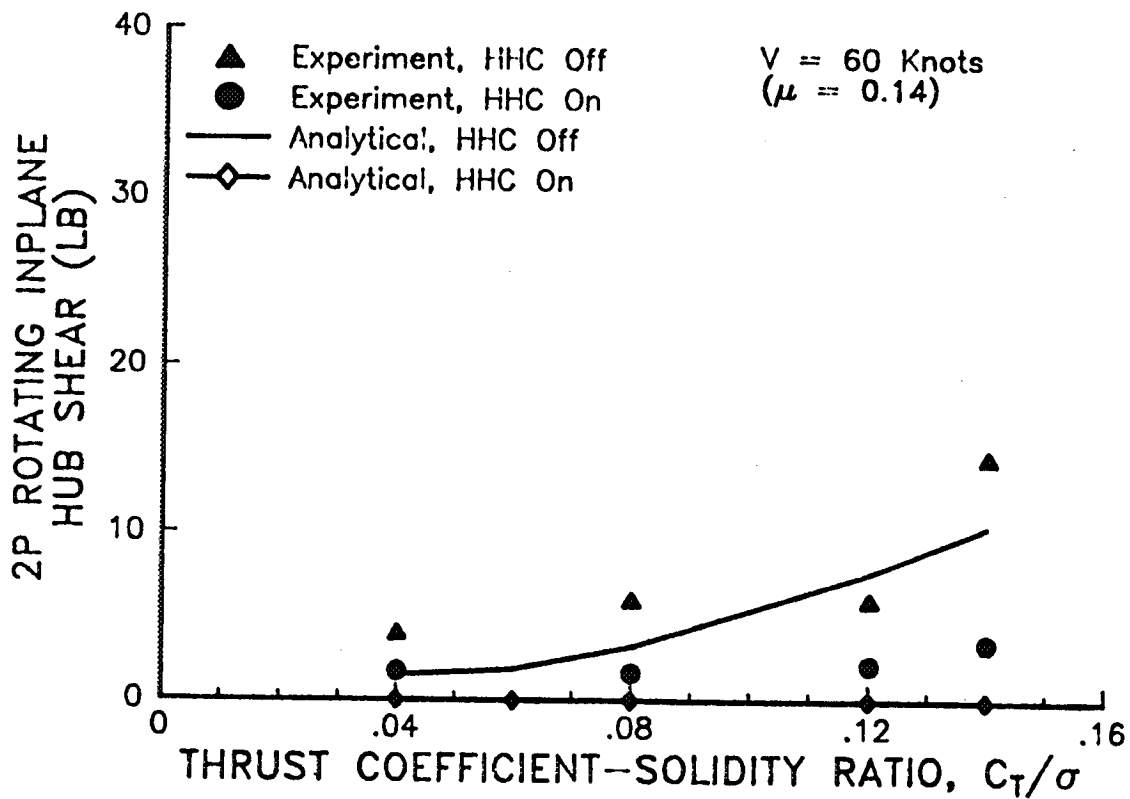


Figure 3.12. Correlation of 2P rotating inplane hub shear with and without HHC effects—variation with rotor thrust ($V = 60$ knots).

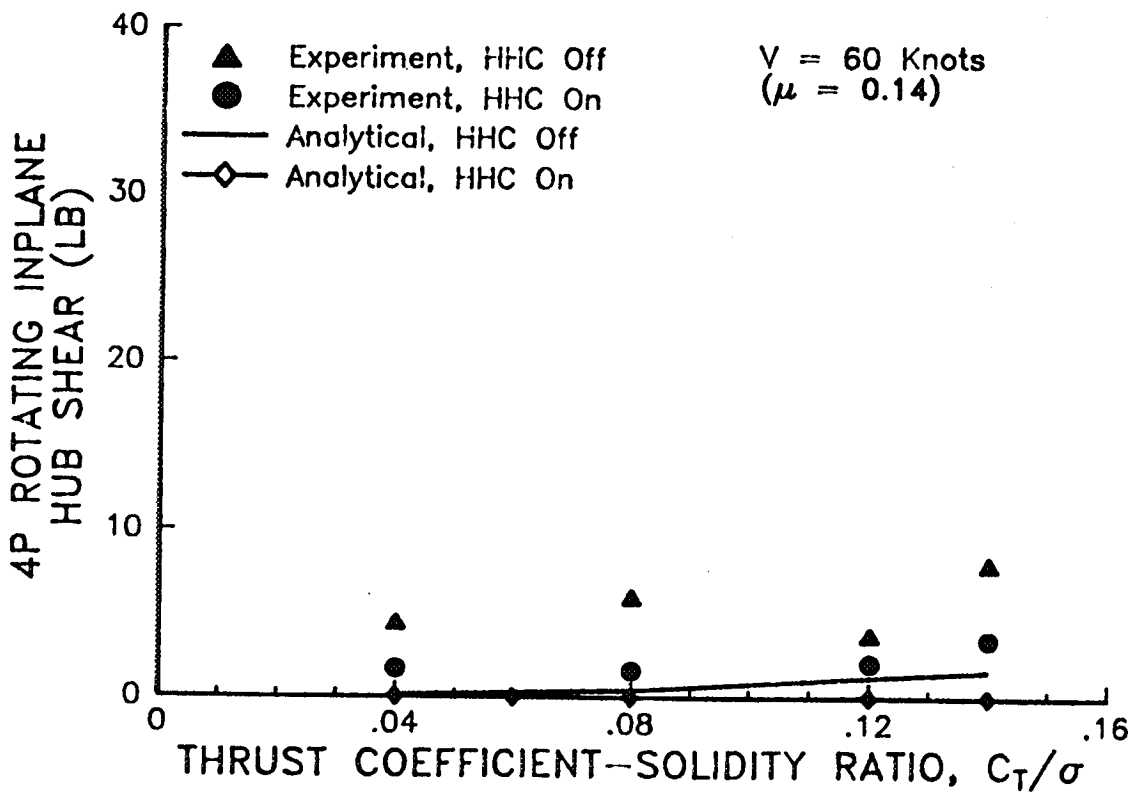


Figure 3.13. Correlation of 4P rotating inplane hub shear with and without HHC effects—variation with rotor thrust ($V = 60$ knots).

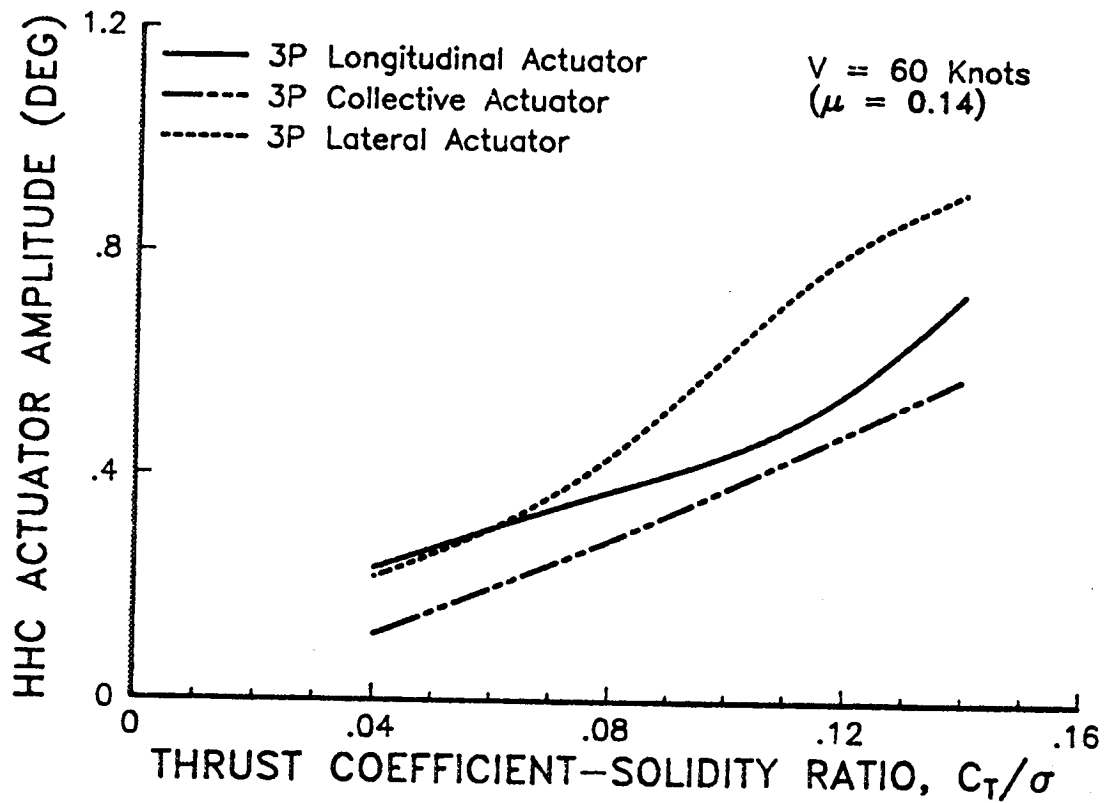


Figure 3.14. Variation of actuator amplitudes with thrust level ($V = 60$ knots).

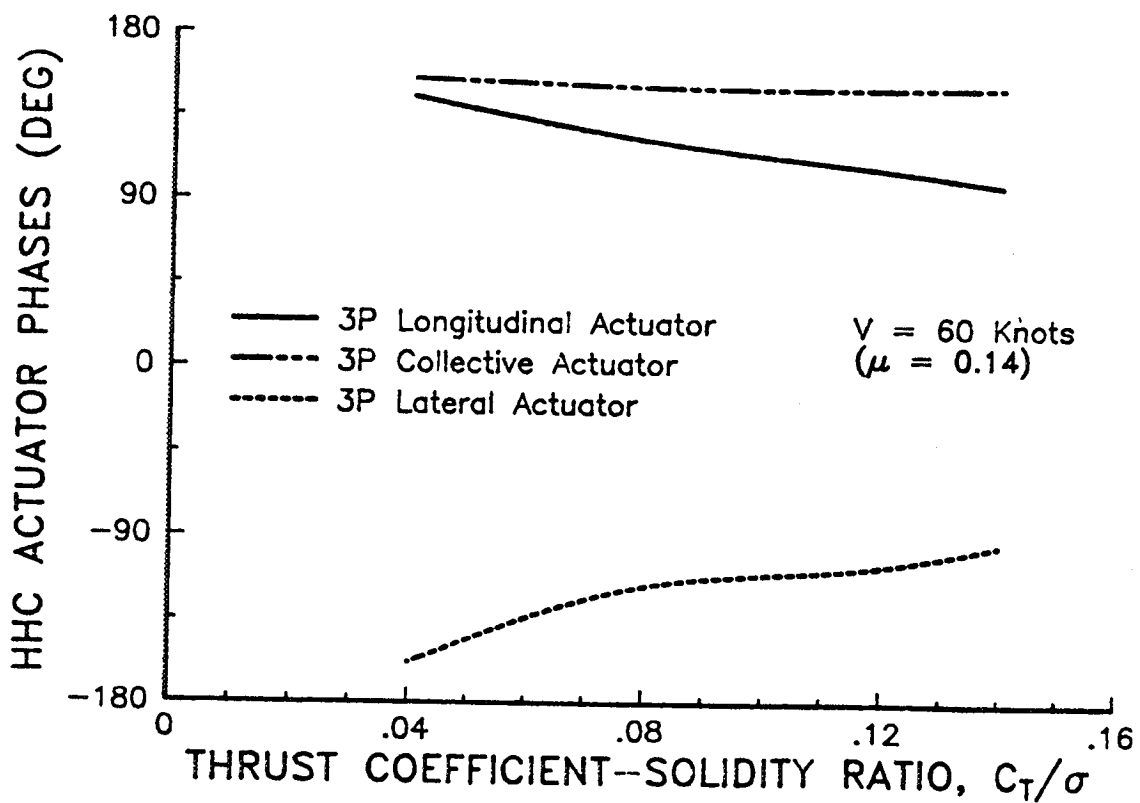


Figure 3.15. Variation of actuator phase angle with thrust level ($V = 60$ knots).

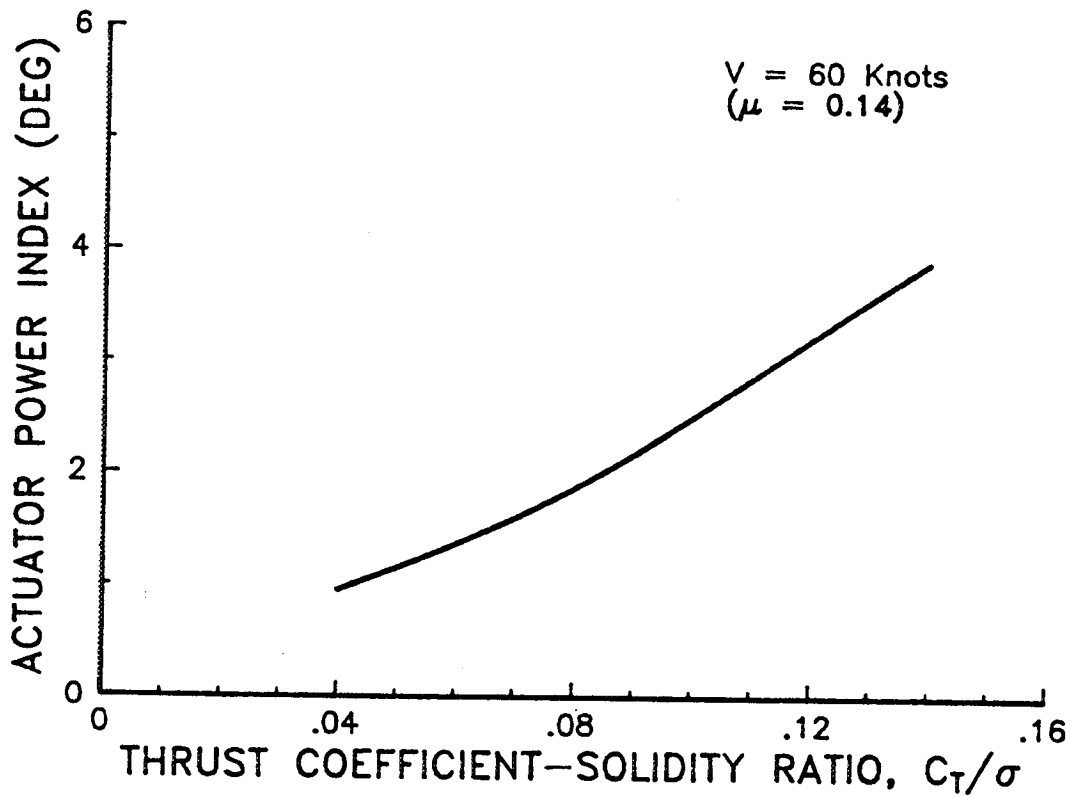


Figure 3.16. Variation of actuator power index with thrust level ($V = 60$ knots).

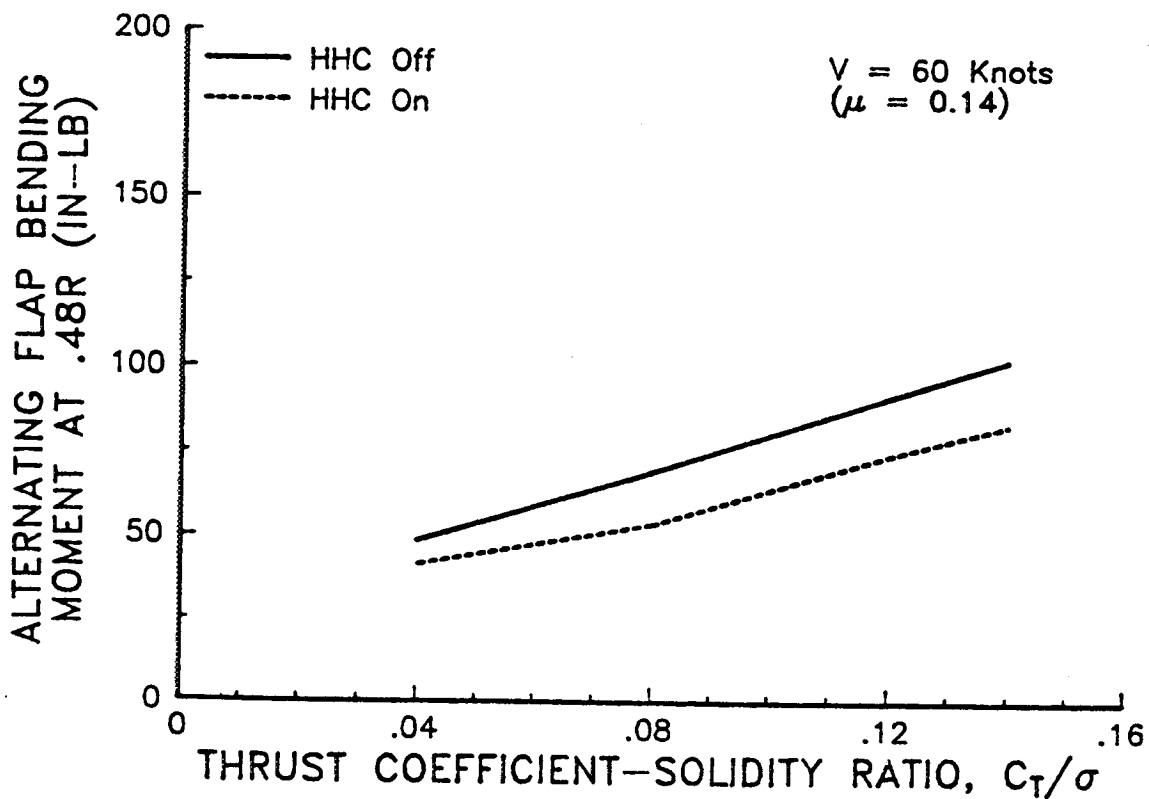


Figure 3.17. HHC effects on the alternating flap bending moment ($V = 60$ knots).

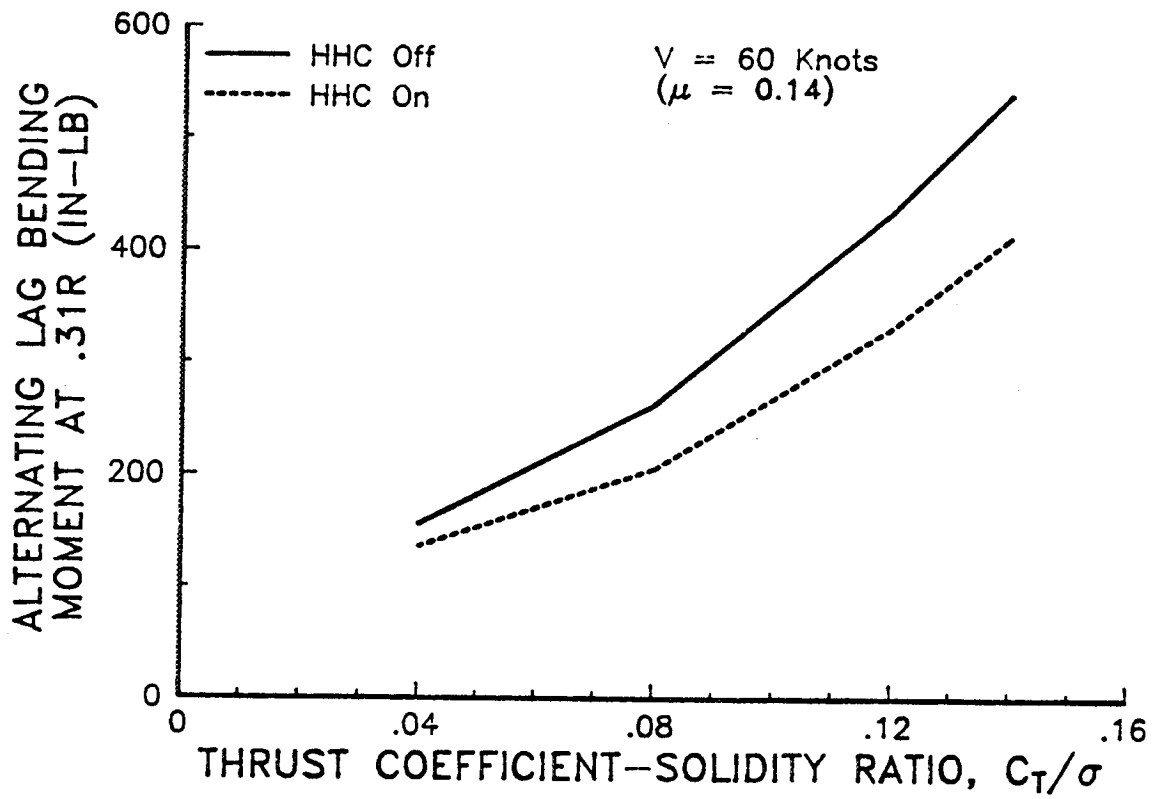


Figure 3.18. HHC effects on the alternating lag bending moment ($V = 60$ knots).

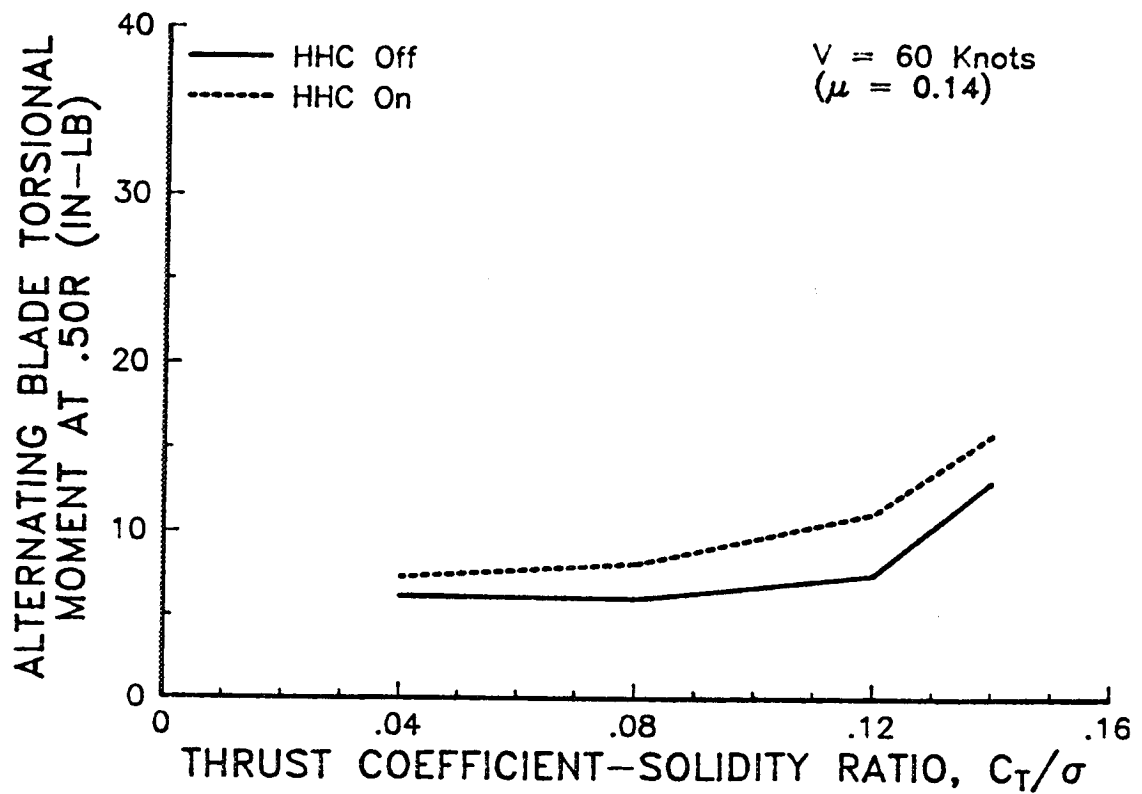


Figure 3.19. HHC effects on the alternating torsional moment ($V = 60$ knots).

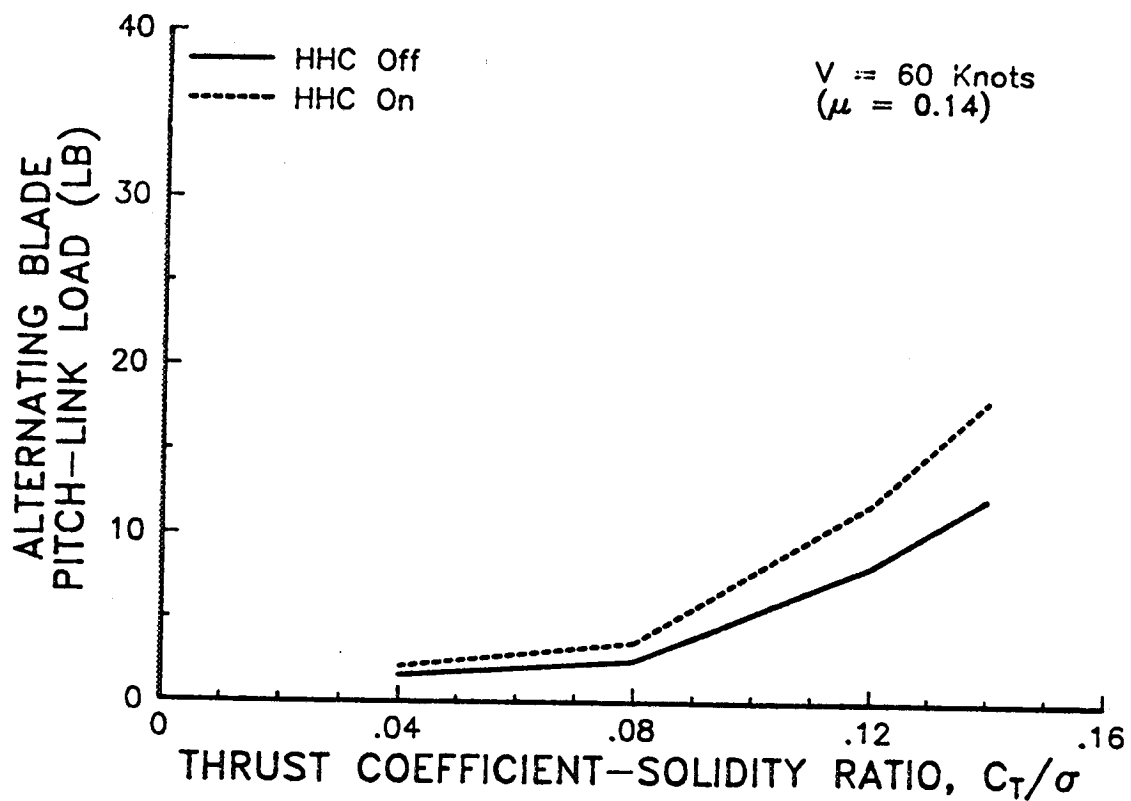


Figure 3.20. HHC effects on the alternating pitch-link load ($V = 60$ knots).

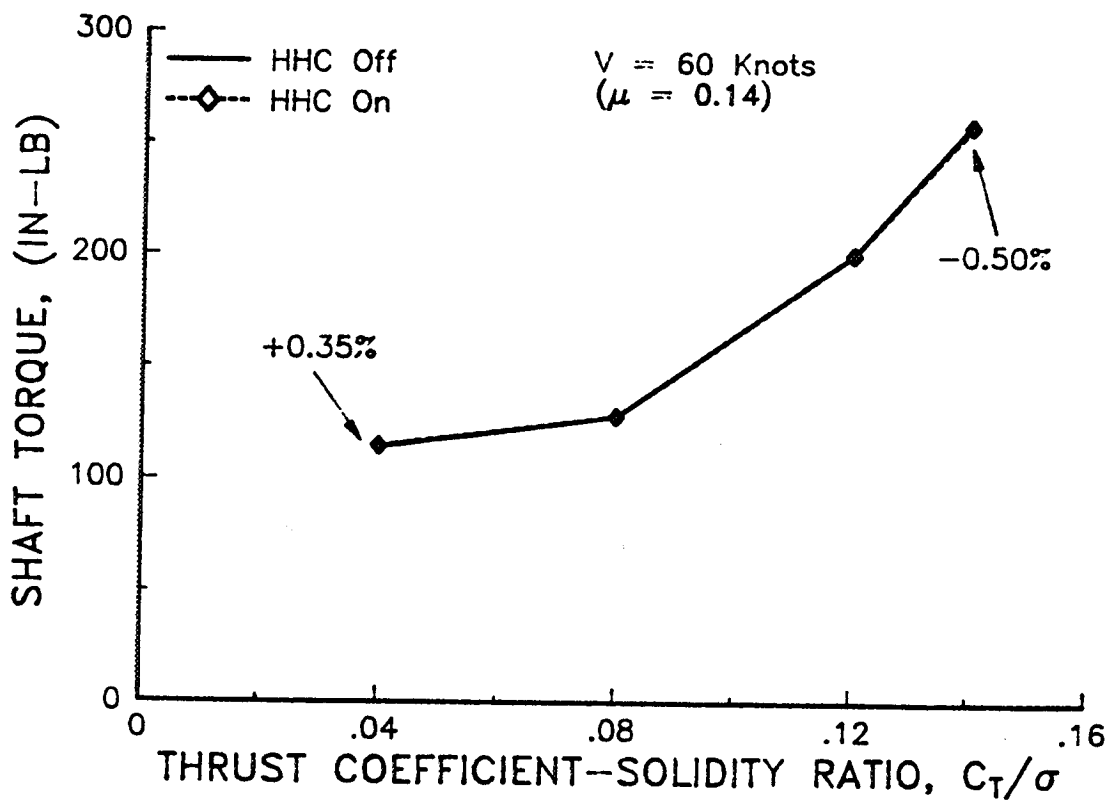


Figure 3.21. HHC effects on the rotor shaft torque ($V = 60$ knots).

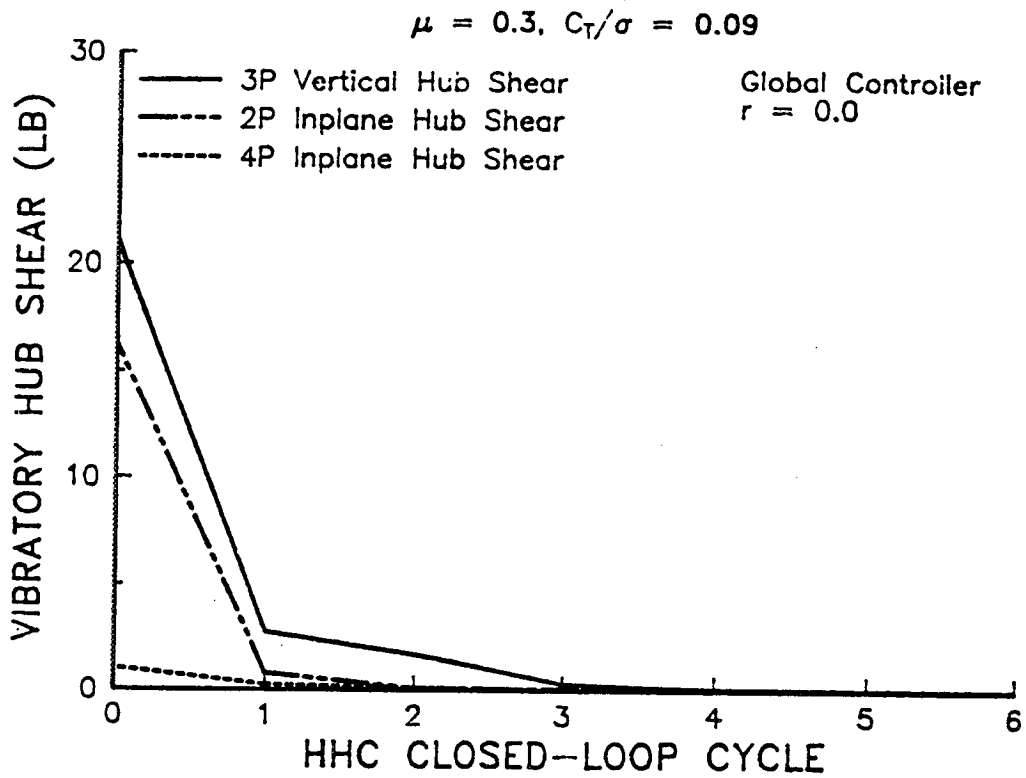


Figure 3.22. Vibratory hub shear responses with fixed-gain HHC controller, $r = 0.0$ ($V = 135$ knots, $C_T/\sigma = 0.09$).

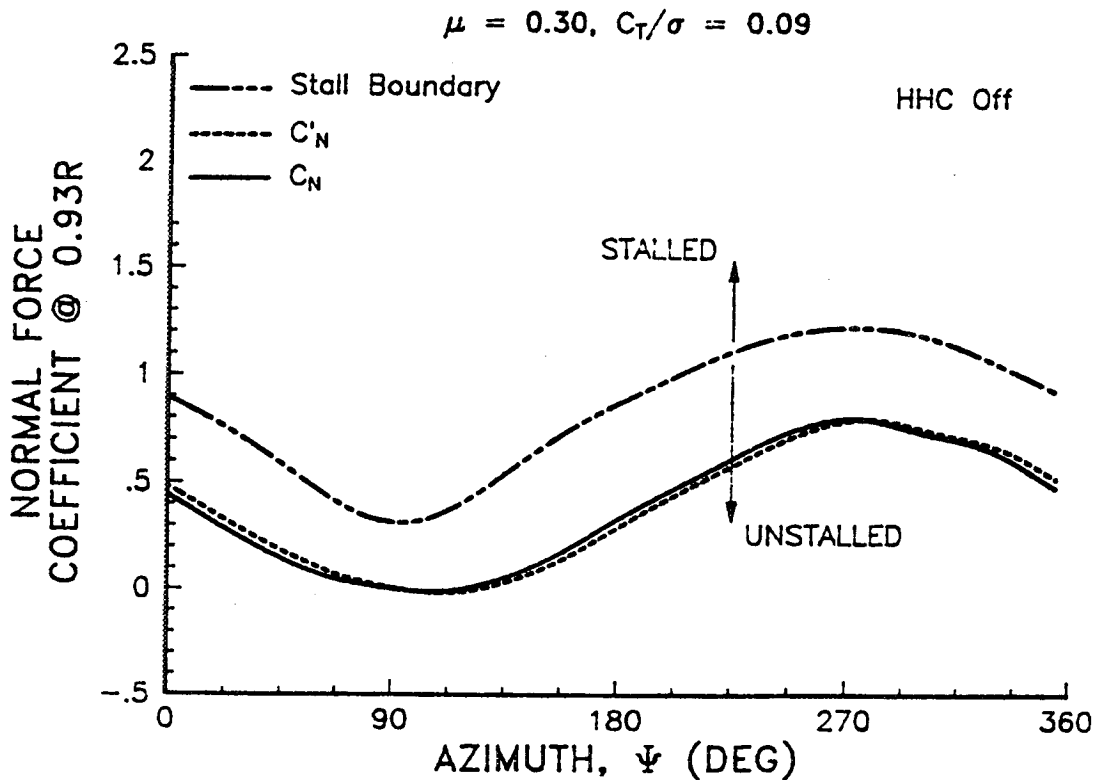


Figure 3.23. Variation of normal force coefficient at 0.93 radius with HHC off ($V = 135$ knots, $C_T/\sigma = 0.09$).

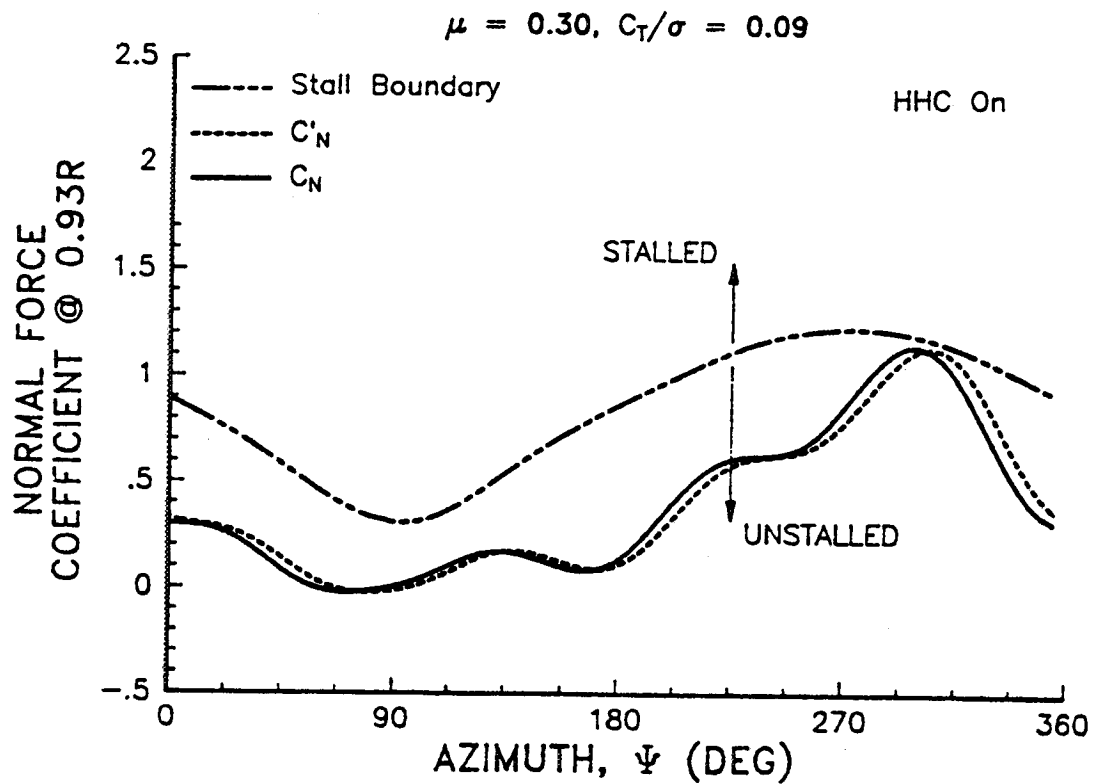


Figure 3.24. Variation of normal force coefficient at 0.93 radius with HHC on, fixed-gain controller, $r = 0.0$ ($V = 135$ knots, $C_T/\sigma = 0.09$).

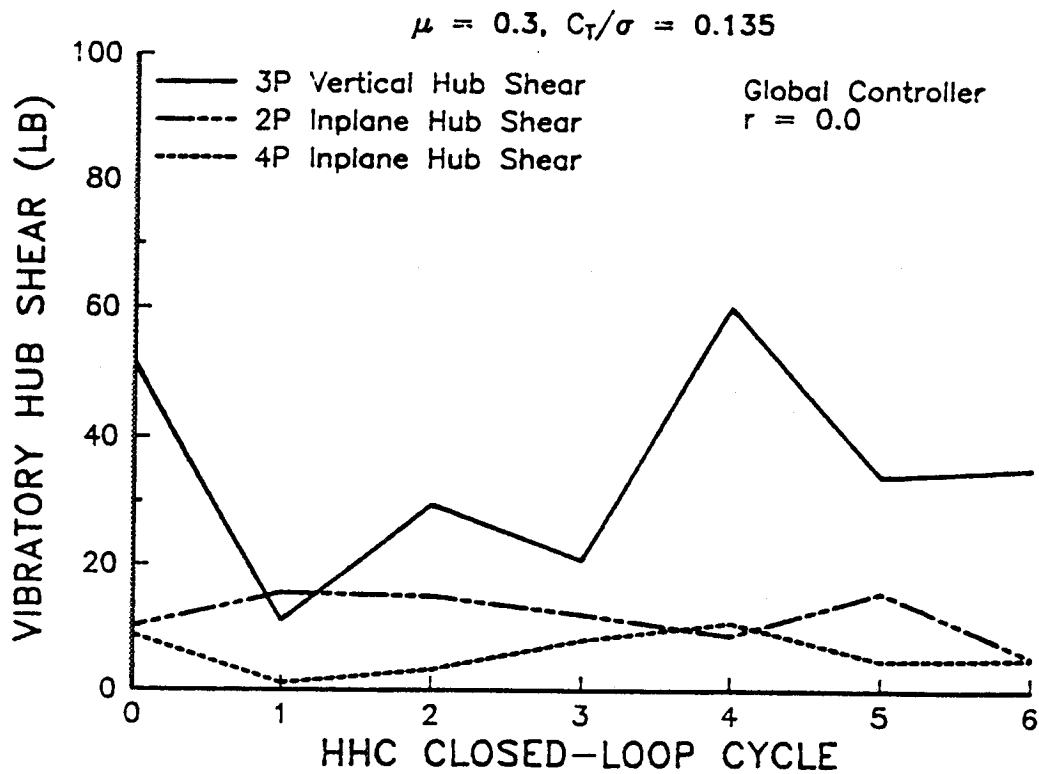


Figure 3.25. Vibratory hub shear responses with fixed-gain HHC controller, $r = 0.0$ ($V = 135$ knots, $C_T/\sigma = 0.135$).

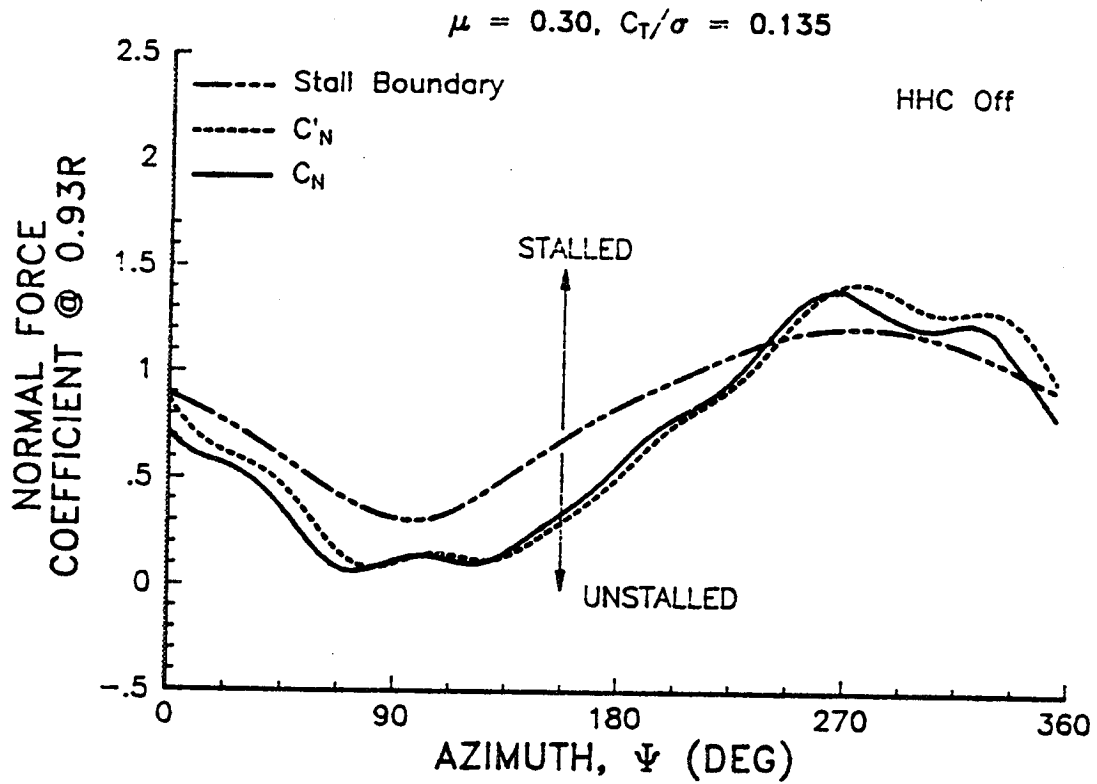


Figure 3.26. Variation of normal force coefficient at 0.93 radius with HHC off ($V = 135$ knots, $C_T/\sigma = 0.135$).

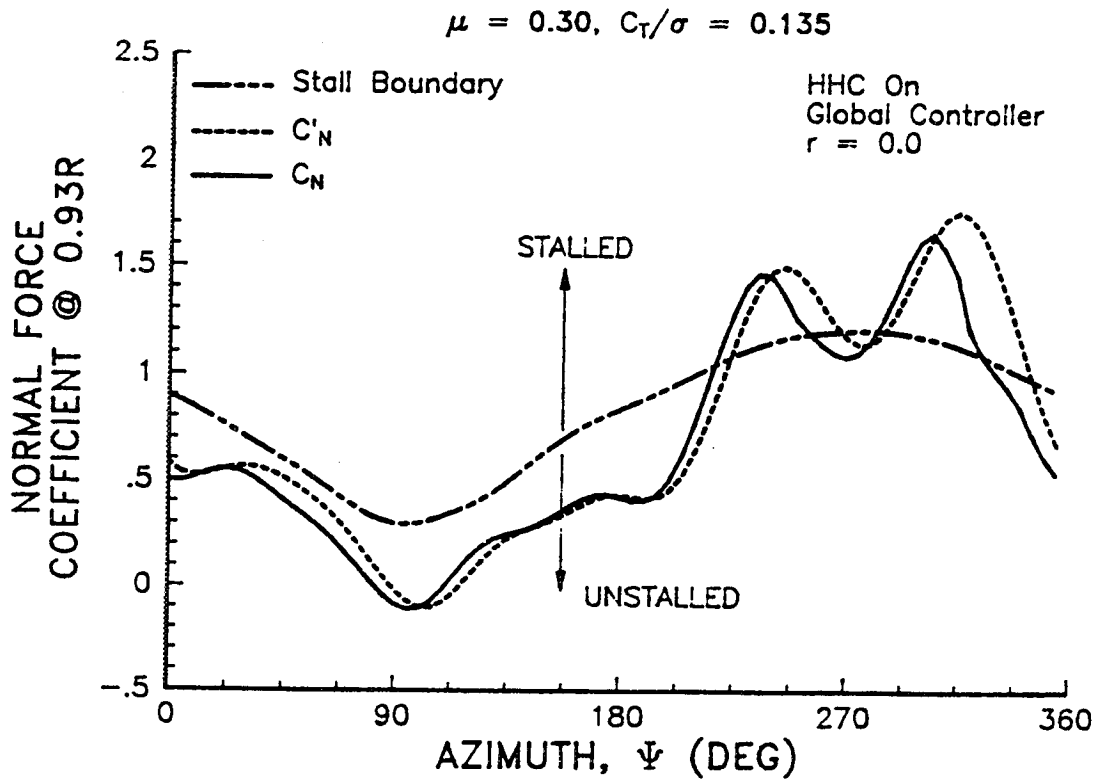


Figure 3.27. Variation of normal force coefficient at 0.93 radius with HHC on, fixed-gain controller, $r = 0.0$ ($V = 135$ knots, $C_T/\sigma = 0.135$).

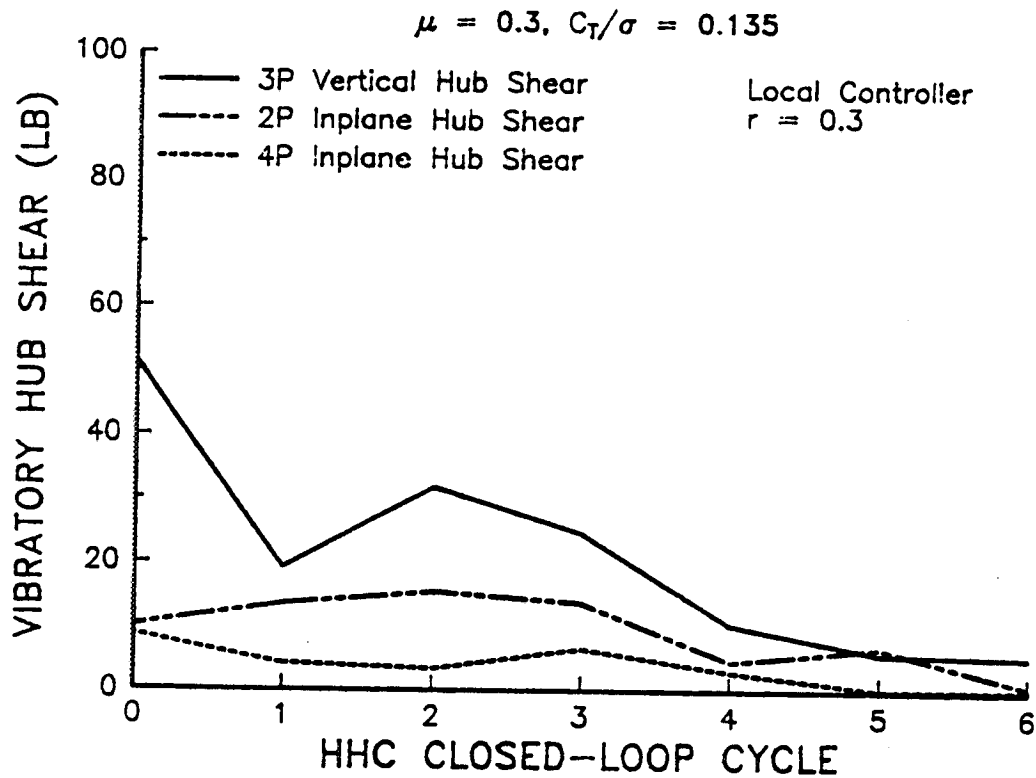


Figure 3.28. Vibratory hub shear responses with adaptive-gain HHC controller, $r = 0.3$ ($V = 135$ knots, $C_T/\sigma = 0.135$).

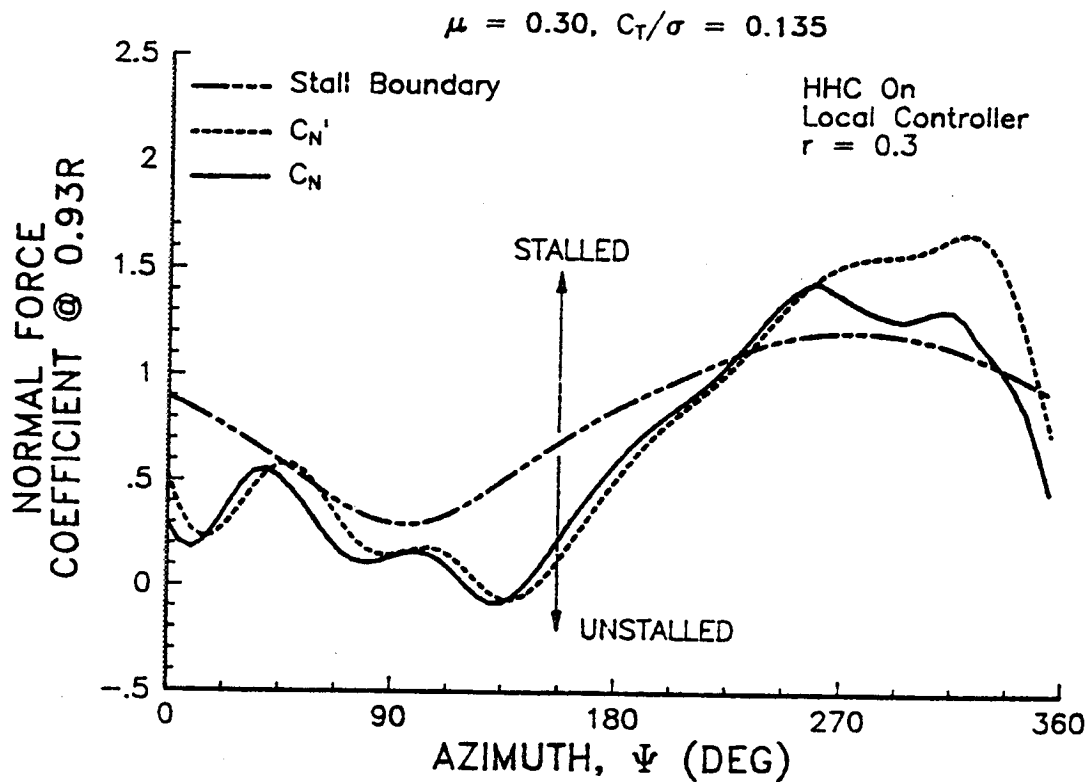


Figure 3.29. Variation of normal force coefficient at 0.93 radius with HHC on, adaptive-gain controller, $r = 0.3$ ($V = 135$ knots, $C_T/\sigma = 0.135$).

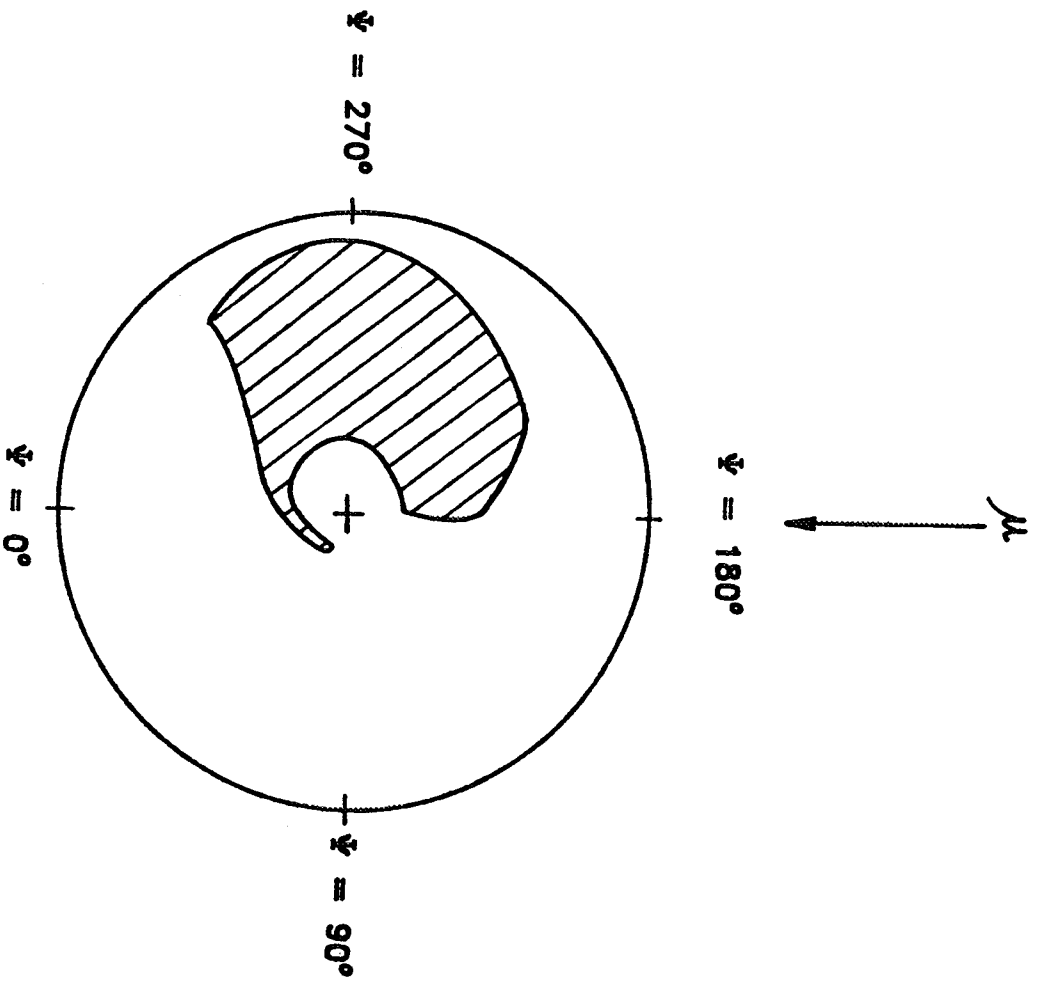


Figure 3.30. Stall area on rotor disk with HHC off ($V = 135$ knots, $C_T/\sigma = 0.12$).

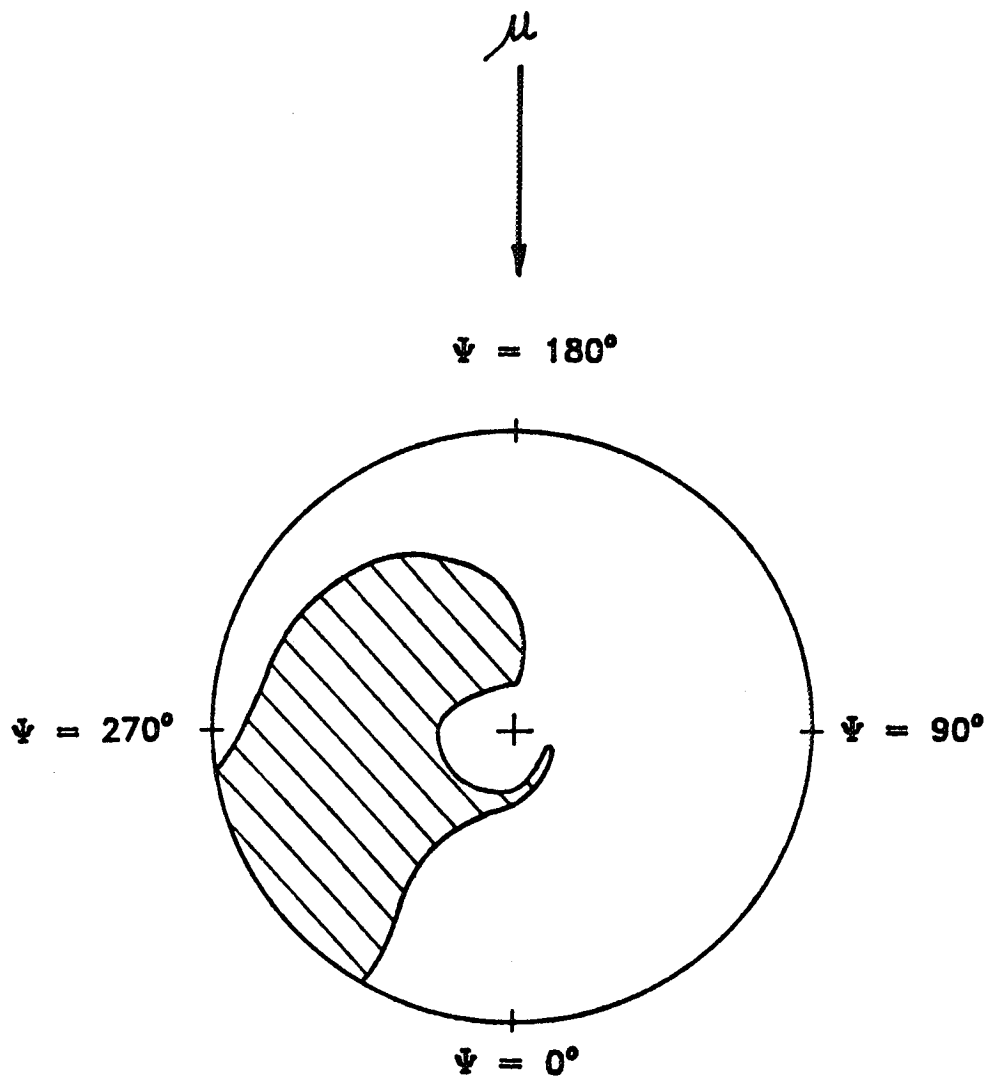


Figure 3.31. Stall area on rotor disk with HHC on, adaptive-gain controller, $r = 0.3$ ($V = 135$ knots, $C_T/\sigma = 0.12$).

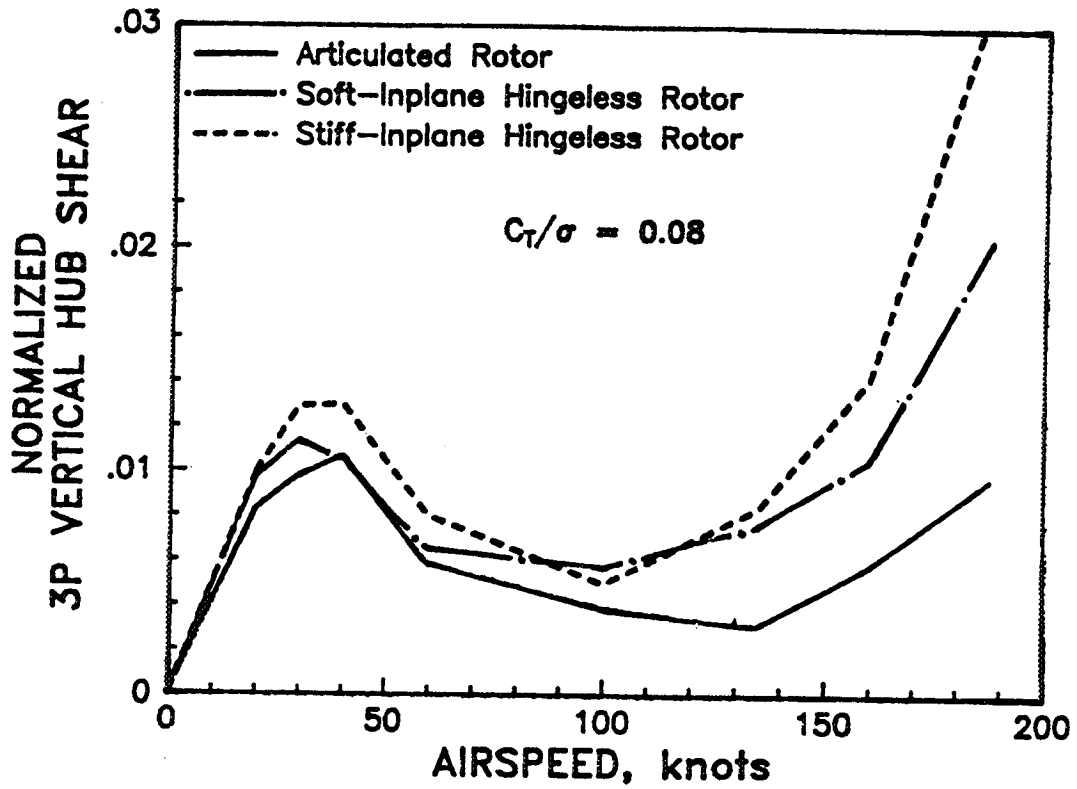


Figure 3.32. Variation of 3P vertical hub shear with forward speed for different rotor systems ($C_T/\sigma = 0.08$).

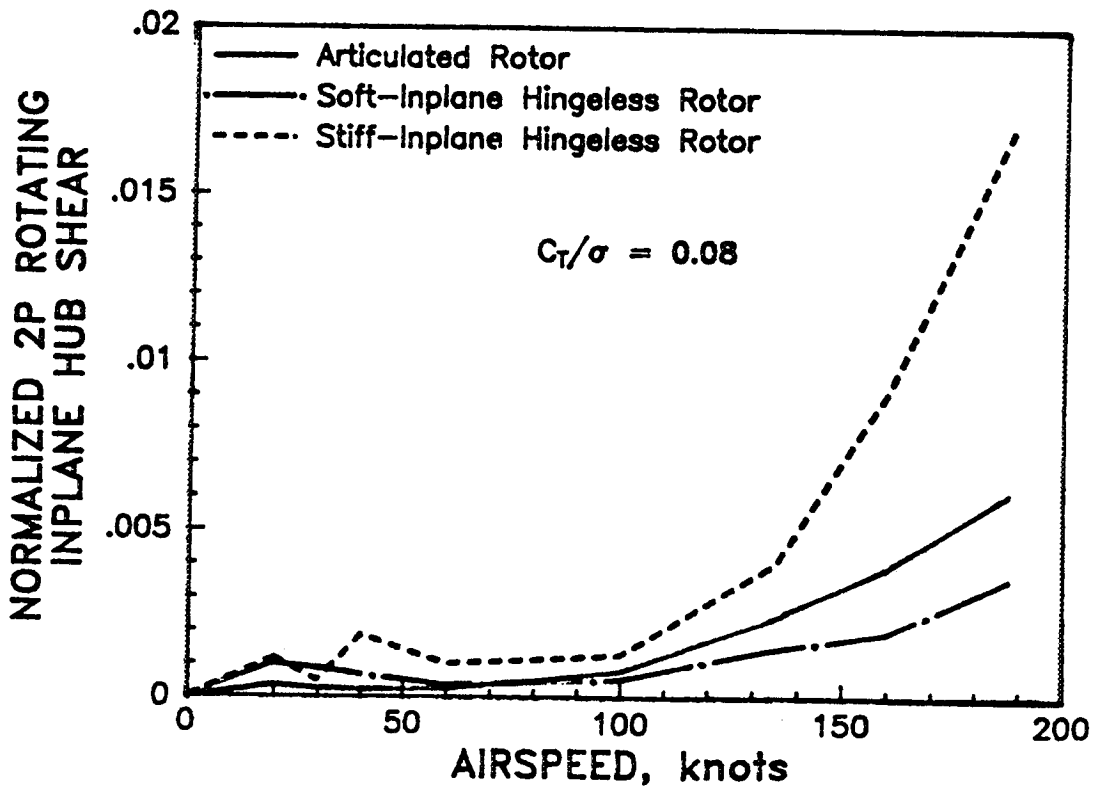


Figure 3.33. Variation of 2P rotating inplane hub shear with forward speed for different rotor systems ($C_T/\sigma = 0.08$).

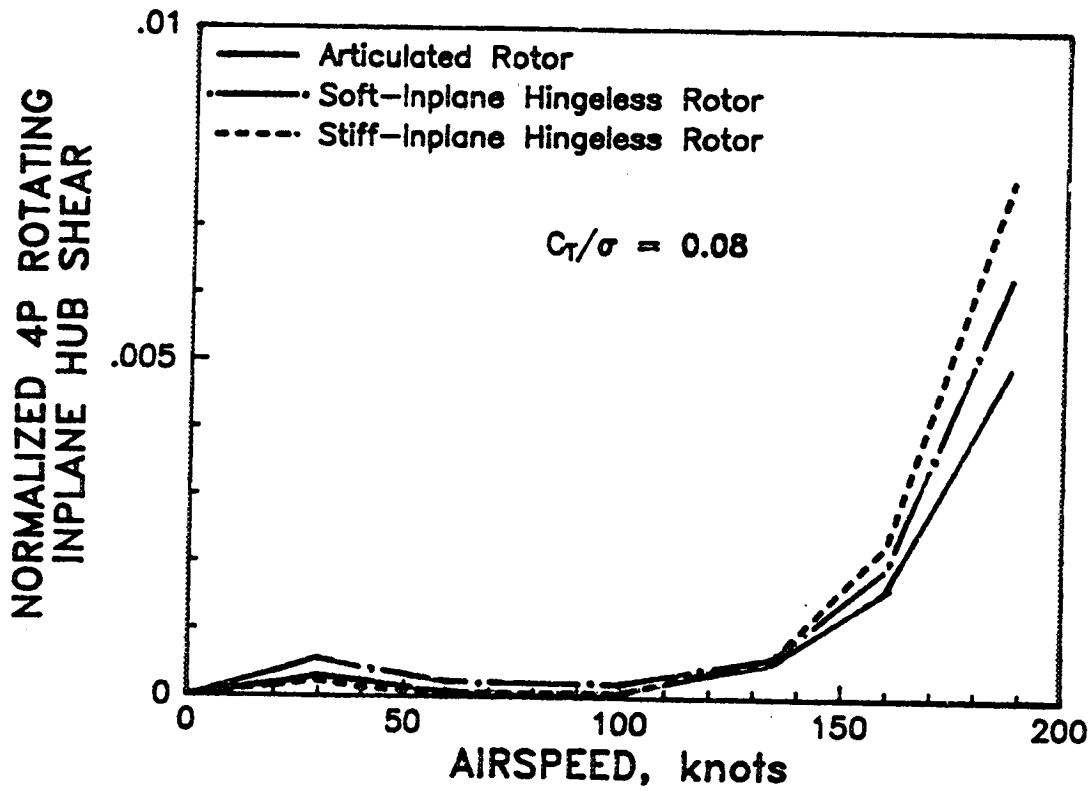


Figure 3.34. Variation of 4P rotating inplane hub shear with forward speed for different rotor systems ($C_T/\sigma = 0.08$).

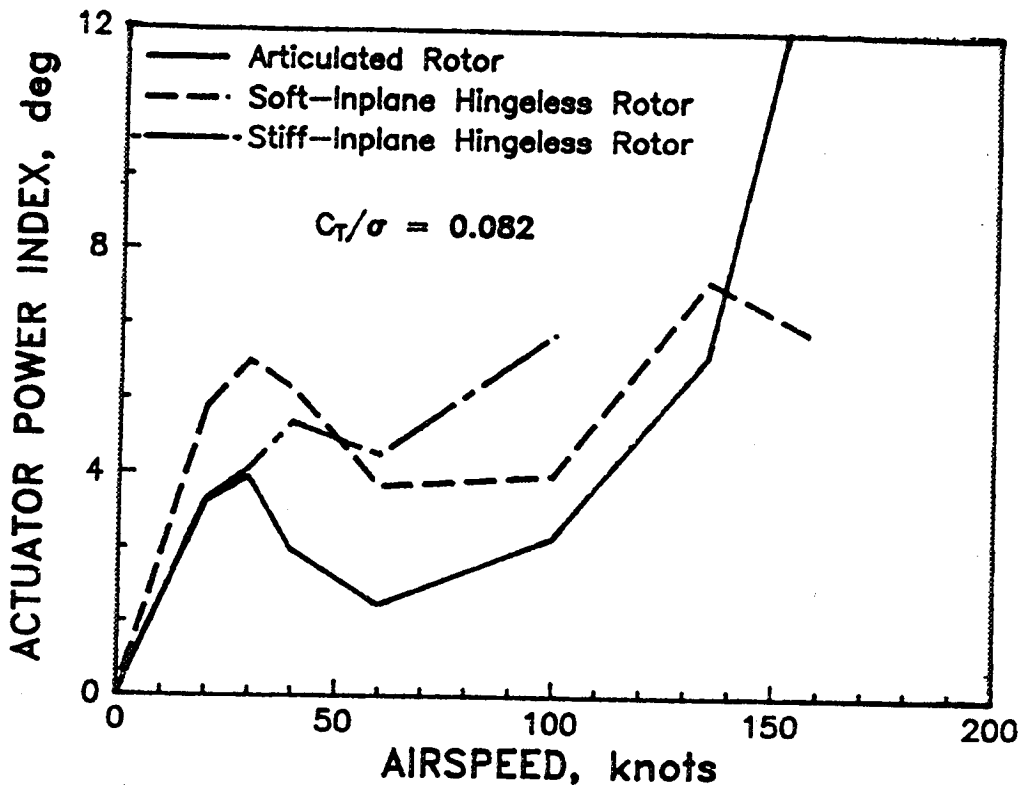


Figure 3.35. Variation of actuator power index with forward speed for different rotor systems ($C_T/\sigma = 0.08$).

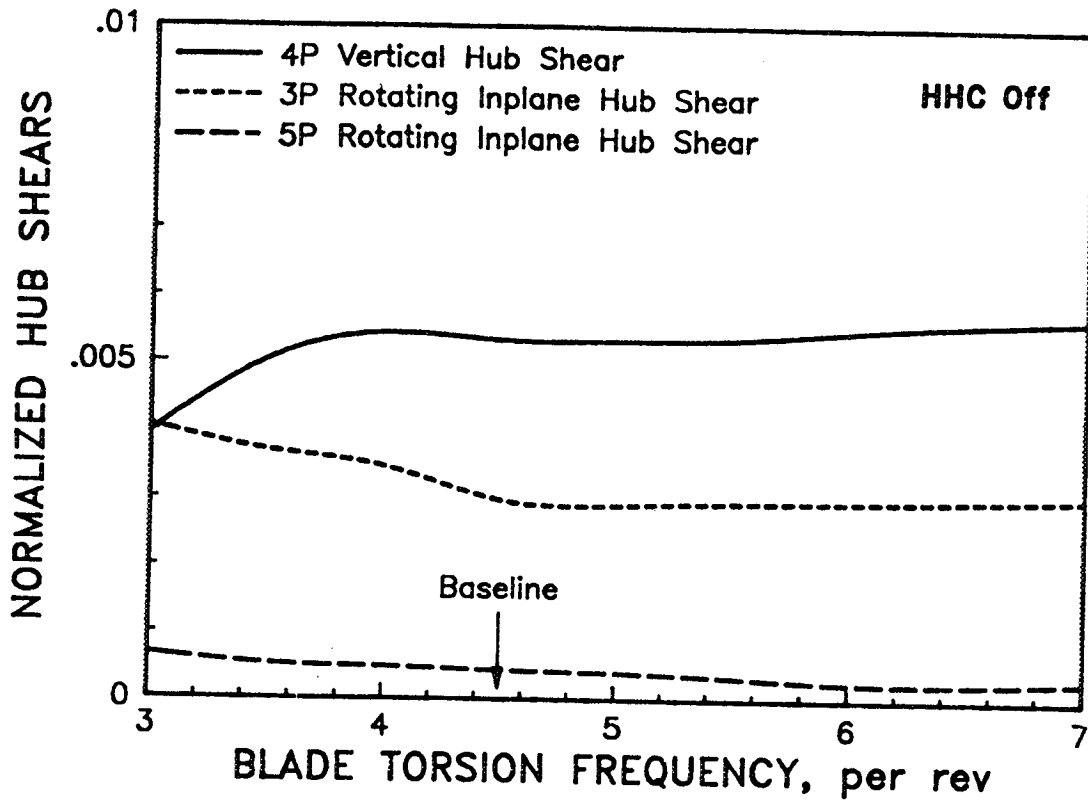


Figure 3.36. Effects of blade torsion stiffness on the uncontrolled vibratory hub shears ($V = 40$ knots, $C_T/\sigma = 0.08$).

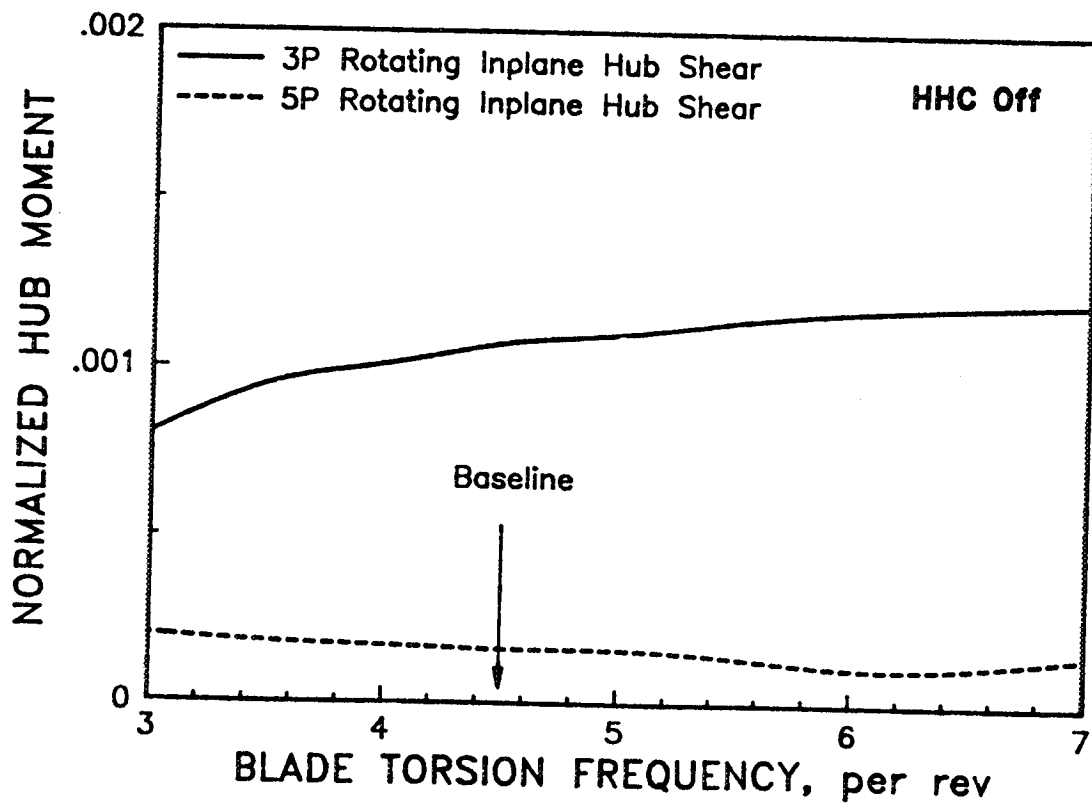


Figure 3.37. Effects of blade torsion stiffness on the uncontrolled vibratory hub moments ($V = 40$ knots, $C_T/\sigma = 0.08$).

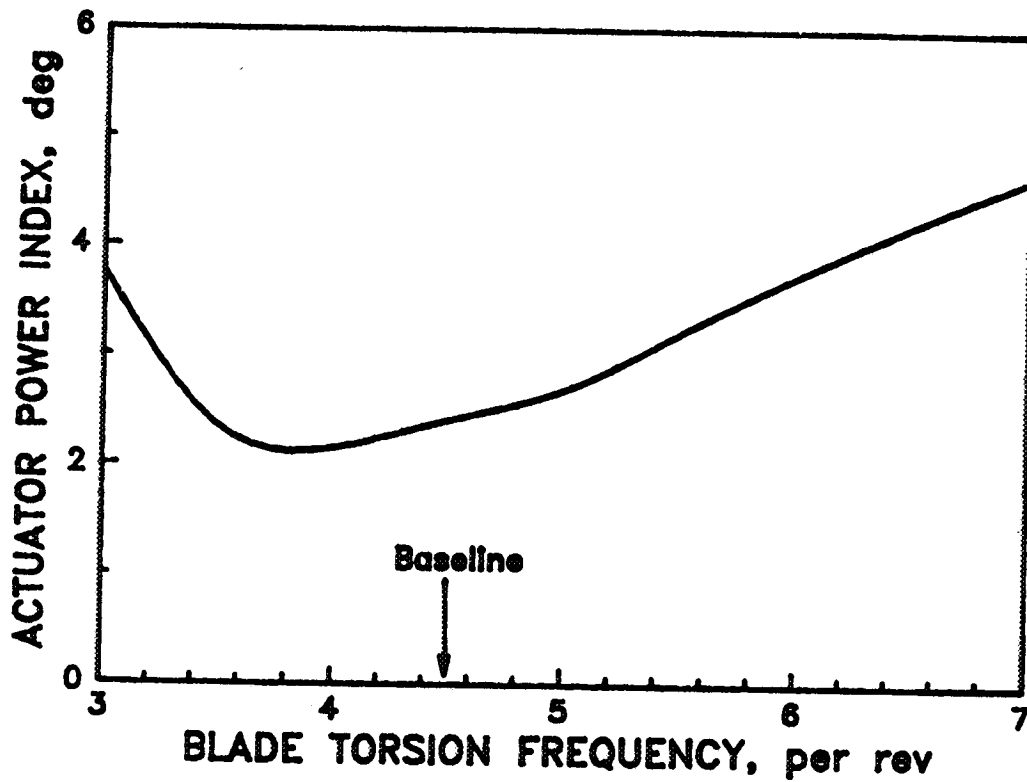


Figure 3.38. Effects of blade torsion stiffness on the HHC actuator power ($V = 40$ knots, $C_T/\sigma = 0.08$).

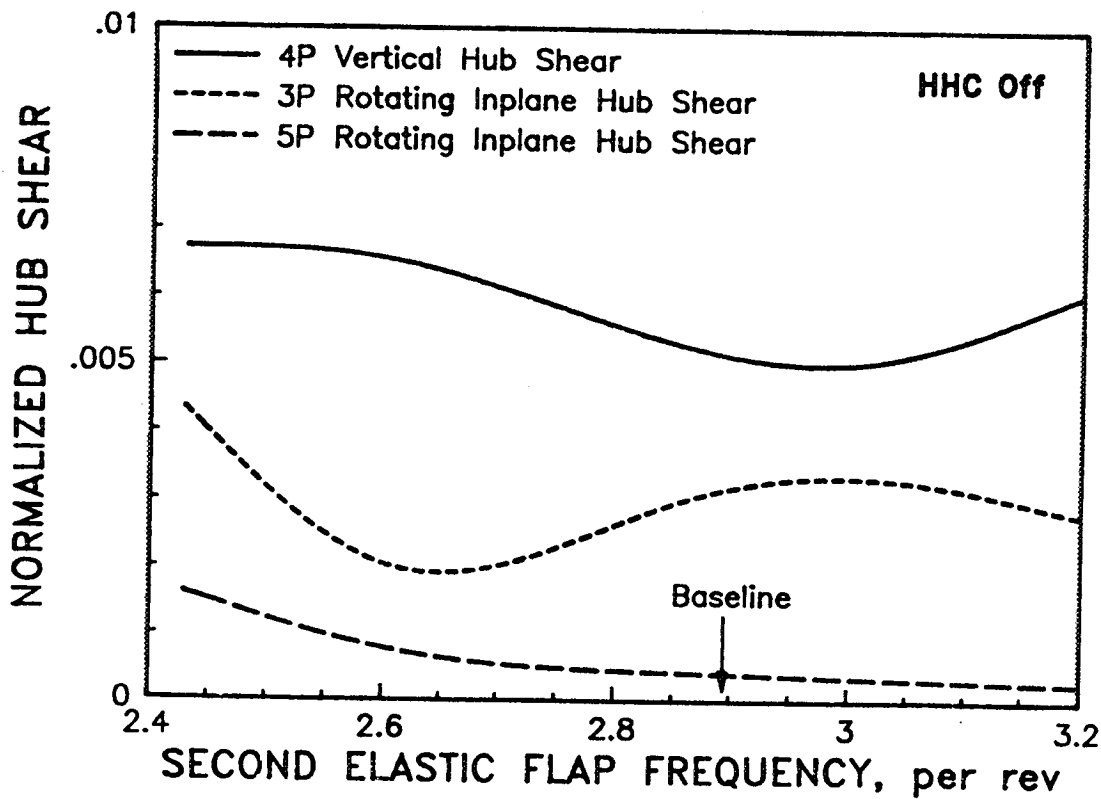


Figure 3.39. Effects of blade flap stiffness on the uncontrolled vibratory hub shears ($V = 40$ knots, $C_T/\sigma = 0.08$).

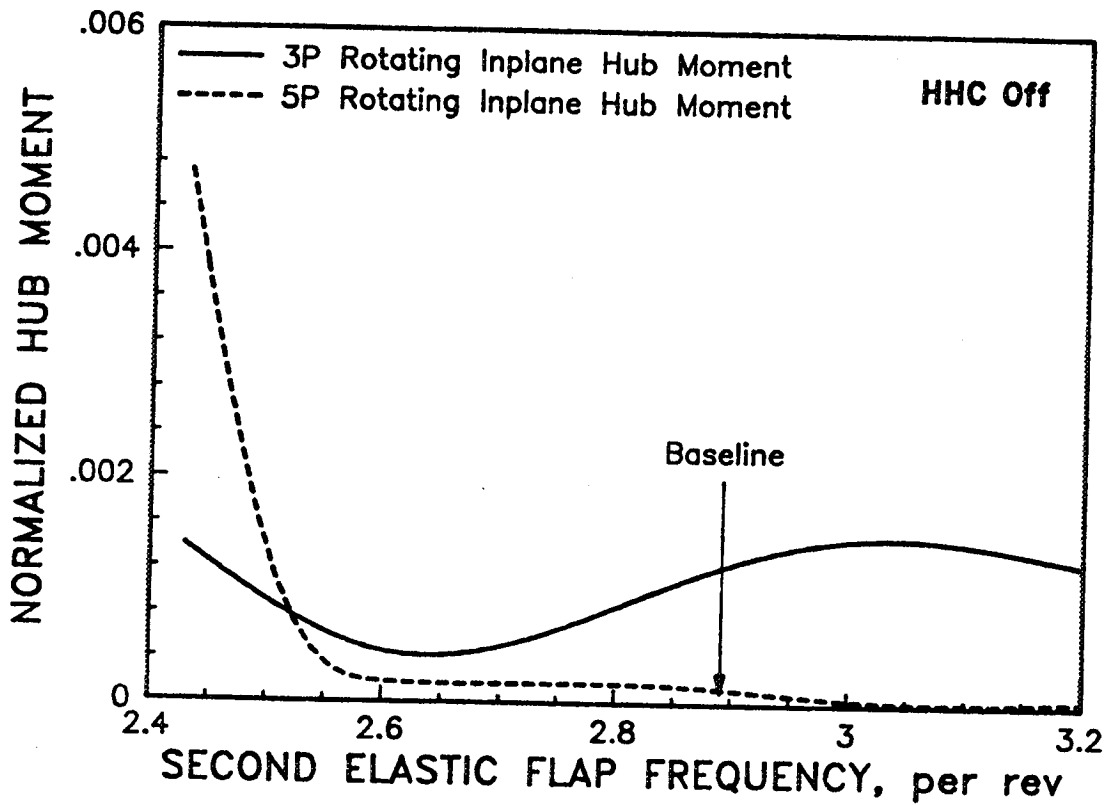


Figure 3.40. Effects of blade flap stiffness on the uncontrolled vibratory hub moments ($V = 40$ knots, $C_T/\sigma = 0.08$).

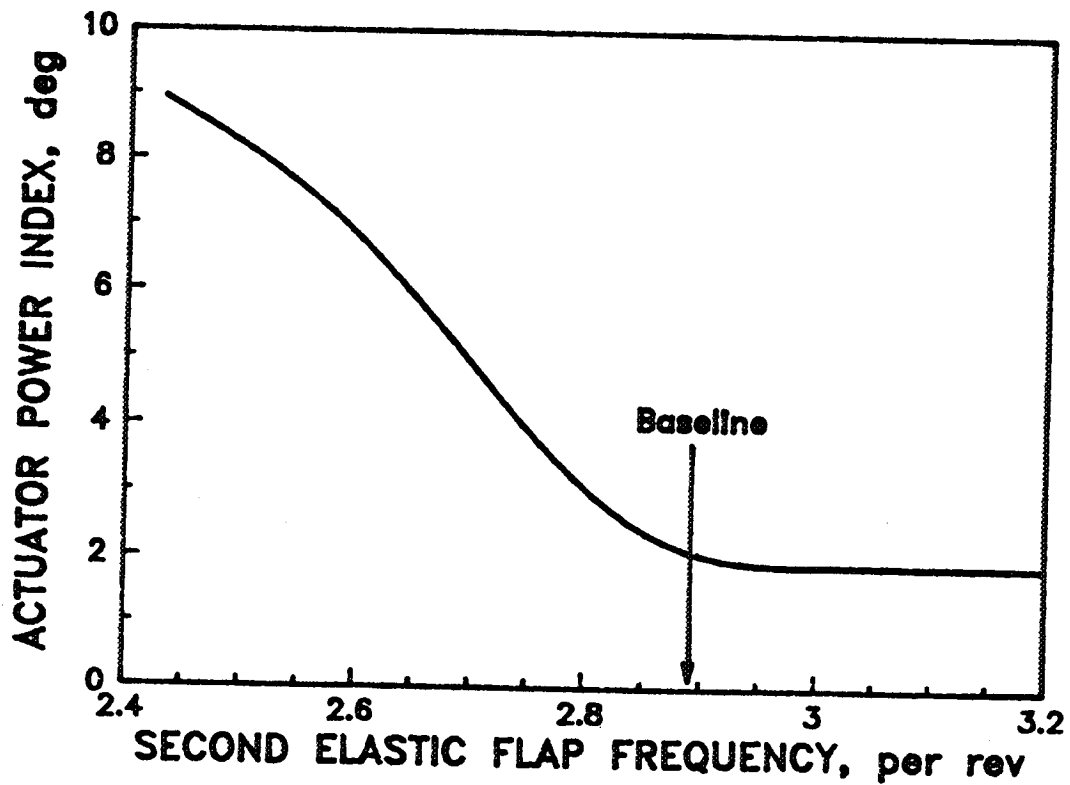


Figure 3.41. Effects of blade flap stiffness on the HHC actuator power ($V = 40$ knots, $C_T/\sigma = 0.08$).

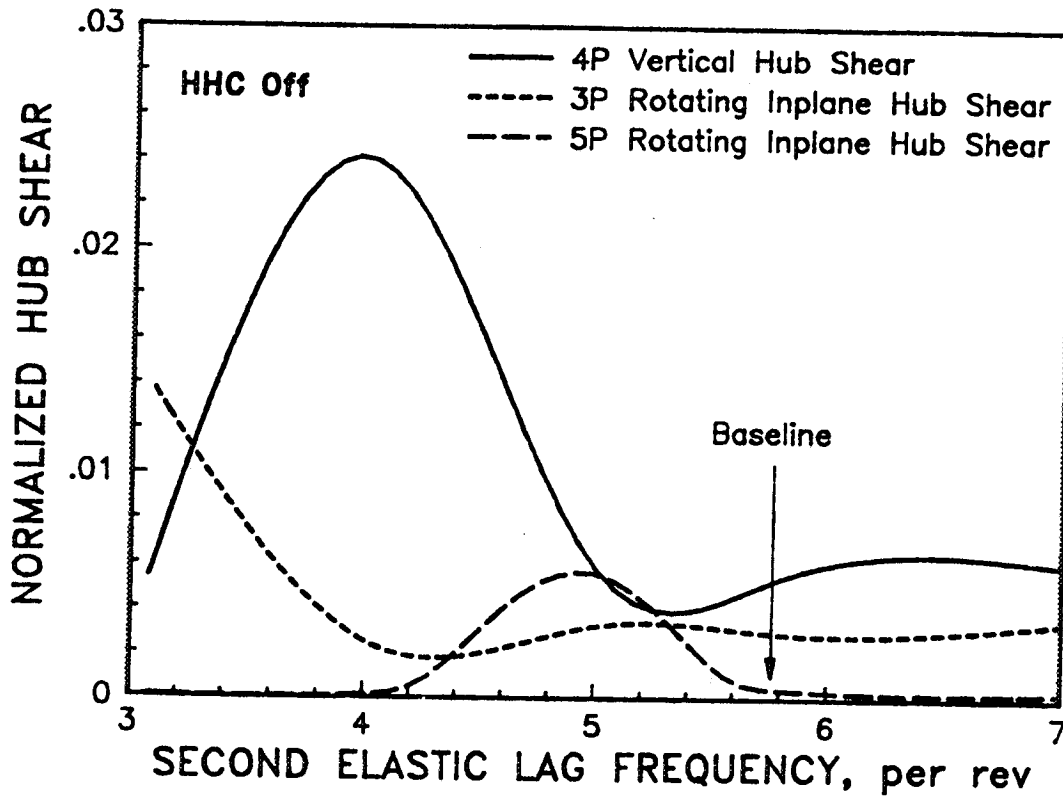


Figure 3.42. Effects of blade lag stiffness on the uncontrolled vibratory hub shears ($V = 40$ knots, $C_T/\sigma = 0.08$).

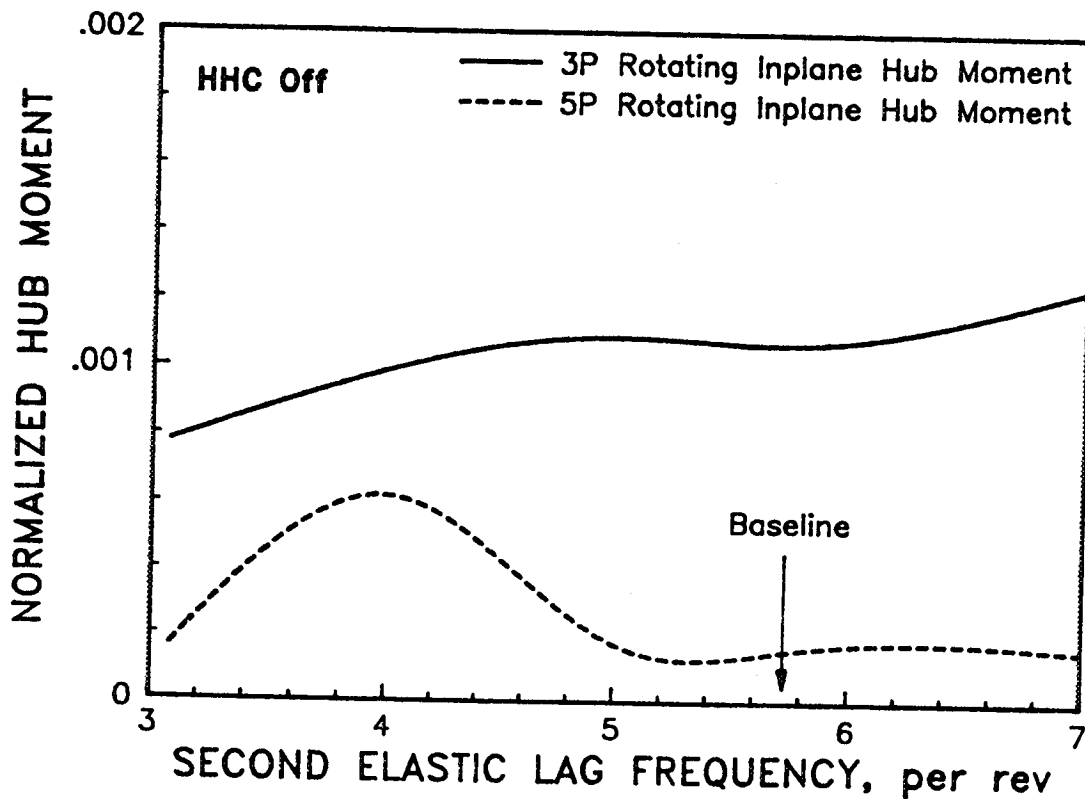


Figure 3.43. Effects of blade lag stiffness on the uncontrolled vibratory hub moments ($V = 40$ knots, $C_T/\sigma = 0.08$).

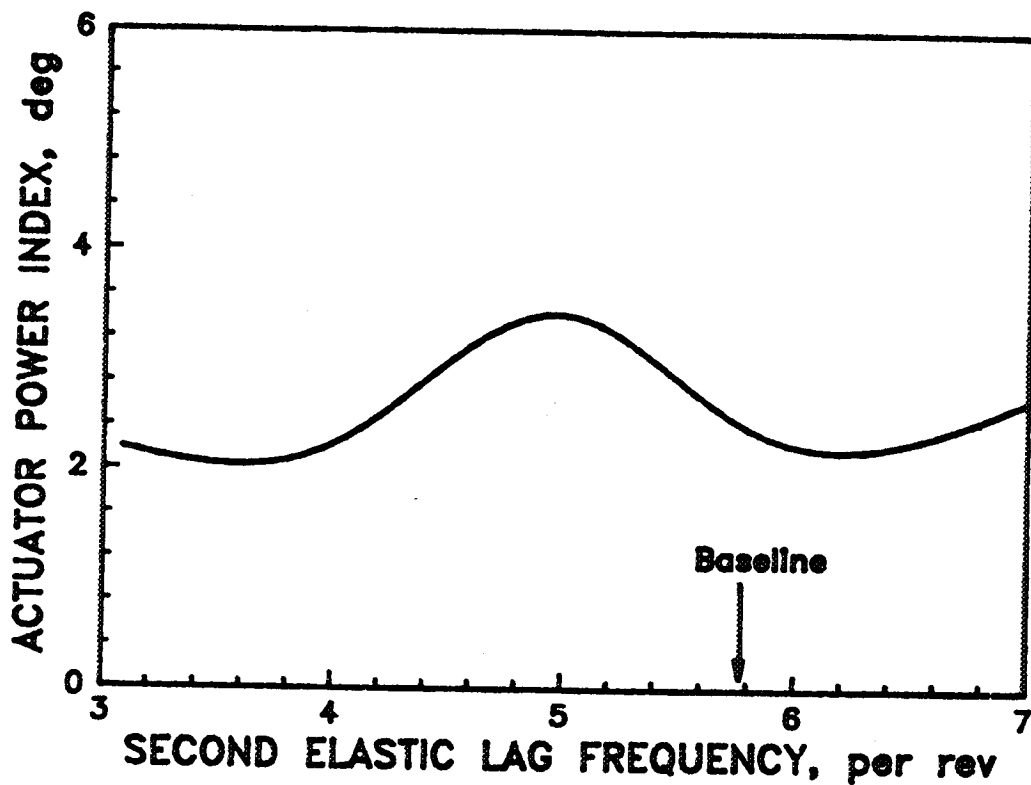


Figure 3.44. Effects of blade lag stiffness on the HHC actuator power ($V = 40$ knots, $C_T/\sigma = 0.08$).

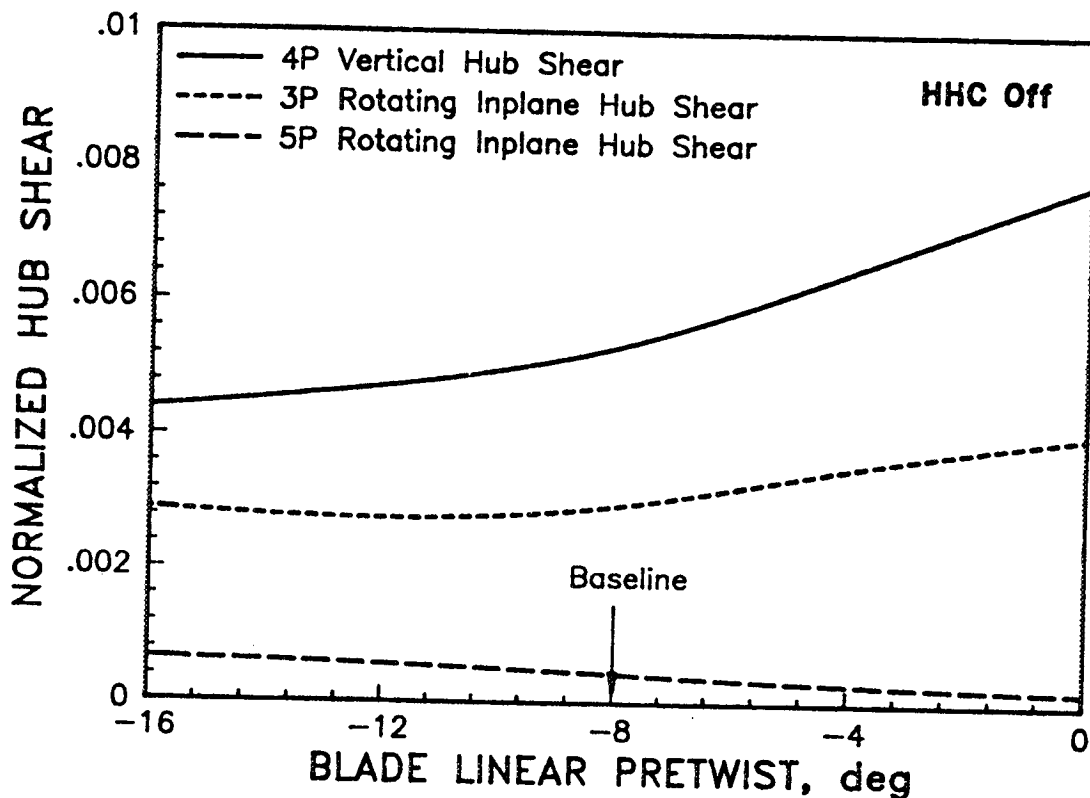


Figure 3.45. Effects of blade linear pretwist on the uncontrolled vibratory hub shears ($V = 40$ knots, $C_T/\sigma = 0.08$).

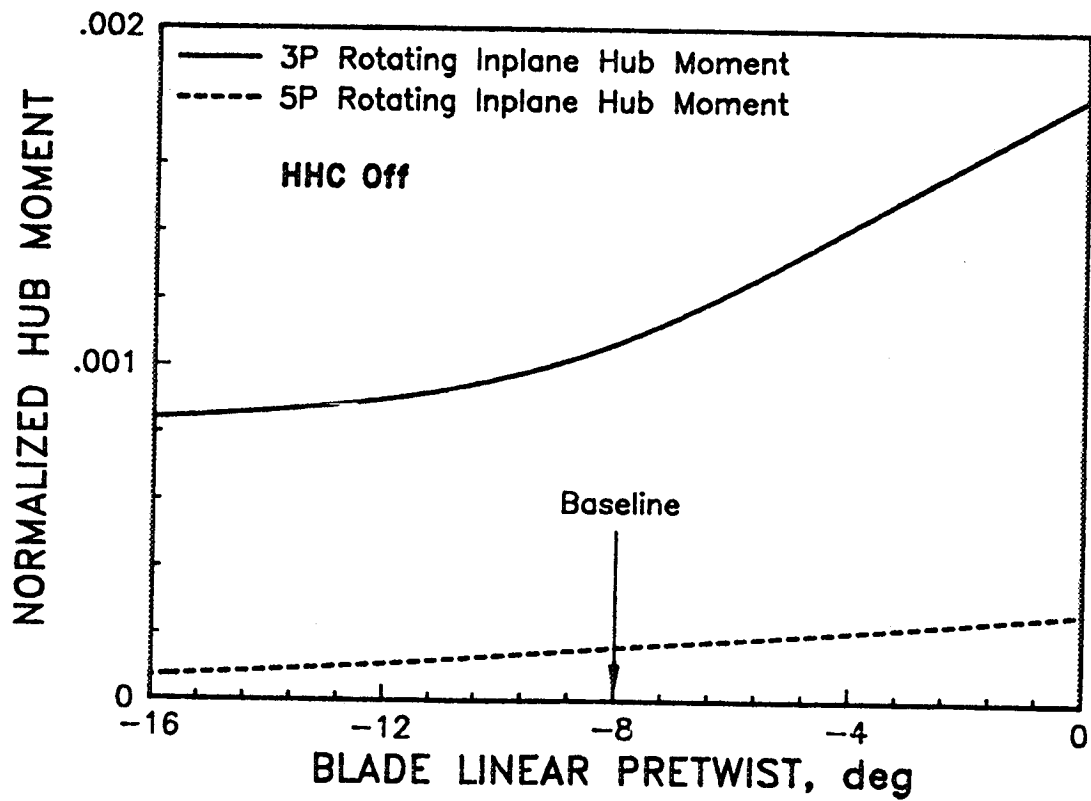


Figure 3.46. Effects of blade linear pretwist on the uncontrolled vibratory hub moments ($V = 40$ knots, $C_T/\sigma = 0.08$).

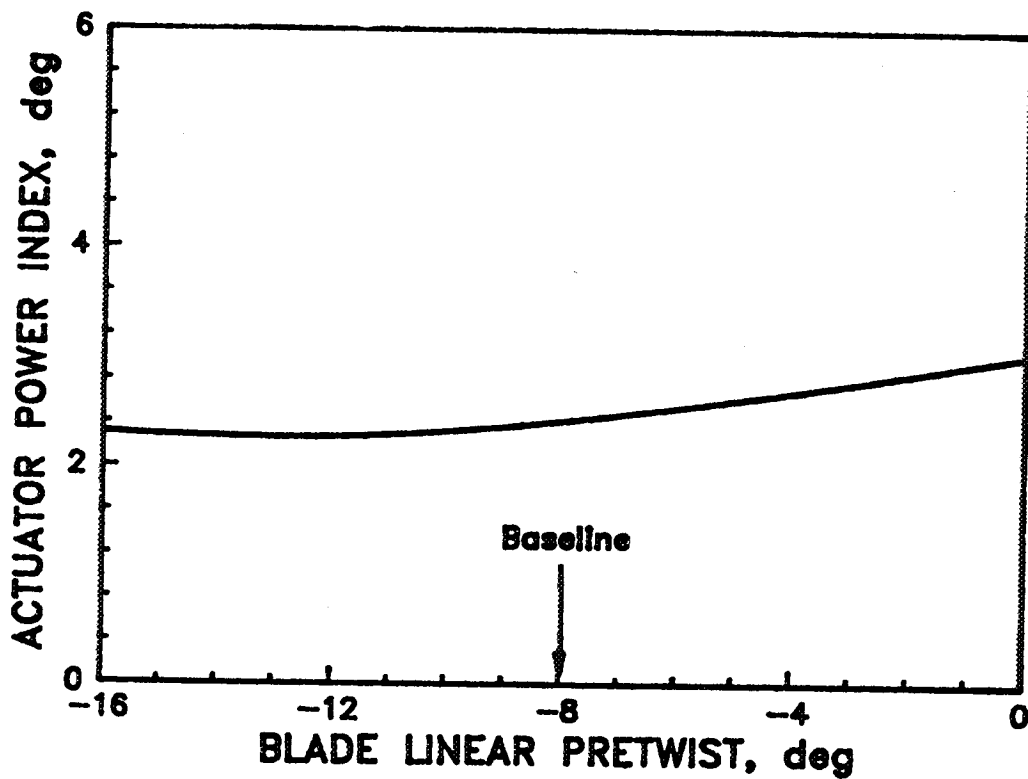


Figure 3.47. Effects of blade linear pretwist on the HHC actuator power ($V = 40$ knots, $C_T/\sigma = 0.08$).

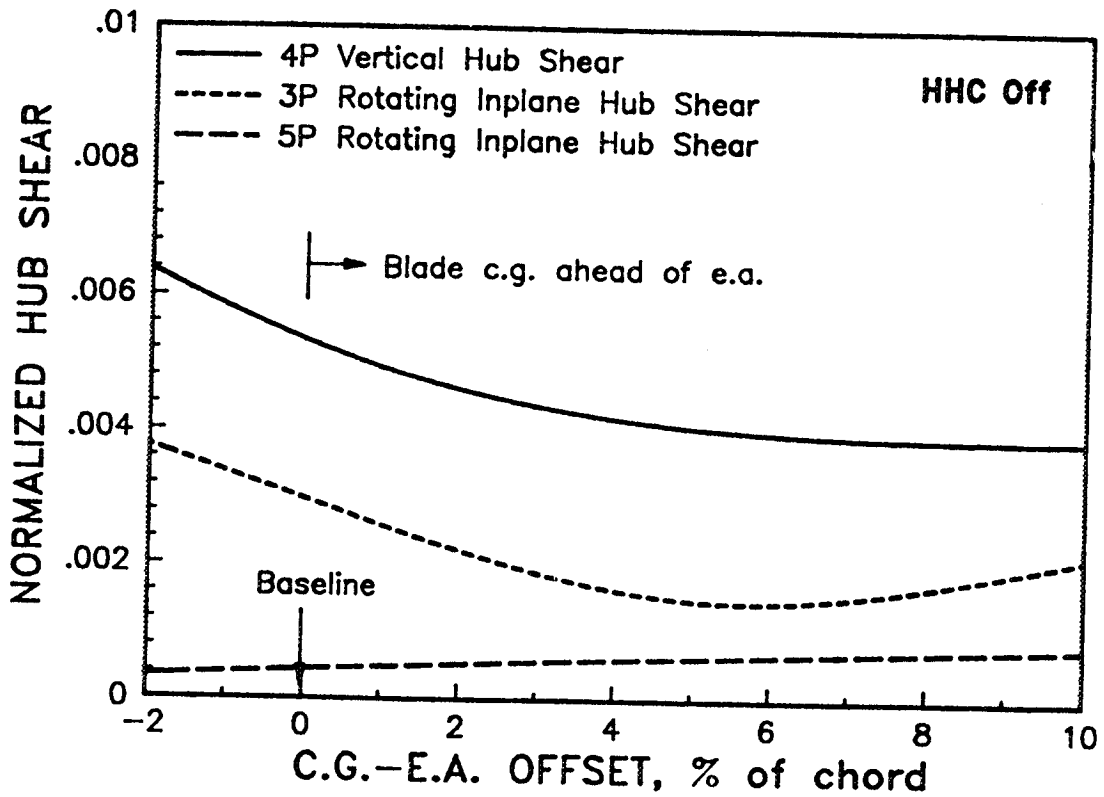


Figure 3.48. Effects of blade center-of-mass offset from elastic axis on the uncontrolled vibratory hub shears ($V = 40$ knots, $C_T/\sigma = 0.08$).

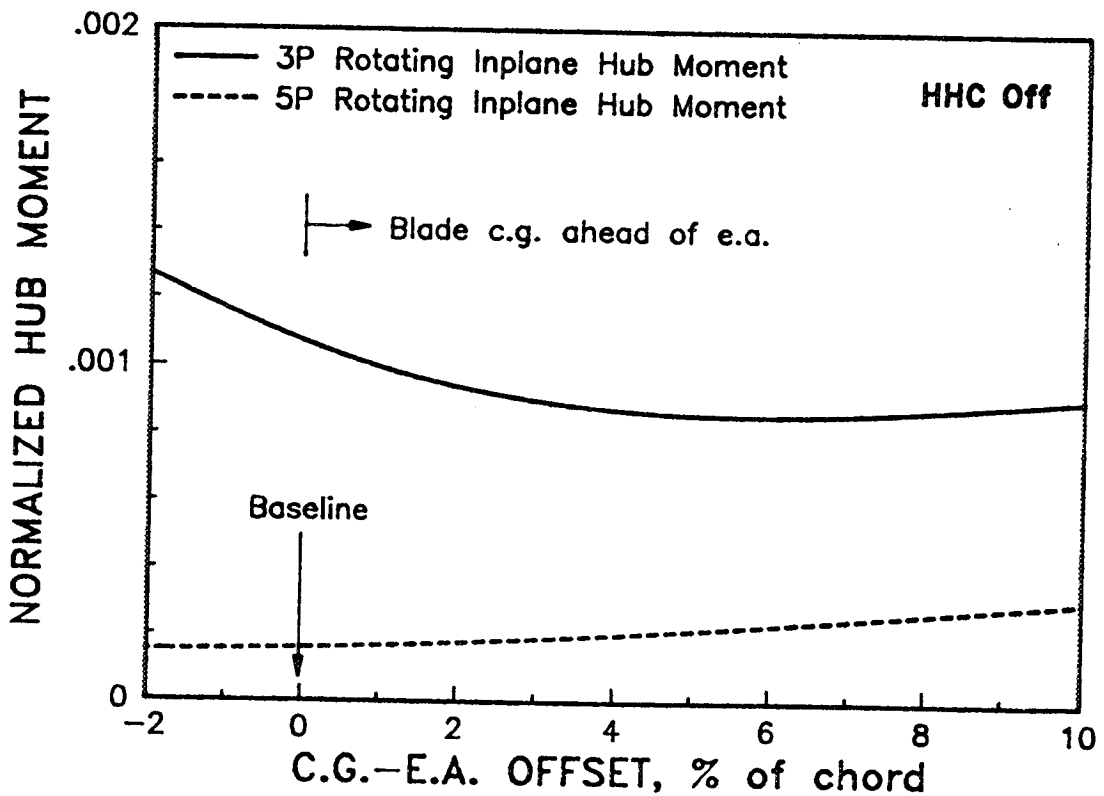


Figure 3.49. Effects of blade center-of-mass offset from elastic axis on the uncontrolled vibratory hub moments ($V = 40$ knots, $C_T/\sigma = 0.08$).

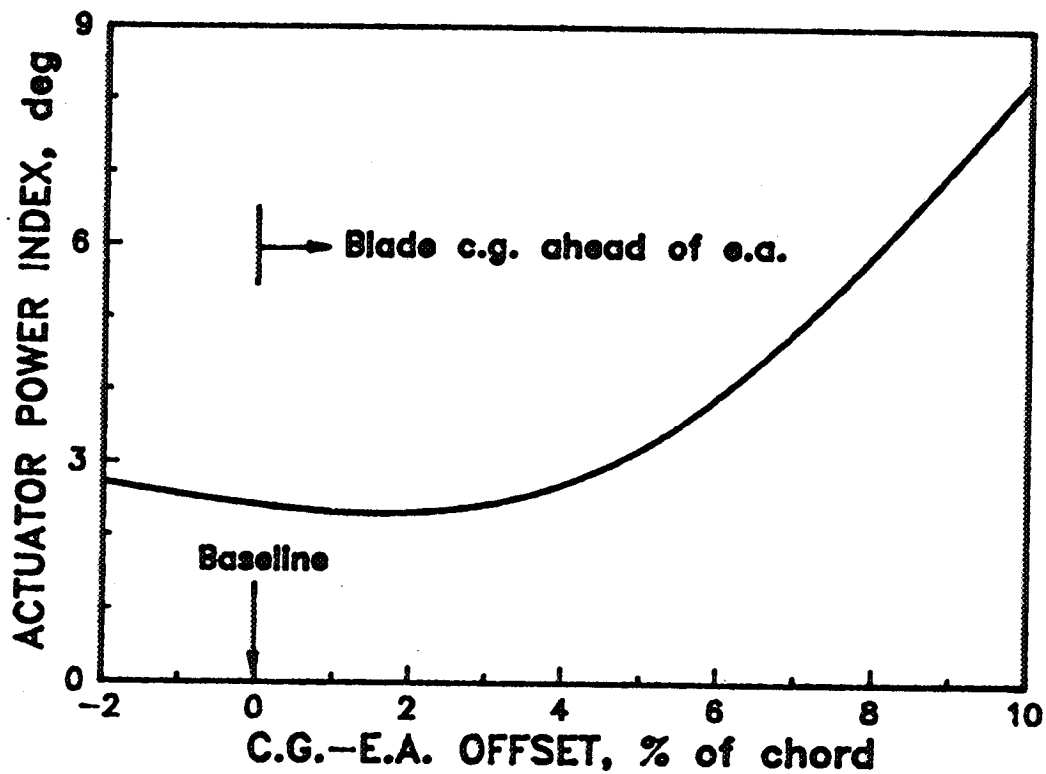


Figure 3.50. Effects of blade center-of-mass offset from elastic axis on the HHC actuator power ($V = 40$ knots, $C_T/\sigma = 0.08$).

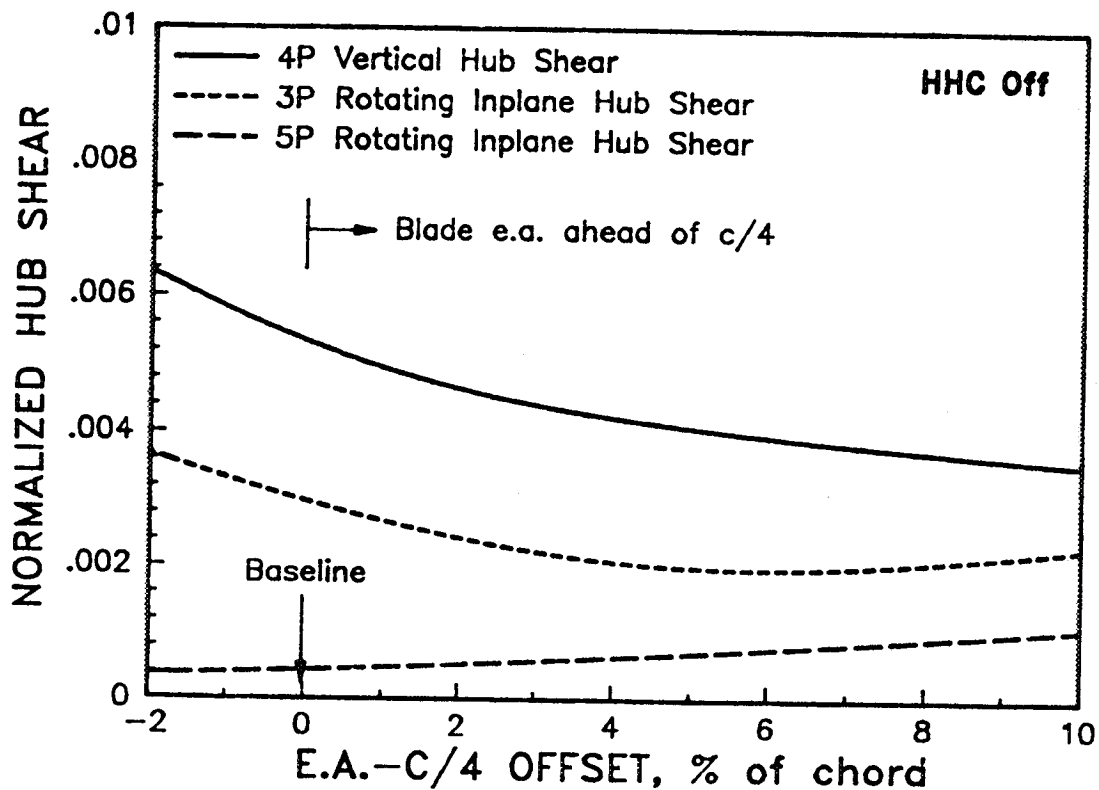


Figure 3.51. Effects of blade elastic axis offset from quarter chord on the uncontrolled vibratory hub shears ($V = 40$ knots, $C_T/\sigma = 0.08$).

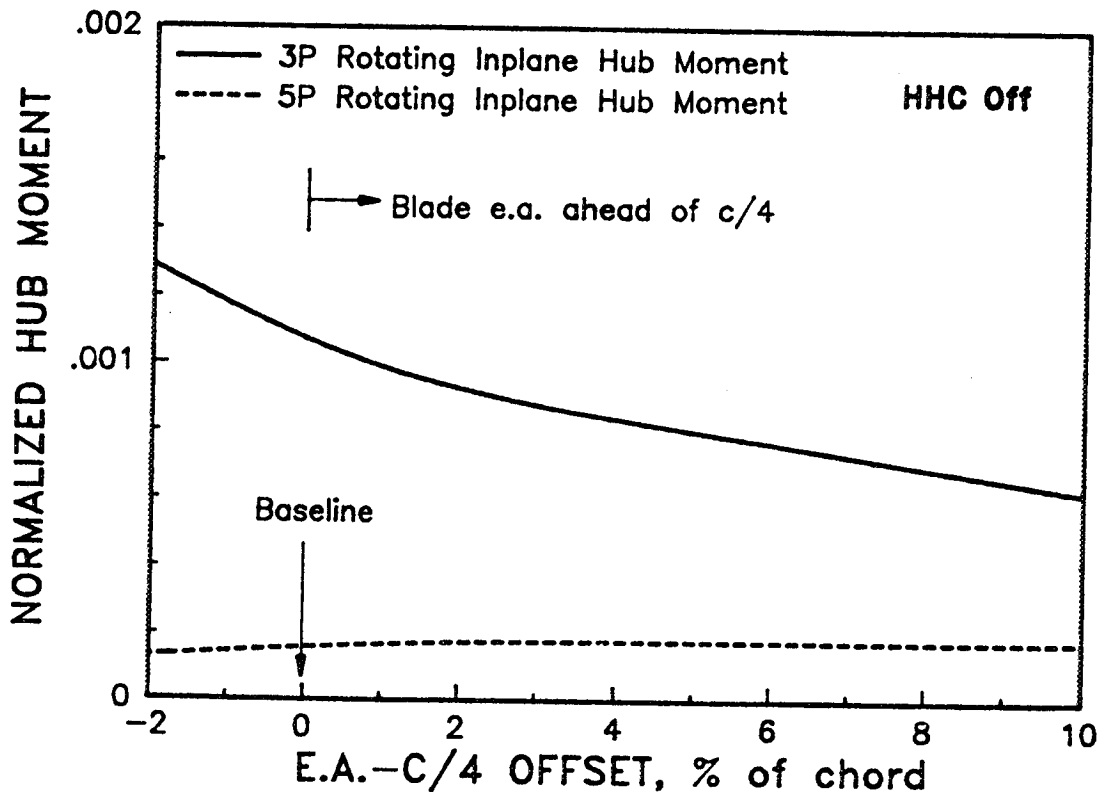


Figure 3.52. Effects of blade elastic axis offset from quarter chord on the uncontrolled vibratory hub moments ($V = 40$ knots, $C_T/\sigma = 0.08$).

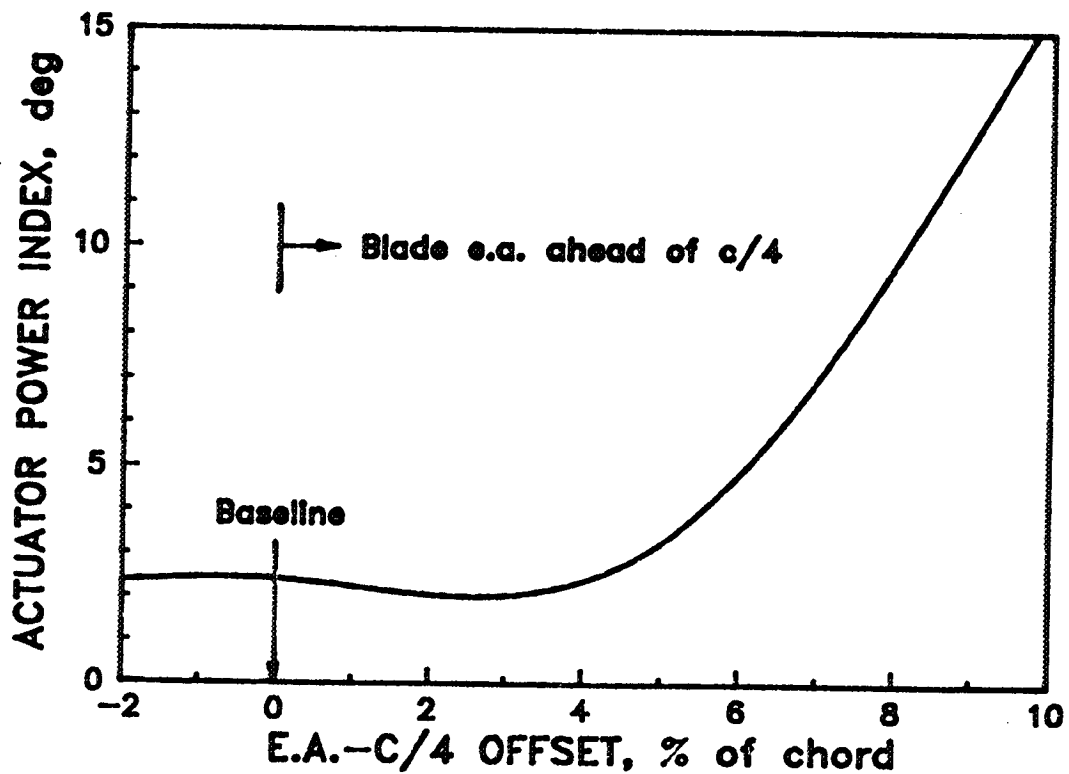


Figure 3.53. Effects of blade elastic axis offset from quarter chord on the HHC actuator power ($V = 40$ knots, $C_T/\sigma = 0.08$).

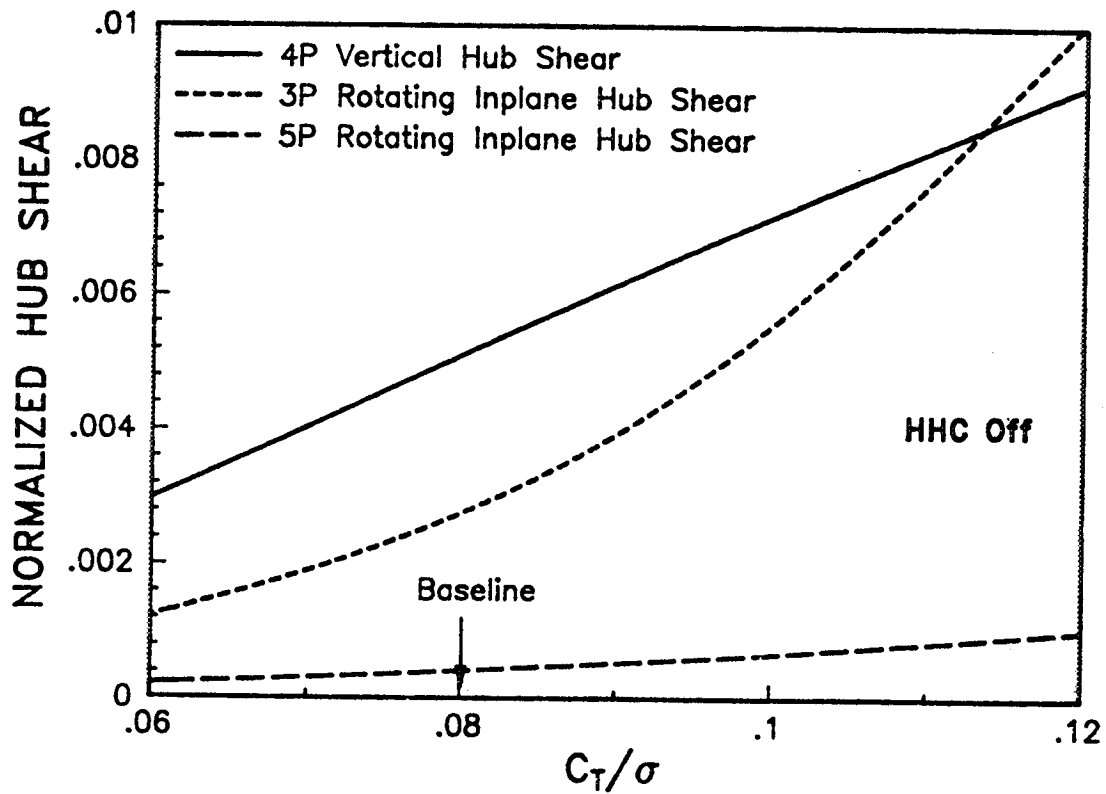


Figure 3.54. Effects of rotor thrust on the uncontrolled vibratory hub shears ($V = 40$ knots, $C_T/\sigma = 0.08$).

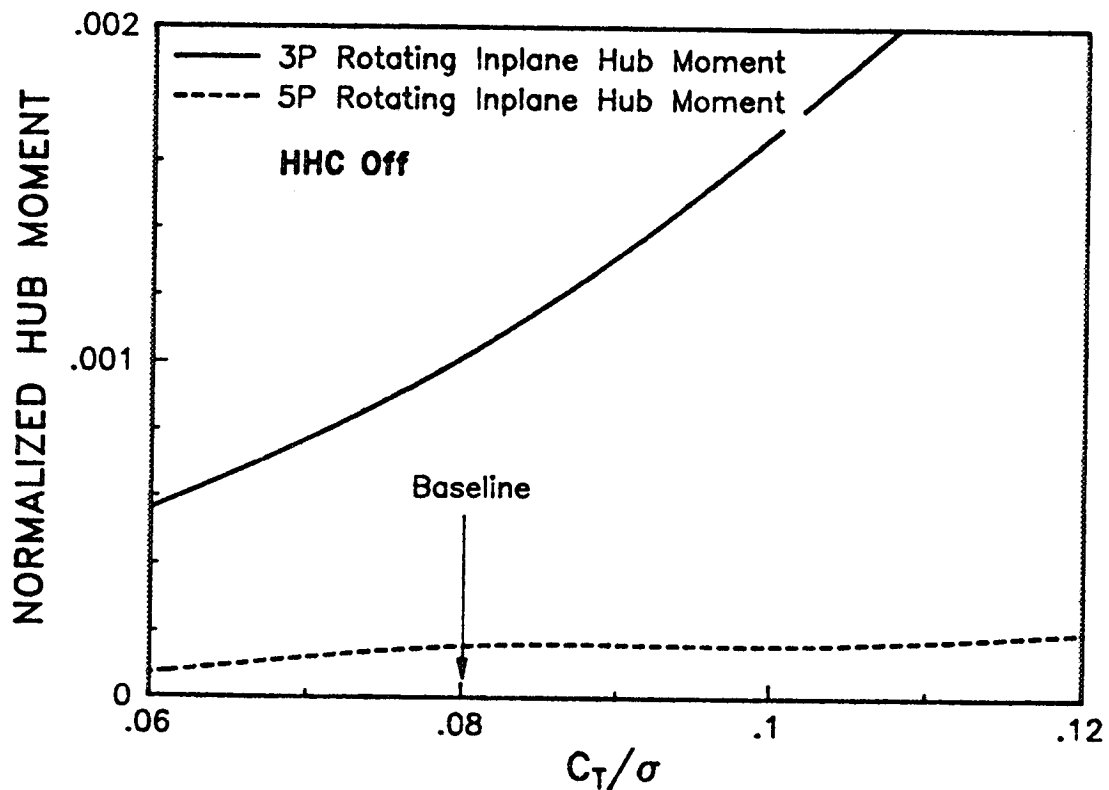


Figure 3.55. Effects of rotor thrust on the uncontrolled vibratory hub moments ($V = 40$ knots, $C_T/\sigma = 0.08$).

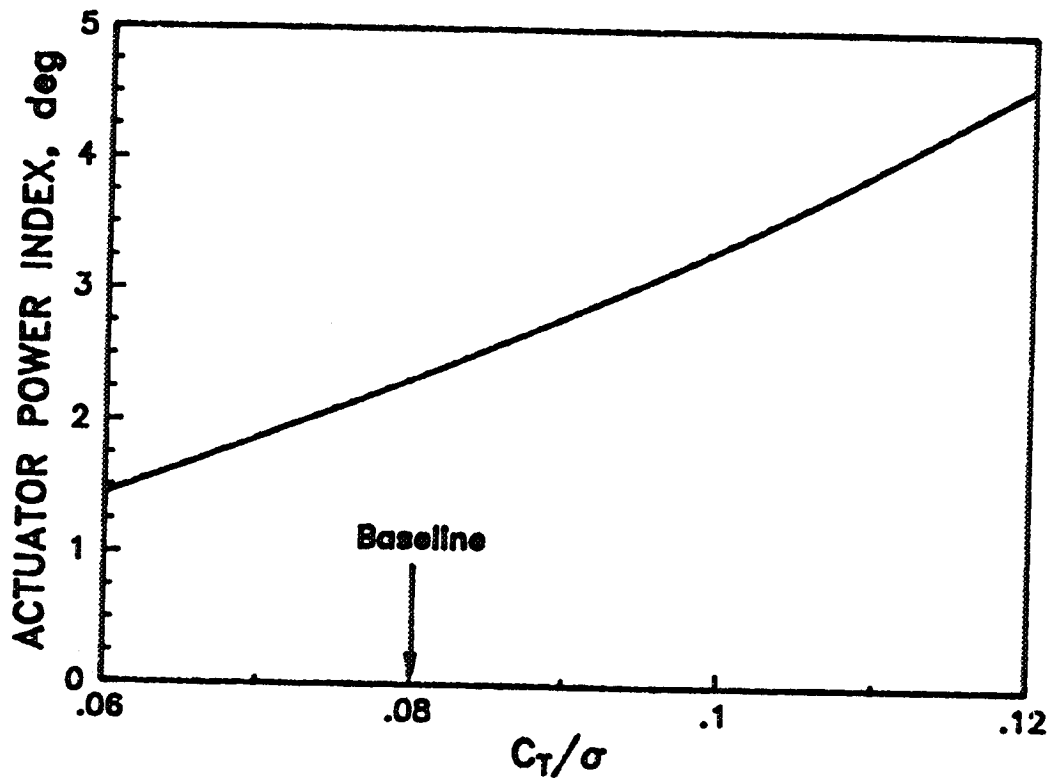


Figure 3.56. Effects of rotor thrust on the HHC actuator power ($V = 40$ knots, $C_T/\sigma = 0.08$).

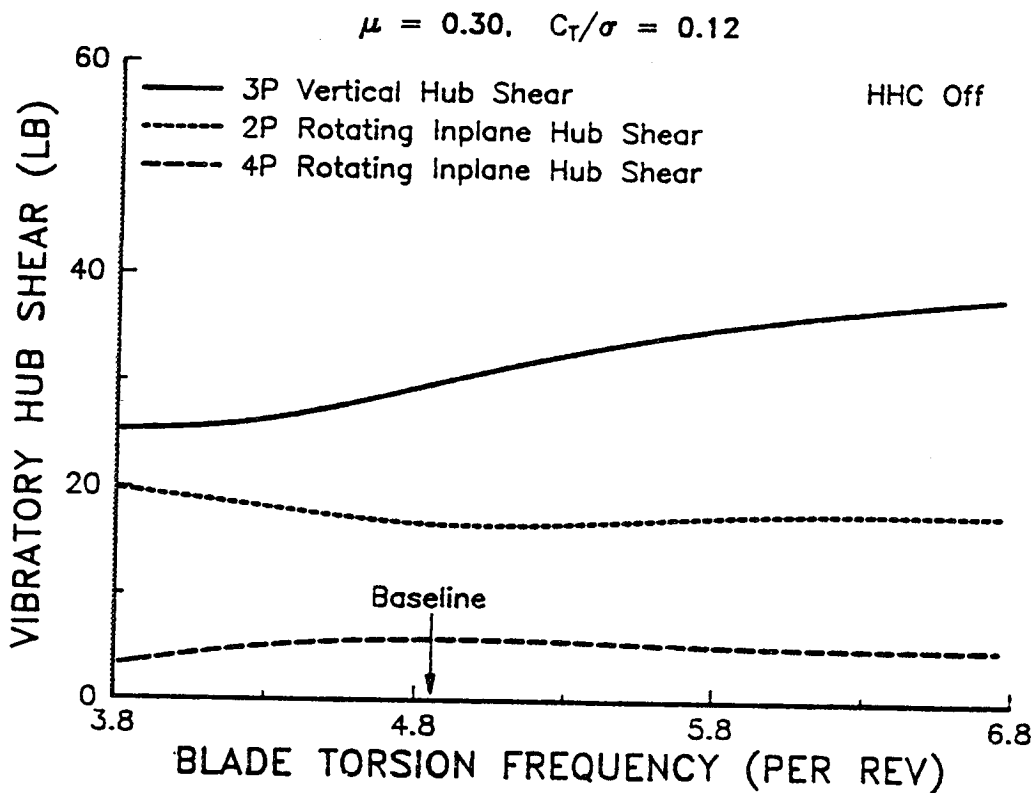


Figure 3.57. Effects of blade torsion stiffness on the uncontrolled vibratory hub shears ($V = 135$ knots, $C_T/\sigma = 0.12$).

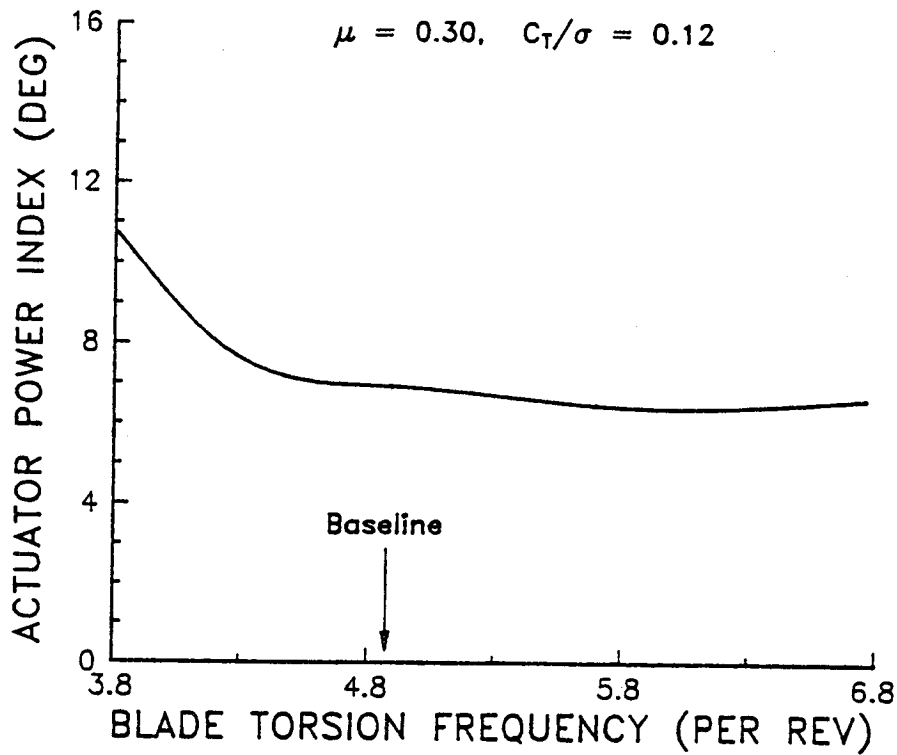


Figure 3.58. Effects of blade torsion stiffness on the HHC actuator power ($V = 135$ knots, $C_T/\sigma = 0.12$).

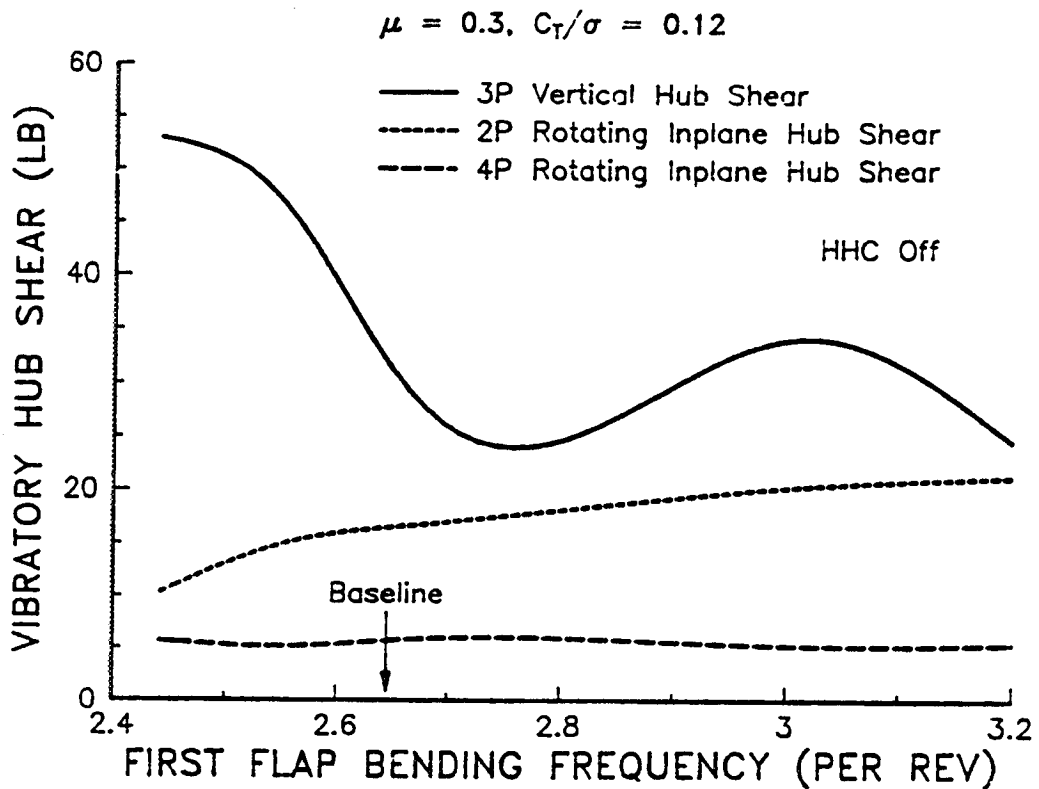


Figure 3.59. Effects of blade flap stiffness on the uncontrolled vibratory hub shears ($V = 135$ knots, $C_T/\sigma = 0.12$).

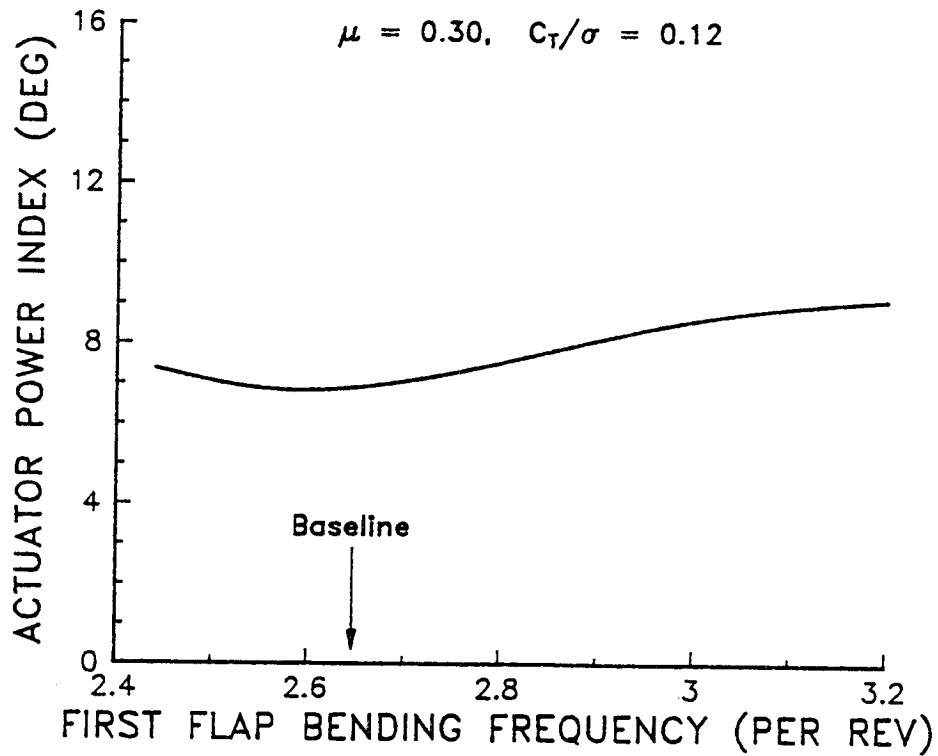


Figure 3.60. Effects of blade flap stiffness on the HHC actuator power ($V = 135$ knots, $C_T/\sigma = 0.12$).

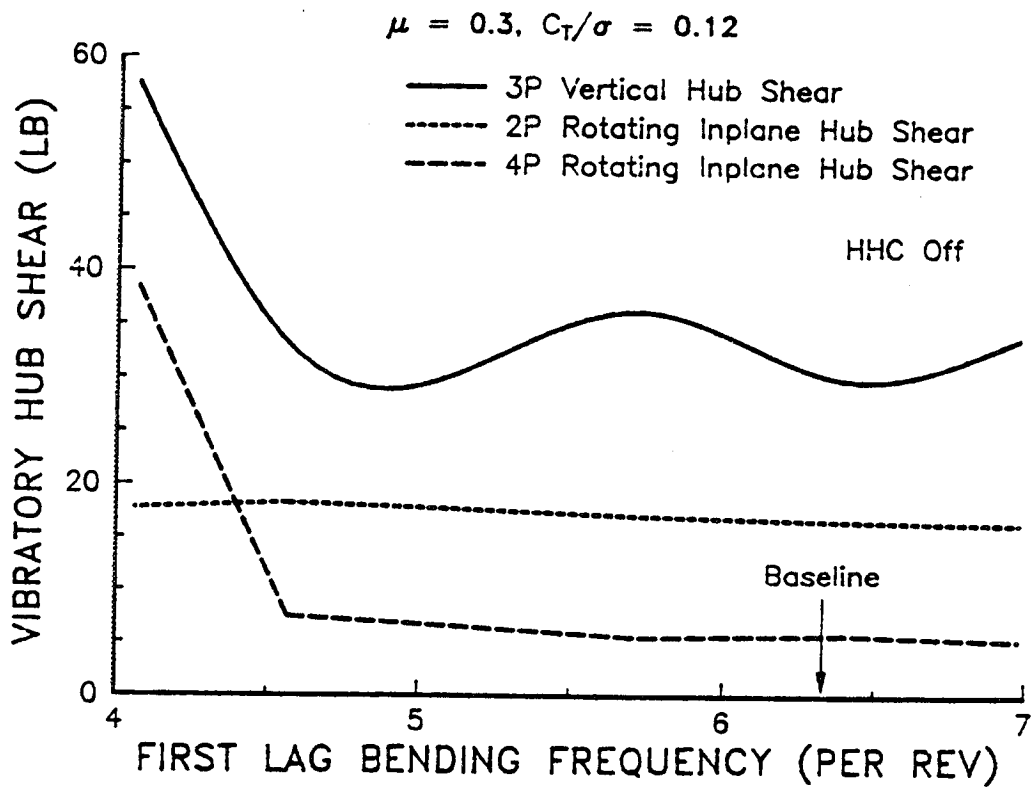


Figure 3.61. Effects of blade lag stiffness on the uncontrolled vibratory hub shears ($V = 135$ knots, $C_T/\sigma = 0.12$).

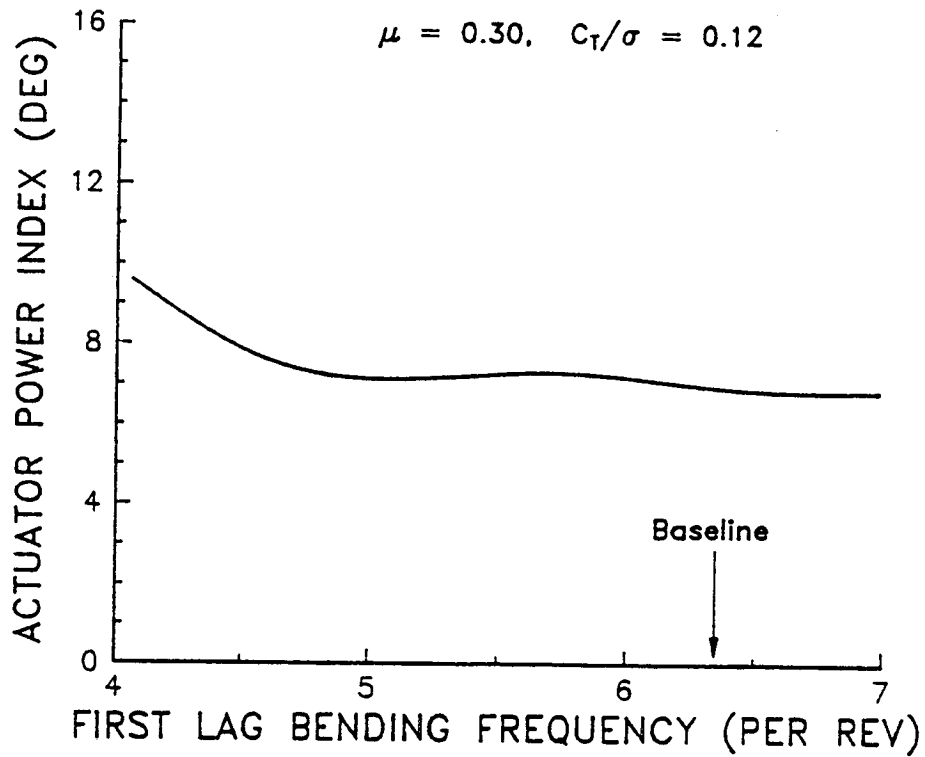


Figure 3.62. Effects of blade lag stiffness on the HHC actuator power ($V = 135$ knots, $C_T/\sigma = 0.12$).

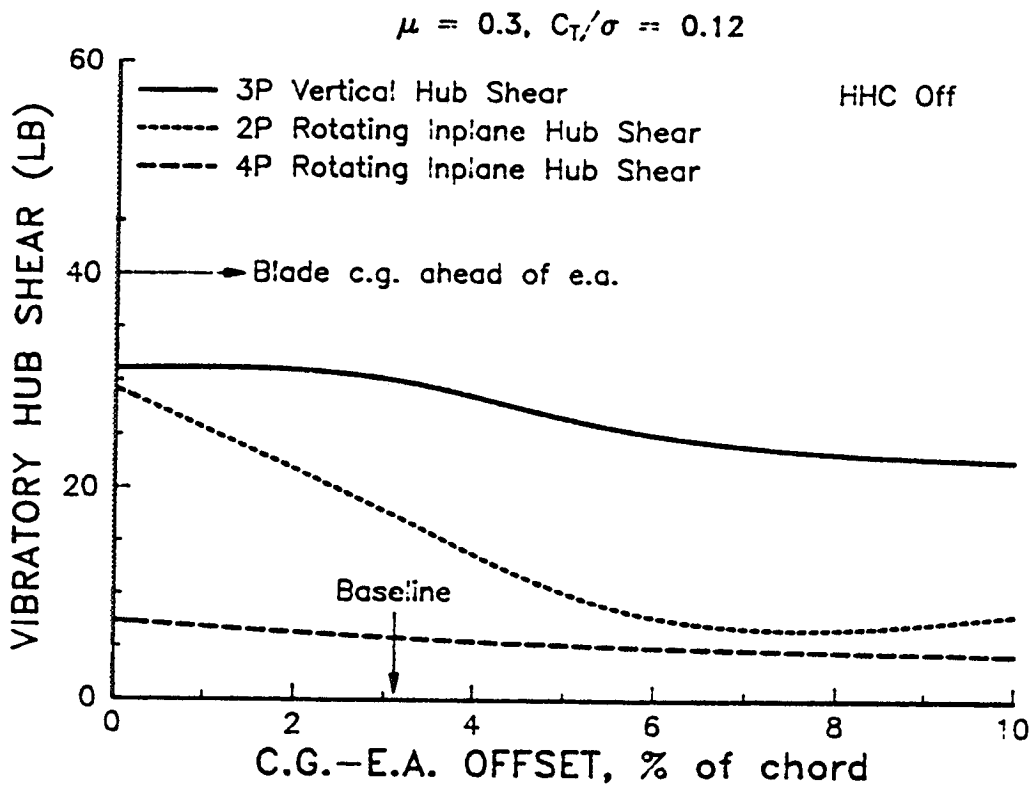


Figure 3.63. Effects of blade center-of-mass offset from elastic axis on the uncontrolled vibratory hub shears ($V = 135$ knots, $C_T/\sigma = 0.12$).

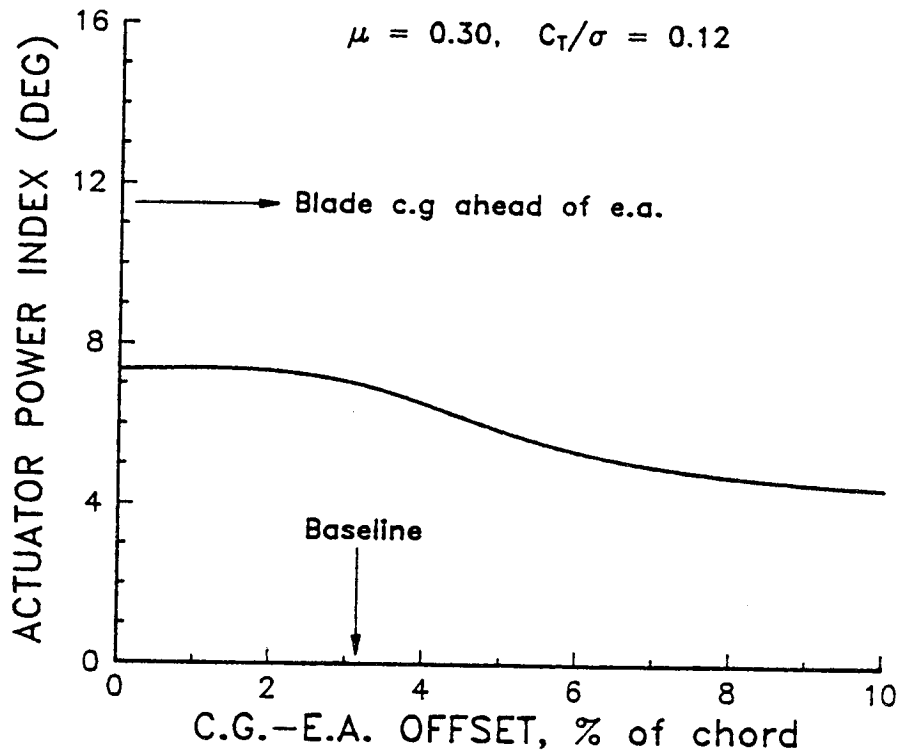


Figure 3.64. Effects of blade center-of-mass offset from elastic axis on the HHC actuator power ($V = 135$ knots, $C_T/\sigma = 0.12$).

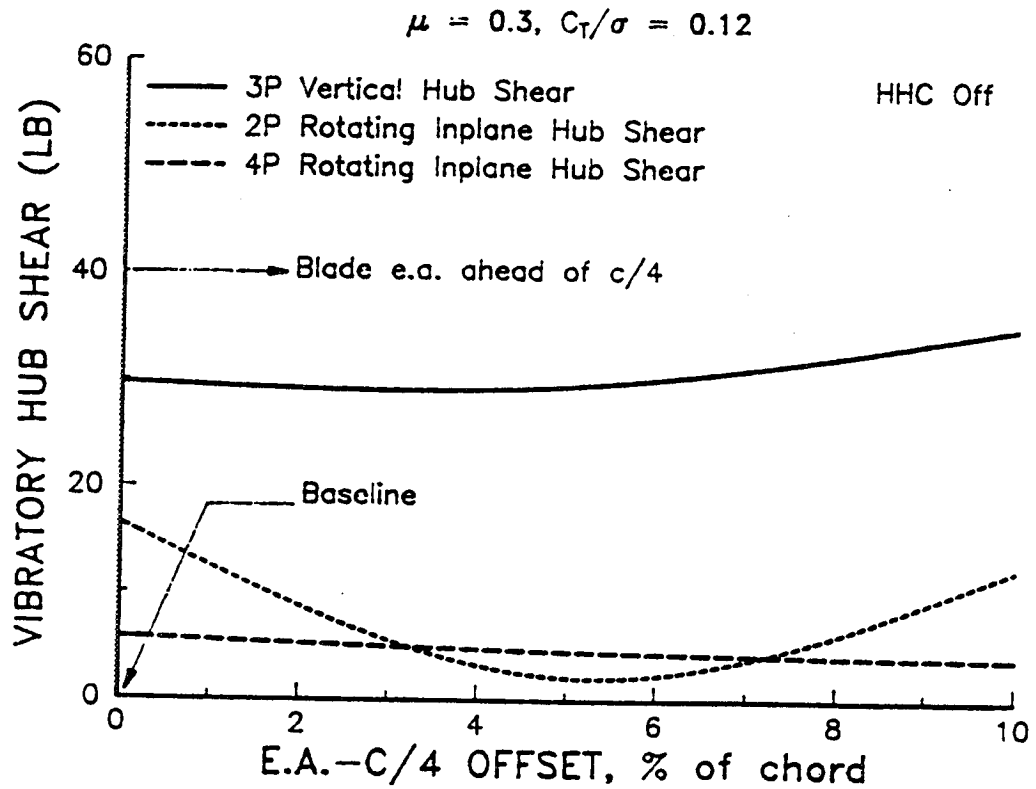


Figure 3.65. Effects of blade elastic axis offset from quarter chord on the uncontrolled vibratory hub shears ($V = 135$ knots, $C_T/\sigma = 0.12$).

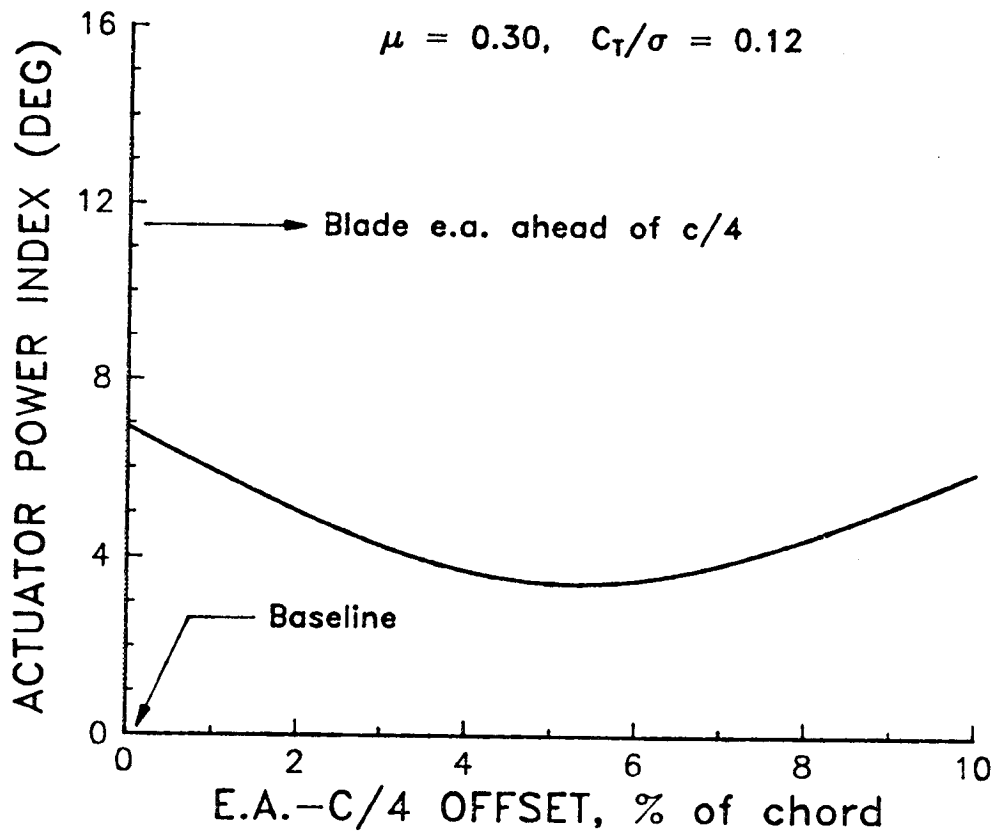


Figure 3.66. Effects of blade elastic axis offset from quarter chord on the HHC actuator power ($V = 135$ knots, $C_T/\sigma = 0.12$).

REPORT DOCUMENTATION PAGE

Form Approved
OMB No. 0704-0188

Public reporting burden for this collection of information is estimated to average 1 hour per response, including the time for reviewing instructions, searching existing data sources, gathering and maintaining the data needed, and completing and reviewing the collection of information. Send comments regarding this burden estimate or any other aspect of this collection of information, including suggestions for reducing this burden, to Washington Headquarters Services, Directorate for Information Operations and Reports, 1215 Jefferson Davis Highway, Suite 1204, Arlington, VA 22202-4302, and to the Office of Management and Budget, Paperwork Reduction Project (0704-0188), Washington, DC 20503.

1. AGENCY USE ONLY (Leave blank)		2. REPORT DATE October 1994	3. REPORT TYPE AND DATES COVERED Technical Memorandum	
4. TITLE AND SUBTITLE Higher Harmonic Control Analysis for Vibration Reduction of Helicopter Rotor Systems			5. FUNDING NUMBERS 505-61-51	
6. AUTHOR(S) Khanh Q. Nguyen				
7. PERFORMING ORGANIZATION NAME(S) AND ADDRESS(ES) Ames Research Center Moffett Field, CA 94035-1000			8. PERFORMING ORGANIZATION REPORT NUMBER A-91113	
9. SPONSORING/MONITORING AGENCY NAME(S) AND ADDRESS(ES) National Aeronautics and Space Administration Washington, DC 20546-0001			10. SPONSORING/MONITORING AGENCY REPORT NUMBER NASA TM-103855	
11. SUPPLEMENTARY NOTES Point of Contact: Khanh Q. Nguyen, Ames Research Center, MS T12-B, Moffett Field, CA 94035-1000; (415) 604-5043				
12a. DISTRIBUTION/AVAILABILITY STATEMENT Unclassified — Unlimited Subject Category 01			12b. DISTRIBUTION CODE	
13. ABSTRACT (Maximum 200 words) An advanced higher harmonic control (HHC) analysis has been developed and applied to investigate its effect on vibration reduction levels, blade and control system fatigue loads, rotor performance, and power requirements of servo-actuators. The analysis is based on a finite element method in space and time. A nonlinear time domain unsteady aerodynamic model, based on the indicial response formulation, is used to calculate the airloads. The rotor induced inflow is computed using a free wake model. The vehicle trim controls and blade steady responses are solved as one coupled solution using a modified Newton method. A linear frequency-domain quasi-steady transfer matrix is used to relate the harmonics of the vibratory hub loads to the harmonics of the HHC inputs. Optimal HHC is calculated from the minimization of the vibratory hub loads expressed in term of a quadratic performance index. Predicted vibratory hub shears are correlated with wind tunnel data. The fixed-gain HHC controller suppresses completely the vibratory hub shears for most of steady or quasi-steady flight conditions. HHC actuator amplitudes and power increase significantly at high forward speeds (above 100 knots). Due to the applied HHC, the blade torsional stresses and control loads are increased substantially. For flight conditions where the blades are stalled considerably, the HHC input-output model is quite nonlinear. For such cases, the adaptive-gain controller is effective in suppressing vibratory hub loads, even though HHC may actually increase stall areas on the rotor disk. The fixed-gain controller performs poorly for such flight conditions. Comparison study of different rotor systems indicates that a soft-inplane hingeless rotor requires less actuator power at high speeds (above 130 knots) than an articulated rotor, and a stiff-inplane hingeless rotor generally requires more actuator power than an articulated or a soft-inplane hingeless rotor. Parametric studies for a hingeless rotor operating in a transition flight regime and for an articulated rotor operating at the level-flight boundary (high speed and high thrust conditions) indicate that blade parameters including flap, lag, torsion stiffness distributions, linear pretwist, chordwise offset of center-of-mass from elastic axis and chordwise offset of elastic axis from aerodynamic center can be selected to minimize the actuator power requirements for HHC.				
14. SUBJECT TERMS Higher harmonic control analysis, Fixed- and adaptive-gain controllers, HHC induced stall, Actuator power, Parametric study			15. NUMBER OF PAGES 139	
			16. PRICE CODE A07	
17. SECURITY CLASSIFICATION OF REPORT Unclassified	18. SECURITY CLASSIFICATION OF THIS PAGE Unclassified	19. SECURITY CLASSIFICATION OF ABSTRACT	20. LIMITATION OF ABSTRACT	